

Ministry of Education and Science of Ukraine
Sumy State University



JOURNAL OF ENGINEERING SCIENCES

Scientific Journal

Volume 8, Issue 2 (2021)

ISSN 2312-2498 (print)
ISSN 2414-9381 (online)

Founded in 2014

Journal of Engineering Sciences is an open-access peer-reviewed scientific journal. It covers urgent issues of up-to-date high-tech production in developing new engineering trends and future technologies. The general topics of the journal include manufacturing, mechanical, and chemical engineering. The publication language is English. The editorial board is represented by scientists from different international research institutions covering the journal's topics and evaluating all the submitted articles. The system of double-blinded review provides a high-quality presentation of articles. The editorial policy, including submission, review, acceptance, and publication of articles, is entirely transparent.

The journal was founded in 2014. It is published by Sumy State University of Ministry of Education and Science of Ukraine under the support of the International Association for Technological Development and Innovations.

ISSN 2312-2498 (print)
ISSN 2414-9381 (online)

The journal is intended for a wide range of scientists, researchers, practitioners, and others interested in manufacturing, mechanical, and chemical engineering. All the publications in the journal are free of articles processing charges (APCs) and articles submission charges.

*Recommended for publication
by the Academic Council of Sumy State University,
(minutes No. 6 of 16.12.2021)*

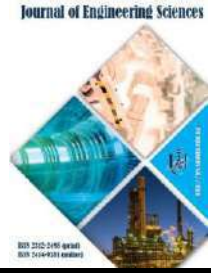
The journal is the scientific professional edition of Ukraine (Category “B”) in Engineering Sciences ordered by the Ministry of Education and Science of Ukraine, November 7, 2018, No. 1218.

Partners:

- International Association for Technological Development and Innovations, <http://iatdi.org>;
- Ministry of Education and Science of Ukraine, <https://mon.gov.ua>;
- Faculty of Mechanical Engineering and Management, Poznan University of Technology (Poland), <https://www.put.poznan.pl>;
- Faculty of Manufacturing Technologies with a seat in Prešov, Technical University of Košice (Slovakia), <http://www.fvt.tuke.sk>;
- Faculty of Mechanical Engineering of University of West Bohemia (Czech Republic), <http://www.fst.zcu.cz>.

Editorial Board: 2, Rymkogo-Korsakova St., 40007, Sumy, Ukraine; Apt. M-211
Contact Phone: +380-993-845-740
E-mail: jes@teset.sumdu.edu.ua
Website: <http://jes.sumdu.edu.ua>

State registration certificate of the print mass-media No. 20499-10299 PR.



TOPICS

Manufacturing Engineering:

- Machines and Tools;
- Technical Regulations and Metrological Support;
- Materials Science.

Mechanical Engineering:

- Dynamics and Strength of Machines;
- Computational Mechanics.

Chemical Engineering:

- Processes in Machines and Devices;
- Energy Efficient Technologies;
- Environmental Protection.

STATISTICS

- **Publication frequency:** biannually (2 issues per year)
- **Papers per issue:** 20
- **Acceptance rate:** 26 %
- **Timeline:**
 - days from submission of the manuscript to first decision: 30
 - days from acceptance at the publisher to published online: 14
- **Editorial Board:**
 - members: 67
 - institutions: 46
 - countries: 25

EDITOR-IN-CHIEF

Ivan PAVLENKO, DSc., Professor, Sumy State University, Sumy, Ukraine

DEPUTY EDITOR-IN-CHIEF

Vitalii IVANOV, DSc., Professor, Sumy State University, Sumy, Ukraine

BOARD OF CO-EDITORS

Manufacturing Engineering

Erwin RAUCH, Ph.D., Professor, Free University of Bozen-Bolzano, Bolzano, Italy

Jose MACHADO, Ph.D., Professor, University of Minho, Braga, Portugal

Mechanical Engineering

Jan PITEL, Ph.D., Professor, Technical University of Kosice, Presov, Slovakia

Noel BRUNETIERE, Ph.D., Senior Researcher, University of Poitiers, Poitiers, France

Oleksandr POGREBNIYAK, DSc., Professor, Sumy State University, Sumy, Ukraine

Chemical Engineering

Alex-Enrich PRAST, Ph.D., Professor, Linkoping University, Linkoping, Sweden

Mathieu GAUTIER, Ph.D., Professor, University of Lyon, Lyon, France

INTERNATIONAL EDITORIAL BOARD

Praveen AGARWAL, Ph.D., Professor, Anand International College of Engineering, Jaipur, India

Katarzyna ANTOSZ, DSc., Associate Professor, Rzeszow University of Technology, Rzeszow, Poland

Peter ARRAS, DSc., Professor, KU Leuven, Leuven, Belgium

Viktor ASTAKHOV, DSc., Professor, Production Service Management Inc., Ann Arbor, USA

Volodymyr ATAMANYUK, DSc., Professor, Lviv Polytechnic National University, Lviv, Ukraine

Eddy BAJIC, Ph.D., Professor, University of Lorraine, Nancy, France

Marian BARTOSZUK, Ph.D., Professor, Opole University of Technology, Opole, Poland

Jean BOUYER, Ph.D., Associate Professor, University of Poitiers, Poitiers, France

Robert CEP, Ph.D., Professor, Technical University of Ostrava, Ostrava, Czech Republic

Olaf CISAK, Ph.D., Associate Professor, Poznan University of Technology, Poznan, Poland

Predrag DASIC, DSc., Professor, VTMS Trstenik, Trstenik, Serbia

Kostiantyn DYADYURA, DSc., Professor, Odessa Polytechnic State University, Odessa, Ukraine

Milan EDL, Ph.D., Associate Professor, University of West Bohemia, Pilsen, Czech Republic

Domenico GUIDA, Ph.D., Professor, University of Salerno, Salerno, Italy

Oleksandr GUSAK, Ph.D., Professor, Sumy State University, Sumy, Ukraine

Michal HATALA, Ph.D., Professor, Technical University of Kosice, Presov, Slovakia

Koichi HASEGAWA, Ph.D., Associate Professor, Chubu University, Kasugai, Japan

Siamak HOSEINZADEH, Ph.D., Post Doc., Sapienza University of Rome, Rome, Italy

Jozef HUSAR, Ph.D., Assistant Professor, Technical University of Kosice, Presov, Slovakia

Yury IVANOV, Ph.D., Associate Professor, Chubu University, Kasugai, Japan

Fuat KARA, Ph.D., Assistant Professor, Duzce University, Istanbul, Turkey

Isak KARABEGOVIC, DSc., Professor, University of Bihac, Bihac, Bosnia and Herzegovina

Jakub KASCAK, Ph.D., Assistant Professor, Technical University of Kosice, Presov, Slovakia

Serhii KLIMENKO, DSc., Professor, Bakul Institute for Superhard Materials, National Academy of Sciences of Ukraine, Kyiv, Ukraine

Dmytro KRYVORUCHKO, DSc., Associate Professor, Sumy State University, Sumy, Ukraine
Czeslaw KUNDERA, DSc., Professor, Kielce University of Technology, Kielce, Poland
Ivan KURIC, Ph.D., Professor, University of Zilina, Zilina, Slovakia
Milovan LAZAREVIC, Ph.D., Associate Professor, University of Novi Sad, Novi Sad, Serbia
Stanislaw LEGUTKO, DSc., Professor, Poznan University of Technology, Poznan, Poland
Oleksandr LIAPOSHCHENKO, DSc., Professor, Sumy State University, Sumy, Ukraine
Athanasios MAMALIS, DSc., Professor, Demokritos National Centre for Scientific Research, Athens, Greece
Arun MATHEW, Ph.D., Associate Professor, Vellore Institute of Technology, Vellore, India
Thomas MATHIA, Ph.D., Professor, Ecole Centrale de Lyon, Lyon, France
Yurii MATSEVITYI, DSc., Professor, Podgorny Institute for Mechanical Engineering Problems, National Academy of Sciences of Ukraine, Kharkiv, Ukraine
Ronald MERSKY, Ph.D., Associate Professor, Widener University, Chester, USA
Arun NAGARAJAH, DSc., Professor, University of Duisburg-Essen, Duisburg, Germany
Eduard Laurentiu NITU, Ph.D., Professor, University of Pitesti, Pitesti, Romania
Dragan PERAKOVIC, Ph.D., Professor, University of Zagreb, Zagreb, Croatia
Alejandro PEREIRA, Ph.D., Professor, University of Vigo, Vigo, Spain
Yurii PETRAKOV, DSc., Professor, National Technical University of Ukraine “Kyiv Polytechnic Institute”, Kyiv, Ukraine
Roman PETRUS, DSc., Professor, Rzeszow University of Technology, Rzeszow, Poland
Leonid PLYATSUK, DSc., Professor, Sumy State University, Sumy, Ukraine
Frantisek POCHYLÝ, Ph.D., Professor, Brno University of Technology, Brno, Czech Republic
Yimin RONG, DSc., Professor, South University of Science and Technology, Shenzhen, China
Vitalii SIMONOVSKIY, DSc., Professor, Sumy State University, Sumy, Ukraine
Vsevolod SKLABINSKYI, DSc., Professor, Sumy State University, Sumy, Ukraine
Michael STORCHAK, DSc., Professor, Institute for Machine Tools of Stuttgart University, Stuttgart, Germany
Fabio TEIXEIRA, DSc., Professor, Federal University of Rio Grande do Sul, Porto Alegre, Brazil
Justyna TROJANOWSKA, Ph.D., Assistant Professor, Poznan University of Technology, Poznan, Poland
Kaname TSUTSUMIUCHI, DSc., Professor, Chubu University, Kasugai, Japan
Raul TURMANIDZE, DSc., Professor, Georgian Technical University, Tbilisi, Georgia
Michal VARCHOLA, Ph.D., Professor, Slovak University of Technology in Bratislava, Bratislava, Slovakia
George-Christopher VOSNIAKOS, Ph.D., Professor, National Technical University of Athens, Athens, Greece
Jozef ZAJAC, DSc., Professor, Technical University of Kosice, Presov, Slovakia
Viliam ZALOGA, DSc., Professor, Sumy State University, Sumy, Ukraine
Lianyu ZHENG, Ph.D., Professor, Beihang University, Beijing, China

PUBLISHING MANAGER

Kristina BERLADIR, Ph.D., Senior Lecturer, Sumy State University, Sumy, Ukraine

MARKETING AND COMMUNICATION MANAGER

Vladyslav KONDUS, Ph.D., Senior Lecturer, Sumy State University, Ukraine

**CONTENTS****MANUFACTURING ENGINEERING****Machines and Tools**

- Shvets S. V., Machado J.
Numerical model of cutting tool blade wear A1–A5
DOI: [10.21272/jes.2021.8\(2\).a1](https://doi.org/10.21272/jes.2021.8(2).a1)

Technical Regulations and Metrological Support

- Panchuk V., Onysko O., Kotwica K., Barz C., Borushchak L.
Prediction of the accuracy of the tapered thread profile B1–B6
DOI: [10.21272/jes.2021.8\(2\).b1](https://doi.org/10.21272/jes.2021.8(2).b1)

- Lasinska N.
Hybrid management methodology for transport projects related to rolling stock B7–B11
DOI: [10.21272/jes.2021.8\(2\).b2](https://doi.org/10.21272/jes.2021.8(2).b2)

- Rudenko S., Berladir K., Trojanowska J., Varenik S., Shvetsov D., Kravets V.
Application of FMEA for assessment of the polymer composite materials quality B12–B18
DOI: [10.21272/jes.2021.8\(2\).b3](https://doi.org/10.21272/jes.2021.8(2).b3)

Materials Science

- Kolawole, M. Y., Awoyemi E. A., Abiona, O. M.
Potentials of date-seed/snail shells as a carburizer for enhanced mechanical properties of mild-steel C1–C6
DOI: [10.21272/jes.2021.8\(2\).c1](https://doi.org/10.21272/jes.2021.8(2).c1)

- Olawore A. S., Oladosu K. O., Sadiq T. O., Ahmed M., Adesope W. A.
Effects of cold extrusion on the mechanical properties of scrapped copper coil C7–C12
DOI: [10.21272/jes.2021.8\(2\).c2](https://doi.org/10.21272/jes.2021.8(2).c2)

- Hovorun T., Khaniukov K., Varakin V., Pererva V., Vorobiov S., Burlaka A., Khvostenko R.
Improvement the physical and mechanical properties of the cutting tool
by applying wear-resistant coatings based on Ti, Al, Si, and N C13–C23
DOI: [10.21272/jes.2021.8\(2\).c3](https://doi.org/10.21272/jes.2021.8(2).c3)

- Harikrishna V., Kumar K. V.
Mechanical behaviors of hybrid composites reinforced with epoxy resin C24–C29
DOI: [10.21272/jes.2021.8\(2\).c4](https://doi.org/10.21272/jes.2021.8(2).c4)

- Chernobrovchenko V. S., Dyadyura K. O., Panda A.
Investigation of the blockchain structure for hydroxyapatite-based scaffolds C30–C35
DOI: [10.21272/jes.2021.8\(2\).c5](https://doi.org/10.21272/jes.2021.8(2).c5)

MECHANICAL ENGINEERING**Dynamics and Strength of Machines**

- Chelabi M. A., Basova Y., Hamidou M. K., Dobrotvorskiy S.
Analysis of the three-dimensional accelerating flow in a mixed turbine rotor D1–D7
DOI: [10.21272/jes.2021.8\(2\).d1](https://doi.org/10.21272/jes.2021.8(2).d1)

Verbovyi A., Khomenko V., Neamtu C., Pavlenko V., Cherednyk M., Vashyst, B., Pavlenko I.
Parameter identification of nonlinear bearing stiffness for turbopump units
of liquid rocket engines considering initial gaps and axial preloading
DOI: [10.21272/jes.2021.8\(2\).d2](https://doi.org/10.21272/jes.2021.8(2).d2) D8–D11

Onysko O., Karabegović I., Dašić P., Penderetskyi M., Melnyk O.
The stress state of compact mechatronic satellites of a cycloidal reducer
DOI: [10.21272/jes.2021.8\(2\).d3](https://doi.org/10.21272/jes.2021.8(2).d3) D12–D17

Computational Mechanics

Kanagasabai L.
Real power loss reduction by enhanced RBS algorithm
DOI: [10.21272/jes.2021.8\(2\).e1](https://doi.org/10.21272/jes.2021.8(2).e1) E1–E9

CHEMICAL ENGINEERING

Processes in Machines and Devices

Kozii I. S., Plyatsuk L. D., Hurets L. L., Volnenko A. A.
Capturing aerosol particles in a device with a regular pulsating nozzle
DOI: [10.21272/jes.2021.8\(2\).f1](https://doi.org/10.21272/jes.2021.8(2).f1) F1–F5

Kun T., Jie H. W., Markovych S., Wang Y.
Dimet Laval nozzle expansion section analysis and optimization
DOI: [10.21272/jes.2021.8\(2\).f2](https://doi.org/10.21272/jes.2021.8(2).f2) F6–F10

Javanbakht T.
Comparative study of rheological properties of polyvinyl alcohol and polyethylene glycol
DOI: [10.21272/jes.2021.8\(2\).f3](https://doi.org/10.21272/jes.2021.8(2).f3) F11–F18

Advanced Energy Efficient Technologies

Ostroverkh A. S., Solomin Yu. M., Bezdorozhev O. V., Ostroverkh Y. M.,
Shcherbatiuk O. M., Dubau M., Kovalenko L. L.
Challenges of fuel cell technologies for the needs of the energy transition to a zero-carbon technology
DOI: [10.21272/jes.2021.8\(2\).g1](https://doi.org/10.21272/jes.2021.8(2).g1) G1–G10

Onyeka V. O., Nwobi-Okoye C. C., Okafor O. C., Madu K. E., Mbah O. M.
Estimation of global solar radiation using empirical models
DOI: [10.21272/jes.2021.8\(2\).g2](https://doi.org/10.21272/jes.2021.8(2).g2) G11–G19

Environmental Protection

Alekseevsky D. G., Chernysh Ye. Yu., Shtepa V. N.
Formalization of the task of creating a mathematical model
of combined wastewater treatment processes
DOI: [10.21272/jes.2021.8\(2\).h1](https://doi.org/10.21272/jes.2021.8(2).h1) H1–H7

Chernysh Y., Plyatsuk L., Roubik H., Yakhnenko O., Skvortsova P., Bataltsev Y.
Application of technological solutions for bioremediation of soils contaminated with heavy metals
DOI: [10.21272/jes.2021.8\(2\).h2](https://doi.org/10.21272/jes.2021.8(2).h2) H8–H16



5th International Conference on Design, Simulation, Manufacturing: The Innovation Exchange June 7-10, 2022 | Sumy, Ukraine



Together we can do more for science, technology, engineering, and education. © DSMIE Team



Together we can do more for science, technology, engineering, and education. © DSMIE Team



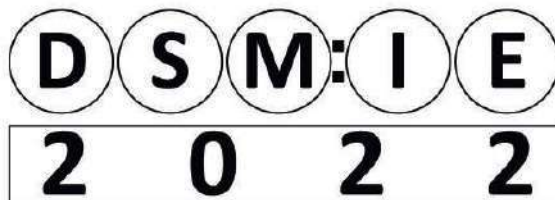
DSMIE-2022 focuses on research challenges in the fields of Manufacturing Engineering, Materials Engineering, Mechanical Engineering, and Chemical Engineering, addressing current and future trends in design approaches, simulation techniques, manufacturing technologies, computer-aided systems and ICT tools and Industry 4.0 strategy implementation for engineering tasks solving.

Full research papers will be published as Conference Proceedings in Lecture Notes in Mechanical Engineering (ISSN 2195-4356, Springer Nature), indexed by Scopus and submitted to Web of Science Core Collection databases.

Paper submission is supported by EasyChair Conference Management System. The deadline is October 15, 2021.



5th Anniversary



5th International Conference on Design, Simulation, Manufacturing: The Innovation Exchange

June 7-10, 2022 | Sumy, Ukraine

<http://dsmie.sumdu.edu.ua>

Organized by Sumy State University and International Association for Technological Development and Innovations, in partnership with Technical University of Kosice, Kielce University of Technology, University of West Bohemia, Poznan University of Technology, Association for Promoting Innovative Technologies - InnovativeFET, Society for Robotics of Bosnia and Herzegovina

Agenda

- June 7 | Registration
- June 8 | Keynote Sessions & Round Table
- June 9 | Technical Sessions & Industry Tour
- June 10 | Technical Sessions & Awards

Contacts

- ✉ dsmie@teset.sumdu.edu.ua
- 📘 DSMIEConferenceSeries
- 🌐 DSMIEConferenceSeries



DSMIE-2022

Where science, industry, and education meet

5th International Conference on Design, Simulation, Manufacturing: The Innovation Exchange



Shvets S. V., Machado J. (2021). Numerical model of cutting tool blade wear. *Journal of Engineering Sciences*, Vol. 8(2), pp. A1-A5, doi: 10.21272/jes.2021.8(2).a1

Numerical Model of Cutting Tool Blade Wear

Shvets S. V.¹, Machado J.²[0000-0002-4917-2474]

¹ Sumy State University, 2, Rymskogo-Korsakova St., 40007 Sumy, Ukraine;

² University of Minho, Campus de Azurém, 4804-533 Guimarães, Portugal

Article info:

Submitted:

July 22, 2021

Accepted for publication:

December 7, 2021

Available online:

December 11, 2021

*Corresponding email:

shvetssta@gmail.com

Abstract. The article investigates a numerical model of wear for cutting tools. The use of the parametric model of the cutting tool blade, under the required values of angles γ , α , α^1 , φ , φ^1 , and λ forms the corresponding working part, the dependences of the wear of the blade on the flank on the size of the worn surface. This allows analyzing the effect of blade geometry and wear parameters on the flank on energy consumption during tool wear calculate the work of blade wear at any amount of tool wear. It turned out that the dependences of wear on the flank h_3 on the main φ and the auxiliary φ^1 angles in the plan are linear. With increasing angles φ , φ^1 , α , and α^1 decreases the work U_h required to achieve given wear on the flank h_3 , and with increasing angles γ and λ , such work increases. Thus, mechatronics combines knowledge and mechanics of wear, electronic parametric model, empirical dependence of wear of the cutting tool.

Keywords: wear, cutting tool, parametric model, blade geometry, wear work.

1 Introduction

Modern metalworking equipment consists of machines, cutting tools, mechanization, and automation tools and devices. Machines and tools are the main components of the technological system of cutting, providing the technological process in dynamic interaction with all other system components.

Modern CNC machine tools are based on integrating mechanical, electronic, and information devices: mechanisms and tools, electronic channels and sensors of direct and feedback, microprocessors, controllers, and computers.

Thus, modern CNC machine tools are mechatronic systems. As you know, “mechatronics is a synergistic integration of mechanical engineering with electronics and intelligent computer control in the design and manufacture of industrial products and processes. Mechatronics combines mechanical systems (mechanical elements, components, and machines), electronic systems (microelectronics, sensor, and executive technology), and information technology. Thus, mechatronic systems are a complex integration of extremely advanced technological components that can perform tasks with high accuracy and flexibility” [1].

Accordingly, the mechatronics of machining materials is a science that integrates knowledge of the process of

chip formation and wear of cutting tools, machine tools, electronics, computers, computer science, and software. It consists of logical and didactic building from fundamental concepts to modern theories.

The quality of machining and process productivity largely depends on the stability of cutting tools, so the analytical determination of wear at given radial and rear wear values is crucial for developing software for CNC machine tools. Determining the tool’s wear on the flank will allow you to develop such software to apply the optimal parameters of the technological process with the available geometry and tool material of the cutting wedge. This will help ensure the necessary product quality parameters with maximum productivity and duration of the cutting process.

2 Literature Review

In the cutting process, different types of blade wear are possible [2-4]. Temperature wear is possible because the blade loses its geometric shape under the action of temperature exceeding the critical value for this tool material. The blade may crack with a sharp change in temperature on its surfaces or break when struck and the formation of stresses exceeding the strength of the tool material. These types of wear can be prevented by adjusting the power and heat loads.

Many research works are devoted to studying blade wear [5-9]. However, there are no non-wearing kinematic pairs. When rubbing two materials of different strengths, both materials wear out (break down). This is since the friction is a cyclic loading of the contact areas and weakens the surface of even stronger material. Thus, the wear of tool material at contact with the process is inevitable, even at the minimum thermal and power loadings in a cutting zone. But, as you know, the formation of chips occurs under conditions of high temperatures and pressures.

Figure 1, under [10, 11], shows the foci of the setting of the processed (top) and tool (bottom) materials. At the single interaction, the processed material is destroyed. Tool material (as stronger) is not damaged. But repeated this process causes fatigue on the surface of the blade. The tensile strength of the tool material in the cyclic field setting is reduced, and there is destruction at some point. The most significant number of such seizures is the maximum number of load cycles of micro-areas. Avalanche of micro destruction – wear.

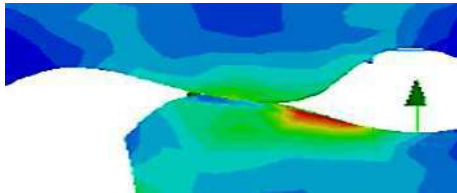


Figure 1 – Contact of surfaces of the processed and tool materials

This is adhesive fatigue wear. Fatigue wear can be observed without adhesion. This occurs during periodic (cyclic) contact of the micro protrusion of the tool material with the processed during their relative movement.

Therefore, with proper technological and instrumental training, which eliminates critical forces and temperatures on the blade surfaces, its wear occurs because of fatigue, which develops under the influence of cyclic loading of micro protrusions on its surface by the volume of the processed material.

3 Research Methodology

3.1 Complete wear work

The work performed can be defined as follows. Let the area of the surface layer of the tool material on area F with a thickness (or height) dx , according to Figure 1, under cyclic bending. Then the elementary work done in its destruction, J :

$$dU = \sigma_c \cdot dx \cdot F \cdot z = \sigma_c \cdot dW \cdot z, \quad (1)$$

where σ_c – the compressive strength of the tool material (for T15K6 – 4.12 GPa); dW – destroyed the elementary volume because of wear; z – the maximum, destructive number of cycles for tool material (for VK8, and T15K6 – $z = 10^5 - 10^6$ [12]).

From here, it is possible to write that the entire work of wear, J :

$$U = \sigma_c z \int dW = W \sigma_c z. \quad (2)$$

The shape and size of the wear surface the worn volume depend on the shape of the cutting wedge. Wear primarily develops at the top of the blade (Figure 2).

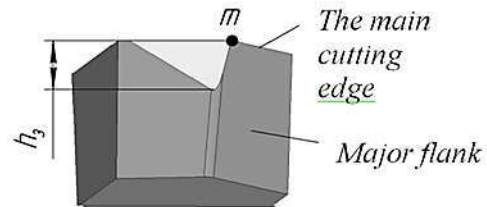


Figure 2 – Wear on the flank

The development of the wear area on the flank along the main cutting edge is limited by the depth of cut (point m). By cutting the blade material with a plane parallel to the cutting speed passing through the point m at different distances from the top, it is possible to simulate the development of blade wear on the flank. The wear criterion is often taken to be the maximum size of the worn surface, measured in the direction of the cutting speed, h_3 .

By choosing the value of the blade geometry (rear angles α and α^1 , angles in plan φ and φ^1 , rake angle γ , cutting edge angle λ), using the capabilities of modern graphic editors, you can calculate the worn volume at given wear on the rear surface h_3 . But it is quite difficult.

For engineering calculations, it is necessary to have a simple mathematical dependence, which can be created based on the analysis of the electronic model of blade wear (Figure 2).

3.2 Dependence of blade wear parameters on its geometry

In the graphic editor, we will form a blade of the cutting tool from preparation in the form of a parallelepiped. Let its initial geometry be: $\gamma = 0^\circ$, $\alpha = 12^\circ$, $\alpha^1 = 12^\circ$, $\varphi = 45^\circ$, $\varphi^1 = 15^\circ$, and $\lambda = 0^\circ$. Then we obtain an electronic parametric model of the blade of the cutting tool, which when setting the required values of angles (γ , α , α^1 , φ , φ^1 , and λ) forms the corresponding working part (Figure 3).

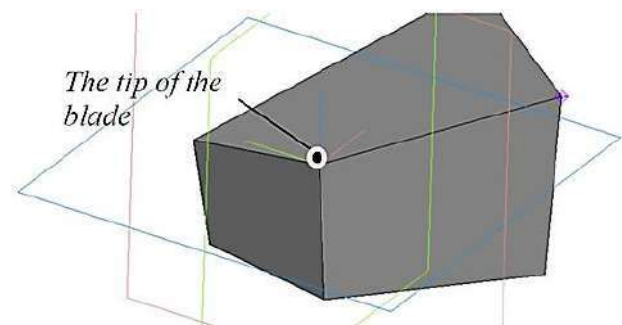


Figure 3 – Parametric model of the blade

Set the value of radial wear, h_r , as the distance from the coordinate plane YZ to the created parallel to it plane and cut the blade on this plane.

As a result, we get the worn volume of tool material W (Figure 4 a) and wear flank (Figure 4 b), the value of which is estimated as “wear on the back surface” h_3 (Figure 4 c) when the radial wear h_r .

Determine the amount of worn volume W . The values of worn volume and wear on the rear surface when changing the blade’s geometry are entered in the appropriate tables and built the appropriate graphs in Microsoft Excel.

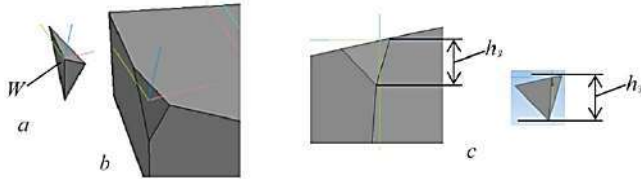


Figure 4 – Wear volume and wear on the tool flank

Construct the power dependences of the worn volume W on the main angle in plan φ at different values of radial wear h_r and find the arithmetic mean of all the established exponents:

$$x_\varphi = \frac{-0.507 - 0.527 - 0.479 - 0.512 - 0.51}{5} = -0.508.$$

Construct the power dependences of the worn volume W on the auxiliary angle in plan φ^1 at different values of radial wear h_r , allow to determine the arithmetic mean of all the established exponents:

$$x_{\varphi^1} = \frac{-0.969 - 0.961 - 0.922 - 0.947 - 0.949}{5} = -0.950.$$

The power dependences of the worn volume W on the main rear angle α at different values of radial wear h_r have an exponent:

$$x_\alpha = -0.269.$$

The power dependences of the worn volume W on the auxiliary rear angle α^1 at different values of radial wear h_r have an exponent:

$$x_{\alpha^1} = -0.730.$$

We construct the power dependences of the worn volume W on the anterior angle γ at different values of radial wear h_r . Because the anterior angle can be negative, the exponential trend line and the corresponding equation cannot be constructed. Therefore, we set the value $(45 + \gamma)$ along the horizontal axis. As a result, we obtain the dependence

$$W = C_\gamma \cdot (45 + \gamma)^{x_\gamma}, \quad (3)$$

the exponent of which:

$$x_\gamma = -0.103.$$

We construct the power dependences of the worn volume W on the angle of the main cutting edge λ at different values of radial wear h_r . Since the angle λ can be

negative, the trend line of the power dependence and the corresponding equation cannot be constructed. Therefore, we set the value as $(45 + \lambda)$ along the horizontal axis. As a result, we obtain the dependence

$$W = C_\lambda \cdot (45 + \lambda)^{x_\lambda}, \quad (4)$$

the exponent of which:

$$x_\lambda = -0.102.$$

The influence of radial wear h_r on the value of the volume wear W at the initial values of the geometry of the blade in the power dependence has an exponent:

$$x_{h_r} = 2.999.$$

The exponent of the degree dependence of the volume wear W on the wear on the rear surface h_3 has the same value.

4 Results

4.1 Determination of the volume wear depending on the radial wear and wear on the flank

Determined exponents allow you to write an expression for calculating the volume wear at different values of the geometric parameters and of the flank wear and radial wear:

$$W_r = C_r \varphi^{x_\varphi} (\varphi^1)^{x_{\varphi^1}} \alpha^{x_\alpha} (\alpha^1)^{x_{\alpha^1}} \times (\gamma + 45)^{x_\gamma} (\lambda + 45)^{x_\lambda} h_r^{x_{h_r}}. \quad (5)$$

In this case, considering expressions (3) and (4): $x_\varphi = -0.508$, $x_{\varphi^1} = -0.950$, $x_\alpha = -0.269$, $x_{\alpha^1} = -0.730$, $x_\gamma = -0.103$, $x_\lambda = 0.102$, $x_{h_r} = 2.999$.

The value of C is determined by the value of the volume wear W at the original geometry of the blade ($\gamma = 0^\circ$, $\alpha = 12^\circ$, $\alpha^1 = 12^\circ$, $\varphi = 45^\circ$, $\varphi^1 = 15^\circ$, $\lambda = 0^\circ$), and radial wear $h_r = 0,25$ mm. Under such conditions $W = 0.520$ mm³. Then:

$$C_r = W_r / [\varphi^{x_\varphi} (\varphi^1)^{x_{\varphi^1}} \alpha^{x_\alpha} (\alpha^1)^{x_{\alpha^1}} \times (\gamma + 45)^{x_\gamma} (\lambda + 45)^{x_\lambda} h_r^{x_{h_r}}]. \quad (6)$$

After substituting the values of all parameters in formula (6), it can be obtained:

$$C_r = 3622.$$

Finally, mm³:

$$W_r = 3622 \varphi^{-0.508} (\varphi^1)^{-0.950} \alpha^{-0.269} (\alpha^1)^{-0.730} \times (\gamma + 45)^{-0.103} (\lambda + 45)^{0.102} h_r^{2.999}. \quad (7)$$

The determined exponent allows also to write the expression for calculation of the volume wear-out at various values of geometrical parameters of a blade and wear on a flank h_3 :

$$W_h = C_h \varphi^{x_\varphi} (\varphi^1)^{x_{\varphi^1}} \alpha^{x_\alpha} (\alpha^1)^{x_{\alpha^1}} \times (\gamma + 45)^{x_\gamma} (\lambda + 45)^{x_\lambda} h_3^{x_{h_3}}. \quad (8)$$

As before $x_\varphi = -0.508$, $x_{\varphi^1} = -0.950$, $x_\alpha = -0.269$, $x_{\alpha^1} = -0.730$, $x_\gamma = -0.103$, and $x_\lambda = 0.102$.

The value of C_h is also determined at radial wear of 0.25 mm at the original geometry of the blade $\gamma = 0^\circ$, $\alpha = 12^\circ$, $\alpha^1 = 12^\circ$, $\varphi = 45^\circ$, $\varphi^1 = 15^\circ$, $\lambda = 0^\circ$. The wear on the flank $h_3 = 1.05$ mm, and the volume wear $W = 0.520$ mm³. Then:

$$C_h = W_h / [\varphi^{x_\varphi} (\varphi^1)^{x_{\varphi^1}} \alpha^{x_\alpha} (\alpha^1)^{x_{\alpha^1}} \times (\gamma + 45)^{x_\gamma} (\lambda + 45)^{x_\lambda} h_r^{x_{h_3}}] \quad (9)$$

After substituting the values of all parameters in formula (9), it can be obtained:

$$C_h = 48.97.$$

Finally, mm³:

$$W_h = 48.97 \varphi^{-0.508} (\varphi^1)^{-0.950} \alpha^{-0.269} (\alpha^1)^{-0.730} \times (\gamma + 45)^{-0.103} (\lambda + 45)^{0.102} h_r^{2.994} \quad (10)$$

4.2 Empirical dependences to determine the work of blade wear

The formula for calculating the wear of the blade on the flank at different values of radial wear h_r is obtained by substituting the expression (5) to (2):

$$U_r = W_r \sigma_c z = 3622 \varphi^{-0.508} (\varphi^1)^{-0.950} \alpha^{-0.269} \times (\alpha^1)^{-0.730} (\gamma + 45)^{-0.103} (\lambda + 45)^{0.102} h_r^{2.999} \sigma_c z. \quad (11)$$

Using for substitution expression (10) to (2), we obtain the formula for calculating the wear of the blade at different values of wear on the flank h_3 :

$$U_h = W_h \sigma_c z = 48.97 \varphi^{-0.508} (\varphi^1)^{-0.950} \alpha^{-0.269} \times (\alpha^1)^{-0.730} (\gamma + 45)^{-0.103} (\lambda + 45)^{0.102} h_3^{2.994} \sigma_c z. \quad (12)$$

Figure 5 shows the effect of blade geometry on the amount of wear at $h_3 = 0.4$ mm. The calculations were performed according to formula (12). In Figure 5 a, $\varphi = 30^\circ-90^\circ$, $\varphi^1 = 10^\circ-30^\circ$. In Figure 5 b, $\alpha = 5^\circ-25^\circ$, $\alpha^1 = 5^\circ-25^\circ$. In Figure 5 c, $\gamma = -15^\circ-15^\circ$, $\lambda = -20^\circ-20^\circ$.

As an example, the wear of the hard alloy T15K6 in which $\sigma_c = 4.12$ GPa and $z = 10^6$ is considered.

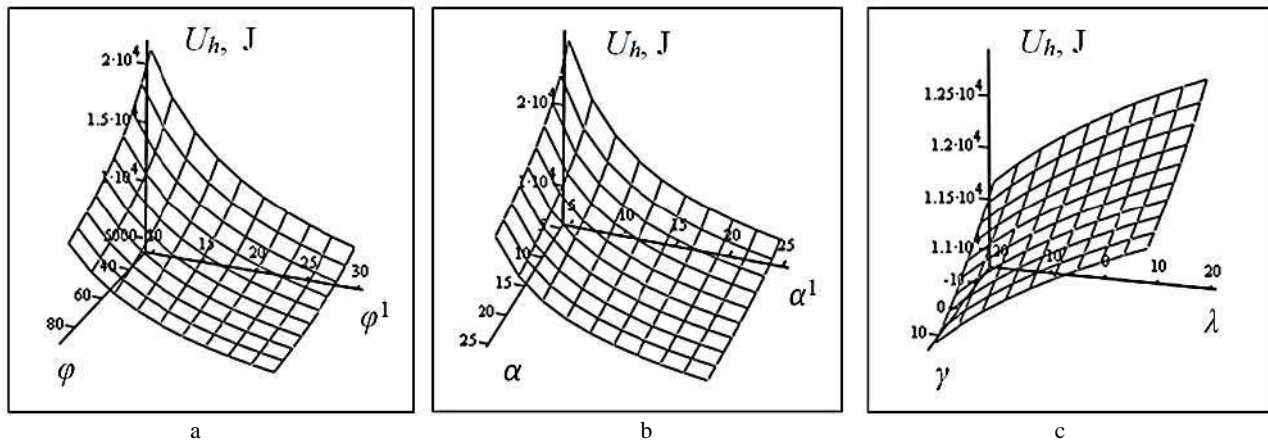


Figure 5 – Influence of blade geometry on wear work

5 Conclusions

Studies of the influence of the blade's geometry and the wear parameters on the flank on the work performed show.

Formulas (11) and (12) allow you to calculate the value of the wear work of the blades with different geometries for any amount of wear of the tool material.

The dependence of wear on the flank h_3 on the value of the main angle in plan φ and the auxiliary angle in plan φ^1 is linear.

The dependences of the volume wear and the wear on the flank on the values of the main and auxiliary rear corners have the same exponents.

The exponent of the degree of dependence of the value of the volume wear W on the radial wear h_r coincides with the exponent of the degree of dependence of the value of the volume wear W on the wear on the flank h_3 .

With increasing angles φ , φ^1 , α , and α^1 decreases the work U_h required to achieve given wear on the flank h_3 , and with increasing angles γ and λ , such work increases.

References

1. Singh, S. B., Ranjan, P., Vakhrushev, A. V., Haghi, A. K. (2021). *Mechatronic Systems Design and Solid Materials. Methods and Practices*, CRC Press, doi: 10.1201/9781003045748.
2. Astakhov, V. P., Shvets, S. V. (2020). Technical resource of the cutting wedge is the foundation of the machining regime determination. *International Journal of Manufacturing, Materials, and Mechanical Engineering*, Vol. 10(2), pp. 1-17, doi: 10.4018/IJMMME.2020040101.
3. Loladze, T. N. (1967). Requirements of tool material – Advances in machine tool design and research. *Proceedings of the 8th International M.T.D.R. Conference University of Manchester*, Part 2, pp. 821-843.

4. Braithwaite, E. R. (1964). *Solid Lubricants and Surfaces*. Pergamon Press, Oxford – London – New York – Paris, 285 pp.
5. Freeman-Gibb, E., Johrendt, J., Tutunea-Fatan, O. R. (2018). The effect of backing profile on cutting blade wear during high-volume production of carbon fiber-reinforced composites. *SAE International Journal of Materials and Manufacturing*, Vol. 11(4), pp. 491-498, doi: 10.4271/2018-01-0158.
6. Miwa, T., Inasaki, I., Yukawa, I. (1999). Blade wear and wafer chipping in dicing processes. *Transactions of the Japan Society of Mechanical Engineers, Part C*, Vol. 65(630), pp. 801-806, doi: 10.1299/kikaic.65.801.
7. Yang, C.-L., Sheu, S.-H., Yu, K.-T. (2009). The reliability analysis of a thin-edge blade wear in the glass fiber cutting process. *Journal of Materials Processing Technology*, Vol. 209(4), pp. 1789-1795, doi: 10.1016/j.jmatprotec.2008.04.028.
8. Freeman-Gibb, E., Johrendt, J., Tutunea-Fatan, O. R. (2018). The effect of backing profile on cutting blade wear during high volume production of carbon fiber-reinforced composites. *SAE Technical Papers*, doi: 10.4271/2018-01-0158.
9. Xue, W., Gao, S., Duan, D., Zhang, J., Liu, Y., Li, S. (2017). Ti6Al4V blade wear behavior during high-speed rubbing with NiAl-hBN abrasible seal coating. *Journal of Thermal Spray Technology*, Vol. 26(3), pp. 539-553, doi: 10.1007/s11666-016-0511-8.
10. Kragelsky, I. V., Dobychin, M. N., Komalov, V. S. (1977). *Fundamentals of Calculations for Friction and Wear*. Mashinostroenie, Moscow, 526 pp.
11. De Laurentis, N., Kadiric, A., Lugt, P., Cann, P. (2016). The influence of bearing grease composition on friction in rolling/sliding concentrated contacts. *Tribology International*, Vol. 94, pp. 624-632, doi: 10.1016/j.triboint.2015.10.012.
12. Ostafiev, V. A. (1979). *Calculation of the Dynamic Strength of the Cutting Tool*. Mashinostroenie, Moscow, 169 pp.



Hybrid 3rd International Conference on Recent Developments in Engineering and Technology (ICRDET-2022)

February 25 - 26, 2022



Jointly organized by
Rajasthan Technical University, Kota
&



ANAND
INTERNATIONAL COLLEGE
OF ENGINEERING

Anand International College of Engineering, Jaipur

**Abstract of all presented papers will be published in Abstract Book with ISBN No.
Selected papers will be published in Special Issues of reputed Journals.**

COMMITTEES ICRDET-2022

STEERING COMMITTEE

- Prof. R. A. Gupta, Honorable Vice Chancellor, RTU, India
- Prof. Valentina E. Balas, Aurel Vlaicu University of Anad, Romania
- Prof. Dumitru Baleanu, University Ankara, Etimesgut 06750, Turkey
- Prof. Xiao-Jun Yang, China University of Mining and Technology, Suzhou, China
- Prof. Mani Mehra, IIT, Delhi, India
- Prof. Griengraij Rajchakit, Maejo University, Thailand
- Prof. Carla M.A. Pinto, Instituto Superior de Engenharia do Porto, Rua Dr. António Bernardino de Almeida, Portugal
- Prof. J. Tenreiro Machado, Institute of Engineering, Polytechnic of Porto, Portugal
- Prof. Serkan Araci, Hasan Kalyoncu University, Turkey
- Prof. Carlo Cattani, University of Tuscia, Italy
- Prof. Xiao-Jun Yang, China University of Mining and Technology, China
- Prof. Dumitru Baleanu, Cankaya University, Turkey
- Prof. J. Tenreiro Machado, Institute of Engineering, Polytechnic of Porto, Portugal
- Prof. Juan J. Nieto, University of Santiago de Compostela, Spain
- Prof. Bashir Ahmad, King Abdulaziz University, Saudi Arabia
- Prof. Mohamed Jleli, King Abdulaziz University, Saudi Arabia
- Prof. Sotiris Ntouyas, University of Ioannina, Greece
- Prof. Michael Ruzhansky, University of Ghent, Belgium
- Prof. Gradimir V. Milovanovic, Serbian Academy of Sciences and Arts, Serbian
- Prof. Silvestru Sever Dragomir, Victoria Univ., Australia
- Prof. Yeol-Je Cho, Gyeongsang National University, South Korea
- Prof. Themistocles M. Rassias, National Technical University of Athens Zografou Campus, Greece
- Prof. Taekyun Kim, Kwangwoon University, S. Korea
- Prof. Filizet A. Aliev, Baku State University, Azerbaijan
- Prof. Aliakbar Montazer Haghighi, Prairie View A&M University, USA
- Prof. Valentina E. Balas, Aurel Vlaicu University of Anad, Romania
- Prof. Yang Quan Chen, Univ. of California, USA
- Prof. Yeliz Karaca, University of Massachusetts Medical School, USA
- Prof. Thiab Taha, University of Georgia, USA

CHIEF PATRONS

- Prof. Gupta
Honorable Vice Chancellor, RTU, Kota, India

PATRONS

- Mr. Manoj Mittal
Chairman, Anand-ICE, Jaipur, India
- Ms. Manika Mittal
Vice Chairperson, Anand-ICE, Jaipur, India
- Prof. Vijay Kumar Sharma
Principal, Anand-ICE, Jaipur, India
- Prof. Praveen Agarwal
Vice Principal, Anand-ICE, Jaipur, India

GENERAL CHAIR

- Prof. Praveen Agarwal, Anand-ICE, Jaipur, India
- Prof. Deepak Bhatia, RTU, Kota, India

ORGANIZING CHAIRS

- Prof. Bhavana Mathur, Anand-ICE, Jaipur, India
- Prof. Harish Sharma, RTU, Kota, India

CONVENERS

- Prof. Anil Dhawan, Anand-ICE, Jaipur, India
- Er. Pramil Sinha, Anand-ICE, Jaipur, India
- Er. Shiv Kumar S, Anand-ICE, Jaipur, India
- Er. Neeraj Manglani, Anand-ICE, Jaipur, India
- Er. Vivek Bhojak, Anand-ICE, Jaipur, India



CALL FOR PAPERS Prospective authors from academia as well as industry are invited to submit their full length papers in ICRDET 2022, which have not been yet submitted/published. Topics of interest for submission include, but are not limited to

Conference Theme

Soft Computing & Advance Computer Applications	Industrial and Intelligent Mechanical Systems	Smart Electrical & Electronics Systems
Civil & Structural Engineering	Fractional Calculus & Special Functions	Material Science and Applied Engineering

Sub themes of conference, but not limited to

Advance Composites & Characterization	Neural Networks, Numerical Analysis, Optimal Control	Digital & analog communication	Fractional Order Modeling and Control in Biomedical Engineering	Solar Cells
Industrial Business Process Management and Modeling	Robotics, Number theory & Cryptography	Challenges and Opportunities for Electric Vehicle	Generalized hypergeometric functions and their extensions	Advanced Construction Management Techniques
Industry 4.0 Internet of Things (IIoT)	Cloud Computing and Virtualization	Electric Vehicles Charging Technology	Fractional Wavelet Applications to the Composite Drug Signals	Modern Transportation Engineering
Advance Composites & Characterization	Sensing and IOT for smart cities	Digital Synchronous	Fractional Transforms and Their Applications	Signal Modeling & Design Techniques
Intelligent Design & Manufacturing	Fuzzy Sets / logic, Genetic Algorithms and Soft computing	Power System Dynamics, Stability and Control	Zeta functions	Sustainable Innovations in Civil Engineering
AI and Data-Driven Applications in Machining	Big Data Analytics	State Estimation, Security, and Reliability Analysis	Accelerator Physics	Recycling & Built Environment

IMPORTANT DATES

- Registration Open Date: 10th January, 2022
- Paper Submission Deadline: 10th February, 2022
- Notification of Acceptance: 15th February, 2022
- Last Date of Registration: 20th February, 2022

REGISTRATION FEES

Category	Indian Participants	Foreign Participants
Attendees	500/-	105
UG Students	1000/-	155
PG/Research Scholars	1500/-	205
Faculty Members	2000/-	255
Industry Persons	2500/-	305

Registration Links

<https://forms.gle/y5aKrF4vpbQfEwAT9>

AUTHOR GUIDELINES

- All the papers should strictly be prepared as per author guidelines of IEEE format.
- The manuscript (Max 10 pages) should be thoroughly checked for grammatical or typographical errors before submission.
- Authors should ensure that the similarity score of their research paper should not above 30 %.
- All the reviewed manuscripts should be submitted in PDF format with authors name & affiliations, at Conference email. id.

Conference website: www.anandice.ac.in/icrdet22

Conference E-mail: icrdet@anandice.ac.in

CONFERENCE VENUE

Anand International College of Engineering
Address: Near Kamote, Agra Road, Jaipur,
Rajasthan, 302012
Phone: 01429-234994, 95

FOR FURTHER INFORMATION

Mr. Nalin Sharma Mobile No.: 9309261326
E-mail: nalin.sharma@anandice.ac.in
Mr. Ajit Mobile No.: 7976733863
E-mail: ajit@anandice.ac.in



Panchuk V., Onysko O., Kotwica K., Barz C., Borushchak L. (2021). Prediction of the accuracy of the tapered thread profile. *Journal of Engineering Sciences*, Vol. 8(2), pp. B1-B6, doi: 10.21272/jes.2021.8(2).b1

Prediction of the Accuracy of the Tapered Thread Profile

Panchuk V.¹[0000-0002-2246-280X], Onysko O.^{1*}[0000-0002-6543-9554], Kotwica K.²[0000-0001-7696-5763], Barz C.³[0000-0001-8028-2981], Borushchak L.¹[0000-0002-4090-0279]

¹ Ivano-Frankivsk National Technical University of Oil and Gas, 15, Karpatska St., 76000, Ivano-Frankivsk, Ukraine;
² AGH University of Science and Technology, 30, Adama Mickiewicza Ave., 30-059, Krakow, Poland;
³ Technical University of Cluj-Napoca, North University Center of Baia Mare, 62A., Victor Babes St., 430083 Baia Mare, Romania

Article info:

Submitted: July 29, 2021
 Accepted for publication: November 4, 2021
 Available online: November 9, 2021

***Corresponding email:**

onysko.oleg@gmail.com

Abstract. The efficiency of drill string largely depends on the pipe-end connector’s accuracy named tapered thread tool joint. Most of those are made by using lathes. Turning tools were made with a profile identical to the thread profile, and all well-known world brands’ plants make the back rake angle of such a cutter with zero value. This is obviously due to the lack of a precise algorithm for calculating the cutter profile and ensuring the accuracy of the tapered thread profile. A virtual experiment was carried out of three-dimensional modeling of the process for shape creation. It showed that in the case of lathe machining of the thread of NC23 type, the deviation from the nominal half profile of the obtained thread is only 0.02°. This result prompted the decision to propose a new algorithm for predictive calculation of the half-angle of the cut profile based on the parameter associated with actual turning – the working height of the profile – h in contrast to previous scientific sources where this calculation was based on the parameter H – not truncated thread Height which is associated with the theoretical base of the accuracy of the thread. The result of the program application, created based on the algorithm proposed in the article, showed that the predicted accuracy of the obtained profile’s half-angle could be in a range from -0.03° to $+0.10^\circ$, which is equivalent to 4–13 % of tolerance of this dimension.

Keywords: flank, not truncated thread Height, back rake angle, half profile angle, angle of inclination.

1 Introduction

Tapered threads are very widely used to connect drill pipes. These threads are made using lathe cutters, the profile of which is equivalent to the profile of the thread itself. However, companies that manufacture these tools adhere to only one value of the leading angle – zero. This is because the theoretical basis has not yet become known, and there is no appropriate algorithm for calculating the profile of the tool’s cutting edge with a non-zero value of the leading angle.

There are a number of publications that, to some extent, represent the study of high-strength and high-precision tool-joint tapered threads. In paper [1], the connection test was carried out on the threaded joint. According to the test data and the simulation results, the final joint thread structure was optimized, which is fundamental in designing a tool joint. But only the stress distribution in the joint thread was indirectly studied. However, the accuracy of the thread was not investigated.

This model is a proper benchmark for assessing the quality of a joint thread seal is presented in [2]. But only the analysis software ANSYS Workbench is applied to stimulate the distribution of contact stress and sealing properties. The accuracy of the manufactured thread was not researched in it.

In the study [3], the implemented data acquisition system allowed us to know, in real-time, the intensity of the cutting force in conventional lathes. But these researchers did not deal with the machining of thread

The cutting tool profile depends on the operating parameters and the required geometry, using a numerical model based on an analytical model based on a tangential motion condition [4]. But this research is about whirling but not threading machining.

2 Literature Review

An impact of the edge and the rake angle of the lathe tool on the strength field was studied experimentally in the paper [5]. In research [6] using the cutting force prediction and using a validated mechanistic force model, the energy consumption in turning can be estimated. The accuracy of manufactured thread is not researched in [5,6].

The study [7] focuses on the threading of non-symmetric profiles. But that method of machining is milling only. The only stress concentration factors in the pin and box are calculated in [7].

In the study [8], the NC35 tool joint with the double shoulder is considered the research object and studied by finite element method (FEM) using nonlinear thermo-mechanical coupled-mode but not using the accuracy parameters of thread. In [9], the generalized mechanics model of multi-point thread turning operations is presented. The model can be used for both turning planning but not for accurate prediction.

The paper [10] deals with the comparison of measured and calculated results of cutting force components. The paper [11] studies the dependence of the dynamic oscillatory movements in the area of drill string sticking on the parameters of the vibrating mechanism only.

In [12], the authors developed a laser triangulation device to measure deformations but not the accuracy of thread joint details. The article [13] deals with studying the vector components of the kinematics of the surface forming of the tapered thread by turning machining and does not study the influence of tool profile on thread accuracy.

The effect of the accuracy of the profile pin threads for equivalent stresses, fatigue safety indicators, and contact pressure in drill pipe joints are studied in paper [14].

So the purpose of this research is: learn the counter algorithm of the influence of the geometric parameters of the tool on the profile deviations of the tapered thread made by the lathe.

3 Research Methodology

3.1 Calculation of the profile angle based on the theoretical parameter H

The algorithm for calculating the profile of the tool-joint tapered thread based on the developed theoretical basis is presented in [15]. Theoretically, it is based on the parameter H – not truncated thread Height (Figure 1).

According to this scheme, the angles are calculated by formulas [15]:

$$\alpha_{AD} = \arctg \left(\frac{|Z_a - Z_d|}{|X_a - X_d|} \right); \quad (1)$$

$$\alpha_{AB} = \arctg \left(\frac{|Z_a - Z_b|}{|X_a - X_b|} \right); \quad (2)$$

$$Z(x) = \operatorname{tg}(\alpha_1) x \frac{\sin \tau}{\sin \gamma} - \frac{P \tau}{2\pi}; \quad (3)$$

$$\tau = \gamma - \arcsin \left(\frac{d_{\text{minor}}}{2x} \sin \gamma \right), \quad (4)$$

where α_1 – the angle of the profile of the cutting edge of the cutter, for a conventional cutter $\alpha_1 = 30^\circ$; P – the thread pitch, d_{minor} – the inner diameter of the thread (Figure 2).

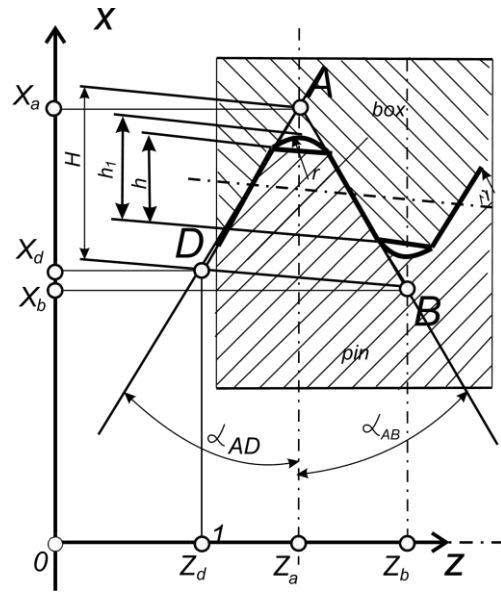


Figure 1 – Scheme used for calculating the half angles of the profile of a tool-joint tapered thread based on the parameter H

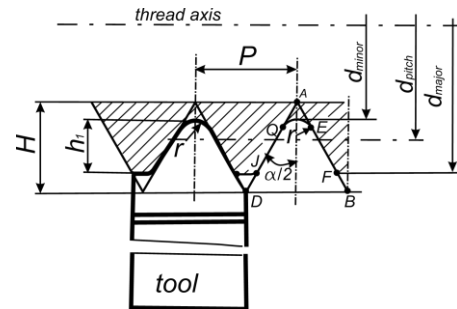


Figure 2 – The scheme of the half angles of the thread profile based on the parameter h

However, the parameter H is theoretical, and the parameters h and h_1 are effective in the real tool-joint tapered thread. The parameter h_1 is the one that is realized with the help of a cutting tool, and the parameter h – the working height of the thread is actually decisive for the straight section of such an implementation. In Figure 2, the profile of the cutter is shown by a bold line, and the obtained straight sections of the profile are marked between the points J and Q and between the points E and F . Half profile angle – $\alpha/2$ is the angle between the straight side section and the axis of symmetry of the threaded turn. The radius of the obtained radial part is r . However, the algorithm represented by equations (1) and (2), based on the scheme in Figure 1, determines the half profile angles of the sides of the original triangle ADB using the coordinates of the points: X_a , X_d , X_b and calculated by formulas (3), (4) and is corresponding to their coordinates Z_a , Z_b , Z_d .

3.2 Calculation of the profile angle based on the actual parameter h

According to the API 7 standard, one of the parameters of a tool-joint tapered thread is the value of b – root truncation (Figure 3). Using this parameter, you can represent the following relationship:

$$H = b + h + b. \quad (5)$$

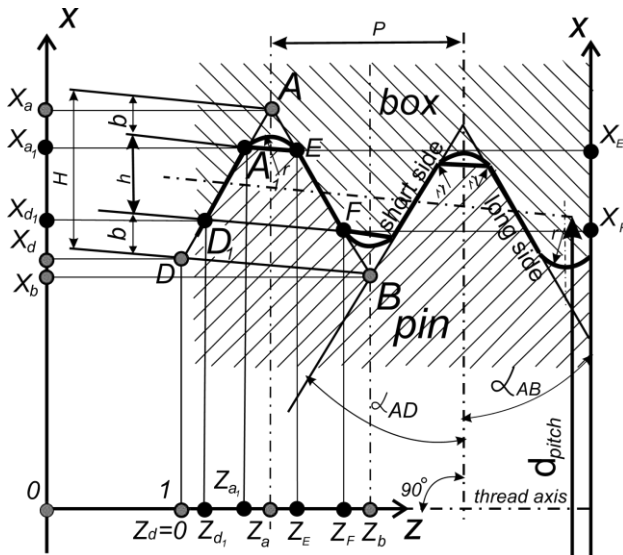


Figure 3 – Scheme used for calculating the half angles of the profile of a tool-joint tapered thread based on the parameter h

Thus, by analogy with equations (1)–(2), we can present the calculation of the half profile angles of the tool-joint tapered thread in its shaping by a real cutter based on Figures 2–3:

$$\alpha_{A_1D_1} = \arctg \left(\frac{|Z_{a_1} - Z_{d_1}|}{|X_{a_1} - X_{d_1}|} \right); \quad (6)$$

$$\alpha_{EF} = \arctg \left(\frac{|Z_F - Z_E|}{|X_F - X_E|} \right), \quad (7)$$

where the coordinates X_{a_1} , X_{d_1} , X_F , X_E can be determined by the formulas:

$$X_{a_1} = X_a - b; \quad (8)$$

$$X_{d_1} = X_d + b; \quad (9)$$

$$X_F = X_b + b; \quad (10)$$

$$X_E = X_d - b. \quad (11)$$

The coordinates Z_{a_1} , Z_{d_1} , Z_F , and Z_E can be determined by formulas (3) and (4).

Figure 4 of [15] can serve as an illustration of the difference between the algorithm based on equations (1)–(2) and the algorithm based on formulas (6)–(7). It shows a red straight line according to the API 7 standard, and a blue curve shows the profile predicted by turning the profile. The Z coordinate of the last point of the blue profile is visibly different from the Z_1 coordinate of the red profile. However, the values of the z -coordinates

corresponding to the points with X coordinates between 34.0 mm and 35.75 mm are not so obvious.

Given that the value of $b = 1.43$ mm, the initial value of $X = 32.6$, and the final $X = 37.1$, we can determine the following: the real range of coordinates X according to formulas (8)–(11) between $32.60 + 1.43 = 34.03$ (mm) and $37.10 - 1.43 = 35.67$ (mm).

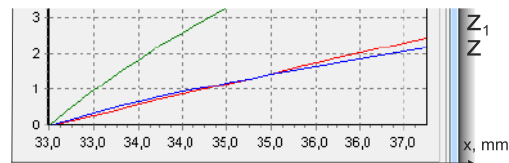


Figure 4 – Diagrams of rectilinear sections of profiles given by the standard thread (red line) and made by a cutter with a non-zero value of the back rake angle

4 Results

4.1 Predicting of the accuracy of the profile obtained by the simulated turning of the thread of size NC23

In order to verify the algorithm declared above, a model of forming a tapered thread of size of NC23 by lathe is submit on Figure 5.

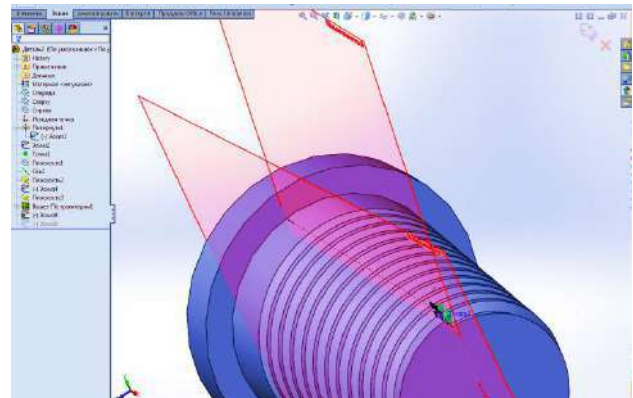


Figure 5 – Model of shaping of tool-joint tapered thread of NC23: 2 – plane, normal to the tangent to the first turn of the thread ($\lambda = 2.61^\circ$); 3 – plane of the rake surface of the tool with negative back rake angle $\gamma = -5^\circ$

The geometric parameters of the tool are selected: the back rake angle $\gamma = -5^\circ$, and the angle of inclination $\lambda = 2.61^\circ$, which corresponds to the slope of the first turn of the thread.

The axial section of the shape-created model of the specified size shows the high accuracy of a thread profile in the axial plane – 60.02° (Figure 6).

The API 7 standard provides for the accuracy of the half-angle of the profile of the notch $\alpha/2 = 30^\circ \pm 0.40'$. Thus, the high accuracy of the cut profile of the thread provided on the 3D model proves the need of the creation on the basis of equations (3)–(11) of a special automatic algorithm for calculating the profile of the thread and the implementation of its analysis of its predicted accuracy.

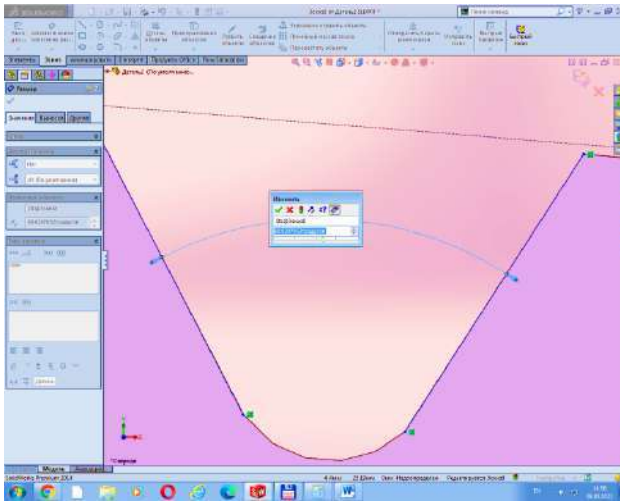


Figure 6 – Prediction of the axial profile on the threaded model NC23

4.2 Software prediction of the accuracy of the profile of the tapered thread NC23 made by lathe

Software implementation of the algorithm for calculating equations (3) and (4) provides for the input parameters: the size of the thread, the back rake angle of the cutter, the angle of inclination of the thread, the step of calculating the X coordinate, as well as selecting the desired distance from the pin end to this turn, long or the small side (A_1D_1) of the EF .

Figure 7 shows a fragment of the program where the back rake angle is -5° , the inclination angle for the turn at a distance of 60.125 mm – 1.8° (Corresponds to the latter in the direction from the end of the turn). The calculating step is 0.1 mm.

Figures 8–10 show fragments of the forecast calculation starting from point D ($X = 27.16$, $Z = 0$), and ending with point A ($X = 32.66$, $Z = 3.18$).

The coordinate Z_1 in the program refers to the profile of the cutter in case of need for its modernization, the coordinate. Coordinate Z_2 is the predicted axial profile according to formulas (3)–(4), obtained by a tool with the specified geometric parameters ($\gamma = -5^\circ$, $\lambda = 1.8^\circ$), and the profile of the cutting edge, which is identical to the nominal profile of the standard thread ($\alpha/2 = 30^\circ$).

Given that the standard API 7, $b = 1.43$ mm (root truncation) and using formula (9), we obtain $x_{d1} = 28.59$ mm, which is closest to the value of 28.56 mm in the program fragment in Figure 9, which means the corresponding value of the coordinate $Z_2 = 0.815$ mm.

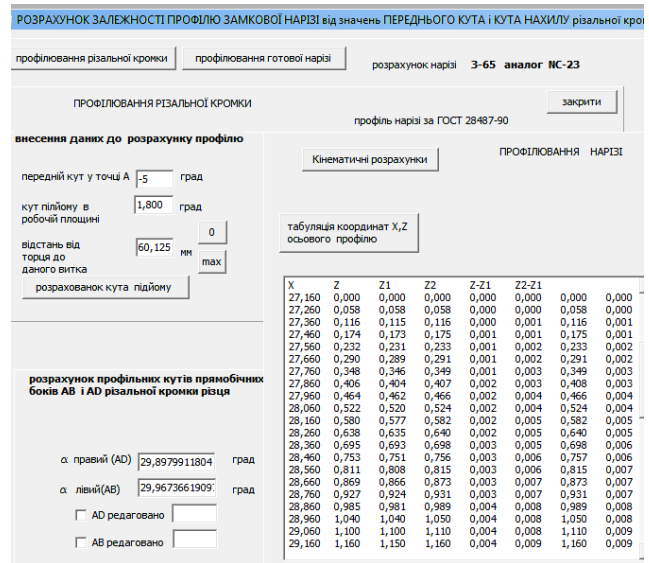


Figure 7 – Visual application for predictive calculation of the profile of the thread NC23

X	Z	Z1	Z2
27,160	0,000	0,000	0,000
27,260	0,058	0,058	0,058
27,360	0,116	0,115	0,116
27,460	0,174	0,173	0,175
27,560	0,232	0,231	0,233
27,660	0,290	0,289	0,291
27,760	0,348	0,346	0,349
27,860	0,406	0,404	0,407
27,960	0,464	0,462	0,466
28,060	0,522	0,520	0,524
28,160	0,580	0,577	0,582
28,260	0,638	0,635	0,640
28,360	0,695	0,693	0,698
28,460	0,753	0,751	0,756
28,560	0,811	0,808	0,815
28,660	0,869	0,866	0,873
28,760	0,927	0,924	0,931
28,860	0,985	0,981	0,989
28,960	1,040	1,040	1,050
29,060	1,100	1,100	1,110
29,160	1,160	1,150	1,160

Figure 8 – Projected thread profile NC23 short side AD last turn (part 1)

Given that the API 7 standard, $b = 1.43$ mm (root truncation) and using formula (8), we obtain $x_{a1} = 31.23$ mm, which is closest to the value of 31.26 mm in the program fragment in Figure 10. Therefore, the corresponding value of the coordinate $Z_2 = 2.38$ mm.

29,060	1,100	1,100	1,110
29,160	1,160	1,150	1,160
29,260	1,220	1,210	1,220
29,360	1,270	1,270	1,280
29,460	1,330	1,330	1,340
29,560	1,390	1,390	1,400
29,660	1,450	1,440	1,450
29,760	1,510	1,500	1,510
29,860	1,560	1,560	1,570
29,960	1,620	1,620	1,630
30,060	1,680	1,670	1,690
30,160	1,740	1,730	1,740
30,260	1,800	1,790	1,800
30,360	1,850	1,850	1,860
30,460	1,910	1,910	1,920
30,560	1,970	1,960	1,980
30,660	2,030	2,020	2,040
30,760	2,080	2,080	2,090
30,860	2,140	2,140	2,150
30,960	2,200	2,190	2,210
31,060	2,260	2,250	2,270
31,160	2,320	2,310	2,330

Figure 9 – Projected thread profile NC23 short side AD last turn (part 2)

30,660	2,030	2,020	2,040
30,760	2,080	2,080	2,090
30,860	2,140	2,140	2,150
30,960	2,200	2,190	2,210
31,060	2,260	2,250	2,270
31,160	2,320	2,310	2,330
31,260	2,370	2,370	2,380
31,360	2,430	2,420	2,440
31,460	2,490	2,480	2,500
31,560	2,550	2,540	2,560
31,660	2,610	2,600	2,620
31,760	2,660	2,660	2,670
31,860	2,720	2,710	2,730
31,960	2,780	2,770	2,790
32,060	2,840	2,830	2,850
32,160	2,890	2,890	2,910
32,260	2,950	2,940	2,960
32,360	3,010	3,000	3,020
32,460	3,070	3,060	3,080
32,560	3,130	3,120	3,140
32,660	3,180	3,180	3,200

Figure10 – Projected thread profile NC23 short side AD last turn (part 3)

The obtained results are entered in Table 1 (right column) and on their basis and using formulas (1) and (6) the forecast calculations $\alpha_{AD} = 30.19^\circ$, and $\alpha_{A1D1} = 30.10^\circ$ are obtained (highlighted in bold in the right column of Table 1).

Table 1 – Data for counting profile angle of short flank AD

Parameters	The 1st turn ($\lambda = 2.61^\circ$)	The last turn, ($\lambda = 1.8^\circ$)
X_a	22.16 mm	27.16 mm
Z_a	0.00 mm	0.00 mm
X_d	27.66 mm	32.66 mm
Z_d	3.20 mm	3.20 mm
α_{AD}	30.19°	30.19°
X_{a1}	23.59 mm	28.59 mm
$X_{a1 \text{ table}}$	23.56 mm	28.56 mm
Z_{a1}	0.815 mm	0.815 mm
X_{d1}	26.23 mm	31.23 mm
$X_{d1 \text{ table}}$	26.26 mm	31.26 mm
Z_{d1}	3.18 mm	2.38 mm
α_{A1D1}	30.09°	30.10°

Similar calculations were performed for the first thread turn of the pin, for which $\lambda = 2.61^\circ$. The prediction of the half profile angle with respect to the long side was performed according to formulas (2) and (7) and using formulas (10) and (11), and these results are presented in Table 2.

Table 2 –Data for counting profile angle of long flank AB

Parameters	First turn($\lambda=2.61^\circ$)	Last turn($\lambda=1.8^\circ$)
X_a	22.16 mm	27.16 mm
Z_a	0.00 mm	0.00 mm
X_b	27.96 mm	32.96 mm
Z_b	3.34 mm	3.34 mm
α_{AB}	29.94°	29.94°
X_E	23.59 mm	28.59 mm
$X_{E \text{ table}}$	23.56 mm	28.56 mm
Z_E	0.805 mm	0.807 mm
X_F	26.53 mm	31.53 mm
$X_{F \text{ table}}$	26.56 mm	31.56 mm
Z_F	2.53 mm	2.54 mm
α_{EF}	29.90°	29.97°

The data in Tables 1–2, which are highlighted in bold, indicate the values of the half profile angles α_{AD} and α_{AB} , which are programmatically predicted based on the theoretical parameter H by formulas (1) and (2) (at the top) and α_{A1D1} and α_{EF} by equations (6) and (7) based on the actual parameter h in the lower part. Three of the four values of the half-angle based on the actual parameter h are ones with a minor deviation from the nominal value of 30° than the value of the half-angle according to the theoretical parameter H

5 Conclusions

The presented forecast calculations give good reasons to consider the equation based on the actual parameter h (working height of the thread). Therefore, the predicted accuracy of lathe machining the thread by the parameter of the half-angle of the profile can reach the initial value in a range from -0.03° to $+0.10^\circ$. This range is equivalent to 4–13 % of the tolerance on the half-angle $\alpha - 45^\circ$.

The three-dimensional model reveals a more accurate execution of the thread profile (0.02°), but the software implementation allows visual-graphical profiling and analytical with any step of calculation accuracy.

References

1. Wang, Y., Qian, C., Zhou, Q., Kong, L., Gong, J. (2020). Design optimization for the thin-walled joint thread of a coring tool used for deep boreholes. *Applied Sciences*, Vol. 10(8), 2669, doi: 10.3390/app10082669.
2. Yu, W., Xia B., Wang Z., Chai, C. (2016). Model of a new joint thread for a drilling tool and its stress analysis used in a slim borehole. *Mechanical Sciences*, Vol. 7, pp. 189-200, doi: 10.5194/ms-7-189-2016.
3. Sineider, F. M., Reina-Munoz, R., Lira, M. V. (2020). System of cutting force data acquisition in mechanical lathes. *Applied Sciences*, Vol. 10(8), 2669, doi: 10.3390/app10082669.
4. Zanger, F., Sellmeier, V., Klose, J., Bartkowiak, M., Schulze, V. (2017). Comparison of modeling methods to determine cutting tool profile for conventional and synchronized whirling. *Procedia CIRP*, Vol. 58, pp. 222-227, doi: 10.1016/j.procir.2017.03.216.
5. Baizeau, T., Campocasso, S., Fromentin, G., Rossi, F., Poulachon, G. (2015) Effect of rake angle on strain field during orthogonal cutting of hardened steel with c-BN tools. *15th CIRP Conference on Modelling of Machining Operations. Procedia CIRP*, Vol. 31, pp. 166-171.
6. Zhang, G., Guo, C. (2016). Modeling flank wear progression based on cutting force and energy prediction in turning process. *Procedia Manufacturing*, Vol. 5, pp. 536-545, doi: 10.1016/j.promfg.2016.08.044.
7. Fromentin, G., Dobbeler, B., Lung, D. (2015). Computerized simulation of interference in thread milling of non-symmetric thread profiles. *15th CIRP Conference on Modelling of Machining Operations. Procedia CIRP*, Vol. 31, pp. 496-501.
8. Luo, S., Wu, S. (2015). Effect of stress distribution on the tool joint failure of internal and external upset drill pipes. *Materials and Design*, Vol. 52, pp. 308-314.
9. Cheng, J., Sun, Y., Yu, Y., Chen, L., Ma, X. (2020). Nonlinear thermo-mechanical coupled analysis of high temperature effect on strength, contact stress and ultimate torque of tool joint. *International Journal of Pressure Vessels and Piping*, Vol, 188, 104221, doi: 10.1016/j.ijpvp.2020.104221.
10. Khoshdarregi, M. R., Altintas, Y. (2015). Generalized modeling of chip geometry and cutting forces in multi-point thread turning. *International Journal of Machine Tools and Manufacture*, Vol. 98, pp. 21-32, doi: 10.1016/j.ijmachtools.2015.08.005.
11. Saglam, H., Unsacar, F., Yaldiz, S. (2006). Investigation of the effect of rake angle and approaching angle on main cutting force and tool tip temperature. *International Journal of Machine Tools and Manufacture*, Vol. 46(2), pp. 132-141, doi: 10.1016/j.ijmachtools.2005.05.002.
12. Moisyshyn, V., Levchuk, K. (2016). The impact of vibration mechanism zone installation on the process of retrieving stuck drill pipes. *Mining of Mineral Deposits*, Vol. 10(3), pp. 65-76, doi: 10.15407/mining10.03.065.
13. Ropyak, L. Ya., Pryhorovska, T. O. (2019). Machining error influence on stress state of conical thread joint details. *Proceedings of the International Conference on Advanced Optoelectronics and Lasers, 06–08.09.2019, Sozopol, Bulgaria*. Retrieved from: <http://igurug.ddns.net/index.php>
14. Medvid, I., Onysko, O., Panchuk, V., Pituley, L., Schuliar, I. (2021). Kinematics of the tapered thread machining by lathe: analytical study. *Advanced Manufacturing Processes. InterPartner 2019. Lecture Notes in Mechanical Engineering. Springer, Cham*, pp. 555-565, doi: 10.1007/978-3-030-68014-5_54.
15. Kopei, V., Onysko, O., Odosii, Z., Pituley L., Goroshko, A. (2021). Investigation of the influence of tapered thread profile accuracy on the mechanical stress, fatigue safety factor and contact pressure. *New Technologies, Development and Application IV. NT 2021, Lecture Notes in Mechanical Engineering. Springer, Cham*, Vol. 233, pp. 177-185, doi: 10.1007/978-3-030-75275-0_21.



Lasinska N. (2021). Hybrid management methodology for transport projects related to rolling stock. *Journal of Engineering Sciences*, Vol. 8(2), pp. B7-B11, doi: 10.21272/jes.2021.8(2).b2

Hybrid Management Methodology for Transport Projects Related to Rolling Stock

Lasinska N.

Lukasiewicz Research Network – Rail Vehicles Institute “TABOR”, 181, Warszawska St., 161-055 Poznan, Poland

Article info:

Submitted:

August 25, 2021

Accepted for publication:

November 17, 2021

Available online:

November 22, 2021

*Corresponding email:

natalia.lasinska@tabor.lukasiewicz.gov.pl

Abstract. Dynamic economic development and the fast implementation pace of innovative, economical solutions force companies to continue finding methods of increasing the efficiency of their operations. One of the ways to increase the effectiveness of activities is to use a project approach that allows achieving all the set goals efficiently. The project approach is gaining popularity due to its high efficiency. Also, it is treated as a separate trend called as “projectification” and “project orientation”. The article defines what a project and project management methodology are. The specificity of railway transport projects concerning rolling stock was characterized. The elements of traditional and agile project management methodologies were described, indicating their differences. Project areas were selected in which the implementation of the elements of agile project management methodologies is the easiest and fastest to carry out.

Keywords: traditional project management, agile project management, methodology, methodology elements.

1 Introduction

Technological development, increasing consumer awareness, and the fast pace of changes in the modern world force enterprises to design, construct and develop products, services, and new technologies in the shortest possible time frame, while also reducing costs [9]. The competitive advantage of enterprises is often related to innovative projects, which is closely related to the use of project management methodology. The increasing complexity of innovative projects forces companies to search for more effective implementation methods. At a particular stage of project complexity, traditional project management methodologies become simply insufficient.

Combining traditional and agile project management methodologies and implementing a transport project for rolling stock based on the resulting hybrid methodology, adapted to the specificity of a given company and industry, can increase the efficiency of project implementation. The hybrid methodology combines elements of traditional and agile methodologies, previously regarded as contradictory to each other. Implementing a project based on the hybrid methodology gradually eliminates the antinomies between the two methodologies and ensures a synergistic effect. Combining elements of two seemingly contradictory methodologies can be performed successfully during the implementation of projects in other industries.

2 Literature Review

The concept of a project is commonly used in many fields, e.g., in education, economy, health care, and public administration. A project is virtually any undertaking with a start and end date involving specific resources (human, financial, material) that end with a specific result. The specificity of project undertakings results primarily from their complexity, periodicity, and innovation. Many project definitions indicate conditions that must be met for a given undertaking to be called a project.

According to the definition developed by the IPMA (International Project Management Association), a project is defined as a unique set of coordinated activities, limited in time and costs, aimed at obtaining a set of predefined products (a scope that meets the project objectives), while maintaining quality standards and requirements [1]. According to the traditional PRINCE2 methodology (“PProjects IN Controlled Environments 2”) [5], a project is a temporary organization established for a period, which is created to deliver one or more business products according to an established business case.

Projects are unique undertakings with a high level of complexity, with a defined implementation period (with the beginning and end marked), requiring the involvement of significant, but limited resources

(material, human, financial, information). Projects are carried out by a team of highly qualified contractors from various fields (interdisciplinary) that is relatively independent of the company's regular repetitive activities [4]. They are associated with a high level of technical, organizational, and economic risk, which forces their implementation to be performed using specialized methods and tools. Most often, a project is carried out by people from various departments of any given organization. This allows for the collection and use of the most valuable skills, which, combined with appropriate coordination, allows achieving results that could not be achieved if the project was entrusted to one department of the organization [10]. Trocki [8] similarly defines a project.

The multitude of definitions and, at the same time, some standard features among them allow summarizing that a project as an undertaking whose genesis is an idea that responds to the existing demand. A concrete idea, translated into an action plan, placed in time and with a specific goal, becomes a project. It is a separate undertaking, not related to the routine activities of the company or institution. It is characterized by temporality, high demand, uniqueness, an appropriate degree of complexity, and novelty. The project uses business opportunities and translates them into real benefits for the company, increasing competitiveness and the company's profitability. Project implementation requires the involvement and separate management of interdisciplinary human resources and financial and material resources. An undertaking characterized by the features mentioned above can thus be described as a project.

Project Management Institute defines project management as applying knowledge, skills, tools, and techniques used for project activities to meet the project requirements [6]. This is achieved by applying and integrating project management processes such as initiation, planning, execution, monitoring and control, and project closure.

Project management is a system of achieving goals and tasks and is treated as a subset of activities related to strategic planning [3]. It provides outcomes and results that can be transformed into business value and financial gains. It is currently perceived as a system for achieving strategic business goals. The use of appropriate project management methods by enterprises is a tool for developing their own business and building up a competitive advantage over their competition. The increase in the project's complexity and the emphasis on shortening the project's duration and reducing costs force the project's implementation to be performed using already proven tools. Project management methods are commonly used in cases where there is a need to implement a complex, atypical, comprehensive project with an inherent risk of failure.

Project management should be executed in line with the general management principles of a given enterprise. Integrating project management with other management processes in the enterprise is the key to the effective

implementation of projects. According to H. Kerzner [2], as shown in Figure 1, project management should be integrated with the following management processes of the company: with the management of engineering works (understood as the core business of the company), along with the management of quality, risk, and change. Such management reduces operating costs, reduces the need for resources, minimizes the documentation necessary to develop, and eliminates duplication of efforts.



Figure 1 – Integration of management processes of an enterprise [2]

There is no one universal method of project management suitable for all types of projects. There are general methods that can be used in the implementation of projects in different branches of the economy, as well as sectoral methods adapted to specific departments, e.g., IT, government administration, or construction. The use of a given method depends on the specificity of a given project. One of the most effective ways to implement projects is to combine selected elements from various project management methods and adapt them to a specific project and the company's specifics, thus creating a hybrid method explicitly made for the implementation of a given project. When selecting activities and tools for project implementation and then adapting them to the needs of a specific project, the nature of the enterprise, its organizational culture, work culture, and general principles of the company's operation should be considered.

3 Research Methodology

Transport and railway rolling stock projects are interdisciplinary, complex projects requiring a large project team, often consisting of several dozen people. Due to their complexity, the implementation of these projects takes on an average of 5–7 years. Rolling stock projects belong to the group of capital-intensive projects with an average budget of several million EUR. The need to engage human and financial resources to such a large extent and over such a long time significantly increases the project risk. Efficient and effective implementation of this project type requires using project management methodologies during the implementation process. Rolling stock projects, the effect of which is implementing a new production solution developed as a part of the project, are most often carried out in a

consortium consisting of two or three companies/scientific institutions. This requires a coordination, a collaboration between consortium members and different project teams. As part of the project roles, a Project Manager is designated, whose task is to coordinate the work and ensure day-to-day cooperation of all members of the consortium, and the Research and Development Manager, who is responsible for the substantive scope of the project work. Separation of these two management areas is necessary to ensure efficient project implementation and substantive work progress. The Project Management Office (PMO) plays an essential role in implementing projects in each institution implementing the project. The PMO is responsible for all administrative, financial, and legal matters related to the project implementation.

4 Results

Criticism of traditional, planar project management methodologies has led to the emergence and development of new trends in project management, which are agile methodologies as part of Agile Project Management (APM) [7]. The initial source of these methodologies was IT projects, characterized by uncontrollable changes in scope, which resulted in a low percentage of projects being successfully completed using traditional project management methodologies. Agile methodologies are intended to eliminate unnecessary administrative activities. They are most effective in areas characterized by high uncertainty and the inability to precisely plan out the entire project. They require a high level of interaction by the project team. The most famous schools of agile thinking include Scrum, XP (“eXtreme Programming”), Lean, and Kanban [7]. Agile methodologies do not treat design as a linear process with easily predicted steps. They are based on the specific competencies of the project team and the incremental creation of value for the client. The project’s effect is not delivered once at the end but gradually over time, as the functionality of the project results increases. In the Agile approach, the design is unpredictable and non-linear. Implementation of projects based on agile methodologies is not based on a precise plan. Usually, the initial stages of a project are scheduled. The agile approach focuses on interpersonal interactions and dynamic planning.

A comparison of selected elements of traditional and agile methodologies is presented in Table 1.

Table 1 – Comparison of traditional and agile project management methodologies

Project elements	Traditional methodologies	Agile methodologies
Project management cycle	<ul style="list-style-type: none"> – deterministic, linear, based on defined stages; – defined key processes; – the basis of the project management is a detailed schedule 	<ul style="list-style-type: none"> – iterative, empirical, based on providing elements of functionality, – adaptability, adapting to changing conditions, – short schedules for the implementation of the next stages
Focus	<ul style="list-style-type: none"> – process and division of tasks; – control procedures; – tools and techniques supporting the project implementation 	<ul style="list-style-type: none"> – stakeholders; – providing functionality
Project goals	<ul style="list-style-type: none"> – precisely defined and in detail under the SMART methodology; – cascade, short-term, and long-term goals based on a needs analysis; – execution of planned works on time, under the schedule and budget 	<ul style="list-style-type: none"> – precisely defined, constitute a hypothesis, speculation for the future; – general vision
Organizational aspect	<ul style="list-style-type: none"> – division of labor within the project; – high level of formalization; – extensive project documentation; – focus on maintaining a balance between limited resources, such as costs, quality, and time 	<ul style="list-style-type: none"> – simplified work organization, focused on quick and flexible adaptation to changes; – low degree of formalization
Project costs	<ul style="list-style-type: none"> – carefully estimated budget for the entire project 	<ul style="list-style-type: none"> – a specific estimated budget only for the first of several initial project stages; – overall cost forecast for the next stages of the project

Project elements	Traditional methodologies	Agile methodologies
Personnel / Project team aspect	<ul style="list-style-type: none"> – a team based on a narrow specialization; – high team competencies; – task-oriented, democratic and inclusive management style; – project manager focused mainly on the budget, schedule, and scope of the project 	<ul style="list-style-type: none"> – work based on small groups of self-organizing and self-disciplined project teams (9–12 people); – emphasis on cooperation, integration, and communication between team members; – a cooperative leadership style based on steering, not controlling
Deviations from the plan / Implementation of changes	<ul style="list-style-type: none"> – difficulties with introducing project changes; – treated as a consequence of incorrect project management; – requires remedial action, – implementation of changes hindered by a bureaucratic, formalized structure 	<ul style="list-style-type: none"> – openness to changes, flexible, adaptive approach to changes; – introducing changes while maintaining previously defined goals; – the causes of deviations form the basis of the analysis and conclusions for the future; – change is the engine of innovative processes
Control	<ul style="list-style-type: none"> – high level of formalization, control of all processes, degree of achievement of goals, time, scope, budget, resources, people 	<ul style="list-style-type: none"> – low level of formalization; – system approach; – control of the degree of achievement of goals and time

Depending on the project specifics, various project management methodologies can be used. The evolution of the project management field is moving away from the traditional approach to the agile methodologies, the greatest advantage of which is adaptability, creativity, and quick customer-oriented actions.

The elements of agile methodologies that can be most easily and quickly implemented in organizations implementing projects so far without the use of any methodology or based on traditional methodologies are:

- involvement of all or, in the case of numerous project teams, the main contractors working on the project together with the project manager at the stage of planning the project work;
- planning works in short periods, e.g., weekly or monthly, depending on the specifics of a given project;
- cyclical, short meetings of the project team, where the current status of the project is discussed (what a specific member of the project team has done since the last team meeting, what will he or she be doing in the near future, to the next meeting and what current problems/obstacles in project implementation are encountered). Regular, status project meetings should take place in the same place, at the same time, preferably standing, so that they do not turn into long meetings;
- regular retrospections, meetings where members of the project team think about how to improve the way they work;
- use of a project status visualization tool, e.g., a task board (physically hanging on the wall or a digital board prepared in a project management program) showing the status of the project and the work to be done in the project.

It allows to visualize the rate of work being done and monitor the progress of work in the project. This provides simultaneous access to project status information for all project team members and stakeholders.

The use of the above elements in the implementation of the project is an introduction to the development of a dedicated hybrid methodology for a given company, and then its implementation, where effective communication between members of the project team and project stakeholders is the foundation of the working methodology.

5 Conclusions

Elements of agile methodologies are beginning to be used in implementing projects previously based on traditional management increasingly more often, which in turn leads to the creation of hybrid methodologies containing elements of both traditional and agile approaches.

The implementation of a transport project regarding rolling stock with the use of elements of agile methodologies, based on a hybrid methodology, adapted to the specificity of a given company/organization, is a response to the growing economic requirements regarding innovation of products/project results, the pace of technology development, shortening the project life cycle, reducing project costs, as well as flexible and effective cooperation with project stakeholders.

Traditional methodologies are used at the level of project management, while elements of an agile approach are used for project management at the project team level. The synergy effect obtained in this way increases the efficiency of project implementation.

References

1. *IPMA Organizational Competence Baseline – The standard for moving organizations forward*. IPMA, Zurich, Switzerland.
2. Kerzner, H. (2009). *Project Management. A Systems Approach to Planning, Scheduling and Controlling*. John Wiley and Sons Inc., New Jersey, USA.
3. Kerzner, H. (2019). *Using the Project Management Maturity Model: Strategic Planning for Project Management*. John Wiley and Sons Inc., New Jersey, USA, pp. 3-4.
4. Knapp, B. W. (2006). *A Project Manager's Guide to Passing the Project Management Exam*. The Project Management Excellence Center. Inc., USA.
5. *Managing Successful Projects with PRINCE2*. The Stationery Office, London, 2017.
6. *Project Management Institute. A Guide to the Project Management Body of Knowledge*, Newton Square, 2004.
7. Stellman, A., Greene, J. (2015). *Agile. A Guide to Agile Programming Methodologies*. HELION, Gliwice, Poland.
8. Trocki, M. (2012). *Modern Project Management*. PWE, Warszawa, Poland.
9. Trojanowska, J., Dostatni, E. (2017). Application of the theory of constraints for project management. *Management and Production Engineering Review*, Vol. 8(3), pp. 87-95, doi: 10.1515/mper-2017-0031.
10. Young, T. L. (2007). *The Handbook of Project Management. A Practical Guide to Effective Policies, Techniques and Processes*. Koghan Page, London, UK.

Rudenko S., Berladir K., Trojanowska J., Varenyk S., Shvetsov D., Kravets V. (2021). Application of FMEA for assessment of the polymer composite materials quality. *Journal of Engineering Sciences*, Vol. 8(2), pp. B12-B18, doi: 10.21272/jes.2021.8(2).b3

Application of FMEA for Assessment of the Polymer Composite Materials Quality

Rudenko S.¹, Berladir K.^{1*}[0000-0002-4287-8204], Trojanowska J.²[0000-0001-5598-3807], Varenyk S.¹, Shvetsov D.¹, Kravets V.¹

¹ Sumy State University, 2, Rymaskogo-Korsakova St., 40007 Sumy, Ukraine;

² Poznan University of Technology, 3, Piotrowo St., 60-965 Poznan, Poland

Article info:

Submitted:

August 30, 2021

Accepted for publication:

November 29, 2021

Available online:

December 3, 2021

*Corresponding email:

kr.berladir@pmtkm.sumdu.edu.ua

Abstract. The paper is devoted to developing a methodology for failure mode and effects analysis on the example of assessment of defects that occur during production and operation of polymer composite materials and industrial products from them. The paper uses the Ishikawa method to illustrate and further analyze the cause of defects in reinforced polymer composite material. The Ishikawa diagram was constructed and analyzed using the method of causal analysis. The types and consequences of failures and defects for polymer composite materials are analyzed. For each type of defect, the value of the priority number of risks is calculated. For the most critical defect, measures to reduce potential defects are proposed. Suggestions for improving the detected defective zones in the structures of polymer composites in the analysis process are given.

Keywords: FMEA, product innovation, quality control, defect, polymer composite material, method Ishikawa, economic productivity.

1 Introduction

All defects in composite materials are divided into two major classes [1]: manufacturing defects that occur in structures or in the process of their manufacture, manufacturing component components, and operational damage that occurs during operation.

According to the degree of danger, the first group includes defects associated with a low degree of curing of the polymer matrix and deviations in the material composition from the entire volume of the normalized values [2]. They lead to a decrease in heat resistance of the material, a sharp deterioration of performance characteristics such as water and moisture resistance, to reduce the resistance of the material to aggressive environments, and changes like material destruction under static and dynamic fatigue loads. Deviations in the composition of a significant amount of material lead to significant changes in the characteristics of strength, elasticity, and operational reliability [3]. These changes depend to varying degrees on the type of deformation (tension, compression, shear), the nature of the stress state (uniaxial, flat, volumetric), as well as the duration and cyclicity of the load.

The second group includes delamination [4] (Figure 1).

Manufacturing and operational defects and damage of composite materials are presented in Table 1.

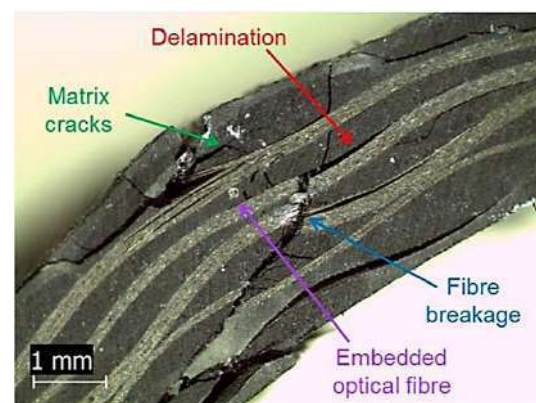


Figure 1 – Delamination in defective composite material [5]

The effect of delamination on the material properties significantly depends on the type of stress state. The tensile strength and modulus of elasticity of the delamination in its pure form are practically not affected. Simultaneously, the compressive strength of the delamination material can be significantly reduced depending on the depth and length of the delamination.

Table 1 – Manufacturing and operational defects and damage of composite materials

Defects and Damages in Composite Structures	Microdefects	Defects of reinforcing fibers
		Matrix defects in the intervals between the elementary fibers
		Defects at the “matrix – fiber” interface
	Minidefects	Twisting the fibers
		Curvature of fibers
		Fiber misorientation
		Different degrees of fiber tension
		Small risks, scratches, dents
		Unreinforced binder areas
		Breakage of individual threads, bundles, or groups of elementary fibers
		Depletion of binder in separate sections of threads or bundles
		Dimensional rejects of composite material blanks
		Dimensional rejects of workpieces during processing
		Chips
	Macrodefects	Cracks and notches that cross the layers inward (through and not through)
		Sinks and dents on the surface of composite material
		Impact defects (not visible, visible not through, though)
		Delamination, bulging, non-adhesion, air micro-connections (open, closed, multi-storey)
		Buckling of the structure
		Overlapping layers or turns of reinforcing material
		Foreign microinclusions
		Significant scratches with a depth of more than one elementary layer of composite material
		Formation of folds of reinforcing material with an influx of binder (internal, surface)
		Local decrease in adhesive strength between layers of composite material
	Operational damage	Mechanical wear
		Fatigue wear
		Aging
		Combat damage
		Emergency damage
		Damage from improper and negligent maintenance
		Other damage

The third group of defects is cracking [6]. Cracks create a high concentration of stresses, disrupt the integrity of the composite, and can lead to delamination of the material.

The fourth group of defects includes local areas with high fiber content, matrix, and pores [7]. The degree of danger of these defects ultimately depends on the defect’s size, shape, and location.

The fifth group includes folds, swirls, shells, foreign inclusions, joints, and overlaps of reinforcing filler [8]. Joints and overlaps mainly affect the physical and mechanical characteristics due to changes in the composition of the material.

Particularly, an increase in the degree of reinforcement in the overlap zone and a decrease in the butt zone, and to a lesser extent, affect mechanics stress concentrators. Folds, swirls, and foreign inclusions have a very similar effect on the physical and mechanical properties of the material, as they lead to the local curvature of the fibers and changes in the composition of the material in the cross-section of the defect. The effect of these defects on the strength and elasticity increases with increasing degrees of reinforcement of the material because these defects affect more layers of material [9].

The sixth group consists of chips, cuts, and holes, concentrating stresses [10]. Studies show [11] that the effect of stress concentrators in the form of spots on the strength of carbon plastics decreases both with prolonged static load over the test duration and with the increasing speed of one-time static and dynamic deformation. Increasing the test temperature also leads to a decrease in the effective stress concentration of carbon fiber with a complex scheme of reinforcement [12].

The seventh group includes defects associated with the curvature of the fibers of the plane of the layers, with a slight deviation of the reinforcement angle from the specified value [13]. In most cases, defects of this type are not large-scale, and the curvature or deviation of the reinforcement angle, as a rule, affect only one or more layers of the composite. Their size is much smaller than the size of the structural element.

Quality control of polymer composite materials (PCM) products must be carried out throughout their life cycle [14]. The life cycle of PCM parts consists of four main stages: design, production, operation (including repair), and utilization (including recycling) [15].

The rule of 10 times A illustrates the cost of eliminating defects. Feigenbaum [16]. The cost of correcting the defect increases ten times at each subsequent stage of the product life cycle:

$$1:10:100:1000$$

1000 monetary units – the necessary operating costs,
 100 monetary units – the necessary costs of production,
 10 monetary units – the necessary costs in preparing for production,
 1 monetary unit – the necessary costs for the design of the product.

In this regard, the actual task is analyzing and assessment the types and consequences of defects that occur during the manufacturing and operation of polymer composite materials and industrial products from them according to the FMEA.

The main application of FMEA is to improve product design (service characteristics) and its manufacturing and operation (service delivery) processes [17]. The analysis can be applied concerning newly created products (services) and processes and existing ones [18].

2 Research Methodology

The research object is defects of PCM and their evaluation by FMEA (Figure 2).

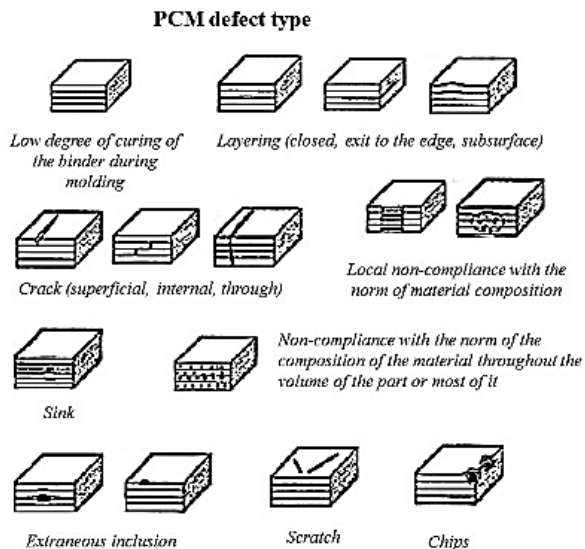


Figure 2 – Different polymer composite material defects, including the research object

Stages of FMEA included:

- 1) construction of structural component, functional and flow models of the object of analysis;
- 2) research models. During the study of models are determined:

- potential defects of each of the elements of the component model of the object. Such defects are usually associated either with the failure of the functional element (its destruction and breakage), with the incorrect performance of its valuable functions (failure of accuracy and performance), or with harmful functions of the element. It is also necessary to consider potential defects during transportation, storage, and external conditions (humidity, pressure, temperature).

- potential causes of defects. Ishikawa diagrams, constructed for each object's functions with the appearance of defects, can be used for detection.

- potential consequences of consumer defects. Since each of the considered defects can cause a chain of failures in the object, the analysis of the consequences uses structural and flow models of the object.

- the ability to control the appearance of defects. It is determined whether the defect can be detected due to the measures provided in the object of control and diagnosis;

- 3) expert analysis of models. The following parameters are defined (Figure 3):

- the parameter of the severity of the consequences of the consumer S. It is an expert assessment, which is usually given on a 10-point scale; the highest score is given for cases where the consequences of the defect lead to legal liability;

Factor S	Factor O	Factor D
1 - very low (almost no problems)	1 - very low	1 - almost immediately the effect will be detected
2 - low (problems are solved by the employee)	2 - low	2 - very good detection
3 - not very serious	3 - not very low	3 - good
4 - below average	4 - below average	4 - moderately good
5 - average	5 - average	5 - moderate
6 - above average	6 - above average	6 - weak
7 - quite high	7 - close to average	7 - very weak
8 - high	8 - high	8 - bad
9 - very high	9 - very high	9 - very bad
10 - catastrophic (danger to people)	10 - 100%	10 - almost impossible to determine

After receiving expert assessments S, O, D calculate the priority number of PCR risk according to the formula: $PCR = S \cdot O \cdot D$

Figure 3 – Assessment of PCM defects

- defect frequency parameter O – it is also an expert assessment, which is given on a 10-point scale; the highest score is given when the estimate of the frequency of occurrence is 1/4 and above;

- defect detection probability parameter D – like the previous parameters, it is a 10-point expert assessment; the highest score is given for hidden defects that cannot be detected before the consequences;

- consumer risk parameter PNR (priority number of risk). It is defined as the product $S \times O \times D$ (Figure 3). This parameter shows what relationship to each other is currently the causes of defects. Defects with the highest risk priority factor (PNR is greater, or 100–120) must be eliminated in the first place.

The assessment of factors S, P, and D are assessed on the qualimetric scales presented in Figure 3.

3 Results and discussion

An analysis of the types and consequences of failures was performed to assess PCM defects discussed above. For each type of defect, the value of the priority number of risks is calculated. For the most critical defect, measures to reduce potential losses are proposed.

To obtain the results, it was not the potential failures considered but those determined from PCM defect statistics analysis.

Due to the structural analysis at different scale levels, the actual material is accumulated, which allows obtaining initial data for structural-parametric modeling:

- determining the values of the effective characteristics of all components of the composite;
- estimates which of these components and at what load will be destroyed in the first place;
- quantitative assessment of the impact of stress concentrators on the growth of the main crack.

Structural modeling allows to describe in general the dynamics of the destruction process but does not give numerical estimates of the obtained models. Among the many parametric models used to describe the behavior of polymeric composite materials under load, the theory of percolation is becoming more widespread. It allows finding a correlation between the corresponding geometric (e.g., considering the scheme of filler, the effect of thickness, and defects) and physical characteristics.

3.1 Construction of the Ishikawa diagram on the example of a defect in the carbon fiber-filled PTFE-composite

The occurrence of the defect of the PCM based on polytetrafluoroethylene and carbon fibers [19] was analyzed.

The practical methodology of the Ishikawa method is illustrated in Figure 4.

First, a macrostructural analysis of the polymer composite was performed. A visual study of the surfaces of the studied samples showed the heterogeneity of the distribution of carbon fiber in the matrix of the polymer (a), the spotted structure (b), and the presence of cracks (c).

During the wear tests, an increase in the temperature in the friction zone up to 200 °C was noted, which led to the sample set with the counter body. It is due to the material's low physical and mechanical properties (low density, uneven distribution of carbon fiber in the matrix), which confirms the results of further tests.

Secondly, tests were conducted to determine carbon fiber-filled PTFE composite's physical, mechanical, and tribotechnical characteristics. The mechanical tests showed that all samples have a low elongation at break

(30-100 %). It is usually a consequence of poor mixing of the source components – coagulated fiber in the composition matrix.

Third, the Ishikawa diagram was constructed using a step-by-step algorithm of the causal analysis method. The causes of defects were divided into six key positions – man, method, material, mechanisms, control, and environment. The most significant causes of this problem were identified in low-skilled workers and in violation of mixing technology.

3.2 Drawing up a protocol for FMEA of PCM defects

For the priority number of risks, a critical limit (PNR_{cr}) should be set in advance from 100 to 125. Reducing PNR_{cr} corresponds to the creation of higher quality and reliable products.

Next, we need to make a list of defects for which the value of PNR exceeds PNR_{cr} . For such defects, it is necessary to recommend ways to eliminate and prevent them, and therefore, general methods to improve the effectiveness of polymer composite materials.

The protocol of the analysis of types, causes, and consequences of polymer composites is given in Table 2.

3.3 Quality control of products from PCM

The use of modern non-destructive testing methods at all stages of the product life cycle eliminates the lack and increases the durability of parts with PCM (Figure 5).

At the design stage, control the technical documentation to produce parts. There are input, interoperative, and output quality control at the production stage. At input, control has checked the quality of the used raw materials.

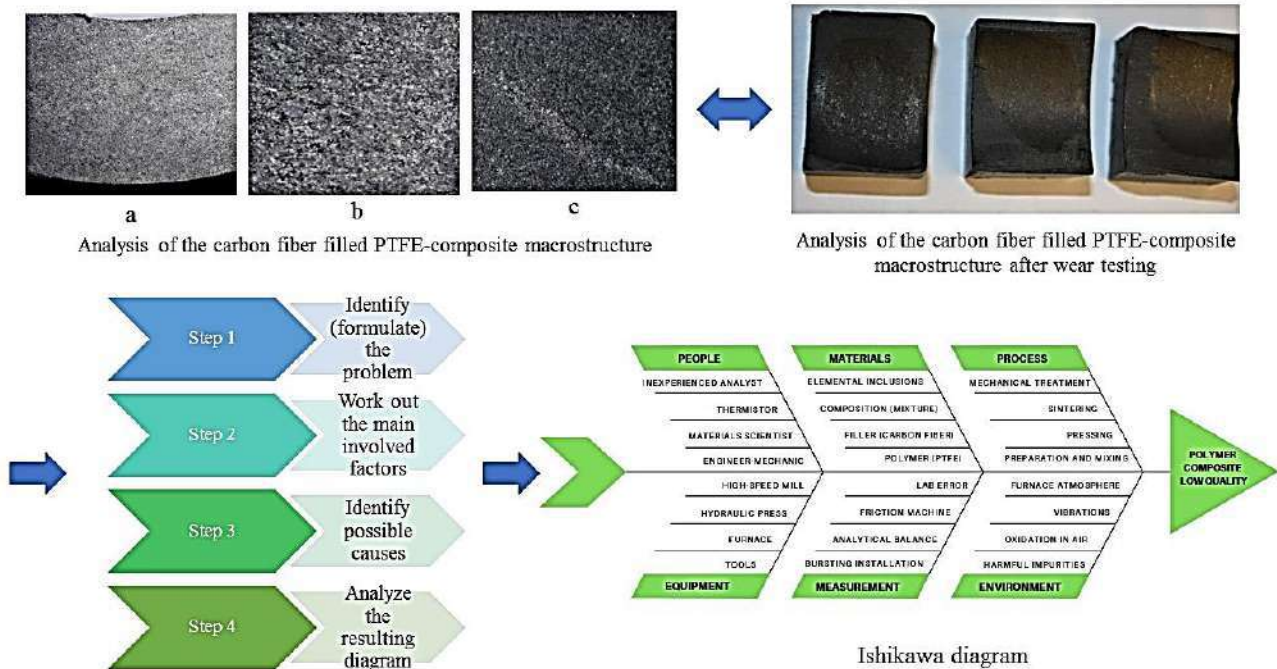


Figure 4 – The detailed practical methodology for the construction of Ishikawa diagram

Table 2 – Protocol for analysis of types, causes, and consequences of defects of polymer composites.

Defect type	Consequences of the defect	Rank “S”, ball	The cause of the defect	Rank “O”, ball	Defect detection measures	Rank “D”, ball	RNR, ball
Low degree of curing of the binder during molding	It leads to significant changes in the characteristics of strength, elasticity, and operational reliability	7	Deviation from the norm in the binder. Non-compliance with the temperature-hour mode of formation	4	The degree of polymerization is less than 95-98 %	4	112
Non-compliance with the norm of the composition of the material throughout the volume of the part or most of it	It leads to significant changes in the characteristics of strength, elasticity, and operational reliability	7	Deviation of the composition of the prepreg from the norm, violation of the terms or conditions of storage. Non-compliance with the formation regime	4	Set volumetric values of matrix (V%), fibers (V%)	4	112
Layering	It leads to significant changes in the characteristics of strength, elasticity, and operational reliability	7	Getting anti-adhesive lubricants, films. Insufficient content of volatile binders. Violation of the mode of formation: increased temperature, high cooling rate, unregulated thermal or mechanical effects. The poor anti-adhesive coating on the surface of the equipment	4	It is determined visually by the shape and size in the plan, the depth of occurrence	4	112
Crack	Destruction of details	9	Violation of the forming mode, high cooling rate. There is a predominance of permissible mechanical loads when removing a part by tooling and transportation. Impact during operation	3	It was determined visually. The size of the defect in the plan. It affected layers and the direction of cracks on the part.	3	81
Sink	Affect the physical and mechanical properties of the material, as they lead to the local curvature of the fibers and changes in the composition of the material in the cross-section of the defect	7	Increased content of volatile elements in the prepreg. Violation of the modes of formation: the heating rate, time, value, applied pressure	5	The size of the defect in the plan. Depth of occurrence	3	105
Extraneous inclusion	Affect the physical and mechanical properties of the material, as they lead to the local curvature of the fibers and changes in the composition of the material in the cross-section of the defect	5	Getting foreign materials in the manufacture of prepreg, when it is exposed calculations	4	Dimensions in plan and thickness of inclusion. Depth of occurrence. Location and orientation of the area on the details	4	80
Local non-compliance with the norm of material composition	Destruction of details	9	An uneasy grip when molded. Uncertainty of rolling	3	Determined visually. The size of the defect in the plan. Affected layers and direction of cracks on the part	3	81
	A local area with a shift in the matrix of abo fibers	9		3		81	
	Local area with pore space	9	Failure to comply with the applied fall heating rate’s forming mode, time, and magnitude. Deflection of prepreg content	4		3	91

In the process of interoperation control, it is necessary to control the correctness and accuracy of compliance with technological regimes, assess their reliability, manufacturability, and design. Finished products are subject to initial control. At this stage, check the

compliance of finished products to the specified requirements.

Input control of raw materials used and output control of finished products can be continuous or selective. A continuous control, each production unit (raw materials) is checked. Continuous control is used in conditions of

exceptionally high requirements for the level of quality of products, in which it is unacceptable to pass defects into further production or operation due to significant losses (material and labor). Also, it may be in cases where the number of parts is insufficient to obtain samples or samples risks of the manufacturer and the consumer, and if technological process (equipment) does not provide stability of quality of the made details.

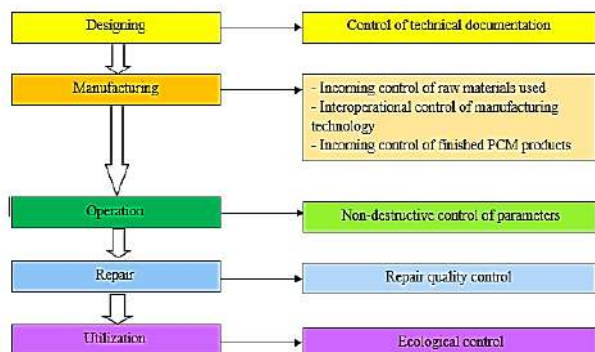


Figure 5 – Methods of quality control at different stages of the life cycle of PCM parts

In the case of selective control, only a specific part of the products (sample) is subject to inspection. Selective control gives a good result in the presence of a stable and well-established technological process of manufacturing parts.

At the stage of operation and repair of products with PKM and methods of visual diagnostics, the most widely used are various non-destructive testing methods. Depending on the physical nature of the signal used and the nature of its interaction with matter, these methods are divided into acoustic, eddy current, dielectric, thermal, and radiometric.

Disassembly, sorting, reusability assessment, and recycling are performed at the disposal stage. Most environmental indicators are monitored (safety of utilization).

4 Conclusions

FMEA is effective in reliability and in creating fault-tolerant systems that any developer should have. This method can allow developers to reduce the risk of

References

1. Heslehurst, R. B. (2014). *Defects and Damage in Composite Materials and Structures*. CRC Press, Boca Raton, FL, USA.
2. De León, A. S., Molina, S. I. (2020). Influence of the Degree of Cure in the Bulk Properties of Graphite Nanoplatelets Nanocomposites Printed via Stereolithography. *Polymers*, Vol. 12, 1103, doi: 10.3390/polym12051103.
3. Muc, A., Romanowicz, P., Chwał, M. (2019). Description of the Resin Curing Process – Formulation and Optimization. *Polymers*, Vol. 11, 127, doi: 10.3390/polym11010127.
4. Suriani, M. J., Rapi, H. Z., Ilyas, R. A., Petru, M., Sapuan, S. M. (2021). Delamination and Manufacturing Defects in Natural Fiber-Reinforced Hybrid Composite: A Review. *Polymers*, Vol. 13, 1323, doi: 10.3390/polym13081323.
5. *Defects and Damage in Composite Materials and Structures*. Available online: <https://www.addcomposites.com/post/defects-and-damage-in-composite-materials-and-structures>, last accessed 2021/09/10.
6. Beaumont, P. W. R., Soutis, C. (2016). Structural integrity of engineering composite materials: a cracking good yarn. *Phil. Trans. R. Soc. A.*, Vol. 374, 20160057, doi: 10.1098/rsta.2016.0057.
7. Li, D., Song, S., Zuo, D., Wu, W. (2020). Effect of Pore Defects on Mechanical Properties of Graphene Reinforced Aluminum Nanocomposites. *Metals*, Vol. 10, 468, doi: 10.3390/met10040468.

critical situations. FMEA also increases product safety and, importantly, is easy to learn.

As a result of the application of the developed FMEA-methodology for the analysis of types and consequences of defects of polymer composites in operation, it was defined:

- the highest value of the priority number of risk (PNR) is 112. It corresponds to the low degree of curing of the binder during molding and non-compliance with the norm of the composition of the material throughout the part or most of it and delamination.

- reduction of PNR for the defect «Low degree of curing of the binder during molding» is possible due to the improvement and automation of control systems of the degree of polymerization less than 95-98 %.

- reducing PNR for the defect «Material composition norms for the entire volume of the part or most of it» is possible by controlling the set value of the volumetric value of the matrix and fibers.

- reducing PNR for the defect «Layering» is possible due to the improvement of mechanical and automated programs.

The paper tested Ishikawa's method to identify the cause of defects in low-quality carbon fiber PTFE-composite, which was divided into six key positions – man, method, material, mechanisms, control, and environment. The most significant causes of this problem were identified in low-skilled workers and in violation of mixing technology.

The task of ensuring high quality, reliability, and competitiveness of PCM products for industrial use, operating in harsh production conditions, cannot be successfully solved without effective modern control methods at all stages of the production cycle and life of this type of technical product. In this case, each step corresponds to its control methods, which are divided by quantitative, qualitative, and alternative characteristics.

5 Acknowledgments

The research was partially carried out within the project “Fulfillment of tasks of the perspective plan of development of a scientific direction “Technical sciences” Sumy State University” funded by the Ministry of Education and Science of Ukraine (State reg. no. 0121U112684).

8. Feraboli, P., Cleveland, T., Ciccu, M., Stickler, P., DeOto, L. (2010). Defect and damage analysis of advanced discontinuous carbon/epoxy composite materials. *Composites Part A: Applied Science and Manufacturing*, Vol. 41(7), pp. 888–901, doi: 10.1016/j.compositesa.2010.03.002.G.
9. Galińska, A., Galiński, C. (2020). Mechanical Joining of Fibre Reinforced Polymer Composites to Metals – A Review. Part II: Riveting, Clinching, Non-Adhesive Form-Locked Joints, Pin and Loop Joining. *Polymers*, Vol. 12, 1681, doi: 10.3390/polym12081681Wq.
10. Kumar, S.A., Rajesh, R., Pugazhendhi, S. (2020). A review of stress concentration studies on fibre composite panels with holes/cutouts. *Proceedings of the Institution of Mechanical Engineers, Part L: Journal of Materials: Design and Applications*, Vol. 234(11), pp. 1461–1472, doi: 10.1177/1464420720944571.
11. Kim, D.-U., Seo, H.-S., Jang, H.-Y. (2021). Study on Mechanical Bearing Strength and Failure Modes of Composite Materials for Marine Structures. *J. Mar. Sci. Eng.*, Vol. 9, 726, doi: 10.3390/jmse9070726.
12. Xie, N., Smith, R. A., Mukhopadhyay, S., Hallett, S. R. (2018). A numerical study on the influence of composite wrinkle defect geometry on compressive strength. *Materials & Design*, Vol. 140, pp. 7–20, doi: 10.1016/j.matdes.2017.11.034.
13. Stankovic, D., Bisby, L. A., Terrasi, G. P. (2021). Influence of Temperature on the Mechanical Performance of Unidirectional Carbon Fiber Reinforced Polymer Straps. *Materials*, Vol. 14, 1903, doi: 10.3390/ma14081903.
14. Tapper, R. J., Longana, M. L., Norton, A., Potter, K. D., Hamerton, I. (2020). An evaluation of life cycle assessment and its application to the closed-loop recycling of carbon fibre reinforced polymers. *Composites Part B: Engineering*, Vol. 184, 107665, doi: 10.1016/j.compositesb.2019.107665.
15. Ead, A. S., Appel, R., Alex, N., Ayranci, C., Carey, J. P. (2021). Life cycle analysis for green composites: A review of literature including considerations for local and global agricultural use. *Journal of Engineered Fibers and Fabrics*, January 2021, doi: 10.1177/15589250211026940.
16. Feigenbaum, A. (1956). Total quality control. *Harvard Business Rev.*, Vol. 34(6), pp. 93–101.
17. Boccaletti, B. C., Mello, L. B. de B., Bastos, I. P. (2021). Principal causes and challenges for reducing product returns: applying FMEA in a case study. *Gestão & Produção*, Vol. 28(2), e5115, doi: 10.1590/1806-9649-2020v28e5115.
18. Kimita, K., Sakao, T., Shimomura, Y., (2017). A failure analysis method for designing highly reliable product-service systems. *Research in Engineering Design*, doi: 10.1007/s00163-017-0261-8.
19. Budnik, O. A., Sviderskii, V. A., Budnik, A. F., Berladir, K. V., Rudenko, P. V. (2016). Composite material for chemical and petrochemical equipment friction assemblies. *Chemical and Petroleum Engineering*, Vol. 52(1), pp. 63–68.



Kolawole, M. Y., Awoyemi E.A., Abiona, O. M. (2021). Potentials of date-seed/snail shells as a carburizer for enhanced mechanical properties of mild-steel. *Journal of Engineering Sciences*, Vol. 8(2), pp. C1-C6, doi: 10.21272/jes.2021.8(2).c1

Potential of Date-Seed/Snail Shells as a Carburizer for Enhanced Mechanical Properties of Mild-Steel

Kolawole M. Y.¹[0000-0001-9012-5533], Awoyemi E. A.¹, Abiona O. M.²

¹ Department of Mechanical Engineering, Kwara State University, PMB 1530, Ilorin, Nigeria;

² Department of Mechanical Engineering, Osun State College of Technology, Esa Oke, Nigeria

Article info:

Submitted:
Accepted for publication:
Available online:

July 13, 2021
November 8, 2021
November 12, 2021

*Corresponding email:

maruf.kolawole@kwasu.edu.ng

Abstract. The suitability of date-seed/snail shells as a carburizer for enhanced mechanical properties of mild-steel using the packed carburization technique was investigated in this work. Standard tensile, impact and hardness test samples prepared from mild-steel were subjected to pack-carburization process using mixtures of date-seed and snail shell in the ratio 60:40 respectively at 800, 900, and 1 000 °C for 3 hours. The carburized samples were quenched in water at room temperature and further tempered at 300 °C for 30 minutes for residual stress relief of the quenching effect. The mechanical properties and optical microstructure of carburized specimen were performed. Results indicated an enhanced mechanical property of the carburized mild-steel using date-steel/snail shell as a carburizer compared to un-carburized same steel material. The tensile strength and hardness increased with increasing carburizing temperature, though with an associated decrease in ductility. The peak hardness (32.82 HRB) and tensile strength (521 MPa) with equivalent 31.28 and 51.45 percentage increments respectively were obtained at carburizing temperature of 1 000 °C. Hence, using date-seed/snail shell powder as a carburizer can enhance the mechanical properties of mild-steel.

Keywords: carburization, mild-steel, mechanical properties, date-seed, snail shell.

1 Introduction

In today's technological world, nearly everyone depends on carbon steels materials. This is due to a wide array of their applications in automotive chassis, body, and component parts, reinforcement of concrete in the structure, fuel, and water tankers, as well as manufacturing of engineering parts (ball bearing, shaft, drill bit, and gear) and equipment for mobility, health, safety and economic well-being of human sustenance [1, 2].

The versatility of mild-steel in engineering applications can be anchored on its moderate yield strength, availability at lower cost, and good toughness and ductility characteristics suitable for various applications. However, the quest for more improved properties of low carbon steel is on the increase for the production of durable machines and structures with high-quality performance and efficiency to meet the present technologically driven-era requirements and attracted researchers' interest [3–5]. Therefore, improving the mechanical strength of mild steel will enhance the structural integrity and widen its suitability in high precision engineering applications. One

of the essential means of achieving this is by heat treatment processes such as carburization. This technique was widely reported to be suitable for improving low carbon steel materials' mechanical and wear properties [4, 6, 7]. This process can be achieved by either gas, packed, vacuum, or liquid methods. However, the packed carburization technique has gained more attention from researchers due to its cost-effectiveness without compromising the quality of parts.

Pack-carburization is a surface impregnation thermo-diffusional heat treatment technique in which metallic specimen usually steels, exposed to packed carbonaceous materials at controlled elevated temperature, pick-up free-carbon from surrounding furnace atmosphere followed by desirable cooling mode to modify the surface and properties of metal. It is one of the most commonly performed heat treatment methods to enhance hardness, wear, and mechanical properties by impregnating alloys of steel surfaces with carbon [8]. Over the years, carburization was usually performed in a conventional carbon-rich environment (coke, activated carbon, and charcoals) using synthetic barium or calcium carbonate as

an energizer. However, recent findings have unveiled the suitability of various agro-wastes, which are readily available, as a carburizer and, in turn, will also help in the maintenance of a clean environment for a healthy life [3, 5, 6, 9–12].

According to Adly et al. [13], the temperature, soaking time, and types of the carburizing atmosphere have a more significant influence on the performance of the carburization process. Consequently, various researchers' findings on the carburization of mild steel under different conditions are well documented in the literature.

Aramide et al. [14] examined the effect of carburizing temperatures (850, 900, and 950 °C) and time 15 and 30 minutes on mechanical properties of mild steel using activated carbon as the carburizing agent. Analysis of their investigation revealed that the carburizing temperature and time significantly influenced the mechanical properties of mild steel. However, the optimum combination of mechanical properties was recorded at 900 °C carburizing temperature followed by quenching in oil.

A similar result was obtained by Olufemi et al. [15], where the best combination of mechanical properties was achieved at 950 °C over a soaking time of 2 hours in carbonized palm kernel carburizing atmosphere.

Furthermore, Umunakwe et al. [6] investigated the suitability of palm kernel shell and coconut shell powders as a carburizer in singular and hybrid forms. It was discovered that tensile strength and hardness properties were better enhanced with mixtures of a carburizer compared to single carburizing media. Furthermore, 80 wt. % of coconut shell and 20 wt. % palm kernel shell hybrid mixtures yielded the peak mechanical properties. In another study [3], charcoal was used as carburizing materials and cow bone as energizer at different weight proportions. The carburization process was carried out at 900 °C for 8 hours in a muffle furnace. Evidence obtained from this experimentation showed an adequate case depth of 2.32 mm with the best hardness profile recorded at 60 wt. % charcoal and 40 wt% cow bone composition, which affirms the usability of cow bone as a suitable energizer for mild steel carburization.

Other wastes explored as carburizing agents for improving mild steel properties include periwinkle snail shells, as reported by Adzor et al. [16]. Prepared mild steel samples were packed in a mixture of 85 % of carbonized periwinkle shell powder and 15 % barium carbonate and were fired at 850, 900, and 950 °C using an electric furnace under different soaking times followed by tempering. The results revealed that hardness increased with increasing carburizing temperature and dwelling time. However, a decreasing trend in impact strength was recorded with increased carburizing temperature and soaking time. This result corroborated with the recent findings of Adzor et al. [5], where 80 wt. % of snail shell and 20 wt. % melon shell mixture was used as a carburizer.

Undoubtedly, available literature has shown that extensive works had been done on the potential of various agro and animal wastes such as date-seed and African giant snail shells as a carburizer to enhance the mechanical properties of mild steel. However, it was observed that

there are still numerous other agro-wastes such as date-seed, whose suitability as an alternative carburizer has not yet been explored in the heat treatment of mild-steel. Date-seeds are discarded parts of a date-fruit after the fleshy parts have been eaten or removed. The challenges of incessant discarding of this seed with no economic value, especially in most Asian countries and northern parts of Nigeria where date-palm fruit are being grown and consumed heavily, are alarming and constituting environmental nuisance [17].

In addition, giant African snail shells are readily available at low or no cost in most tropical parts of Africa and the western region of Nigeria, where they are consumed as meat for food. The use of these wastes (date-seed and African snail shell) as a carburizer are rarely found in the literature despite their discarding consequence on the environment and human health concerns. Hence, this study aims to present the suitability of date-seed and giant African snail shells as a carburizer to enhance the mechanical properties of mild steel.

2 Materials and Methods

2.1 Materials and equipment

The materials and equipment used in this study include mild steel with chemical composition as shown in Figure 1, date-seed wastes, African giant snail shells, Sieving machine, steel boxes, muffle furnace, optical microscope, weighing balance, fired clay, tong and bench-vice, water, Universal tensile testing machine (UTM), impact testing machine and Rockwell hardness tester (HRB).

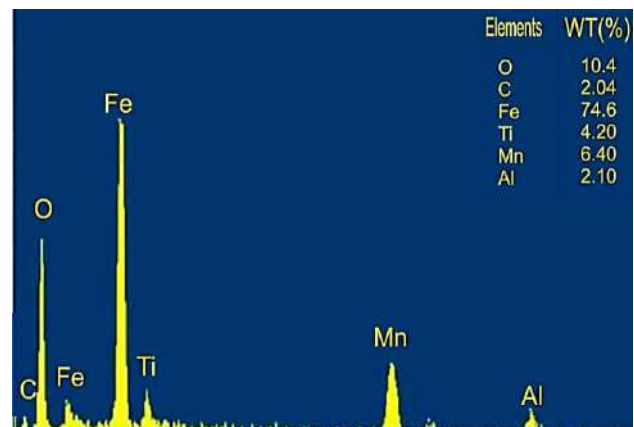


Figure 1 – Chemical composition of mild-steel specimen

2.2 A carburizer and specimen preparation

Date-seed was procured from Iyata market in Ilorin, Kwara state Nigeria, and the snail-shell used was sourced from a DJ restaurant in Osogbo, Osun state Nigeria. To remove moisture, the date-seed was washed and oven-dried at 110 °C for eight hours (8 hours). The dried seed was crushed with hammer mill, pulverized using a disc mill, and sieved down to 200 µm particle size at Land and Water Engineering Laboratory, National Centre for Agricultural Mechanization (NCAM), Ilorin, Kwara State,

Nigeria. A similar procedure was adopted in processing snail shell before it was sieved down to 200 μm sizes. The clay powder retained on 150 μm sieve sizes was used for sealing purposes in this study to prevent oxidation. Each of the sieved samples was kept intact at different air-tight containers before use. This work used a mild steel rod (10232) of dimension 1 000 mm in length and 20 mm diameter with percentage carbon of 0.05–0.25 % procured at Agodi Market, Ibadan Oyo State, Nigeria. Tensile test specimens were machined out of this sample according to ASTM E8/E8M-16a standard (see Figure 2 a, hardness (20 mm height by 10 mm diameter) Figure 2 b and impact specimens with 2 mm depth V-notched shape under ASTM D256 specification and as reported by Oluwafemi et al. were used in this work.

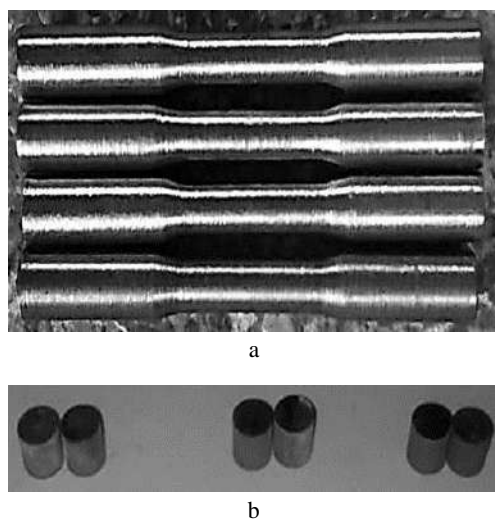


Figure 2 – Samples of a specimen prepared for tensile (a) and hardness (b) testing

2.3 Carburization heat treatment of mild-steel samples

The calculated and weighed amount of the carburizing ingredients in the ratio 60:40 wt. % of date-seed and snail shells, respectively, were mixed. The mixture (date-seed and snail shell) was then packed around prepared specimens (tensile, impact, and hardness samples) in triplicates inside a rectangular metallic box and covered. All air-openings in the packed box were sealed with sticky, moist clay to prevent oxidation of the samples and placed in the chamber of an electric muffle furnace with the temperature set to 800 $^{\circ}\text{C}$ and fired at a heating rate of 10 $^{\circ}\text{C}/\text{min}$ with a dwelling time of one hour. After that, the carburized samples were quenched in water at room temperature, tempered in the furnace at 300 $^{\circ}\text{C}$ for 30 minutes, and air-cooled to room temperature. The same procedure was adopted for the heat treatment of other samples at 900 and 1 000 $^{\circ}\text{C}$, while the control specimens for the same examination were left without heat treatment.

2.4 Evaluation of mechanical properties and microstructure

In this work, tensile, impact, and hardness tests were used to evaluate the mechanical properties of both carburized and uncarburized standardized samples. The tensile test was carried out at National Centre for Agricultural Mechanization Ilorin, Kwara State Nigeria, under ASTM E8/E8M-16a standard on Testometric Universal Testing Machine (0500-10080). The samples were subjected to a uniaxial tensile loading at 10 mm/min machine test speed until failure occurred. Both treated and untreated samples' hardness was performed on Rockwell hardness tester (HRB) with 5 indentations taken from Materials Science and Engineering Laboratory, Malet, Kwara State University. The average of the five indentations was used as the hardness of the sample for each of the variations. Impact strength testing of the V-notched specimen was performed by applying a constant impact force on the Avery Dension Impact testing machine located at the material testing laboratory, University of Ilorin, Ilorin, Nigeria.

Samples for surface morphology examinations were first cut using parting-off tools on the lathe machine. The surface was flattened and smoothed using different sizes of emery paper of 400, 600, 800, and 1 000 μm grit size in that order on a rotating disc grinding machine. The polished samples were etched using 2 % Nital solution, after which surface morphology was viewed using Olympus BX 41M microscope.

3 Results and Discussion

3.1 Tensile strength behavior

The influence of the date-seed/snail shell powder packed-carburizing process on yield tensile strength of mild-steel at 0, 800, 900, and 1 000 $^{\circ}\text{C}$ temperatures are as shown in Figure 3. It was revealed that the yield tensile strength of mild-steel increases with an increase in carburizing temperature though at the expense of ductility, as discernible in Figure 3. The yield tensile strength was lowest in uncarburized mild-steel samples with a magnitude of 344 MPa and 32 % as percentage strain. The yield strength rose to 357 MPa with no significant loss in ductility when carburized at 800 $^{\circ}\text{C}$. A similar trend was noticed as the carburizing temperature increases to 900 and 1 000 $^{\circ}\text{C}$ with the corresponding yield strength of 514 MPa and 521 MPa, respectively. Hence, the peak ultimate tensile strength was obtained when the mild steel was carburized at 1 000 $^{\circ}\text{C}$. However, the percentage strain decreases to 30 and 24 % at 900 and 1 000 $^{\circ}\text{C}$ carburizing temperatures, respectively. This implies a loss of ductility as yield strength increases due to increasing carburizing temperatures. The increase in strength observed in this work could be attributed to the increased diffusibility of carbon in date-seed as energized by thermal decomposition of snail shell brought about by carburizing temperature. The increasing carburizing temperature tends to increase the diffusion process for more infiltration of a carbon atom at the interstices of the atomic structure. This,

in turn, increases the dislocation density at the surface to a particular depth level of the carburized materials. Consequently, the strength of mild-steel increases. This result was in good agreement with authors [13, 14, 18, 19], where increment in ultimate tensile strength was reported using various types of a carburizer and carburizing parameters.

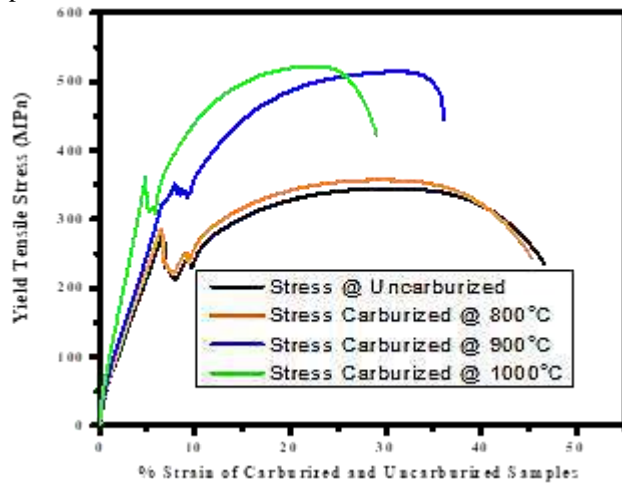


Figure 3 – Influence of carburizing temperature on the yield strength of mild steel

3.2 Impact energy

Figure 4 shows the impact strength of un-carburized and carburized mild-steel at different temperatures (800, 900, and 1 000 °C). It was observed that the carburizing temperature influenced the impact strength of mild steel. The lowest impact strength (96 J) was recorded in uncarburized mild-steel samples. But when it was carburized at 800 °C, the impact strength rose to 133.5 J. Increasing the carburizing temperature to 900 °C only had little influence on the impact strength by increasing it to 137 J. At 1 000 °C carburizing temperature, the impact strength of mild-steel decreases to 133.5 J. The equivalent increase in impact strength carburized at 800, 900, and 1 000 °C respectively is 39, 43, and 40 % compared to uncarburized mild steel. As obtained in this work, these findings indicated a deviation from earlier researchers [11, 14–16], where an increase in carburizing temperature resulted in impact strength reduction of the carburized mild-steels. However, the initial rise in impact strength as presented in this study can be attributed to the case hardening effect of the mild-steel due to carbon depositions below the saturation limit at 800 °C. But as the carburizing temperature increases, more deposition of carbon atoms occurs closer to the saturation limit. This results in increased hardness of the mild-steel, and consequently, brittleness of the mild-steel rises. The high hardness value resulting from increasing carburizing temperature, which in turn translates to brittleness, can be responsible for the 3 % drop in impact strength as discernible in Figure 3 when the carburizing temperature was raised from 900 to 1 000 °C.

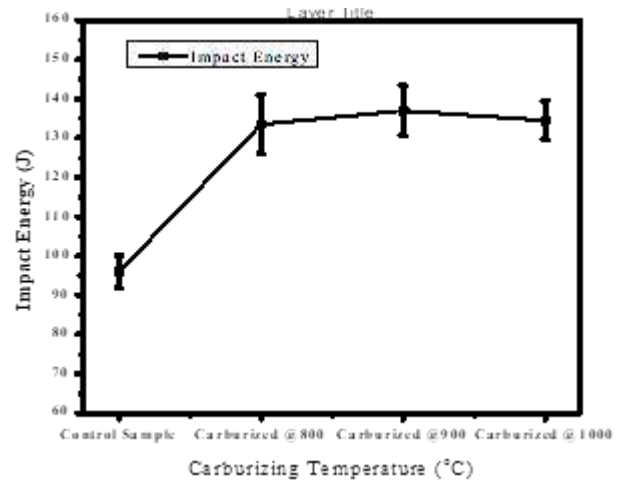


Figure 4 – Impact energy of date-seed/snail shell carburized mild-steel at different temperatures

3.3 Hardness properties of carburized steel

The hardness distribution of uncarburized and carburized mild steels at a distance of 2 mm to the surface are presented in Figure 5. It was observed that the carburizing temperature significantly influences the hardness distributions of samples. The least hardness (25 HRB) was obtained in uncarburized mild steel samples, and when it was carburized at 800 °C, the hardness rose to 27.83 HRB. Similar increment characteristics were recorded at 900 and 1 000 °C. The peak hardness (32.82 HRB) was obtained when carburized at 1 000 °C. This increment is equivalent to 31.32 % relative to uncarburized sample. The increase in hardness with increasing carburizing temperature as obtained in this work follows a typical pattern of results reported by earlier findings [5, 18, 19]. The increase in hardness observed in this work can be attributed to the formation of a well-dispersed hard martensitic phase in all carburized samples, as discernible in Figure 6. The higher carbons content at the surface due to carbon diffusion implies higher hardness on the surface than in the core, as evidenced in Figure 6.

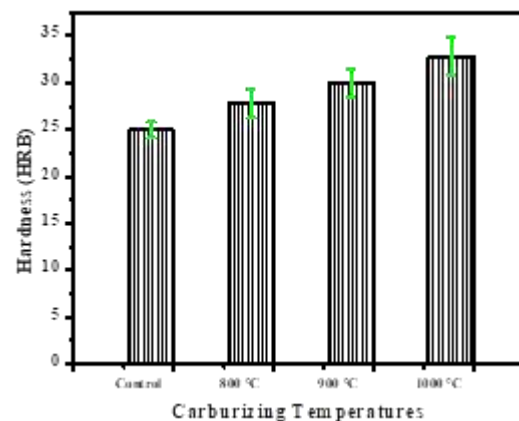


Figure 5 – Hardness behavior of mild-steel at varying carburizing temperatures

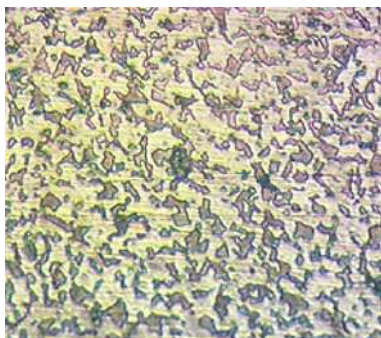
3.4 Microstructural examination

Figure 6 shows the optical micrographs of uncarburized and carburized mild-steels at different carburizing temperatures taken at 1 mm from the surface for all specimens. It was evidenced from Figure 6 that morphological transition occurred from uncarburized to carburized mild-steel samples. For uncarburized sample, the micrograph displayed mixtures of coarse ferrite and pearlite microstructure. But when carburized, quenched, and tempered, the morphology of the mild-steel became altered in terms of size and geometries of the pearlite, ferrite, and martensitic structure. The mild-steel carburized at 800 °C, quenched and tempered, shows a reduction in the size of pearlite and ferrite structure with some traces of carbon infiltration in the interstices of pearlite and ferrite.

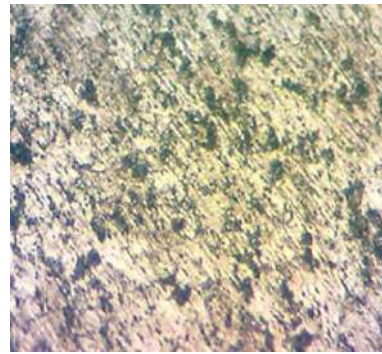
Further increase in carburizing temperature (900, 1 000 °C) revealed a finer microstructure than uncarburized and 800 °C carburized samples. Black finer particles of carbon which were highest in Figure 6 d, were seen been dispersed in the microstructure of highly dark dense pearlite. This indicated the formation of hard martensitic (Fe_3C) darker structure in carburized samples compared to un-carburized samples, which could be responsible for increased hardness. This finding agrees with the results of Thee and Chaiyawat [20], where the microstructure displayed the formation of the hard phase responsible for the increment in hardness of the carburized samples.



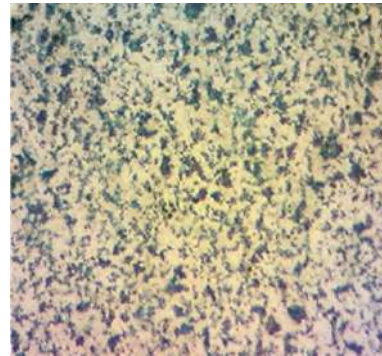
a



b



c



d

Figure 6 – Optical micrograph of carburized mild-steel at different temperatures

4 Conclusions

This work carried out the suitability of date-seed/snail shell as a carburizer on the mechanical properties of pack carburized mild steel, and the following deductions were made.

The date-seed/snail shell has good potential to be used as a carburizer for improved mechanical properties of mild-steel.

The parabolic nature of impact strength behavior with an increase in carburizing temperature and least value recorded in un-carburized sample implies that the tempering process after quenching can enhance the toughness of packed date-seed/snail shell carburized mild-steel.

The peak tensile strength (521 MPa) and hardness (32 HRB) were obtained at 1 000 °C carburizing temperature. These values translate to a 52 % and 31 % increase in tensile strength and hardness, respectively, relative to un-carburized samples.

It is recommended that a comprehensive study of carburizing variables such as particles sizes of date-seed in carbonized form, temperature, and soaking time be considered in further studies to determine the carburization parameters that will produce the optimum surface hardness, wear-resistance, and mechanical properties suitable for critical engineering applications.

References

1. Joseph, O. O., Leramo, R. O., Ojudun, O. S. (2015). Effect of heat treatment on microstructure and mechanical properties of SAE 1025 Steel : Analysis by one-way ANOVA. *Journal of Materials and Environmental Science*, Vol. 6, pp. 101-106.
2. Singh, M. (2016). Application of steel automotive industry. *International Journal of Emergence Technology and Advanced Engineering*. Vol. 6, pp. 246-253.
3. Ihom, P. A. (2013). Case hardening of mild steel using cowbone as energiser. *African Journal of Engineering Research*, Vol. 1, pp. 97-101.
4. Alias, S. K., Abdullah, B., Jaffar, A., Latip, S. A., Kasolang, S., Izham, M. F. (2013). Mechanical properties of paste carburized ASTM A516 steel. *Procedia Engineering*, Vol. 68, pp. 525-530, doi: 10.1016/j.proeng.2013.12.216.
5. Abella, A. S., Aondona, I. P. (2018). Utilization of melon and snail shell waste mixtures in the carburization of mild steel. *International Journal of Trend in Scientific Research and Development*, Vol. 2, pp. 1032-1040, doi: 10.31142/ijtsrd11353.
6. Umunakwe, R., Okoye, O.C., Madueke, C.I., Komolafe, D.O. (2017). Effects of Carburization with Palm Kernel Shell/Coconut Shell Mixture on the Tensile Properties and Case Hardness of Low Carbon Steel. *FUOYE Journal of Engineering Technology*, Vol. 2(1), pp. 101-105, doi: 10.46792/fuoyejt.v2i1.83.
7. Blaoui, M. M., Zemri, M., Brahami, A. (2018). Effect of heat treatment parameters on mechanical properties of medium carbon steel. *Mechanics and Mechanical Engineering*, Vol. 22, pp. 909-918, doi: 10.2478/mme-2018-0071.
8. Nwoke, V. U., Nnuka, E. E., Odo, J. U., Obiorah, S. M. O. (2014). Effect of process variables on the mechanical properties of surface hardened mild steel quenched in different media. *International Journal of Scientific and Technology Research*, Vol. 3(4), pp. 388-398.
9. Prime, M. B., Prantil, V. C., Rangaswamy, P., Garcia, F. P. (2000). Residual stress measurement and prediction in a hardened steel ring. *Materials Science Forum*, Vol. 347-349, pp. 223-228.
10. Afolalu, S. A., Oladipupo, S., Edun, Bose, M., Abioye, A. A., Adejuyigbe, S. B., Ajayi, O. O. (2019). Agro waste - A sustainable source for steel reinforcement-review. *Journal of Physics: Confence Series*, Vol. 1378(3), 032032, doi: 10.1088/1742-6596/1378/3/032032.
11. Madu, K. E., Uyaelumuo, A. E. (2018). Parametric effects of carburization time and temperature on the mechanical properties of carburized mild steel. *Research in Material Science*, Vol. 2018, 3209937, doi: 10.2139/ssrn.3209937.
12. Akanji, O., Fatoba, O., Aasa, A. (2015). The Influence of Particle size and soaking time on surface hardness of carburized AISI 1018 steel. *British Journal of Applied Science and Technology*, Vol. 7, pp. 37-44, doi: 10.9734/bjast/2015/13552.
13. Adly, M., El-Kashif, E., Shash, A.Y., Hamed, A. (2018). Effect of coke size on the mechanical and wear properties of carburized mild steel. *Arabian Journal of Science and Engineering*, Vol. 43, pp. 1083-1092, doi: 10.1007/s13369-017-2724-7.
14. Aramidea, F. O., Ibitoye, S. A., Oladele, I. O., Borode, J. O. (2009). Effects of carburization time and temperature on the mechanical properties of carburized mild steel, using activated carbon as carburizer. *Material Research*, Vol. 12, pp. 483-487, doi: 10.1590/s1516-14392009000400018.
15. Oluwafemi, O. M., Oke, S. R., Otunniyi, I. O., Aramide, F. O. (2015). Effect of Carburizing temperature and time on mechanical properties of AISI/SAE 1020 steel using carbonized palm kernel shell. *Leonardo Electron Journal of Practices and Technologies*, Vol. 14, pp. 41-56.
16. Adzor, S. A., Nwoke, V. U., Akaluzia, R. O. (2016). Investigation of the suitability of periwinkle snail shells as carburizing material for the surface hardness improvement of low carbon steel. *European Journal of Material Science*, Vol. 3, pp. 13-23.
17. Abdulkareem, S., Edache, E. J., Olowosule, I. I., Kolawole, M. Y., Ahmed, I. I., Ajiboye, T. K. (2018). Effect of Date seed particulates on mechanical properties of aluminium alloy. *Acta Technology Corviniensis-Bulletin Engineering*, Vol. 11, pp. 89-94.
18. Negara, D. N. K. P., Widiyarta, I. M. (2019). The study on mechanical properties of pack carburized low carbon steel using BaCO₃ as energizer. *IOP Conference Series: Material Science Engineering*, Vol. 673, 012125, 10.1088/1757-899X/673/1/012125.
19. Verma, M., Dhillon, K. S., Verma, M. (2015). Improvement in the wear resistance and mechanical properties of carburized mild steel by varying carburization temperature and constant tempering temperature. *International Journal of Innovation and Scientific Research*, Vol. 15, pp. 379-388.
20. Thee, C., Peeratatsuwat, C. (2020). Microstructure and hardness evolution of carburized mild steel. *Engineering Journal of Research and Development*, Vol. 31(4), pp. 145-152.



Olawore A. S., Oladosu K. O., Sadiq T. O., Ahmed M., Adesope W. A. (2021). Effects of cold extrusion on the mechanical properties of scrapped copper coil. *Journal of Engineering Sciences*, Vol. 8(2), pp. C7-C12, doi: 10.21272/jes.2021.8(2).c2

Effects of Cold Extrusion on the Mechanical Properties of Scrapped Copper Coil

Olawore A. S.^{1,2}, Oladosu K. O.^{1*}, Sadiq T. O.², Ahmed M.¹, Adesope W. A.³

¹ Department of Mechanical Engineering, Kwara State University, PMB 1530, Ilorin, Nigeria;

² School of Mechanical Engineering, Universiti Teknologi Malaysia, 80990, Johor Bahru, Malaysia;

³ Department of Mechanical Engineering, Oyo State College of Agriculture and Technology, Igboora, Iseyin Rd, 201102, Nigeria

Article info:

Submitted:

August 18, 2021

Accepted for publication:

December 3, 2021

Available online:

December 10, 2021

*Corresponding email:

kamoru.oladosu@kwasu.edu.ng

Abstract. The recycling of copper coil into finished products via sand casting with subsequent cold extrusion was investigated. This paper examined the effects of cold extrusion on the mechanical properties of the scrapped copper coil using a locally manufactured extruder with a conventional face die. The mechanical properties tested on the extrudates are limited to hardness, tensile, and compressive strength. The results reveal that the hardness of extruded copper of 11.10 mm and 11.45 mm improved significantly by 39 % and 41 %, respectively, compared with respective non-extruded copper. The compressive and tensile strength increases by 42 % and 22 %, respectively, for 11.10 mm extruded copper compared with the corresponding non-extruded copper. Also, the elongation of the extruded copper of 11.10 mm and 11.45 mm increases by 33 % and 34 %, respectively. It was deduced that the extruded copper is more ductile than the non-extruded copper. The micrograph reveals that grains in non-extruded copper are relatively coarse and nonuniform with voids, but fine and relatively uniform grains are obtained in extruded copper. The grains are refined during cold extrusion, and voids and dislocations are reduced significantly.

Keywords: billet, extrudate, extrusion, die, deformation.

1 Introduction

Scrap metals, machining chips, and coils which are environmental nuisance and contaminants can be recycled into ingot or die-casting products using different metal forming processes to reduce environmental degradation [1]. Scrap materials can be recycled with remarkable properties through processes like rolling, extrusion, and forging [2].

Copper is a non-ferrous metal with a reddish appearance, and it has an excellent conductor of heat and electricity with a crystal structure of face-centered cubic (FCC) [3, 4]. The copper present in pre-alloyed iron powder (comprising copper, nickel, and molybdenum) boosts hardenability and strength in the powder metallurgy part [5].

Extruded materials possess a combination of properties such as high strength and density, high ductility, good workability and weldability [6], high hardness, tensile and compressive strength [7], yield, and ultimate tensile strength [8]. Severe plastic deformation methods can produce ultrafine-grained material with high ductility and strength [9].

Impact test on specimens parallel to the direction of rolling demonstrated a higher impact toughness value in contrast to the specimen perpendicular to the direction of rolling [10].

Extrusion involves compacting metal scraps, chips, and coils into billets through a die to produce extrudates of the constant cross-section according to the profile of the die orifice [11]. An increase in die angle decreases the extrusion load. The surface roughness and hardness increased with the die angle [12]. The grain size of copper tubes under hydrostatic extrusion increases as the extrusion ratio increases [13].

The processing parameters of ECAP, such as extrusion pass, die angle and pressing velocity, affect the mechanical properties [14]. The ductility of aluminum chips extruded with solid rectangular profile through porthole dies increased compared to the profile extruded through a flat-face die [6]. The annealing twins available after the hot extrusion in powder metallurgy materials deteriorate after cold working [15].

2 Literature Review

Many researchers have studied the mechanical properties and microstructural analysis of extruded metals. Kahlani and Jafarzadeh [16] investigated the mechanical properties and microstructure of bimetallic Al-Cu composite rods fabricated via the spiral extrusion technique. The experimental results show that the bonding quality of the specimen increased due to the application of spiral extrusion. Lv et al. [17] analyzed the CuAl₇ alloy plane micro spring fabricated through the cold extrusion process using a micro-extrusion die. The micro spring microstructure depicted the equiaxed grains with both internal and surface cracks.

Berndt et al. [9] investigated the effect of cold and warm extrusion on the microstructure and mechanical characterization of cylindrical rods that were extruded from cast billets of an AA6060 aluminum alloy at room temperature (RT) and 170 °C (aging temperature of the alloys) respectively. Li et al. [18] experimentally investigated the microstructure changes of Al-Mg-Si alloys produced via hot extrusion and cold rolling. The results showed that the grain growth and dynamic recrystallization occur during hot extrusion, resulting in coarse and equiaxed grain structure.

Vignesh et al. [19] studied the influence of hot extrusion on graphene platelets (GNPs) dispersed aluminum composites. The result showed that the strain hardening exponent and strength coefficient values of aluminum composites with 1.5 wt % GNPs dispersion produced by hot extrusion was two times higher than aluminum and non-extruded Al-GNPs composites. Chen et al. [20] studied the evolution of the microstructure and texture in copper processed via repetitive extrusion-upsetting (REU) and subsequently annealed at different temperatures. There were significant changes in grain morphology and crystallographic texture during the REU process.

Adequate lubrication is needed in the cold extrusion process because it reduces extrusion loads and wear. It also improves the tool life and quality of the products [21]. Kamitani et al. [22] evaluated the performance of different lubricants for producing products with smooth surfaces

during the cold extrusion process. Their findings showed that the smooth surface roughness of the billet was retained when paraffinic mineral oil was used as a lubricant.

Another manufacturing process involved in this study is casting. This method involves the process in which molten metal flows into the mold due to gravity or another force, and the molten metal is cooled and solidified according to the form of the mold [3, 23, 24]. One of the techniques of the casting of metals is sand casting. Sand casting involves pouring molten metal into a mold made from a mixture of sand and solidifies in the mold at room temperature [25]. It has a rough surface finish, dimensional inaccuracy, and occasional surface impurities [26]. The low crystallization rate in sand casting of copper silumins leads to the development of a rough microstructure that is consequently accountable for relatively low strength and ductility [27].

The mold is usually made of sand particles bound together with an inorganic agent like resin-bonded, green sand, clay binder. [23]. This process is also relatively cheap and suitable for producing metals with complex shapes in a low production volume [28].

This research investigates the effect of sand casting and cold extrusion on the mechanical properties and microstructure analysis of scrapped copper coil using a locally manufactured extruder. The mechanical properties tested on the extrudates are limited to hardness, tensile, and compressive strength.

3 Research Methodology

3.1 Material preparation

The material used in this research was scrapped copper coil, which was thoroughly cleaned. Acetone was further used to remove impurities and stains from the copper scraps. The elemental composition of the scrapped copper coil is indicated in Table 1 using optical emission spectroscopy.

The materials were pounded into small shapes and sizes to be easily accommodated by the crucible pot before being put into the pit furnace for casting.

Table 1 – Elemental composition of the scrapped copper coil, wt %

Zn	Cu	Pb	Si	Ni	Fe	Co	Al	Sn	P
0.02	99.5	0.015	0.15	0.04	0.03	0.04	0.01	0.02	0.05

3.2 The casting of the sample

The casting process adopted in this study was sand casting. The sand mold was used to form a cylindrically shaped mold cavity which was crushed to remove the cast copper.

The sand was packed around the pattern to create the mold. The copper scrap was fed into a crucible pot and heated to about 1120 °C.

The molten copper was charged into the mold and cooled at room temperature for solidification.

The cast sample (copper) with the dimensions from 20 mm to 18 mm tapered diameter and 120 mm long was fixed on the 3-jaw chucks lathe machine and machined to the dimensions of 16 mm diameter and 120 mm long as shown in Figure 1.



Figure 1 – Machined copper sample

3.3 Cold extrusion of cast copper

Cold extrusion of cast copper was carried out on a locally fabricated extruder. The locally manufactured extruding machine is situated at the Department of Mechanical Engineering, Kwara State University, Malete, Nigeria. The conventional flat face die was employed during cold extrusion under the extrusion ratio of 1.14. The die of 14 mm diameter was used to extrude the copper rod that was machined to 16 mm diameter. The ram of the extruder was lubricated correctly to reduce the friction between the barrel and ram/piston. The copper billet was inserted between the ram and die. Then the barrel cover was closed and tightened to the endpoint of the barrel to provide a barrier that prevents the free fall of the die. The extrusion machine was powered electrically, and the electric motor was operated with an adjusted speed of 450 rpm. Then a copper extrudate with a final diameter of 14 mm is produced, as shown in Figure 2.



Figure 2 – Extruded copper

The two samples that were provided for testing are stated in Table 2.

Table 2 – List of samples provided for testing

Sample	Copper type	Rod diameter, mm
A	Non-extruded	11.10
B	Extruded	11.10
C	Non-extruded	11.45
D	Extruded	11.45

3.4 Testing of mechanical properties and microstructural analysis

Tensile strength testing of all specimens was conducted under ASTM E8/E8M-11. Two identical test specimens for each section thickness per sample were tested at room temperature with a strain/ loading rate of 5 mm/min using a computerized Instron Testing (model 3369). The Brinell hardness test was performed according to ASTM E10-18. Using a Brinell hardness tester, the test was done on the

extruder and non-extruded copper samples. Compressive test analysis was carried out on all the samples at room temperature using a Universal Testing Machine (UTM). This was done according to ASTM E9. Each of the specimens was placed on the jaw of UTM one after the other. Loads of 2.5 kN and 4.7 kN were then applied to each copper sample until the specimen failed.

The samples were grounded using silicon carbide papers of different grades 220, 320, 400, and 600 grits and polished with cloth swamped with the solution of 0.5 μm Silicon carbide until a mirror-like surface was attainable. The samples were subsequently etched with 2 % NITAL (2 % Nitric Acid and 98 % Ethyl Alcohol) and dried in desiccators. The microstructure of the samples was characterized by light optical microscopy under polarized light.

4 Results and Discussion

4.1 Compressive test

The compressive test was carried out on the samples (11.10 mm) for non-extruded and extruded copper. Figure 3 presented the graph of compressive stress against the compressive strain (mm/mm) of all the samples.

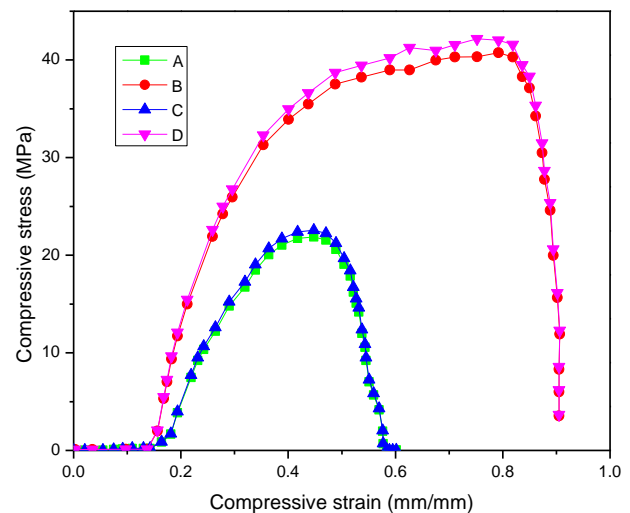


Figure 3 – Compressive strength for all the samples

The maximum compressive strength for samples A, B, C, and D is 22.0 MPa, 37.6 MPa, 23.2 MPa, and 41.3 MPa, respectively.

The study revealed that the maximum load-bearing capacity, compressive strength, and breaking a load of sample B increase by 43 %, 42 %, and 94 %, respectively, when compared with sample A.

4.2 Tensile test

The tensile test results (stress/strain curve) of the copper samples before and after extrusion are presented in Figure 4, respectively. The maximum load-bearing capacity, the ultimate tensile strength, and breaking load for sample A (non-extruded copper) are 3.48 kN, 271.0 MPa, and 46.8 N, respectively. The maximum load-bearing capacity, the ultimate tensile strength, and breaking load values for sample B (extruded copper) is

5.20 kN, 348.0 MPa, and 736.8 N, respectively. The study revealed that the extruded copper's maximum load-bearing capacity, tensile strength, and breaking load increased by 33 %, 22 %, and 94 %, respectively. Also, the elongation of the extruded copper of 11.10 mm and 11.45 mm approximately increases by 33 % and 34 %, respectively, compared with the corresponding non-extruded copper, as shown in Figure 4. It can be deduced from the analysis that the extruded copper is more ductile than the non-extruded copper.

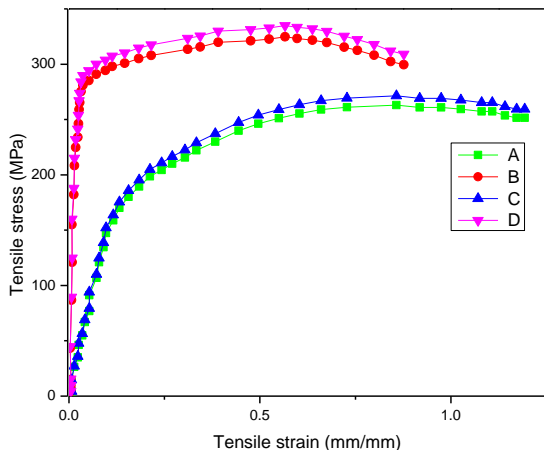


Figure 4 – Tensile strength for the copper samples

4.3 Hardness test

The hardness test was carried out on each sample of copper. The test was performed on a Brinell hardness tester. The tests carried out on the samples were presented in Figures 5–6.

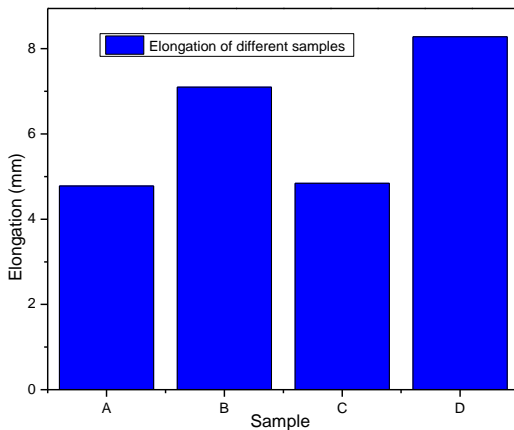


Figure 5 – Elongation for the copper samples

The values recorded for sample 11.10 mm (non-extruded and extruded) copper increases from 49.7 BHN to 69.1 BHN. Therefore, it can be inferred that the hardness of the extruded copper has a reasonable increment compared to the material before extrusion. The hardness improved significantly by 39 % and 41 % for extruded copper of 11.10 mm and 11.45 mm, respectively, compared with respective non-extruded copper.

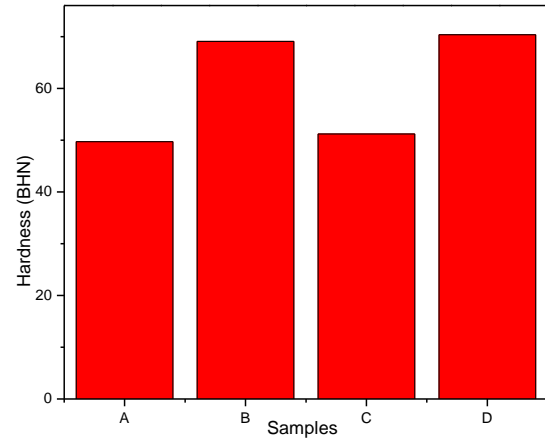
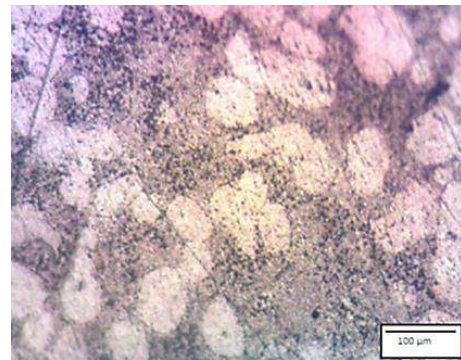


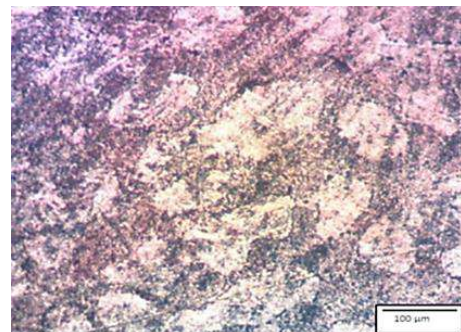
Figure 6 – The hardness of the samples

4.4 Microstructure analysis

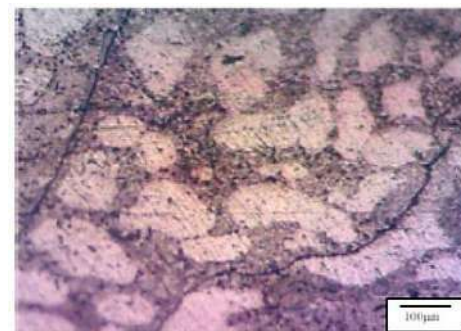
In the metallographic examination, the microstructure images of all extruded and non-extruded copper samples were examined at 100 μm , as depicted in Figure 7.



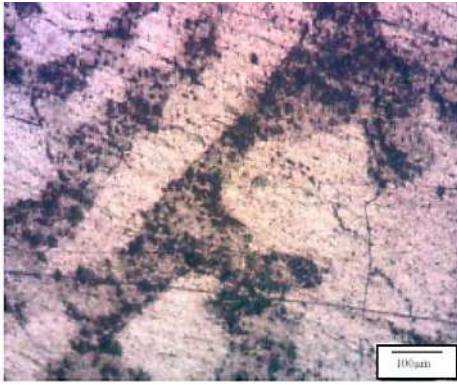
a



b



c



d

Figure 7 – Optical micrograph of non-extruded (a, c) and extruded (b, d) copper: a, b – 11.10 mm; c, d – 11.45 mm

The grains in non-extruded copper are relatively coarse and nonuniform with voids, but fine and relatively uniform grains are obtained in extruded copper. These coarse grain structures and voids are probably due to the slow cooling and formation of oxides at the interface during the deposition in sand casting. Also, the nonuniformity of the grain structure in non-extruded copper is due to the presence of silica during the sand casting.

Significant shear deformation in the particles is apparent compared to the microstructure before extrusion. The change in orientation of grains during and after extrusion would lead to a more homogeneous grain size than the copper before extrusion. The grains are refined during cold extrusion, and voids and dislocations are reduced significantly.

References

- Haase, M., Tekkaya, A. E. (2015). Cold extrusion of hot extruded aluminum chips. *Journal of Materials Processing Technology*, Vol. 217, pp. 356-367.
- Eyercioglu, O., Yılmaz, N. F. (2021). A simplified formula for determination of relative pressure in the precision forging of spur gears. *Journal of Engineering Research*, Vol. 9(2), pp. 234-248.
- Ardhyananta, H., Wibisono, A. T., Ramadhani, M., Widyastuti, Farid, M., Gumilang, M. S. (2018). Effects of aluminum and copper chill on mechanical properties and microstructures of Cu-Zn-Al alloys with sand casting. *AIP Conference Proceedings*, Vol. 1945, 020026, doi: 10.1063/1.5030248.
- Felicia, D. M., Rochiem, R., Laia, S. M. (2018). The effect of silver (Ag) addition to mechanical and electrical properties of copper alloy (Cu) casting product. *AIP Conference Proceedings*, Vol. 1945, 020075, doi: 10.1063/1.5030297.
- Sazegaran, H., Teimoori, F., Rastegarian, H., Naserian-Nik, A. M. (2021). Effects of aluminum and copper on the graphite morphology, microstructure, and compressive properties of ductile iron. *Journal of Mining and Metallurgy, Section B: Metallurgy*, Vol. 57(1), pp. 145-154.
- Güley, V., Güzel, A., Jäger, A., Ben Khalifa, N., Tekkaya, A. E., Misiolek, W. Z. (2013). Effect of die design on the welding quality during solid state recycling of AA6060 chips by hot extrusion. *Materials Science and Engineering: A*, Vol. 574, pp. 163-175.
- Blindheim, J., Grong, Ø., Welo, T., Steinert, M. (2020). On the mechanical integrity of AA6082 3D structures deposited by hybrid metal extrusion & bonding additive manufacturing. *Journal of Materials Processing Technology*, Vol. 282, 116684.
- Kang, D. H., Kim, T. W. (2010). Mechanical behavior and microstructural evolution of commercially pure titanium in enhanced multi-pass equal channel angular pressing and cold extrusion. *Materials and Design*, Vol. 31(1), pp. S54-S60.
- Berndt, N., Frint, P., Böhme, M., Wagner, M. F. X. (2017). Microstructure and mechanical properties of an AA6060 aluminum alloy after cold and warm extrusion. *Materials Science and Engineering: A*, Vol. 707, pp. 717-724.
- Kaya, Y., Kalyon, A., Kahraman, N. (2020). ANN prediction of impact toughness of ship steel/ stainless steel plates produced by explosive welding. *Journal of Engineering Research*, Vol. 8(2), pp. 266-284.
- Kumari, S., Rai, A. K., Sinha, D. K., Francis, R. C. (2015). Deformation behavior and characterization of copper alloy in extrusion process. *International Journal of Mechanical Engineering and Technology*, Vol. 6(7), pp. 72-78.

5 Conclusions

Scrapped copper coils were recycled through sand casting and subsequently subjected to cold extrusion in this research work. The extruded copper's microstructural analysis, hardness, and tensile and compressive test were compared with the non-extruded copper. The following conclusions were deduced from the analysis.

The hardness of extruded copper of 11.10 mm and 11.45 mm improved significantly by 39 % and 41 %, respectively, compared with the respective non-extruded copper samples.

The compressive test reveals that the maximum load-bearing capacity, compressive strength, and breaking load of the extruded copper increases by 43 %, 41.6 %, and 94 %, respectively, compared with the non-extruded copper.

The tensile test indicates that the maximum load-bearing capacity, tensile strength, breaking load, and elongation of the extruded copper increase by 33 %, 22 %, 94 %, and 33 %, respectively, compared with non-extruded copper.

The micrograph reveals that grains in non-extruded copper are relatively coarse and nonuniform with voids, but fine and relatively uniform grains are obtained in extruded copper. The coarse grains are refined during cold extrusion, and voids and dislocations are reduced significantly. The limitation of this research is associated with the constructed extrusion machine that cannot withstand the extrusion of copper material that exceeds 11.45 mm. More research would be done to redesign the extrusion machine.

12. Kumar, A. V., Ratnam, C. H., Rao, V. V. S. K., Kumar, C. R. (2019). Study on influence of die angle in cold extrusion on properties of nano sic reinforced 6061 aluminum alloy. *Materials Today: Proceedings*, Vol. 18(7), pp. 4366-4373.
13. Lee, J., Jeong, H., Park, S. (2019). Effect of extrusion ratios on microstructural evolution, textural evolution, and grain boundary character distributions of pure copper tubes during hydrostatic extrusion. *Materials Characterization*, Vol. 158, 109941.
14. Ji, X., Li, R. (2019). Simulation of microstructure evolution during static recrystallization of ultrafine-grained purity copper. *Materials Transactions*, Vol. 60(10), pp. 2229-2233.
15. Wasserbäch, W., Skrotzki, W., Chekhonin, P. (2020). Strengthening of ods silver wires. *Materialia*, Vol. 12, 100818.
16. Kahlani, B., Jafarzadeh, H. (2020). Microstructure and mechanical properties of aluminum/copper composite rod fabricated by axisymmetric spiral extrusion. *Transactions of the Indian Institute of Metals*, Vol. 73(3), pp. 515-520.
17. Lv, J., Hu, F., Cao, Q. D., Hong, X., Dong, X., Zhang, X. (2017). Fabrication and mechanical characterization of cold extruded aluminum bronze planar microsprints. *Journal of Materials Engineering and Performance*, Vol. 26(6), pp. 2919-2927.
18. Li, Z., Chen, L., Tang, J., Zhao, G., Zhang, C., Chu, X. (2020). Microstructure evolution, plastic anisotropy, and intergranular corrosion of Al-Mg-Si sheet processed through a combination of hot extrusion and cold rolling. *Materials Characterization*, Vol. 164, 110299.
19. Vignesh Kumar, R., Harichandran, R., Vignesh, U., Thangavel, M., Chandrasekhar, S. B. (2021). Influence of hot extrusion on strain hardening behaviour of graphene platelets dispersed aluminium composites. *Journal of Alloys and Compounds*, Vol. 855(2), 157448.
20. Chen, Q., Shu, D. Y., Lin, J., Wu, Y., Xia, X. S., Huang, S. H., Zhao, Z. D., Mishin, O. V., Wu, G. L. (2017). Evolution of microstructure and texture in copper during repetitive extrusion-upsetting and subsequent annealing. *Journal of Materials Science and Technology*, Vol. 33(7), pp. 690-697.
21. Huang, S. H., Wu, Y., Xia, X. S., Zhao, Z. D., Chen, Q., Shu, D. Y. (2019). Assessment of cold extrusion effect on stress-strain curves of pure copper arc parts based on the cosine velocity model. *Strength of Materials*, Vol. 51(4), pp. 569-577.
22. Kamitani, S., Nakanishi, K., Guo, Y. M. (2014). Performance evaluation of lubricant for producing smooth surface product in cold extrusion of aluminum using tool with microgroove arrays. *Procedia Engineering*, Vol. 81, pp. 1878-1883.
23. Eqal, A. K. (2021). Experimental and simulation study of solidification of commercial pure aluminium by sand casting. *Materials Today: Proceedings*, Vol. 45, pp. 5122-5127.
24. Winiarski, G., Dziubińska, A., Majerski, K., Szucki, M., Drozdowski, K. (2018). Investigation of the deformability of aluminium-copper casting alloys. *Advances in Science and Technology Research Journal*, Vol. 12(3), pp. 242-249.
25. Aramide, F. O., Adelusi, O. P., Adediran, A. A., Shongwe, M. B., Popoola, A. P. (2019). Mechanical properties and phase evolutions in heat-treated cast Al-Ni-Cu₂O metal matrix composites. *Materials Research Express*, Vol. 6(8), 086518.
26. Campbell, J. (2015). Casting metallurgy. *Complete Casting Handbook: Metal Casting Processes, Metallurgy, Techniques, and Design*, pp. 951-953.
27. Medvedeva, S. V., Zolotarevskii, V. S., Yakovtseva, O. A. (2019). Possibility of elevation of mechanical properties of sand-cast copper silumins. *Metal Science and Heat Treatment*, Vol. 60(9-10), pp. 560-565.
28. Yilmaz A., H., Uslu, G., Kahmaz, Y., Atay. (2020). Investigations of microstructure and mechanical properties of brass alloys produced by sand casting method at different casting temperatures. *IOP Conference Series: Materials Science and Engineering*, Vol. 726(1), pp. 012018.

Hovorun T., Khaniukov K., Varakin V., Pererva V., Vorobiov S., Burlaka A., Khvostenko R. (2021). Improvement of the physical and mechanical properties of the cutting tool by applying wear-resistant coatings based on Ti, Al, Si, and N. *Journal of Engineering Sciences*, Vol. 8(2), pp. C13-C23, doi: 10.21272/jes.2021.8(2).c3



Improvement of the Physical and Mechanical Properties of the Cutting Tool by Applying Wear-resistant Coatings Based on Ti, Al, Si, and N

Hovorun T.^{1*}, Khaniukov K.¹, Varakin V.¹, Pererva V.¹, Vorobiov S.², Burlaka A.¹, Khvostenko R.¹

¹ Sumy State University, 2, Rymskogo-Korsakova St., 40007 Sumy, Ukraine;

² Institute of Physics, P. J. Šafárik University in Košice, 2, Šrobárova St., 041 54 Košice, Slovakia.

Article info:

Submitted:

August 25, 2021

Accepted for publication:

December 7, 2021

Available online:

December 11, 2019

*Corresponding email:

hovorun@pmtkm.sumdu.edu.ua

Abstract. From the great variety of methods to improve the efficiency of cutting tools, it is necessary to highlight the methods of applying wear-resistant coatings, which in recent years are increasingly used. Applying wear-resistant coatings on the cutting tool can significantly increase its efficiency and intensify machining modes. Mechanisms of strengthening the wear-resistant coating for materials have been analyzed under the impact of technological parameters of coating condensation process on its structure parameters and mechanical properties, formation of single and multi-element coatings based on titanium nitrides, aluminum, and silicon, the transformation of coating properties by obtaining complex coatings, and principles formation of complex coatings designed for different cutting tools. The influence of the coating on the mechanical properties of high-speed steel is shown. In the magnetron sputtering coatings on P6M5 steel samples, the microhardness of the coatings is TiN – 20–24 GPa, AlN – up to 16 GPa, TiAlN – up to 35 GPa, AlTiN – up to 32 GPa, TiAlSiN – 32–37 GPa, including while the microhardness of the substrate of steel P6M5 – 6–9 GPa. The microhardness of TiAlN and TiAlSiN coatings applied on an instrumental basis is 1,5 - 1,9 times higher than the microhardness of TiN, AlN coatings. It was found that the wear intensity of P6M5 steel without coating is 6 times higher than with AlTiN, TiAlN, and TiAlSiN coating, 3 times higher than with TiN and AlN coating. The coated tool is characterized by increased reliability and higher stability and allows the processing process with higher cutting modes.

Keywords: coating, cutting tool, structure, properties, wear resistance.

1 Introduction

The low life of tools and machine parts is mainly due to rapid wear and corrosion damage to their surface layers.

To eliminate or inhibit the processes that adversely affect the performance of products, use various methods of targeted changes in the properties of the surface layers of materials. One of the effective ways to increase the efficiency of the cutting tool is to apply wear-resistant coatings to its working surfaces. Wear-resistant coatings allow the tool to obtain working surfaces with the required performance characteristics, usually without changing the properties of the base material.

Advantages of application of the cutting tool with a covering: transition to higher modes of cutting; increase the service life of the tool; improving the quality of the treated surface; efficient use of equipment; reducing the cost of products [1].

Based on the operating conditions of the tools, wear-resistant coatings must have: high hardness and store it at cutting temperatures; inertness to adhesion and high-temperature corrosion with the processed material in the whole range of cutting temperatures; stability of mechanical properties up to the temperature of heat resistance of tool material; inertness to dissolution in the processed material at high temperatures; resistance to failure at significant fluctuations in temperature and stress [2-4].

The urgency of the work is to study the effect of nanostructured wear-resistant coatings based on nitrides Ti, Al, Si, obtained by reactive magnetron sputtering, on the structural-phase state, mechanical and tribological properties of materials for cutting tools.

Wear-resistant coatings, having a lower coefficient of friction than the tool substrate and a higher stability temperature, significantly affect the various parameters of the cutting process. In particular, reduce the length of elastic and plastic contact of chips with the tool's

working surfaces, reduce the cutting force, reduce the temperature in the machining area, change the angle of the conditional shear plane, and, consequently, affect the formation of surface layer quality.

In this regard, the development of the coating composition, which has high strength characteristics, wear-resistant and tribological properties, is an urgent scientific and technical task.

2 Literature Review

In modern production, wear-resistant coatings of cutting tools are subject to increased requirements due to complex factors. These factors are related to improving the properties of coatings, the composition of the “coating – tool material”, and the optimization of the operating conditions of the cutting tool. Optimization of conditions of use of the tool relates to a decrease in the growth and intensity of adhesive-fatigue processes, increase in rigidity of the design of the tool and the machine tool equipment. Coatings can be considered an intermediate technological environment between tools and processed materials [3, 4].

Based on this provision, the general requirements for protective coatings have been systematized, which are the basis of some specific coating requirements for cutting tools. Such requirements can be classified into three main groups based on the provision that coverage should [4]:

- overtime to function stably on the contact pads of the tool without premature failure (the role of the coating as a single solid body);
- to provide favorable transformation of contact processes at cutting (official purpose of a covering);
- have a strong adhesive bond with the substrate material (substrate) (tool materials and coating materials must function as a single solid body).

Refractory metal-metalloid (Me-X) compounds are used as wear-resistant coating materials, where refractory metals of groups IV-VI of the Periodic Table of the Elements are used as a metal, and carbon, nitrogen, and oxygen are used as metalloids.

There is a three-level division of factors that determine the properties of coatings [3-6]:

1. Factors related to the coating process parameters (e.g., substrate temperature and the process itself, the interaction of reagents and reaction products, mechanical stresses arising in the coating due to thermal and shock action by a bombardment of streams, and various particles).

2. Factors related to the condition of the substrate, the coating, and the entire system “substrate – coating” in general.

3. Factors associated with structural strengthening (microstructure), including grain size and orientation, grain boundaries, density (porosity).

ZrN, CrN, TiN, AlN, BN, Mo(W)S₂ coatings were widely researched. Those coatings and modified TiAlN, AlCrN, and other coatings and successfully used in industry [3, 7].

The following areas of improvement of the cutting tool with wear-resistant coatings are considered [5, 6, 8, 9]: improved coating technology and new coating compositions, development, and improved multilayer coating structures.

Thus applied nitride coatings of TiAlN, TiCN, TiZrCN, TiZrN increase the period of stability of end mills with carbide inserts MK8 in 1.5–3.0 times in comparison with the cutting tool with TiN coating in the processing of billets of steel 5HNM, 18H18N10T and titanium alloy [8, 10-11].

The influence of the parameters of coating TiN and ZrN by methods of magnetron sputtering and CIB on their hardness is considered in the works [2, 8, 10, 12-16]. The maximum hardness of coatings at a stoichiometry of structure reached by optimization of technological parameters – the pressure of reaction gas, bias voltage, induction of a magnetic field, and discharge current is noted.

The influence of condensation temperature in the coating process is considered in the works [15-18]. A method of increasing the efficiency of the cutting tool by applying coatings in the combined temperature mode is proposed. The temperature of the coating affects its defect and, consequently, its strength and hardness, as well as the strength of the adhesive bond with the tool base and the level of residual stresses. Deposition of the lower layer of the coating at high process temperatures helps to increase the strength of adhesion to the tool base and the formation of the upper layer at lower temperatures, increasing the hardness and wear resistance of the coating.

The authors of the work [19] consider the effect of plasma flow separation on the structure, physical and mechanical characteristics, and wear resistance of TiN coating. Reducing the content of the dripping phase, improving the structural characteristics lead to an increase in wear resistance of such coatings by 1.5–2.0 times.

Coatings based on modified titanium nitride have become the most widespread in world practice. Zirconium, aluminum, molybdenum, chromium, iron, and silicon are alloying elements. [3, 6, 20]. The influence of alloying elements is manifested in the improvement of the physical and mechanical properties of coatings, changing the conditions of contact interaction of the coating with the processed material and the strength of its adhesion to the tool base. Studies of physicomechanical properties of TiN coatings doped with molybdenum, chromium, and silicon [3, 6, 20], have shown that doping with these elements increases the microhardness of coatings by 18-25 %, residual compressive stresses – 1.3–1.9 times; at the same time, the strength of adhesion to the tool base decreases, as evidenced by the increase in the coefficient of exfoliation by 35-80 %.

The study of the influence of the composition of TiMoN coating obtained from separate cathodes on the physical and mechanical properties and performance of the coated cutting tool was carried out in the following work [20]. The studied coatings have a 1.5 to 1.6 times

higher microhardness than TiN coatings. There is a decrease in the bond strength with the tool material for the coating based on titanium nitride and molybdenum. The use of TiMoN coating allowed increasing the period of stability of carbide plates when turning workpieces from steels 30HGSA and 12H18N10T in 1.2–2.2 times in comparison with one-element TiN coating. The use of silicon as an alloying element has a number of advantages [20].

Therefore, this work aims to establish the influence of physical and technological parameters of deposition, working gas pressure, and shear potential on the formation of nanostructured nitride coatings Ti, Al, Si, and N, establishing their structural-phase state, mechanical and tribological characteristics, as in the use of single-element coatings, and as in the use of complex coatings.

It is necessary to determine the nature of the material's behavior in operating conditions before and after coating.

3 Research Methodology

3.1 Research objects

The cutting tool (Figure 1) on which the coating is applied has types that conditionally classify it as manual and machine.



Figure 1 – Varieties of cutting tools [21]

Currently used tool materials are divided into the following groups: carbon and low-alloy tool steels, fast-cutting steels, hard alloys, mineral ceramics and cermets, synthetic compositions of boron nitride, synthetic and natural diamonds.

Depending on the materials for the cutting tool, the coating methods shown in Figure 2 are used [22].

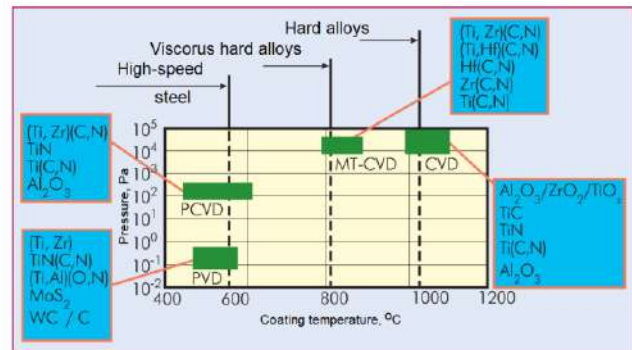


Figure 2 – Parameters and basic methods of coating [22]

Within these groups, there are a large number of coating methods, including combined or methods with support or activation of the process from other energy sources.

3.2 Research methods

A variety of PVD methods based on glow discharge is magnetron sputtering. Magnetron ion sputtering systems are diode-type sputtering systems in which atoms of the sprayed material are removed from the surface of the target by bombarding it with ions of working gas (usually argon) formed in the plasma of an abnormal glow discharge. For increasing the spray rate, it is necessary to increase the intensity of ion bombardment of the target, i.e., the ionic current density on the surface of the target [2, 8].

Magnetron sputtering (DCMS) refers to sputtering materials by ion bombardment.

The main elements of the magnetron sputtering system are a flat cathode made of sprayed material, an anode mounted on the perimeter of the cathode, a magnetic system (usually based on permanent magnets), and a water-cooling system (Figure 3).



a



b

Figure 3 – Magnetron for vacuum deposition of coatings: a – appearance; b – an arrangement in GDP-5M; 1 – one of the targets; 2 – holder for samples with the possibility of rotation; 3 – is the gas supply pipe between the sample holder and the magnetron [2, 8]

Magnetron sputtering of titanium, aluminum, and silicon in the reaction medium of nitrogen and argon allows obtaining coatings that do not contain hydrogen, oxide, and other impurities.

Gases were used for the processes of magnetron sputtering of coatings:

- gaseous nitrogen of exceptional purity 99.999 % (GOST 9293-04);
- argon gaseous high purity of 99.999% (GOST 10157-07).

The uniformity of the composition in the thickness of the coating will be high, and at the lowest thicknesses, the porosity will be minimal. The condensation rate varied depending on the voltage applied to the target and the gas flow.

Investigations of the structure and properties of TiN, AlN, TiAlN, and TiAlSiN films deposited by magnetron sputtering at the VUP-5M unit at a residual pressure in the working chamber $10^{-3} - 10^{-4}$ Pa were performed on samples of fast-cutting steel P6M5 after standard heat treatment and polished plates of monocrystalline silicon. The rate of deposition and measurement of the thickness of the coatings was controlled by the in-situ method using a quartz thickness gauge according to standard methods.

P6M5 steel substrates were placed over the magnetron with subsequent table rotation to ensure uniformity of coatings in thickness. Before the application process, the vacuum chamber was pumped to a residual pressure of $1 \cdot 10^{-3}$ Pa. The formation of a gas mixture of argon and nitrogen in the required proportions took place from independent sources in the spraying process. For removing uncontrolled contamination of the target surface and substrates, short-term etching with argon bombardment ions was used.

The coatings' structure was studied using a Tescan VEGA 3 scanning electron microscope (EDX spectra were obtained using additional detectors on the same microscope), a PEM 125K transmission electron microscope, and atomic force microscopy (AFM).

Tests for wear resistance of coatings were carried out under conditions of "dry" friction on a friction machine SMT-1, which is designed for testing for friction and wear, to study the friction and wear processes of metals, alloys, and rigid structural plastics. Counter-body material - hard alloy coated with cubic boron nitride, hardness of counter-body – 80 HRC, dimensions of counter-la – Ø 30 mm, load on the sample (F) – 2 941 g/cm², friction path of test – 2 km, number of revolutions of the counterbody – 355 rpm, test time – 60 and 120 minutes.

3.3 Heat treatment of P6M5 steel substrate for applying coatings

Research of the structure and properties of TiN, AlN, TiAlN, and TiAlSiN coatings deposited by magnetron sputtering at the VUP-5M unit were performed on P6M5 high-speed steel samples after standard heat treatment.

The chemical composition of the substrate P6M5 is shown in Table 1.

Table 1 – Chemical composition of steel P6M5, %

C	Si	Mn	Ni	S	P	Cr	Mo	W	V	Co
0.82	0.30	0.44	0.35	0.008	0.027	4.34	4.83	5.91	1.94	0.27

Standard heat treatment of P6M5 steel consists of preliminary heat treatment – isothermal annealing for 6 hours; final heat treatment – hardening with two heats for 0.75 hours and three times for 1 hour each (Figure 4).

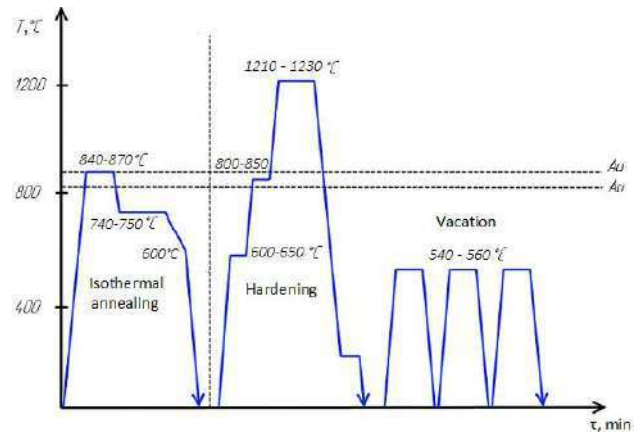


Figure 4 - Graph of heat treatment of experimental plates made of P6M5 steel

After proper heat treatment, the steel had a martensite structure with evenly distributed small and medium-sized carbides (Figure 5).

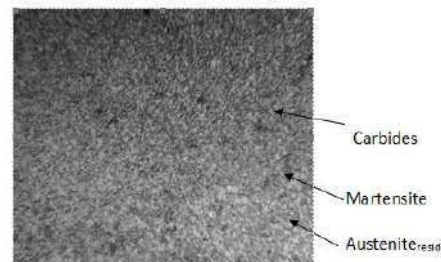


Figure 5 – Microstructure of P6M5 steel after heat treatment (isothermal annealing, quenching with heating, triple tempering), x500

The hardness of the tool after tempering was 63–65 HRC. The proposed final heat treatment reduces the amount of residual austenite in the steel and increases the wear resistance of the tool by 2.5–4.0 times.

Before deposition of the coatings, the substrates were polished by a mechanical method combined with a diamond grinding wheel. Then the substrates were sonicated for 10 minutes, successively in acetone and ethyl alcohol.

4 Results

4.1 Study of coatings

4.1.1 Study of TiN coatings

Titanium nitride TiN is a widely used, traditional compound applied to carbon, stainless and fast-cutting steels, and hard alloys and ceramics. In metalworking, the tool's temperature is reduced due to the high surface

density of titanium nitride. TiN was one of the first-facing materials used in industrial cutting tools, and it is still used as diffusion barriers and for decorative coatings.

The material can be obtained by physical vapor deposition (PVD) and chemicals. Like most other ceramic materials, it has a brilliant appearance and golden color, relatively good mechanical and thermal properties. Titanium nitride is oxidized at a reasonably high temperature (above 450 °C), one of its main disadvantages when used as a coating tool. Evaporation of the nitride coating in an inert atmosphere leads to a decrease in its internal hardness due to the annihilation of defects and stress relaxation.

To study the effect of deposition parameters on the characteristics of titanium nitride coatings applied to substrates - polished plates of monocrystalline silicon Si using a magnetron spray system on a universal vacuum unit GDP 5M in Ar and N₂, changing the flow rate of nitrogen into the working chamber and the distance between target and substrate “L_{s-c}” (s – substrate, c – coating). The deposition was carried out in the mode of power limitation (3 kW) while maintaining a constant value of argon flow. The thickness of TiN coatings was about 0.4 μm. For assessing the effect of magnetron discharge plasma on the formation of TiN films and their physical and mechanical properties, the distance between the target and the substrate (L_{s-c}) was chosen 100 and 50 mm.

The performance of MRS depending on the flow rate of nitrogen Q(N₂) at different values of L_{s-c} is shown in Figure 6.

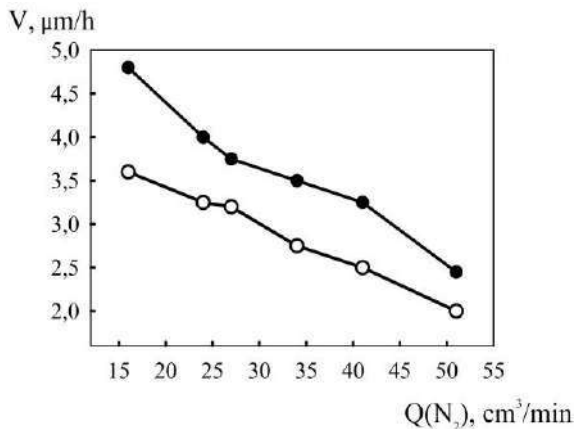


Figure 6 – The influence of nitrogen flow rate Q(N₂) on the productivity of the process of applying Ti coatings TiN at different distances between the plane of the target and the substrate L_{s-c}: ● – 100 mm; ○ – 50 mm

Due to the imbalance of the magnetic field of the magnetron, the growing coating is digested by the ionic flow of the plasma discharge. There is a decrease in the deposition rate of TiN by an average of 20 % when approaching the plane of the substrate to the target by 50 mm.

The decrease in system performance with increasing Q(N₂) is due to the “poisoning” of the titanium cathode with a layer of TiN and a lower coefficient of sputtering of the target with nitrogen ions.

Photomicrographs of the surface and cross-section of thin TiN coatings applied by reactive magnetron sputtering are shown in Figure 7.

The photomicrograph of the surface (Figures 7 a, b) shows a relatively high homogeneity of the studied coatings (no punctures).

As an illustration, Figure 7 c shows a fractogram of TiN coating. You can see that the obtained coating has a columnar structure inherent in the ion-plasma coating. A study of the surface morphology of coatings Showed that they have good quality.

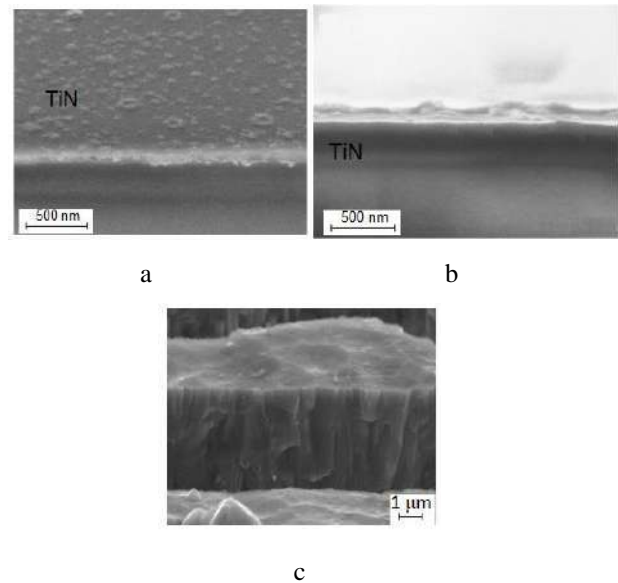
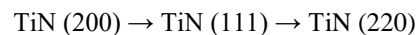


Figure 7 – Microstructure of thin TiN coatings: surface (a), cross-section (b), and fractogram of fracture for TiN coating obtained by magnetron sputtering (c)

According to the results of X-ray diffraction studies of experimental samples, we have a TiN coating with a polycrystalline structure and orientation in the crystallographic directions (111), (200), (220). Peaks of intensities (311) and (222) are weakly shown.

The orientation of the growth of coatings in one of the crystallographic directions is associated with changes in the energy of scattered particles and ions falling on the substrate. Increasing the energy of the generated particles stimulates the formation of titanium nitride coatings according to the following scheme:



The crystallographic direction (220) becomes predominant in the nitride coating when the specific energy losses of the precipitated particles become significant. TiN coatings obtained at L_{s-c} = 100 mm are more oriented along the axes (111) and (200). When the substrate approaches the target (50 mm), intensity peaks become significant (220).

The formation of TiN coatings with a predominant orientation (111) occurs in a gaseous medium N₂, without the supply of Ar. Changing the flow rate of nitrogen into the working chamber stimulates a decrease in the intensity of reflexes (200) and (220) for the distance

“target-substrate” L_{s-c} 100 and 50 mm, respectively. From the X-ray diffraction data, the values of the parameters of the crystal lattice of the experimental samples 4.22–4.25 Å correlate well with the data for work [14].

There is no evident dependence of the mechanical properties of the coatings on the N_2 flux. Reducing the “target – substrate” distance reduces the mechanical properties of the coatings.

4.1.2 Study of coatings based on AlN

AlN coatings were formed by magnetron jet spraying cylindrical targets with Al in a gas mixture of Ar^+ 40–60 % vol. N_2 at a pressure of 0.6–0.9 Pa. The working gases were fed separately (Ar – in the spray area of the target, N_2 – in the substrate area) and as a mixture.

The obtained coatings have a fibrous (columnar) structure, while AlN fibers have a hexagonal lattice. Crystalline phases of AlN coating are detected using electron microscopy.

The disadvantage of the magnetron sputtering method is the presence of drip phase in coatings, which leads to deterioration of the integrity and corrosion properties (Figure 8) of the scanning electron microscope (SEM).

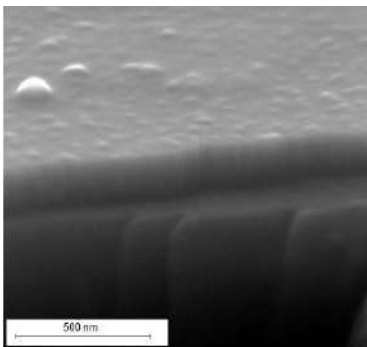


Figure 8 – Structure (SEM) of the surface of the AlN coating obtained by magnetron sputtering on a polished substrate of stainless steel P6M5

By varying the pressure N_2 in the vacuum chamber, it is possible to change the color of the treated surface to some extent. Arc evaporation forms coatings with a smooth surface corresponding to the roughness of the substrate.

At low rates of deposition of coatings, as well as the absence of electrical displacement on the substrate holders, formed coatings consisting of equiaxed disordered crystallites (Figure 9 a). Changing the synthesis conditions promotes the formation of crystallites in the form of fibers.

The structure of the growth and chip surface of the AlN film obtained on a substrate of P6M5 steel shows (with appropriate changes in the parameters of the deposition process) the transition of the lamellar structure to fibrous and fine-grained with equilibrium grains (Figure 9 b).

After studying the coatings of TiN and AlN, it was concluded that they have certain disadvantages that can be significantly reduced by obtaining compounds based on components of Ti-Al-N.

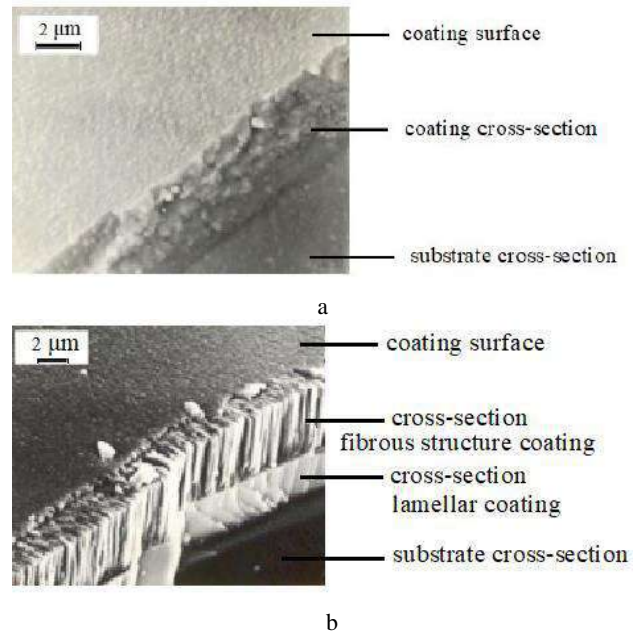


Figure 9 – Structure (SEM) of AlN coatings formed by magnetron sputtering

4.1.3 Structure and properties of coatings based on TiAlN

In the manufacture of tools from reinforcing coatings, the main focus is on the TiAlN compound, due to good performance properties, which are characterized by obtaining a wide range of stoichiometric composition and reproducibility of their production, so the application of carbonitride coatings (e.g., TiCN) is much more difficult to control. Nitride coatings are the most technological in production, and it can be argued that TiAlN and its modifications (e.g., AlTiN, TiAlCrN, TiAlCrYN) have become the flagship of the global coatings industry and are widely used as completely self-sufficient coatings and in various multilayer compositions. (TiAl)N have unique performance properties: high hardness at high temperatures in the cutting contact zone; thermal and chemical resistance, high elasticity; low thermal conductivity. One of the essential advantages of (TiAl)N coating is its tendency to oxidize and form relatively stable surface oxide films. You can increase the wear resistance (TiAl) of N coatings during cutting by grinding the grain to the nanoscale level (grain size less than 100 nm). This is possible by doping (TiAl)N coatings on the tool material by magnetic arc filtration. The coating is used for processing titanium and nickel alloys, stainless steel, hardened materials, cast steel, and plastics. The temperature stability of the coating determines the possibility of its use in high-speed and emulsion-free processing of materials.

The results of studies of the crystal structure of samples by transmission electron microscopy (TEM) showed the following: increasing the value of the negative voltage applied to the substrate during deposition of wear-resistant coatings from the target $Ti_{0.5}Al_{0.5}$ in the N atmosphere increases the concentration of defects and dislocations in the structure. The

dependence of the average grain size D on the value of the negative voltage V_S applied to the substrate in the condensation process of the samples is shown in Table 2.

Table 2 – Dependence of the average grain size d on the value of the negative voltage applied to the substrate

V_S , V	0	50	75	100	125	150	250
d , nm	105	95	60	55	45	42	40

As can be seen from Table 1, the value of d decreases from 105 nm to 55 nm when changing the value of the negative voltage V_S from 0 to 100 V. Further increase in the negative voltage on the substrate during condensation does not significantly affect the grain size change and even at $V_S = 250$ V. The grain size remains about 40 nm.

Figures 10 a, b show the surface microstructures and the cross-section for single-layer TiAlN coatings, respectively.

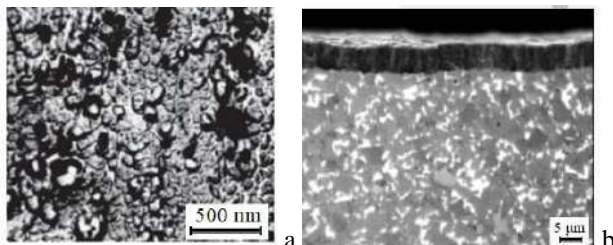


Figure 10 – Surface (a) and cross-section (b) of a plate of high-speed steel P6M5 with TiAlN coatings (5 μ m)

Energy-dispersion spectra, typical for all series of TiAlN coatings on silicon plate substrates and characterizing their stoichiometry, are shown in Figure 11. The concentration of Al varies from 34 to 35 %, the concentration of Ti varies from 52 to 54 %, and the concentration of N is within 10 %.

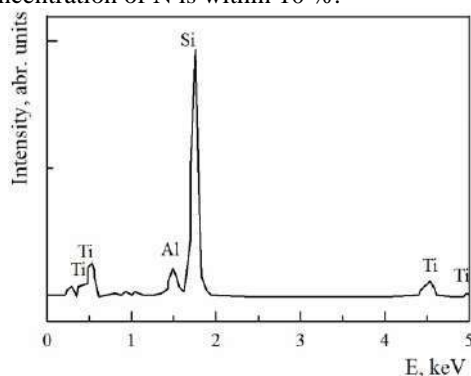


Figure 11 – Energy dispersion spectra and the elemental composition of TiAlN coating determined by them

The main components of the coatings obtained in a mixture of argon and nitrogen are TiN, AlN, and nitride phase of variable composition $(Al_xTi_{1-x})N$ with cubic lattices based on TiN. The concentration of the coating components depends on both the concentration of the metal components Ti and Al and the pressure of the reaction gas composition present in the deposition zone. The average size of the formed crystallites: for TiN – 10 nm, $(Al_xTi_{1-x})N$ – 5 nm, and AlN – 10–100 nm. Similar results were obtained by the authors [23].

Figure 12 shows the dependencies of hardness on the

applied negative stress on the substrates.

As shown in Figure 8, the higher the electric field on the substrates, the greater the hardness of the coating $[Ti(Al)]_xN_{1-x}$.

This is due to the phase transition from hcp-AlN (MSN AlN_x) to c-TiN (cubic-TiN) and can be explained by the high level of compressive stresses (5–6 GPa), which is confirmed by other authors [11].

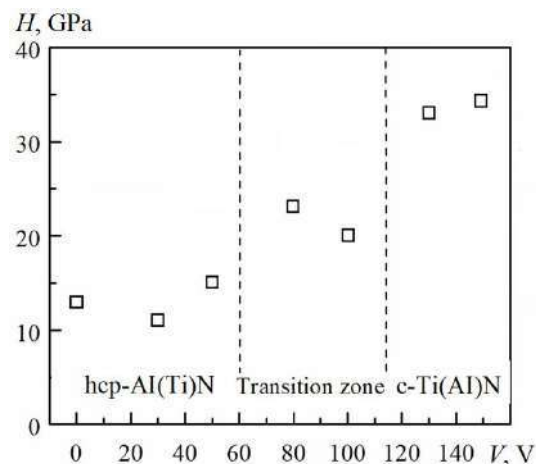


Figure 12 – Dependence of hardness on the applied shear stress on P6M5 steel substrates during condensation

The lowest values of hardness are observed when AlN_x structure crystallizes in coatings. By increasing the value of the negative stress on the substrate, in this case, you can achieve a slight increase in hardness due to the slow growth of compressive stresses in the sample and reducing the grain size, respectively, as in work [11].

We can conclude that by regulating the energy and flux density of metal ions of alloying elements, it is possible to control the processes of microstructure formation and the hardness of nanocrystalline coatings.

4.1.4 Structure and properties of TiAlSiN coatings

TiAlN coating is superior to TiN coating in hardness, wear resistance, and especially oxidation resistance. The cutting temperature in the modern high-speed cutting industry can reach 1 000 °C, which can cause oxidation and reduced hardness of TiAlN coatings. Due to this, nanocomposite coatings based on Ti, Al, Si, and N are now increasingly used for cutting tools. Compared to traditional durable TiN, AlN, or TiAlN coatings, the TiAlSiN coating, which forms the structure of the amorphous Si_3N_4 shell for the TiAlN nanocrystalline coating, has attracted worldwide attention due to its enhanced properties as a complex coating for multilayer coatings and multicars [3, 6, 20, 24-29].

Ti-Al-Si-N coatings were prepared by magnetron sputtering using different bias voltages applied to 30 V and 130 V substrates and deposition energy. In this way, the microstructures and mechanical properties of the coatings can be adjusted, such as grain size, orientation, and hardness.

As the bias voltage increased, the composition of the coatings remained almost unchanged, maintaining the composition of $Ti_{0.19}Al_{0.25}Si_{0.05}N_{0.51}$.

Figure 13 presents X-ray diffraction patterns of sprayed coatings Ti-Al-Si-N at bias voltages of -30 V and -130 V. We see cubic TiAlN (111), (200), (220), and diffraction peaks of wurtzite AlN (002) in coatings, except for the peak of the Si substrate. However, the diffraction peaks of SiN_x phases in coatings are not observed. This can be explained because silicon can exist as an amorphous silicon nitride, which corresponds to the work [28-29].

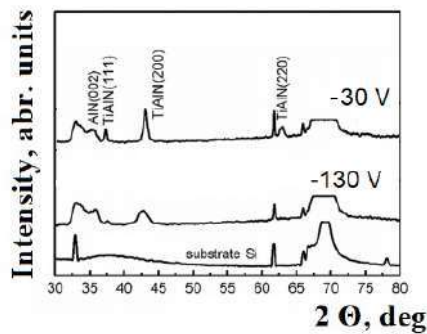


Figure 13 – X-ray diffraction patterns of Ti-Al-Si-N coatings deposited at different displacements stresses applied to the substrate

As shown in the cross-sectional images in Figure 14, obtained on a silicon substrate, the thickness of the coating Ti-Al-Si-N is about 1.8 to 1.9 μm . As can be seen from the figure, there were no voids in the coatings, and the microstructure was dense. At a displacement of -30 V, very thin columns of the morphology of zone I can be seen in the model, which ended with the structure of the surface zone. At a displacement of -130 V, the sections were flat and did not have such a pronounced columnar structure.

According to diffraction measurements, the nanolayer TiAlSiN coating consists of crystalline phases of solid solution-TiN and amorphous phase Si₃N₄. TEM analysis showed that TiSiN layers block the growth of TiAlN crystallites, which are balanced and about 5 nm in size. As a result, the TiAlSiN coating shows high hardness ($H = 37$ GPa), which is explained by the limited dislocation activity in small crystals and the suppression of sliding grain boundaries.

The diffraction peaks of TiAlN coating are shifted to higher diffraction angles compared to stoichiometric TiN, which indicates a decrease in the lattice parameter (0.418 nm compared to 0.424 for pure TiN) [24-25].

No signals were received from the crystalline silicon nitride or titanium silicide phase, indicating that the Si-containing phase is amorphous or too thin.

In Figure 15, SEM images of the cross-section of TiAlSiN coating on P6M5 steel are shown. The coating adheres well to the substrate. It is uniform in thickness and has no structural defects such as cracks and voids. Columnar growth is observed in the coating.

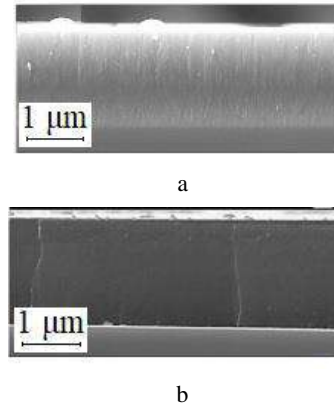


Figure 14 – Image in cross-section of Ti-Al-Si-N coatings applied at different bias voltages -30 V (a) and -130 V (b)

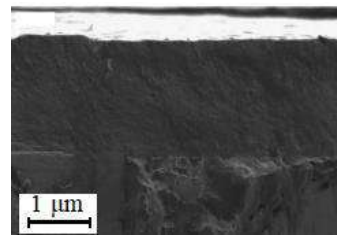


Figure 15 – Photomicrograph of cross-section, showing the structure of TiAlSiN coating on P6M5 steel

The H hardness of Ti-Al-Si-N nanocomposites varied at shear stresses -30 V and -130 V. With increasing shear stress, the hardness increased from 32 GPa to 37 GPa, and at a voltage of -130 V, the coating showed the most significant hardness. High values of TiAlSiN coating hardness since it has high resistance to cracking.

The increase in mechanical properties is mainly due to increasing the residual stress during compression and reducing the grain size in the Ti-Al-Si-N coating. TiAl-Si-N coatings with high hardness values and dense macrostructure showed increased resistance to cracking and wear, which is in agreement with the literature [30].

It is well known that hardness increases with decreasing grain size, which can be explained by an increase in areas of grain boundaries that interfere with dislocation movements in the form of dislocation accumulations (Hall-Patch effect) [24-25].

Ti-Al-Si-N nanocomposite coating maintained high hardness at annealing temperature up to 1000 °C and has increased resistance to oxidation up to 1115 °C.

4.2 Determination of mechanical properties of coatings

The hardness of the material characterizes the degree of its ability to resist plastic deformation, and the fracture toughness is a measure of its resistance to crack propagation and fracture. With the optimal combination of hardness and resistance to destruction, the service life of the coating is determined by its wear.

Mechanical properties and characteristics of wear-resistant coatings are given in Table 3.

P6M5 steel samples and samples of the same steel but coated were tested for wear for 60 and 120 minutes. The test results are shown in Table 4.

Table 3 – Mechanical properties and characteristics of wear-resistant coatings

Coating	Color	Hardness $H\mu$, GPa	Thickness, μm	Maximum temperature, $^{\circ}\text{C}$
TiN	gold	20-24	2–7	600
AlN	gray	12-16	2-5	600
AlTiN	gray-purple	32	1-3	800
TiAlN	purple-black	35	1-7	900
TiAlSiN	brown	32-37	1-4	1 100
Uncoated steel P6M5	gray	6-9	N/A	N/A

Table 4 - Wear intensity of TiN and TiAlN coatings on P6M5 steel samples

Coating	Wear intensity I, 10^{-7}kg/m^2	
	after 60 min	after 120 min
TiN	7.6	18.0
AlN	8.8	19.9
TiAlN	3.8	9.0
TiAlSiN	4.8	9.3
Uncoated steel P6M5	25.0	54.0

As a result, it was found that the wear intensity of steel after 120 minutes of uncoated tests is 5–6 times higher than with TiAlN and TiAlSiN coating, 3 times - than with TiN and AlN coatings.

When comparing the productivity during drilling with a P6M5 steel tool, it is shown that the number of holes drilled with an uncoated drill is 47 when using a drill with TiN coating – 88 holes, when using a drill with TiAlN coating – 246 holes. That is, coating increases the productivity of the tool by 2–5 times, which is confirmed by the work of other authors [3, 6, 13-16, 20].

The obtained coatings TiN, AlN, TiAlN, AlTiN, and TiAlSiN are layers that are very difficult to erase, well protect the tool from surface wear, reduce energy consumption, increase tool reliability and redness.

Cutting properties of the protected tool, 1.5–5.0 times higher than the tool without covering.

5 Conclusions

The structural-phase and mechanical properties of wear-resistant coatings based on Ti, Al, Si, and N obtained by magnetron sputtering were analyzed.

By varying the synthesis conditions, you can change the coatings' phase composition and structure. Functional properties largely depend on the composition and morphology of coatings.

The advantage of TiN is good elasticity and adhesion. According to X-ray diffraction data, the TiN samples obtained by us have a polycrystalline structure (111), (200), and (220).

The surface morphology strongly depends on the distance “target – substrate” TiN coatings have a crystalline structure of NaCl and an average lattice parameter of 4.24 \AA , and the structure consists of covalent, metallic, and ionic bonds. The covalent bond explains the high hardness of up to about 20 GPa.

Resistance to loads of textured AlN films is provided both due to the high concentration in the protective coating of crystalline AlN. When the grains of the crystalline phase of the protective coating is oriented parallel to the direction of mechanical loads' action, the coating's integrity is preserved under the influence of shock loads.

TiAlN material is used in various areas, such as protective and wear-resistant coatings, diffusion barriers, and optical devices. The hardness of AlTiN and TiAlN reaches 32–35 GPa depending on the deposition conditions and composition. TiAlN has excellent resistance to high temperatures. Suitable for high-speed processing, it can be used without coolant.

Ti-Al-Si-N nanocomposite coatings were obtained by magnetron sputtering at bias voltages of –30 and –130 V. With increasing shear stress of the substrate, Ti-Al-Si-N coatings had a decrease in (200) -preferential orientation: dense columnar the structure (zone I) of Ti-Al-Si-N coatings gradually evolved into an uncharacteristic and flat structure. With increasing shear stress, the hardness increased from 32 GPa to 37 GPa, i.e., at a displacement of –130 V, the coatings had the highest hardness. Ti-Al-Si-N nanocomposite coating maintained high hardness at annealing temperature up to 1 000 $^{\circ}\text{C}$ and has increased resistance to oxidation up to 1 115 $^{\circ}\text{C}$. TiAlSiN coatings are characterized by high hardness values, which means high viscosity of their destruction, high resistance to cracking, and should be helpful in tribological applications.

In the obtained magnetron sputtering coatings on samples of P6M5 steel, the microhardness of coatings is TiN – 20–24 GPa, AlN – up to 16 GPa, TiAlN – up to 35 GPa, AlTiN – up to 32 GPa, TiAlSiN – 32–37, while the microhardness of the substrate itself steel P6M5 – 6–9 GPa. The microhardness of two-element TiAlN coatings applied to the tool base is 1.5 to 1.9 times higher than the microhardness of one-element TiN and AlN coatings.

It was found that the intensity of steel wear after 120 minutes of uncoated tests is 6 times higher than with AlTiN and TiAlN coating, 3 times higher than with TiN coating.

References

1. Möhring, H.-Ch., Kushner, V., Storchak, M., Stehle, Th. (2018). Temperature calculation in cutting zones. *Manufacturing Technology*, Vol. 67 (1), pp. 61–64, doi: 10.1016/j.cirp.2018.03.009.
2. Panda, A., Dyadyura, K., Hovorun, T., Dunaeva, M., Pandová, I. (2019). Nanostructured wear-resistant coatings based on refractory metals nitrides: Physical-mechanical properties and structural-phase state. *Management and Production Engineering Review*, Vol. 10(4), pp. 133–139, doi: 10.24425/MPER.2019.131453.
3. Pogrebnjak, A. D., Lisovenko, M. A., Turlybekuly, A., Buranich, V. V. (2021). Protective coatings with nanoscale multilayer architecture: Current state and main trends. *Physics-Uspekhi*, Vol. 64(3), pp. 253–279, doi: 10.3367/UFNe.2020.08.038823.
4. Vereschaka, A. A., Vereshchaka, A. S., Mgaloblishvili, O., Morgan, M. N., Batako, D. L. (2014). Nano-scale multilayered-composite coatings for the cutting tools. *The International Journal of Advanced Manufacturing Technology*, Vol. 72(1-4), pp. 303–317, doi: 10.1007/s00170-014-5673-2.
5. Pimenov, D. Yu., Mia, M., Gupta, M. K., Machado, A. R., Tomaz, I. V., Sarikaya, M., Wojciechowski, S., Mikolajczyk, T., Kapłonek, W. (2021). Improvement of machinability of Ti and its alloys using cooling-lubrication techniques: a review and future prospect. *Journal of Materials Research and Technology*, Vol. 11, pp. 719–753, doi: <https://doi.org/10.1016/j.jmrt.2021.01.031>.
6. Abadias, G., Chason, E., Keckes, J., Sebastiani, M., Thompson, G. B., Barthel, E., Doll, G. L., Murray, C. E., Stoessel, C. H., Martinu, L. (2018). Stress in thin films and coatings: Current status, challenges, and prospects. *J. Vac. Sci. Technol. A*, Vol. 36, pp. 020801, doi: 10.1116/1.5011790.
7. Torvik, P., Langley, B. (2015). Material properties of hard coatings developed for high damping. *Proceedings of the 51st AIAA/SA/ASEE Joint Propulsion Conference (Orlando, Florida, USA, July 29, 2015)*, doi: 10.2514/6.2015-4195.
8. Hovorun, T. P., Pylypenko, O. V., Berladir, K. V., Dyadyura, K. O., Dunaeva, M. N., Vorobiov, S. I., Panda, A. (2019). Physical-mechanical properties and structural-phase state of nanostructured wear-resistant coatings based on nitrides of refractory metals Ti and Zr. *Funct. Mater.*, Vol. 26 (3), pp. 548–555, doi: <https://doi.org/10.15407/fm26.03.548>.
9. Zaulychny, Ya. V., Hignjak, V. G., Harchenko, N. A., Hovorun, T. P., Hignjak, O. V., Dolgikh, V. Y. (2016). Influence of interatomic interaction processes on the mechanical properties of carbide coatings based on Ti, V and Cr, obtained by diffusion metallization. *J. Nano- Electron. Phys*, Vol. 8(4(1)), 04008, doi: 10.21272/jnep.8(4(1)).04008.
10. Kravchenko, Y. O., Coy, E., Peplińska, B., Iatsunskyi, I., Załęski, K., Kempniński, M., Beresnev, V. M., Pshyk, A. V., Pogrebnjak, A. D. (2020). Micro-mechanical investigation of (Al₅₀Ti₅₀)N coatings enhanced by ZrN layers in the nanolaminate architecture. *Applied Surface Science*, Vol. 534, 147573, doi: 10.1016/j.apsusc.2020.147573.
11. Hovorun, T. P., Pylypenko, O. V., Hovorun, M. V., Dyadyura, K. O. (2017). Methods of obtaining and properties of wear-resistant coatings based on Ti and N and Ti, Al and N. *J. Nano- Electron. Phys*, Vol. 9(2), 02026, doi: 10.21272/jnep.9(2).02026.
12. Wu, Z., Wu, Y., Wang, Q. (2019). Comparative investigation on structure evolution of ZrN and CrN coatings against ion irradiation. *Heliyon*, Vol. 5, e01370, doi: 10.1016/j.heliyon.2019.e01370.
13. Vereschaka, A., Tabakov, V., Grigoriev, S., Akseenko, A., Sitnikov, N., Oganyan, G., Shevchenko, S. (2019). Effect of adhesion and the wear-resistant layer thickness ratio on mechanical and performance properties of ZrN-(Zr, Al, Si)N coatings. *Surface and Coatings Technology*, Vol. 357, pp. 218–234, doi: 10.1016/j.surfcoat.2018.09.087.
14. Ashmarin, A. A., Betsofen, S. Y., Petrov, L. M., Lebedev, M. A. (2020). Effect of bias voltage on the texture of the TiN and ZrN coatings deposited by vacuum ion-plasma method. *IOP Conference Series: Materials Science and Engineering*, Vol. 889(1), 012019, doi: 10.1088/1757-899X/889/1/012019.
15. Vereschaka, A., Volosova, M., Chigarev, A., Sitnikov, N., Ashmarin, A., Sotova, C., Lytkin, D. (2020). Influence of the thickness of a nanolayer composite coating on values of residual stress and the nature of coating wear. *Coatings*, Vol. 10(1), 63, doi: 10.3390/coatings1001006.
16. Maksakova, O. V., Simoės, S., Pogrebnjak, A. D., Bondar, O. V., Kravchenko, Y. O., Koltunowicz, T. N., Shaimardanov, Z. K., Maksakova, O. V. (2019). Multilayered ZrN/CrN coatings with enhanced thermal and mechanical properties. *J. Alloy. Compd*, Vol. 776, pp. 679–690, doi: 10.1016/j.jallcom.2018.10.342.
17. Brus, V. V. (2012). Open-circuit analysis of thin film heterojunction solar cells. *Solar Energy*, Vol. 86(5), pp. 1600–1604, doi: 10.1016/j.solener.2012.02.022.
18. Zheng, Y., Chen, C.-H., Pearlman, H., Flanery, M., Bonner, R. (2015). Effect of porous coating on condensation heat transfer. *9th Boiling and Condensation Conference*, pp. 1–9. Available online: <https://www.1-act.com/wp-content/uploads/2015/05/Zheng-Effect-of-Porous-Media-Coating-on-Condensation-Heat-Transfer.pdf>
19. Shayestehaminzadeh, S., Tryggvason, T. K., Karlsson, L., Olafsson, S., Gudmundsson, J. T. (2013). The properties of TiN ultra-thin films grown on SiO₂ substrate by reactive high power impulse magnetron sputtering under various growth angles. *Thin Solid Films*, Vol. 548, pp. 354–357, doi: 10.1016/j.tsf.2013.09.025.
20. Pogrebnjak, A. D., Ivasishin, O. M., Beresnev, V. M. (2016). Arc-evaporated nanoscale multilayer nitride-based coatings for protection against wear, corrosion, and oxidation. *Usp. Fiz. Met.*, Vol. 17(1), pp. 1–28, doi: <https://doi.org/10.15407/ufm.17.01.001>.

21. Mazur, M. P., Vnukov, Yu. M., Dobroskok, V. L., Zaloga, V. O., Novosiolov, Yu. K., Yakubov, F. Ya. (2000). *Fundamentals of Materials Cutting*. Novyi Svit, Lviv, Ukraine.
22. Zhao, B. Y.-H., Liao, X.-Zh., Cheng, S., Ma, E., Zhu, Y. T. (2006). Simultaneously increasing the ductility and strength of nanostructured alloys. *Adv. Mater.*, Vol. 18, pp. 2280–2283, doi: 10.1002/adma.200600310.
23. Guillaumot, A., Lapostolle, F., Langlade, C., Billard, A., Oliveira, J. C., et al. (2010). Influence of substrate biasing on (Al, Ti)N thin films deposited by a hybrid HiPIMS/DC sputtering process. *IEEE Transactions on Plasma Science*, Vol. 38 (11), pp. 3040–3045. doi: (10.1109/TPS.2010.2052931).
24. Malvajerdi, S. S., Malvajerdi, A. S., Ghanaatshoar, M., Habibi, M. Jahdi, H. (2019). TiCrN-TiAlN-TiAlSiN-TiAlSiCN multilayers utilized to increase tillage tools useful lifetime. *Scientific Reports*, Vol. 9, 19101, doi: <https://doi.org/10.1038/s41598-019-55677-8>.
25. Liu, H., Yang F.-C., Tsai Y.-J., et al. (2018). Effect of modulation structure on the microstructural and mechanical properties of TiAlSiN/CrN thin films prepared by high power impulse magnetron sputtering. *Surface and Coatings Technology*, Vol. 358, pp. 577–585, doi: 10.1016/j.surfcoat.2018.11.069.
26. Kumar, C. S., Patel, S. K. (2019). Effect of duplex nanostructured TiAlSiN/TiSiN/TiAlN-TiAlN and TiAlN-TiAlSiN/TiSiN/TiAlN coatings on the hard turning performance of Al₂O₃-TiCN ceramic cutting tools. *Wear*, Vol. 418-419, pp. 226–240, doi: S0043164818307713.
27. Li, G., Sun, J., et al. (2018). Microstructure, mechanical properties, and cutting performance of TiAlSiN multilayer coatings prepared by HiPIMS. *Surface and Coatings Technology*, Vol. 353, 81, doi: 10.1016/j.surfcoat.2018.06.017.
28. Durmaz, Y. M., Yildiz, F. (2019). The wear performance of carbide tools coated with TiAlSiN, AlCrN and TiAlN ceramic films in intelligent machining process. *Materials Science: Ceramics International*, Vol. 45, pp. 3839–3848, doi: 10.1016/J.CERAMINT.2018.11.055.
29. Gao, F., Li, G., Xia, Y. (2017). Influence of hysteresis effect on properties of reactively sputtered TiAlSiN films. *Applied Surface Science*, Vol. 431, pp. 160–164, doi: 10.1016/j.apsusc.2017.07.283.
30. Chen, H., Zheng, B.C., Ou, Y. X., Lei, M. K. (2020). Microstructure and thermal conductivity of Ti-Al-Si-N nanocomposite coatings deposited by modulated pulsed power magnetron sputtering. *Thin Solid Films*, Vol. 693, 137680, doi: 10.1016/j.tsf.2019.137680.



Harikrishna V., Kumar K. V. (2021). Mechanical behaviors of hybrid composites reinforced with epoxy resin. *Journal of Engineering Sciences*, Vol. 8(2), pp. C24-C29, doi: 10.21272/jes.2021.8(2).c4

Mechanical Behaviors of Hybrid Composites Reinforced with Epoxy Resin

Harikrishna V.¹, Kumar K. V.²

¹M. Tech. Scholar Department of ME, JNTUH College of Engineering, Jagtial, T.S., India;

²HOD Department of ME, JNTUH College of Engineering, Jagtial, T.S., India.

Article info:

Submitted:

July 26, 2021

Accepted for publication:

December 9, 2021

Available online:

December 13, 2021

*Corresponding email:

vadicherla.harikrishna@gmail.com

Abstract. Natural fibres have emerged as a renewable and cheaper substitute to synthetic materials such as glass and carbon. A composite material can be defined as combining two or more materials that result in better properties. The constituents are reinforcement, and the other is a matrix. The main advantages of composites are high strength, stiffness combined with low density. As natural fibres are gaining more importance in recent times, many industries are focusing on these natural fibre composites, so that is why they are used as a component in composite materials. In this experiment, the analysis aims to characterize different natural fibres when combined with different ratios of the coconut coir and the bamboo. So, to fabricate the specimen, the hand lay-up method is used. The coconut coir and the bamboo composition are considered in three different variations. Then the natural fibres are subjected to resin and hardener compositions to test the suitability, tensile strength, flexural strength, and shore hardness test. We also conduct static analysis through ANSYS software.

Keywords: natural fibre, composite material, tensile strength, finite element analysis.

1 Introduction

The interest in natural fibre composite material is rapidly growing in the mechanical sector. There is a profound change in both the industrial application and the fundamental research. Natural fibres are mostly preferred because they are a renewable source, non-toxic to nature, cheap, partially recyclable, and biodegradable. Plants like flax, cotton, hemp, jute, sisal, pineapple, bamboo, banana, and silkworm are primarily used for very long years due to their properties. They are generally used as lignocelluloses fibres. The availability, renewability, low density and price, and satisfactory mechanical properties make them an attractive ecological alternative to glass, carbon, and manufactured fibres used to manufacture composites. These are environmentally friendly and used in transportation like railway coaches, aerospace, military applications, building, and construction consumer products.

Recently, car manufacturers have been interested in incorporating natural fibre composites into the interior and exterior parts. So, many companies such as Mercedes Benz, Toyota, and Daimler Chrysler have already accomplished this and are looking to expand the use of natural fibre composites. This serves to lower the vehicle's overall weight of the vehicle thus increasing fuel efficiency

and increasing the sustainability of their manufacturing process. The two major factors currently limit the large-scale production of natural fibres composites. Firstly, they are the strength of natural fibre composites, which is very low compared to glass. Secondly, they limit the large-scale production of natural fibre composites in water absorption. Generally, the natural fibres absorb water from the air and direct contact with the environment.

In addition to the naturally occurring composites, many other materials are generally used. They have been in use for a very long time. The demand will be placed according to the material's performance so that no other material can satisfy them. Natural fibres are now considered the most important and have a severe alert. Due to their applications and advantages, the properties of natural fibre composites can be modified by several factors based on the fibre combinations, processing methods, and fibre volume fraction.

Currently, natural fibre composites are used for the production of passenger cars. For example, Daimler Chrysler cars are equipped with an under-floor protection using abaca fibre (natural fibre) obtained from a plant called Musa Family, which belongs to the banana family. Many natural fibre composites are used in most electronic goods such as mobile phones, tablets, and laptops for

weight reduction without any trade-off strength. The properties of the natural fibre are determined by the architecture together, defined by the chemical composition and the structural features. These are highly applicable in civil aviation and in mass transportation.

Properties of different natural fibres are presented in Table 1.

Table 1 – Properties of different natural fibres

Property	Coir	Bamboo
Tensile strength, MPa	144	330
Modulus, GPa	31.0	9.80
Elongation, %	32.3	20.0
Density, kg/m ³	670	450

The materials that make up the composites are matrix, resins, additives, and reinforcements.

The resin is the main ingredient in composites. Thermoplastics and thermosets are the main resin systems. The thermoplastics resin is solid at room temperature, melts when supplied heat, and solidifies when cooled. The most commonly used resins in composites are unsaturated polyesters and vinyl esters.

The glycidic ethers, and amines are the main epoxies in the composites. The material properties are hardening are to be manipulated to get the good performances. The applications of epoxies are in the aeronautical industries and electrical device applications.

Application of fibre composites is represented by the following groups, which are 70 % of the total market value: automotive (23%), building and public works (21 %), aeronautics (17 %), and sports (11 %).

North America represents 40 % of the composites industry's total market value, 22 % in the Asia-Pacific region, and 3 % of the rest of the world.

2 Literature Review

Satyanarayana et al. [1] initiated research on the structural property studies of coir fibres. Fibres from different parts of the coconut palm tree were examined for properties such as size, density, electrical resistivity, ultimate tensile strength, initial modulus, and percentage elongation. Their research determined the stress-strain diagrams of the fracture mode, micro fibrillary angle, and cellulose and lignin contents of these fibres.

Shibata et al. [2] discovered composites reinforced with natural fibres and observed properties of biocomposites made from short abaca fibre and biodegradable polyester.

Rout et al. [3] show that the untreated coir fibres have weak interfacial bonding with the polyester matrix and the mechanical properties of the composites are poor.

Rajak et al. [4] investigated that the glass fibre or synthetic fibre reinforced polymeric composites acquire more strength. But these application areas are limited due to their very high fabrication cost. It also identifies natural fibers' four potential environmental improvements as substitution of higher volume natural fibres for some base polymer material. Lower environmental impact from

natural fibre production compared to glass fibre production, lower emission while in use due to weight reduction, and energy/carbon credits from the end of life incineration.

Haneefa et al. [5] studied the tensile and flexural properties of short banana and glass hybrid fibre reinforced polystyrene composites. They observed that the elongation at break decreases with an increase in the volume fraction of fibres.

Ahmed and Vijayarangan [6] evaluated the tensile, flexural, and interlaminar shear properties of woven jute and jute-glass fabric reinforced polyester composites by arranging different stacking sequences. The above two researchers listed the systematic procedure for evaluating tensile and flexural properties in their work.

Syduzzaman et al. [7] studied that natural fibres are advantageous over glass fibre as they buckle rather than break during processing and fabrication. In addition, cellulose possesses a flattened oval cross-section that enhances stress transfer by presenting an effectively higher aspect ratio.

Mohammed et al. [8] studied the advantages mentioned above. The natural fibre composite also has disadvantages, such as poor compatibility between hydrophobic polymer matrix and hydrophilic fibres, leading to weak interfaces and poor mechanical properties.

Khanam et al. [9] investigated tensile, flexural, and compressive properties of coir-silk fibre reinforced composites, and Dong [10] reviewed studies evaluating tensile properties for glass and bamboo fibres reinforced polyester hybrid composites.

Therefore, the present project work aims to fabricate various composite laminates with epoxy resin. The fibres involved in this experimental analysis are bamboo and coir. These are subjected to different ratios (bamboo 70 % + coir 30 %, bamboo 60 % + coir 40 %, and bamboo 80 % + coir 20 %). This experimental fabrication is done by the hand lay method. ASTM D638 finds the tensile strength. Analysis done is done through ANSYS software.

The main objectives are:

- to test the strength of the specimen when different bamboo and coir are in different ratios;
- to study the tensile strength of each material separately to apply in automotive applications;
- to study the SHORE hardness property of the material when mixed with different proportions.

3 Research Methodology

3.1 Materials selection

Natural fibres are taken initially for fabrication. The epoxy is used to make the composite laminate. The fabrication process has been done to fabricate the FRP laminate. This process is done by the hand lay method.

The materials have been selected according to the fibers' usage and availability. The following are some essential points for material selection. They are:

- to develop an alternative new solution for the given applications;

- to use quantitative methods in material selection;
- to find reliable properties sources of material properties;
- to analyze the performance requirements;
- to evaluate the different solutions.

The raw materials used in this experimental process are natural fibre (coconut coir and bamboo), epoxy resin, and hardener.

Coir is a versatile natural fibre extracted from mesocarp tissue or husk of coconut fruit. Generally, fibre is of a golden color when cleaned after removing from coconut husk.

Coir is the fibrous husk of the coconut shell. Being tough and naturally resistant to seawater, the coir protects the fruit enough to survive months floating on ocean currents to be washed up on a sandy shore where it may sprout and grow into a tree if it has enough freshwater because of all the other nutrients it needs have been carried along with the seed. These characteristics make the fibres quite valuable for the floor and outdoor mats.

The term “bamboo fabric” widely refers to many different textiles made from the bamboo plant. Fabrics have been made from bamboo for thousands of years, but it is only in contemporary times that the process of making this hardy and fast-growing wood into fabric has been perfected.

Epoxy is the chemical name, and Araldite is the marketing name by Hindustan international (India) private limited manufacturing company.

Epoxy has the following properties: high strength, good sticky nature, toughness, water resistance, and tasteless and non-toxic.

Epoxy resin is defined as a molecule containing more than one epoxy group. This has high mechanical properties, like a large cohesive force. It has flexibility and diversity in design. It also has excellent stability without impurities. These have good strength and low absorption of moisture. These are relatively high in viscosity, so that they are usually moulded at temperatures in the region of 50–100 °C. When these get reacted with hardeners, they are set to a hard mass that does not melt or dissolve in solvents. Hardeners are typically amine anhydride-based chemistry. They are usually synthetic, most commonly derived from petrochemicals, but are partially natural.

3.2 Hand lay-up method

This experimental process follows the Hand lay method. This is one of the most traditional methods used in the industry. It is a straightforward process, where each ply is handled only by hand and is stacked layer by layer up to the desired thickness.

Although this method is reliable, it requires much labor, and the procedure requires more time than the advanced manufacturing methods. Brushes and rolls are used in this method to apply the resin and reduce the air bubbles. There is no heat required during the curing process, and it is usually left until cured at room temperatures.

They are prepared by respecting some steps. First, the mould surfaces are treated by releasing an anti-adhesive agent to avoid sticking polymer to the surface.

Then, a thin plastic sheet is applied at the top and bottom of the mould plate to get the smooth surfaces of the product. The layers of woven reinforcement are cut to required shapes and placed on the surface of the mould.

Thus, previously mentioned, the resin is thoroughly mixed with the hardener and poured uniformly on the mats.

It is seen that no air bubbles should roll inside the sheets. The mould is then closed and pressured on the single mat.

After it is cured at room temperature, the mould is opened, and woven composite is removed from the mould surface.

3.3 Experimental procedure

The experimental technique follows the hand lay method. This has a long wide plate used as a base. The resin and hardener are mixed firstly, and then the coating is applied uniformly on the entire area of the required size of the laminate. Then a layer of fiber is evenly placed over the resin, then a small amount of force is applied on it with the roller. Then again, a coating is kept on it.

This process is repeated until the required thickness is obtained. Then a coating of wax is kept to finish the product, or a Teflon sheet is kept on it with a little weight.

The laminate setting on the board is gently removed by releasing the Teflon sheet. The laminate has on the edges with the fibres are cut in to make laminate to a uniform shape. The carpentry chisel cuts fibres. The chisel also cuts the extra parts. The tensile and flexural tests specimens were cut on a CNC machine as per ASTM standards: length – 165 mm; width – 19 mm; thickness – 3 mm.

4 Results

The laminate setting on the board is gently removed by releasing the Teflon sheet. The laminate has on the edges with the fibres are cut in to make laminate to a uniform shape. The carpentry chisel cuts fibres. The chisel also cuts the extra parts. As per ASTM standards, the tensile and flexural tests specimens were cut on the CNC machine.

The numerical simulation results are presented in Figure 1 and summarized in Tables 2–3. The results for different material compositions are also presented in Figure 2.

Shore D Hardness is a standardized test measuring the depth of penetration of a specific indenter. Test methods used to measure shore D hardness are ASTM D2240 and ISO 868. The results are presented in Table 4.

Flexure tests are generally used to determine flexural modulus or flexural strength. A flexure test is more affordable than a tensile test, and test results are slightly different. The material is laid horizontally over two points of contact (lower support span), and then a force is applied to the top of the material through either one or two

points of contact (upper loading span) until the sample fails. The maximum recorded force is the flexural strength of that particular sample. The results are also presented in Table 4.

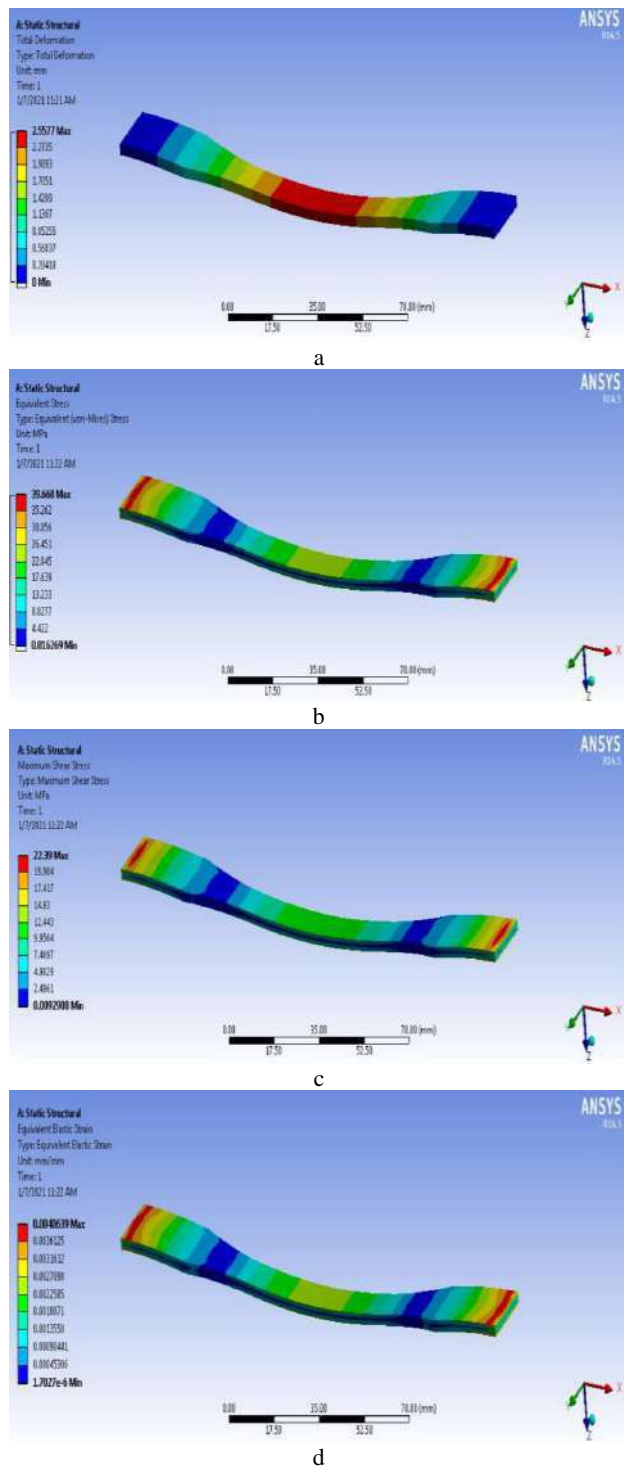
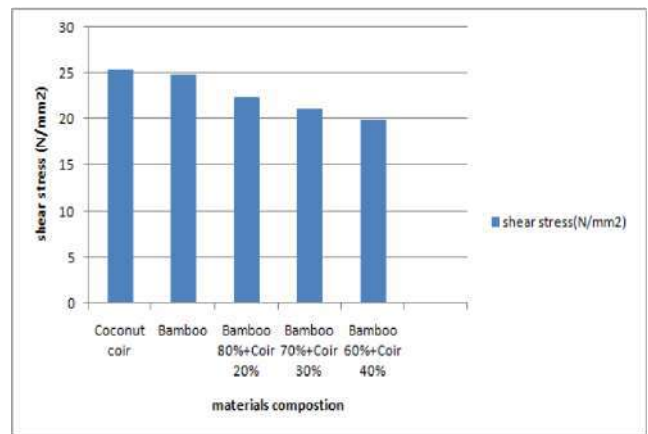
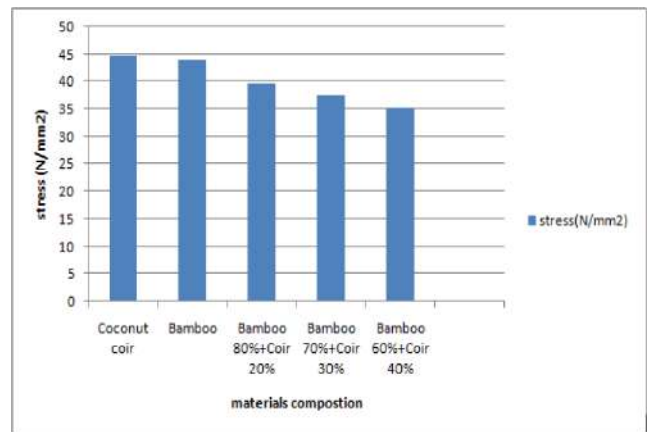
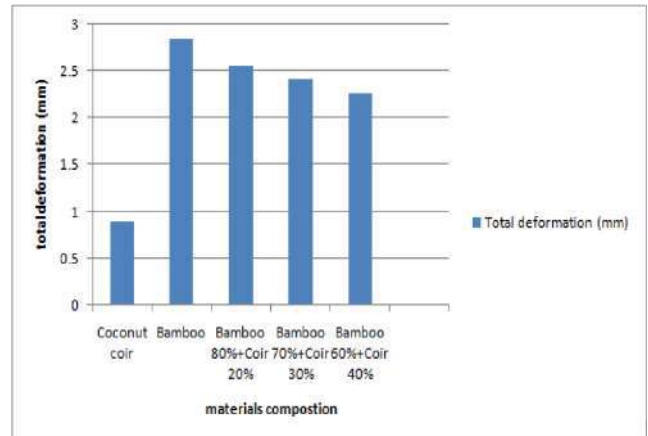
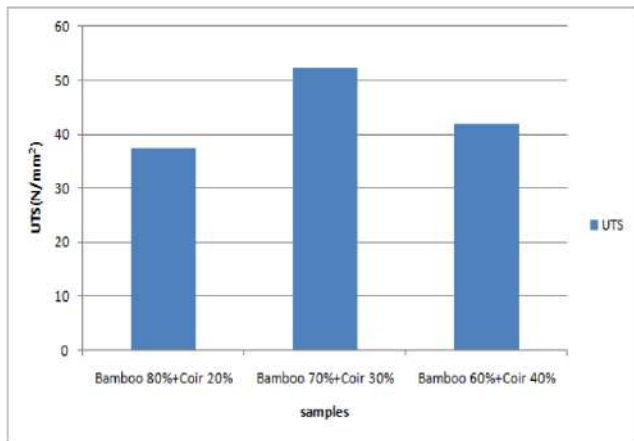


Figure 1 – The numerical simulation results: a – total deformations; b – von Mises equivalent stress; c – shear stress; d – strain

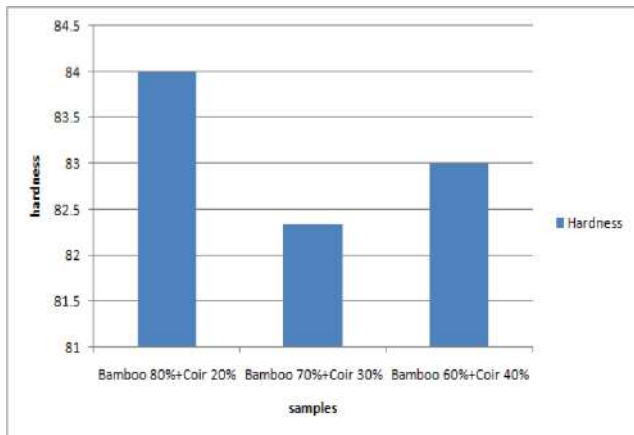
Table 2 – The numerical simulation results

Material	Total deformation, mm	Equivalent stress, MPa	Shear stress, MPa	Strain, 10^{-3}
Coir	0.90	44.8	25.4	1.45
Bamboo	2.84	44.1	24.9	4.51
Bamboo 80 % + Coir 20 %	2.56	39.7	22.4	4.06
Bamboo 70 % + Coir 30 %	2.42	37.5	21.1	3.84
Bamboo 60 % + Coir 40 %	2.27	35.3	19.9	3.61

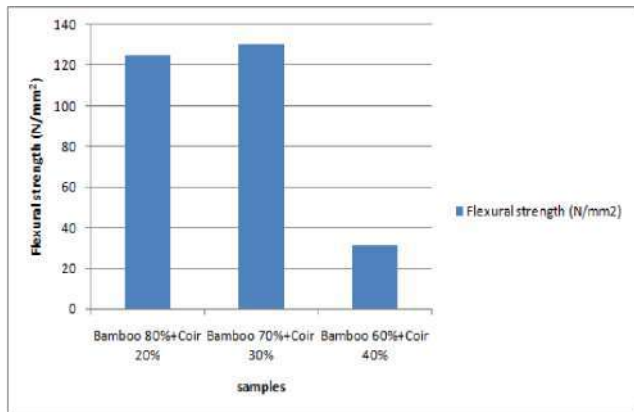




d



e



f

Figure 2 – Material composition vs total deformation (a), von Mises equivalent stress (b), shear stress (c), tensile stress (d), hardness (e), and flexural stress (f)

Table 3 – Experimental results on tensile stress

Sample	UTS, MPa	Elongation, %
Bamboo 80 % + Coir 20 %	37.4	1.44
Bamboo 70 % + Coir 30 %	52.6	0.60
Bamboo 60 % + Coir 40 %	42.1	0.84

Table 4 – Shore D hardness test and elongation results

Sample	Hardness	Elongation, %
Bamboo 80 % + Coir 20 %	84	125
Bamboo 70 % + Coir 30 %	82	131
Bamboo 60 % + Coir 40 %	83	31

5 Conclusions

The present project work aims to fabricate various composite laminates with epoxy resin. The fibers involved in this experimental analysis are bamboo and coir. These are subjected to different coir ratios (bamboo 70 % + coir 30 %, bamboo 60 % + coir 40 %, and bamboo 80 % + coir 20 %). This experimental fabrication is done by the hand-lay method. ASTM D638 finds the tensile strength. Analysis done is done through ANSYS software.

The laminates are fabricated by hand lay-up method effectively. The experimental study reveals enhanced mechanical properties like hardness, flexural strength and tensile strength.

The hardness improved by adding reinforcements to the base alloy. The addition of epoxy resin particles improved the hardness, and the improved wear properties resulted from the addition of hardener and epoxy resin. Further, the mechanical properties are enriched by heat treatment. Hardness and tensile strength were improved by the composition of (bamboo 70 % + coir 30 %, compared to other samples.

References

1. Satyanarayana, K. G., Pillai, C. K., Sukumaran, K., Pillai, S. G., Rohatgi, P.K., Vijayan, K. (1982). Structure property studies of fibres from various parts of the coconut tree. *Journal of Materials Science*, Vol. 17, pp. 2453-2462, doi: 10.1007/BF00543759.
2. Shibata, M., Ozawa, K., Teramoto, N., Yosomiya, R., Takeishi, H. (2003). Biocomposites made from short abaca fiber and biodegradable polyesters. *Macro-Molecular Materials and Engineering*, Vol. 288(1), pp. 35-43, doi: 10.1002/mame.200290031.
3. Rout, J., Tripathy, S. S., Misra, M., Mohanty, A. K., Nayak, S. K. (2001). The influence of fiber surface modification on the mechanical properties of coir-polyester composites. *Polymer Composites*, Vol. 22(4), pp. 468-476, doi: 10.1002/pc.10552.

4. Rajak, D. K., Pagar, D. D., Menezes, P. L., Linul, E. (2019). Fiber-reinforced polymer composites: manufacturing, properties, and applications. *Polymers*, Vol. 11(10), 1667, doi: 10.3390/polym11101667.
5. Haneefa, A., Bindu, P., Aravind, I., Thomas, S. (2008). Studies on tensile and flexural properties of short banana/glass hybrid fiber reinforced polystyrene composites. *Journal of Composite Materials*, Vol. 42(15), pp. 1471-1489, doi: 10.1177/0021998308092194.
6. Ahmed, K. S., Vijayarangan, S. (2008). Tensile, flexural and interlaminar shear properties of woven jute and jute-glass fabric reinforced polyester composites. *Journal of Materials Processing Technology*, Vol. 207(1-3), pp. 330-335, doi: 10.1016/j.jmatprotec.2008.06.038.
7. Syduzzaman, M., Al Faruque, M. A., Bilisik, K., Naebe, M. (2020). Plant-based natural fibre reinforced composites: a review on fabrication, properties and applications. *Coatings*, Vol. 10(10), 973, doi: 10.3390/coatings10100973.
8. Mohammed, L., Ansari, M. N. M., Pua, G., Jawaid, M., Islam, M. S. (2015). A review on natural fiber reinforced polymer composite and its applications. *Natural Fiber Reinforced Polymer Composites*, Vol. 2015, 243947, doi: 10.1155/2015/243947.
9. Noorunnisa Khanam, P., Ramachandra Reddy, G., Raghu, K., Venkata Naidu, S. (2010). Tensile, flexural, and compressive properties of coir/silk fiber-reinforced hybrid composites. *Journal of Reinforced Plastics and Composites*, Vol. 29(14), pp. 2124-2127, doi: 10.1177/0731684409345413.
10. Dong, C. (2018). Review of Natural Fibre Reinforced Hybrid Composites. *Journal of Reinforced Plastics and Composites*, Vol. 37(5), pp. 331-348.



Chernobrovchenko V. S., Dyadyura K. O., Panda A. (2021). Investigation of the blockchain structure for hydroxyapatite-based scaffolds. *Journal of Engineering Sciences*, Vol. 8(2), pp. C30-C35, doi: 10.21272/jes.2021.8(2).c5

Investigation of the Blockchain Structure for Hydroxyapatite-Based Scaffolds

Chernobrovchenko V. S.^{1*}, Dyadyura K. O.¹, Panda A.²

¹ Sumy State University, 2, Rymaskogo-Korsakova St., 40007 Sumy, Ukraine;

² Faculty of Manufacturing Technologies, Technical University of Košice, 080 01 Prešov, Slovakia

Article info:

Submitted:

July 15, 2021

Accepted for publication:

December 10, 2021

Available online:

December 14, 2021

*Corresponding email:

vadim-golik@ukr.net

Abstract. Regenerative biomechanics provides exciting technologies for developing functional substitutes, intending to restore and regenerate damaged tissues and organs. Scaffolds are in great demand. However, there are risks of biocompatibility when using scaffolds. Each bone substitute has its chemical composition, and other characteristics have advantages and disadvantages. Reproducibility, data sharing, privacy concerns, and patient participation in clinical trials are significant problems in modern clinical trials. In the era of the Internet, data is collected constantly. Today we need applications that ensure the privacy of users' data. Blockchain technology helps to compensate for severe data management problems (e.g., patient recruitment, ongoing monitoring) in clinical trials (CT). The article examines the principles of blockchain operation and approaches to bone substitutes' design. Based on this data, a blockchain model for biomaterial surgery has been created, facilitating interaction between the parties and reducing errors.

Keywords: life cycle assessment, clinical trials, biomaterial, implant, risk assessment, transaction.

1 Introduction

Biomaterials differ in chemical composition, the biological mechanism of action, and other characteristics. Each of them has its advantages and disadvantages [1]. A compromise is required between mechanical and biological characteristics when using synthetic materials.

Since scaffolds are not permanent implants, their leading role is to promote extracellular matrix formation [2, 3]. Because of this, there are risks of biocompatibility when using scaffolds [4].

Clinical Trials (CT) help test and validate the safety of newly discovered drugs in specific patient populations. However, such research usually faces many challenges (massive financial costs, regulatory and administrative barriers, and an insufficient labor force).

In addition, CT faces several data management challenges related to protocol compliance, patient registration, transparency, traceability, data integrity, and sample reporting [5]. Confidentiality of personal data and patient inclusion in clinical trials are essential for modern clinical trials [6].

In the Internet era, personal data is collected continuously. Today, we need privacy apps that always keep users in control of their data [7].

Blockchain can potentially solve such problems due to its intrinsic characteristics and properties [5]. The principle of the blockchain is that any service entrusted to trusted third parties can be built in a transparent, decentralized, secure "trustless" way at the top of the blockchain (in fact, there is trust, but it is hardcoded into the blockchain protocol due to the complex cryptographic algorithm) [6].

The purpose of this work is to investigate approaches to the design, manufacture, and intended use of scaffolds based on life cycle principles and approaches to risk assessment, as well as methods for building blockchains, and create blockchain technology for regenerative biomechanics that could facilitate data exchange between different parties and reduce errors.

2 Research Methodology

2.1 Principles of bone tissue production

Cells, scaffolds, and growth factors are the main components of tissue engineering.

Figure 1 is a diagram showing the concept of skeletal tissue regeneration using scaffold-based tissue engineering strategies, including its components (cells, biomaterials/scaffolds, and growth factors) and the

influence of the environment for the pre-preparation of engineered implants [8].

According to the QbD concept, there are three approaches to scaffold design, where eight quality dimensions are used [9]. 3D printing technology is the preferred manufacturing process for regenerative engineering applications. This technology can successfully form a well-defined complex and can be developed from the data of three-dimensional scans of individual patients.

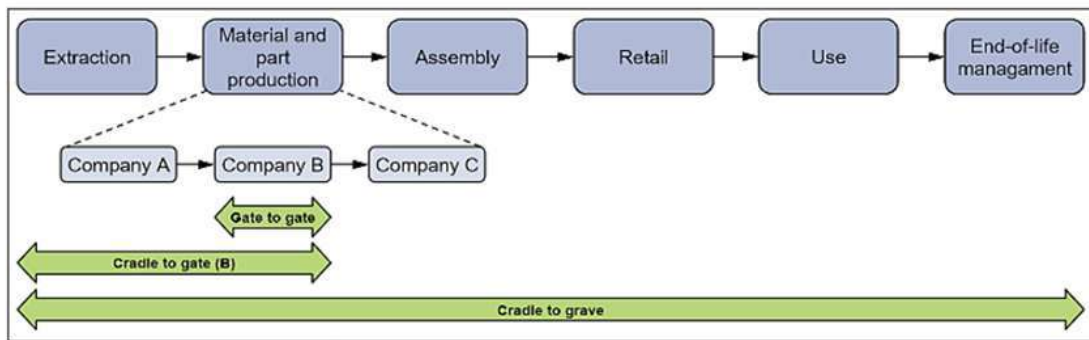


Figure 1 – The concept of skeletal tissue regeneration across the boundaries of the LCA scaffold system [10]

Preclinical trials are assessed by *in vitro* and *in vivo* tests before regulatory approval [11]. Risk assessment is carried out under the ISO 14971 standard (Figure 2) [12]. Risk management data is communicated to regulatory authorities at all stages, but especially in the first three stages, when hazards are identified, and measures are taken to manage them.

At stages of the life cycle, environmental risk is regulated by the ISO 14040: 2006 standard (Figure 3) [10].

2.2 Blockchain technology in biomedicine

Blockchain technology has opened up tremendous opportunities in healthcare, discovering the actual value of interoperability. Blockchain technology features such as data provenance, transparency, decentralized transaction verification, and immutability can help offset severe data management challenges (such as patient recruitment, ongoing monitoring, data management, and data analysis and accurate reporting) in clinical trials (CT) [13].

When patients undergo a medical examination, their information is registered at the registration desk, and a smart contract is established. Next comes the diagnosis. The examination results are collected using Internet-based devices and recorded in an electronic medical record system connected to a smart contract in the blockchain, where the data is encrypted. Once added to the blockchain, it is impossible to change the data, but authorized parties can only access it. Each patient is provided with an electronic medical record account when registering for an appointment. It is unique and contains the patient's identification number and personal information.

The person gives personal information (name, age, contact details, medical history). After that, the account is added to the blockchain, waiting for further updates after the medical results. The smart contract is activated on the blockchain stored in the EHR account. It has coded rules that control new registrations, and it focuses on the execution of transactions added to the chain, such as forcing transactions to obtain consent from both healthcare providers and patients before allowing a third party to view. The following types of policies are recommended for inclusion in a smart contract. The privacy policy of personal data is related to how healthcare institutions collect and use patients' personal information. They also inform patients about what specific information is collected and whether it is kept confidential and protected from misuse or abuse by sharing it with partners. The Health Records Policy governs the types of data collected and recorded, standards for medical records and management, and the responsibilities of healthcare professionals in data processing. These principles should be consistent with common law and best practices. The Third Party Involvement Policy addresses the rights and obligations of pharmaceutical companies, insurance companies, and governments in collecting and using patient information and treatment outcomes. After registering an EHR account, patients provide their digital signature to activate the smart contract. Contract violations can be identified, and a warning issued to the patient and individuals. The smart contract governs the creation of new identities. Registration of a person is carried out only in certified institutions. It also contains a PPR contract issued by the interaction of data received from both parties. This contract defines data ownership and access to permissions

associated with medical records maintained by healthcare professionals.

PPR defines data metrics attached to a hash of a subset of patient data that make it impossible to change the data at the source. It also allows customers to have full access to and control their data and share it with others. Finally, it contains a list of links to the PPR contract, which lists all prior and current information exchanges between two nodes in the system, such as all people served by a healthcare professional or all

healthcare providers who provided services to a patient, or a third party with whom the patient shares records. The blockchain and smart contract maintain all medical journals for an indefinite period, so one participant can always access the journals by updating the latest blockchain from the network. Figure 4 shows this process [14].

The rest of the blockchain models are presented in Table 1.

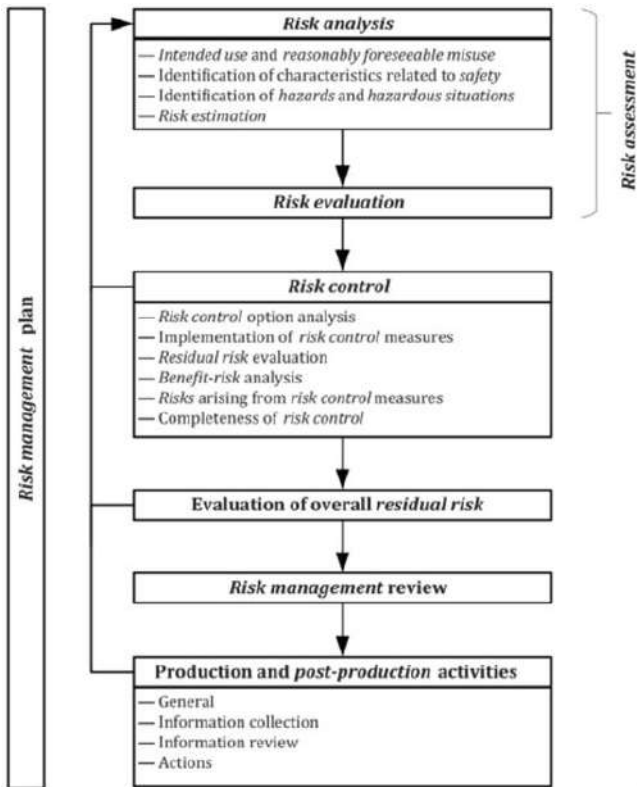


Figure 2 – Quality risk management process [12]

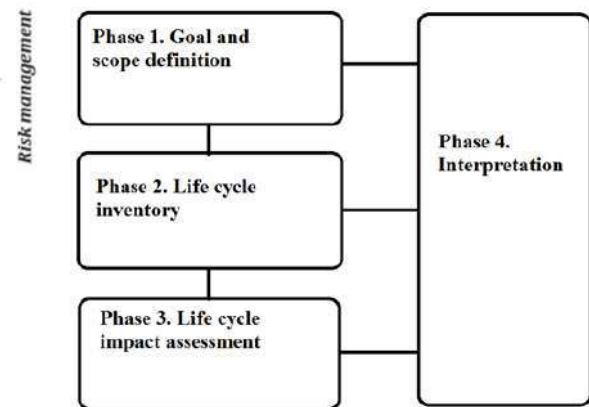


Figure 3 – Environmental risk assessment

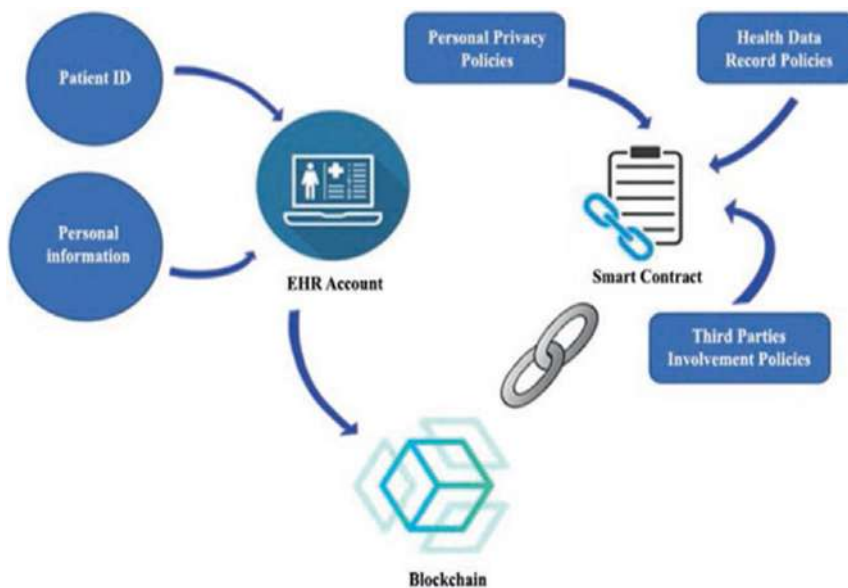


Figure 4 – Patient registration and personal profile setting [14]

Table 1 – Some blockchain models

Blockchain technology	Data	Benefits	Disadvantages	Source
Private blockchain	EHR	A smart blockchain-based application for managing and sharing healthcare data	No scalability or availability considerations, data exchange is limited	[15]
Proof of work	Location	Layered location sharing scheme	There is no discussion of under what critical condition the patient’s whereabouts data will be obtained	[16]
Ethereum platform	Health data	Economic smart contracts	Interaction between different parties is not considered	[17]

3 Results

3.1 Blockchain process structure

Our proposed process for transferring health information on the blockchain consists of the following steps.

3.1.1 Registration

The patient is registered at the clinic. His data is recorded, a smart contract is established with the insurance company. The patient is the leading party receiving treatment based on personal information. Doctors enter information about treatment use of drugs. A smart contract is entered into when patients fulfill certain insurance contract conditions to pay the surgical fees. Smart contracts are self-executing contracts on the blockchain network. Contracts are converted into computer code, saved, and executed by the blockchain network.

3.1.2 Survey

A medical examination of the patient is carried out. The results are forwarded to the manufacturer. Some images may be needed here, such as an MRI scan to determine the condition of the patients [18].

3.1.3 Manufacturing

The manufacturer designs the implant and assesses the risks according to ISO 14971 and ISO 14040:2006 standards.

Life Cycle Assessment is a tool for assessing a product’s environmental and potential aspects. It is carried out by compiling a list of inputs and outputs, assessing the environmental impact, the impact of inputs and outputs, and interpreting the results for the study [10]. The results are reported to the regulatory authorities.

3.1.4 Preclinical studies

The material is preclinically tested in the laboratory, the results are reported to the regulatory authorities. Medical devices are tested for cytotoxicity, genotoxicity, sensitization, and irritation [11].

3.1.5 Implantation

The material is implanted into the patient (Figure 5).

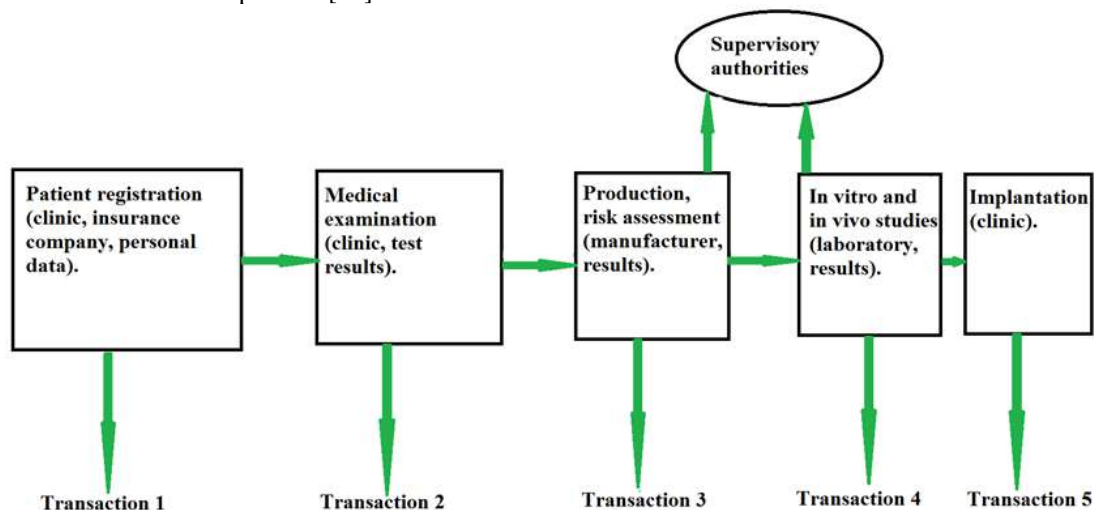


Figure 5 – Proposed blockchain process

3.2 Data structure

The data structure is determined by members and assets [18]. Participants – doctor, patient, insurance company, biomaterial manufacturer, regulatory

authorities, laboratories. Assets have patient records (survey data), product information (material, dimensions), transactions, risk assessment results, and preclinical testing (Figure 6).

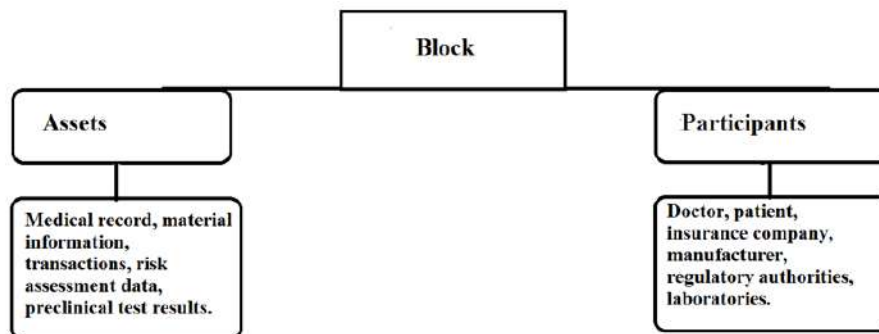


Figure 6 – Proposed data structure

The patient is the main participant who receives the treatment, with personal data such as health information and medical data.

The doctor conducts diagnostics operates on the patient. He assesses the patient's condition and decides which surgery is necessary and which implant he needs. Patient information and implant characteristics will be sent to the manufacturer.

The implant manufacturer receives information from the surgeon. Depending on the diagnosis made by the surgeons, the implant can be custom-made according to the patient's characteristics or using a standard implant.

The patient can purchase health insurance from an insurance company. This establishes a smart contract that enforces the contract between the patient, the hospital, the implant manufacturer, and the insurance company.

Regulatory authorities receive information on risk assessments from the manufacturer.

The material is sent to the laboratory for preclinical studies on cytotoxicity sensitization. Information about them is also transmitted to the regulatory authorities.

4 Conclusions

Clinical testing helps confirm the safety of open-label drugs in specific patient populations. But such research usually faces many challenges, such as massive financial costs, regulatory and administrative barriers, and several data management challenges related to protocol compliance, patient registration, and transparency.

The blockchain network is used in the biomedical field to store and exchange patient data across hospitals, diagnostic laboratories, pharmacies, and doctors.

Blockchain programs can pinpoint severe errors in the medical field.

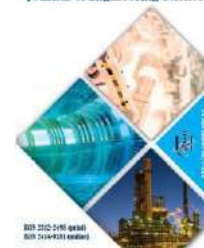
Thus, it can improve the healthcare system's productivity, safety, and transparency of health data exchange.

This paper proposes a blockchain network for scaffolds based on hydroxyapatite, considering the life cycle of scaffolds, approaches to risk assessment, and clinical testing. This blockchain structure will improve its integration into implant surgery in the future.

References

1. Sukhodub, L. F., Diadiura, K. O. (2018). Design and fabrication of polymer-ceramic nanocomposites materials for bone tissue engineering. *Journal of Nano- and Electronic Physics*, Vol. 10(6), 06003, doi: 10.21272/jnep.10(6).06003.
2. Bouler, J. M., Pilet, P., Gauthier, E. O. (2017). Verron biphasic calcium phosphate ceramics for bone reconstruction: A review of biological response. *Acta Biomaterialia*, Vol. 53, pp. 1-12, doi: 10.1016/j.actbio.2017.01.076.
3. Rustom, L., Boudou, T., Lou, S., Pignot-Paintrand, I., Nemke, B. W., Lu, Y., Markel, M. D., Picart, C., Johnson, A. J. W. (2016). Micropore-induced capillarity enhances bone distribution in vivo in biphasic calcium phosphate scaffolds. *Acta Biomater*, Vol. 44, pp. 144-154, doi: 10.1016/j.actbio.2016.08.025.
4. Miclăuș, T., Valla, V., Koukoura, A., Nielsen, A. A., Dahlerup, B., Tsianos, G.-I., Vassiliadis, E. (2020). Impact of design on medical device safety. *Therapeutic Innovation and Regulatory Science*, Vol. 54(4), pp. 839-849, doi: 10.1007/s43441-019-00022-4.
5. Omar, I. A., Jayaraman, R., Salah, K., Simsekler, M. C. E., Yaqoob, I., Ellahham, S. (2020). Ensuring protocol compliance and data transparency in clinical trials using Blockchain smart contracts. *BMC Medical Research Methodology*, Vol. 20(1), pp. 1-17.
6. Benchoufi, M., Ravaud, P. (2017). Blockchain technology for improving clinical research quality. *Trials*, Vol. 18(1), pp. 1-5.
7. Angeletti, F., Chatzigiannakis, I., Vitaletti, A. (2017). The role of blockchain and IoT in recruiting participants for digital clinical trials. *25th IEEE International Conference on Software, Telecommunications and Computer Networks (SoftCOM)*, pp. 1-5.
8. Da Silva Presa, R. M. (2019). Development of a novel 3D-Scaffold to promote bone regeneration. Available online: <https://mechse.illinois.edu/people/profile/ajwj>.

9. Martinez-Marquez, D., Mirnajafizadeh, A., Carty, C. P., Stewart, R. A. (2018). Application of quality by design for 3D printed bone prostheses and scaffolds. *PLoS One*, Vol. 13(4), e0195291.
10. Tajurhim, N. A. N., Mahmood, S., Saman, M. Z. M., Ngadiman, N. H. A. (2021). Life cycle assessment of 3D-printed bone tissue engineering scaffolds, doi: 10.21203/rs.3.rs-497484/v1.
11. Assad, M., Jackson, N. (2019). Biocompatibility evaluation of orthopedic biomaterials and medical devices: A review of safety and efficacy models. *Encyclopedia of Biomedical Engineering*, Vol. 2019, pp. 281-309, doi: 10.1016/B978-0-12-801238-3.11104-3.
12. Sandoval, E. (2019). Risk-Based Design Control Process to Promote a Quality by Design Infrastructure in the Medical Device Industry. Ph.D. Thesis, California State University, Dominguez Hills.
13. Omar, I. A., Jayaraman, R., Salah, K., Yaqoob, I., Ellahham, S. (2021). Applications of blockchain technology in clinical trials: Review and open challenges. *Arabian Journal for Science and Engineering*, Vol. 46(4), pp. 3001-3015.
14. Chanchaichujit, J., Tan, A., Meng, F., Eaimkhong, S. (2019). Blockchain technology in healthcare. *Healthcare 4.0*, pp. 37-62.
15. Yue, X., Wang, H., Jin, D., Li, M., Jiang, W. (2016). Healthcare data gateways: found healthcare intelligence on blockchain with novel privacy risk control. *Journal of Medical Systems*, Vol. 40(10), pp. 1-8.
16. Ji, Y., Zhang, J., Ma, J., Yang, C., Yao, X. (2018). BMPLS: Blockchain-based multi-level privacy-preserving location sharing scheme for telecare medical information systems. *Journal of Medical Systems*, Vol. 42(8), pp. 1-13.
17. Al Omar, A., Bhuiyan, M. Z. A., Basu, A., Kiyomoto, S., Rahman, M. S. (2019). Privacy-friendly platform for healthcare data in cloud based on blockchain environment. *Future Generation Computer Systems*, Vol. 95, pp. 511-521.
18. Tang, Y. M., Ho, G., Jack, W. U. (2018). Integrating blockchain for improving data sharing in implant surgery. *Proceedings of ISER 147th International Conference*, pp. 27-31.



energies

an Open Access Journal by MDPI



Practical and Scientific Aspects of Multiphase Systems

Guest Editors:

Prof. Dr. Marek Ochowiak

Department of Chemical Engineering and Equipment, Poznan University of Technology, 60-965 Poznan, Poland

marek.ochowiak@put.poznan.pl

Dr. Szymon Woźniowski

Institute of Chemical Technology and Engineering, Poznan University of Technology, 60-965 Poznan, Poland

szymon.wozniowski@put.poznan.pl

Dr. Sylwia Włodarczak

Department of Chemical Engineering and Equipment, Poznan University of Technology, 60-965 Poznan, Poland

sylwia.wlodarczak@put.poznan.pl

Deadline for manuscript submissions:

31 October 2022

Message from the Guest Editors

Dear Colleagues,

A multiphase system is characterized by the simultaneous presence of several phases, the two-phase system being the simplest case. The term two-component is sometimes used to describe flows in which the phases comprise different chemical substances. The analysis of multiphase systems can include consideration of multi-compound materials, multiphase flow, and multiphase heat and mass transfer.

The present Special Issue of *Energies*, entitled “Practical and Scientific Aspects of Multiphase Systems”, invites contributions on multiphase flows, multi-component systems, and chemical reactors of both experimental and computational studies. The Issue is focused on recent advances in conjunction to various practical aspects of chemical engineering, especially those related to the process intensification, process design, practical applicability of rheology, control systems, process safety, plant design, chemical technology, environmental engineering, materials, etc. We welcome communications, original research articles and review articles.



mdpi.com/si/90101

Special Issue



Chelabi M. A., Basova Y., Hamidou M. K., Dobrotvorskiy S. (2021). Analysis of the three-dimensional accelerating flow in a mixed turbine rotor. *Journal of Engineering Sciences*, Vol. 8(2), pp. D1-D7, doi: 10.21272/jes.2021.8(2).d1

Analysis of the Three-Dimensional Accelerating Flow in A Mixed Turbine Rotor

Chelabi M. A.¹[0000-0002-4880-9496], Basova Y.²[0000-0002-8549-4788], Hamidou M. K.¹, Dobrotvorskiy S.²[0000-0003-1223-1036]

¹Laboratory of Applied Mechanics, Faculty of Mechanical Engineering, University of Science and Technology Mohamed Boudiaf-El Mnouar, PO Box 1505 Bir El Djir 31000 Oran, Algeria;

²Department of Mechanical Engineering Technology and Metal-Cutting Machines, Educational and Scientific Institute of Mechanical Engineering and Transport, National Technical University "Kharkiv Polytechnic Institute", 2, Kyrpychova St., 61002 Kharkiv, Ukraine

Article info:

Submitted: July 19, 2021
 Accepted for publication: November 17, 2021
 Available online: November 22, 2021

*Corresponding email:

chelabilma.usto@yahoo.com

Abstract. An investigation on new rotor blade designs conceived to produce higher exit relative kinetic energy of a mixed flow turbine is undertaken. Accelerating the flow through the rotor in a relative frame of reference improves energy transfer to the shaft, which is only produced in a rotating rotor. A three-dimensional converging rotor channel might respond to the analysis requirements in the subsonic flow regimes. Effectively, the machine experiences a 3.71 % and 3.67 % increase in work output and efficiency, respectively, representing this study's primary intent. This has been accomplished by varying the shroud profile to a lesser eye tip diameter, then the hub profile to a larger eye root diameter. At last, both shroud and hub profiles are varied. It appears possible to enhance the performance of the rotor in terms of optimum work done and efficiency by devising suitable blade geometry designs. ANSYS CFX 15 is the code of all simulation works.

Keywords: blade, vane-to-vane plane, hub, shroud, meridional plane.

1 Introduction

The mixed inflow turbines combine the advantages of both the axial and the radial types. They can use higher flow rates and operate at a higher specific rate. The maximum efficiency is attained at a lower ratio of tip speed over the velocity. The bending stresses on the new blade geometry are lesser compared to the radial turbines. Also, the use of variable nozzle blades is efficient even at off-design point operation. This type of turbine covers large ranges of power, rate of mass flow, and rotational speeds. Among their applications, one cites Diesel engines in pulsating flow regimes.

One is concerned with the rotor through-flow area effect on the turbine performance. It must be observed that the rotor channel cross-sectional area, from inlet to exit, is designed to ensure specific variations during the gas expansion. Besides, it is pointed out that on the one hand, the passage of the flow in the vane-to-vane Plane is converging, which implies flow acceleration in the moving reference frame for subsonic flow regimes. On the other hand, the meridional channel surface is diverging. The main reason for this design is to increase the specific volume during the fluid flow expansion, which would

require an increase in flow area. Since the flow regime is subsonic, a flow deceleration is expected. Apparently, the flow parameters are affected by the combined effects of the sidewalls of the rotor channel. As a result, a little change in the relative velocity is revealed. Based on these arguments, investigations regarding the blade geometry are undertaken to shape a three-dimensional converging rotor through a flow sectional area for achieving greater flow acceleration rates. This might cause energy transformation into relative kinetic energy with greater energy transfer to the rotor into higher specific output work done.

A few arrangements might be employed to design new blade configurations for the analysis. A numerical simulation using Ansys ICEM is adopted to explore the feasibility and the physical significance of the proposed design cases. The quantities and the geometry of the mixed inflow turbine rotor relative to which the results of the present study may be compared are those of the turbine designed and tested at Imperial College of London. Several research works have been conducted on this mixed turbine. One might cite papers related to the team of the Laboratory of Applied Mechanics of Oran-Algeria.

2 Literature Review

Abidat et al. [1] designed and analyzed the volute of a radial and a mixed flow turbine, Litim et al. [2] studied the effect of blade number on the mixed inflow turbine performances. Maghaine et al. [3] presented the influence of volute cross-section shape on the mixed inflow turbine performances. Hamel et al [4] investigated a twin entry flow turbine volute. In papers [5-7] presented the aerodynamic performance of the mixed flow turbine blade design. Bencherif et al. [8] studied the unsteady performance of a twin-entry mixed flow turbine. Abidat [9] and Abidat et al. [10] developed a new method of blade profile generation using the Bezier polynomials. The works [11-12] include research to ensure high-quality mechanical machining of turbine blades for regular operation. Abidat et al. [13] studied the clearance effect between the rotor blades and the casing on the mixed turbine performance. In two cases, papers [14, 15] studied the effects of the cone and the inlet blade angles on mixed inflow turbine performance. The first is for a fixed outlet volute section and the second for a variable outlet volute section. Some geometric parameters were held fixed to keep the same rotor casing. Other researchers have examined this type of turbine; Rajoo et al. [16] offered a comprehensive review of mixed-flow turbines. Palfreyman et al. [17] obtained the rotor geometry of the mixed flow turbine by radially scanning the leading edge of a radial turbine. Whitfield et al. [18] established a relationship between the blade angle, the cone angle, and the camber angle. Watson et al. [19] compared the efficiency of axial, radial, and mixed turbines for different speed ratios and worked to improve the performance of the turbocharged engine with variable geometry. Pesiridis [20], Pesiridis and Martinez-Botas [21–23] modified the mechanism of actuation of sliding vanes to adapt to the nature of pulsating flow of the exhaust gas by inducing artificially sinusoidal motion. Wallace and Blair [24] reported the earliest experimental study of the irregular flow effect on mixed inflow turbine performance. Yamaguchi et al. [25] analyzed four rotors of mixed inflow turbines having different camber curves. Ketata et al. [26] studied a Mixed Flow Turbine Volute numerically Operating in Various Steady Flow Conditions. Leonard et al. [27] studied the inlet mixed inflow turbine geometry. Bernhardt Lüddecke et al. [28] compared the efficiencies of mixed and radial inflow turbines for different rotational speeds. Padzillah et al. [29] studied numerically and experimentally the flow angle effect on mixed inflow turbine performance and discovered that only one rotor blade part operates in optimal conditions.

3 Research Methodology

3.1 Initial rotor design

The rotor of the mixed inflow turbine under examination is a constant blade angle type, named type A. Since the meridian plane of the rotor represents main interest of this study, it is profitable to have its description given in Figure 1. The values of the geometrical parameters are represented in Table 1. As stated before, changes will be

made to the shroud and the hub profiles. For all the subsequent calculations, the optimum expansion ratio is adopted, which is equal to 2.91. It is retained from ABIDAT's thesis analysis [30].

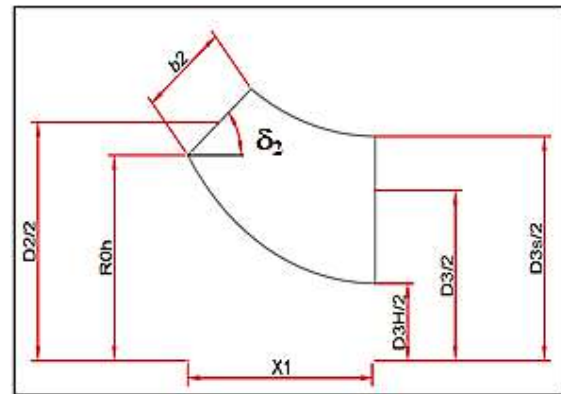


Figure 1 – The blade meridian view

Table 1 – The geometrical parameter values (mm)

b_2	D_2	R_{0h}	X_1	D_{3H}	D_3	D_{3S}	$\delta_2(^{\circ})$
17.99	83.58	36	40	27.07	59.7	78.65	40

3.2 A new design approach

The new rotor impellers under consideration are designed as follows. To lessen the degree of the meridional plane surface divergence, the first alternative is achieved by lowering the blade's eye tip diameter, which implies lowering the shroud profile as shown in Figure 2.

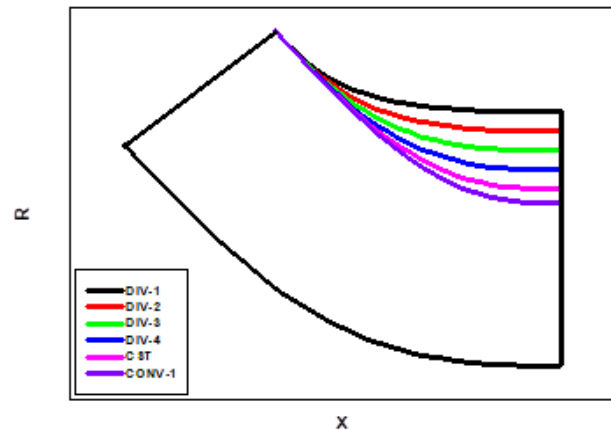


Figure 2 – Different blade meridian views for different shroud exit diameters

The second alternative would be lifting the hub profile for a higher eye root diameter as depicted in Figure 3. Finally, both shroud and hub profiles vary for a smaller exit diameter, as presented in Figure 4. The initial rotor design taken as a reference for comparison will be called: Div-1.

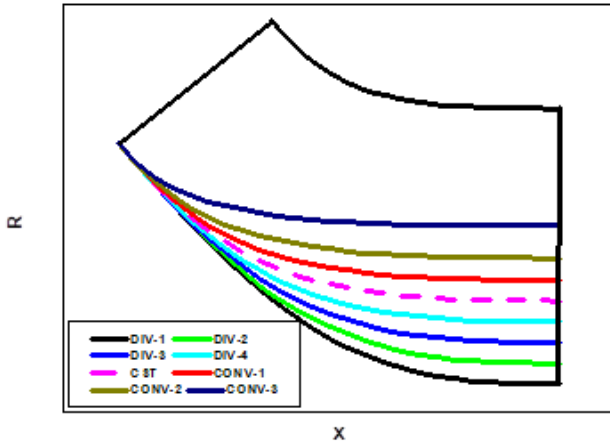


Figure 3 – Different blade meridian views for different hub exit diameters

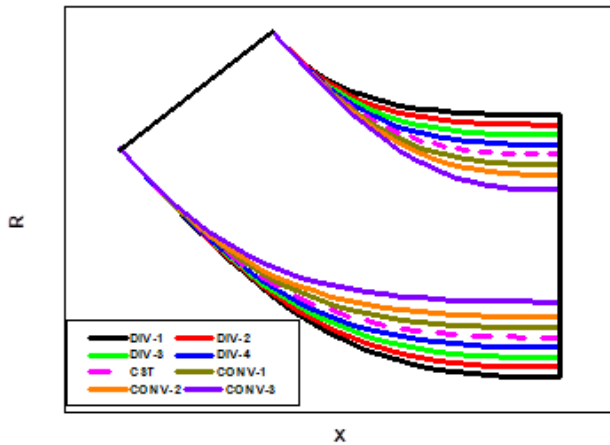


Figure 4 – Different blades meridian view by changing of hub and shroud diameters

3.3 Rotor blade profile generation

The method for designing the blade profile of the mixed turbine rotor is to use the pressure balance flow path principle by considering the faces acting on a particle fluid flow in a rotor path. The Bezier polynomial is adopted for the shape generation of the rotor under examination. The following expression gives the radius:

$$r = (1 - u)^4 r_0 + 4u(1 - u)^3 r_1 + 6u^2(1 - u)^2 r_c + 4u^3(1 - u)r_2 + u^4 r_3. \quad (1)$$

The distance in the axial direction is presented by the following equation:

$$x = (1 - u)^4 x_0 + 4u(1 - u)^3 x_1 + 6u^2(1 - u)^2 x_c + 4u^3(1 - u)x_2 + u^4 x_3. \quad (2)$$

The leading edge is obtained by the following relations:

$$\theta = \theta_{ref} + \frac{1}{\sin(\delta_2)} \int_{x_{ref}}^x \tan(\beta_{2b}) \frac{dx}{r}, \quad (3)$$

$$r = r_{0h} + (x - x_{0h}) \tan(\delta_2). \quad (4)$$

The following equations calculate the trailing edge:

$$x = (1 - u)^4 x_0 + 4u(1 - u)^3 x_1 + 6u^2(1 - u)^2 x_b + 4u^3(1 - u)x_2 + u^4 x_3, \quad (5)$$

$$\theta = (1 - u)^4 \theta_0 + 4u(1 - u)^3 \theta_1 + 6u^2(1 - u)^2 \theta_b + 4u^3(1 - u)\theta_2 + u^4 \theta_3. \quad (6)$$

The camberline blade is shown in Figure 5.

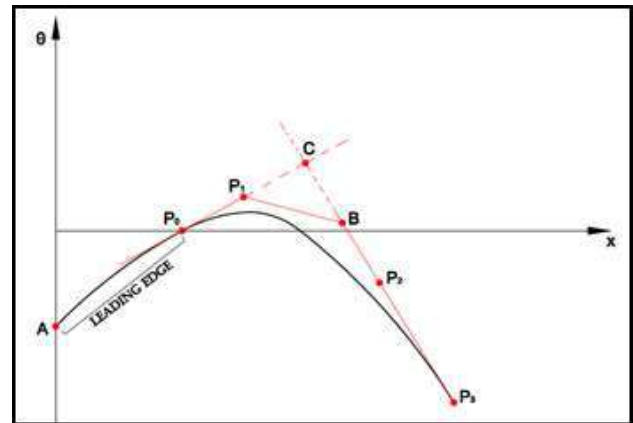


Figure 5 – The camberline blade view

The three-dimensional blade profiles are depicted in Figure 6 corresponding to the case hub held fixed; Figure 7 corresponds to the casing shroud held fixed and the last on Figure 8 corresponds to the case where both hub and shroud are varied. Each meridional plane surface is defined by the ratio of the cross-sectional area, exit over inlet sections. Depending on them through flow sectional area shape; they are called DIV for diverging, CST for constant, and CONV for converging channels.

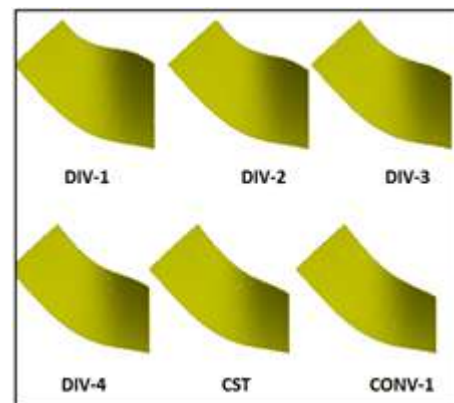


Figure 6 – Blade geometrical shape views for different shroud exit diameter

3.4 Mesh optimization and Numerical model validations

The unstructured hexahedral grid is used because it responds well with turbomachine simulations.

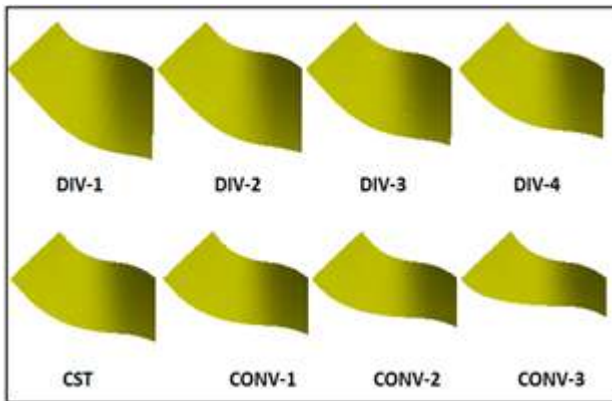


Figure 7 – Blade geometrical shape views for different hub exit diameter

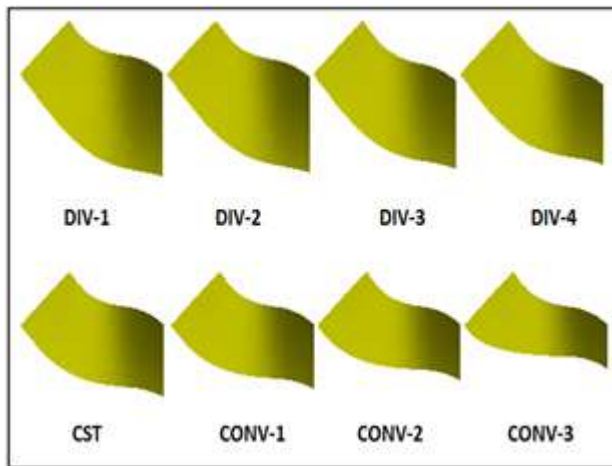


Figure 8 – Blade geometrical shape views for different hub and shroud exit diameters

Because the numerical simulation solutions are only approximations, the analysis of mesh quality and its influence on the results deserve particular attention. The numbers of mesh elements tested are 107 214, 233 814, 333 372, and 415 030. The analysis of the graphs shows that the number of elements does not have any influence on the torque and the mass flow rate (Figure 9), a negligible influence on the static pressure distribution around the rotor blade (Figure 10). On the other hand, there exists a variation in the efficiency graph. Figure 9 shows that the optimal grid number is higher or equal to 333372 elements which are applied in the numerical simulations.

The numerical validation is confirmed by the experimental works of Chen and Abidat [10] on rotor type A. The pressure ratio is defined as the total pressure at the inlet relative to the static pressure at the outlet; the distribution is in the axial direction of the blade. The results are shown in Figure 11. A good agreement between numerical simulations and experimental results is remarked.

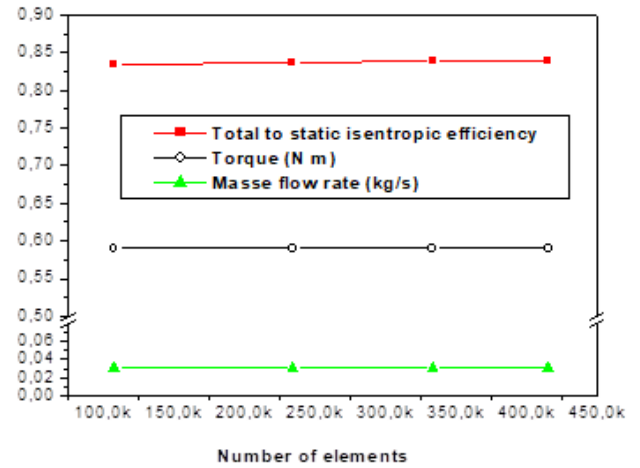


Figure 9 – Effect of element number on efficiency, torque and mass flow rate

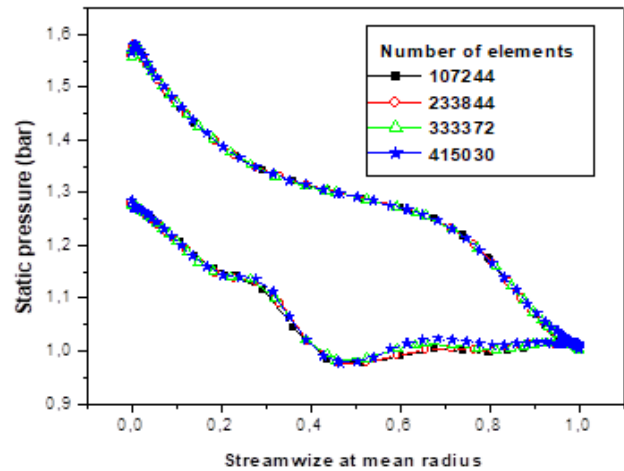


Figure 10 – Effect of element number on static pressure

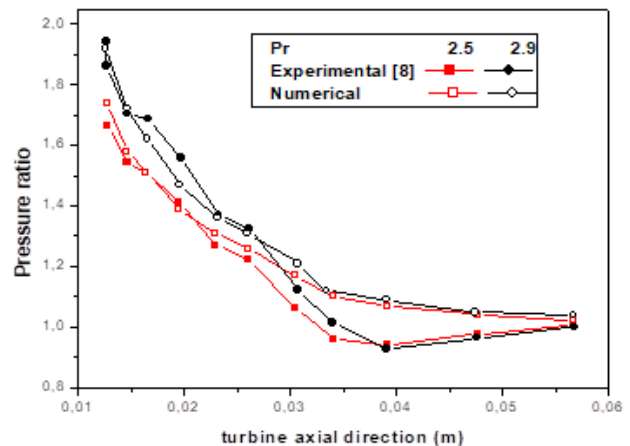


Figure 11 – Numerical result validation

4 Results and Discussion

The channel geometry of the rotor has a significant influence on the flow, on the energy transformation of the turbine. For the sake of comparison, the simulation results for the three alternatives at full rotational speed are

reported on the same diagram versus cases of channel geometries. The first alternative, which corresponds to the analysis of a blade shroud varied in profile shape keeping the hub profile unchanged, reveals relatively poor performance variables. The optimum design case remains for a diverging meridional plane surface, namely the Div-3 case for a maximum output work (Figure 12) and the Div-2 case for a maximum power developed (Figure 13).

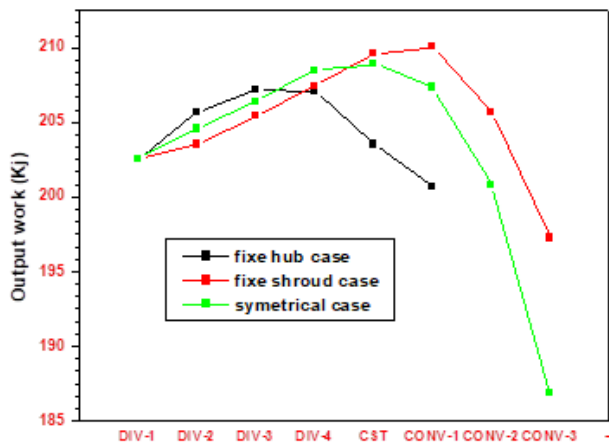


Figure 12 – Output work at 98 000 rpm for three alternatives

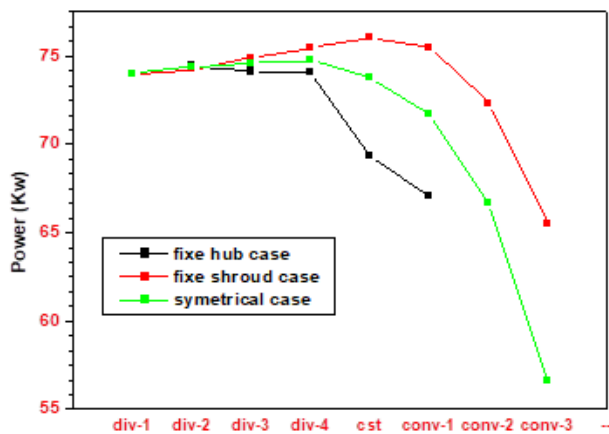


Figure 13 – Power at 98 000 rpm for three alternatives

Then, the channel convergence effect ceases to have significance in terms of beneficial gains.

This is observed by a faster fall off the mass flow rate (Figure 14), the output work (Figure 12), the power developed (Figure 13), and the efficiency (Figure 15). When keeping the shroud profile fixed and varying the hub profile, which represents the second alternative, the most efficient rotor blade profile for the best effect on the work generation is obtained. The Conv-1 case is retained for its maximum output work, but the Const case for its maximum power developed. This is probably due to the fluid deflection and compression effects by the new curvature of the meridional streamline and the vane-to-vane plane curvature. A remarkable feature is noticed,

although the flow passage is restricted from a design case to the next one for a smaller exit area, the mass flow rate remains almost invariable from the initial design case: Div-1 until the Conv-1 design case. Then it falls off as depicted in Figure 14.

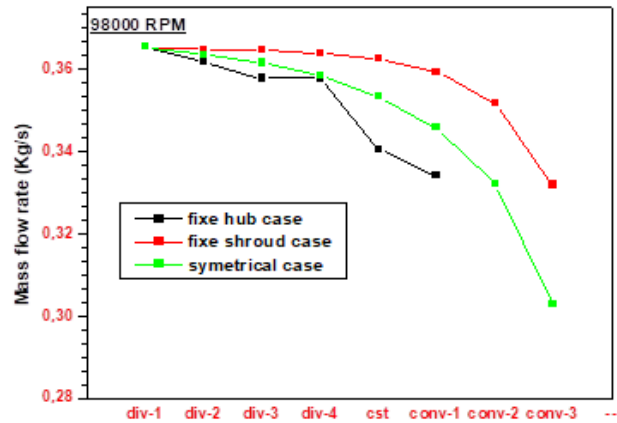


Figure 14 – Power at 98 000 rpm for three alternatives

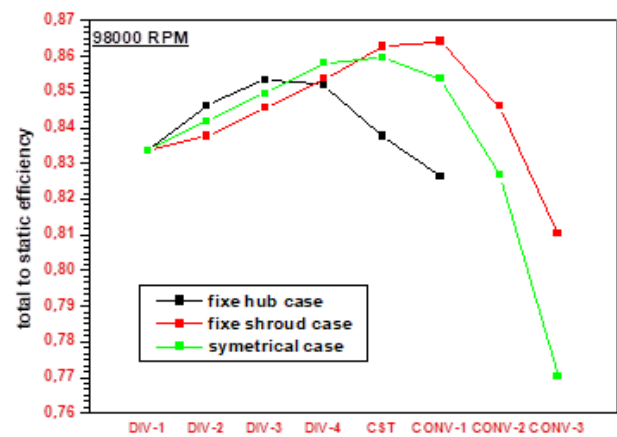


Figure 15 – Total to static efficiency for three alternatives

All the performance parameters are more significant than the two other alternatives seen in Figures 12–15. The channel aerodynamic shape is adequate for transforming the inlet available energy into shaft work. The last alternative where both hub profile and shroud profile are varied, named the symmetric case, approaches the performances of the second alternative. The Const design case shows maximum output work and the Div-4 design case for maximum power output, as reported in Figures 12–13. Based on the simulation results, the estimated gains (% increase) compared to the initial design case: Div-1, for the three alternatives, are listed in Table 2.

The decisive advantage of either a maximum power developed or a maximum efficiency (max output work) represents a compromise between two different aerodynamic blade profiles.

Table 2 – Maximum gain estimation for three alternatives

Case	Maximum gain	Geometry	Mass flow rate, %	Output work, %	Power, %	Total to static efficiency, %
Fixe hub	Power	DIV-2	-0.93	1.54	0.59	1.52
	Output work	DIV-3	-2.06	2.29	0.18	2.27
Fixe shroud	Power	CST	-0.72	3.49	2.74	3.49
	Output work	CONV-1	-1.63	3.71	2.02	3.67
Symmetrical	Power	DIV-4	-1.89	2.93	0.99	2.94
	Output work	CST	-3.27	3.13	-0.24	3.13

5 Conclusions

Several channel geometry configurations have been explored to increase the energy transformation. The interdependence of the flow parameters and the complex three-dimensionality of the machine reveals some instructive results. Effectively, the analysis based on channel argument appears suitable for specific rotor designs, which confirm improvement in the turbine performance.

Their effects on the work generation capacity are observed. We retain from the analysis. It appears that for each alternative, two facets emerge. The maximum obtained in the output work is related to the maximum efficiency for a specific optimum design case. But the maximum power developed are recorded the maximum expansion ratio and the minimum absolute kinetic energy at the rotor exit, corresponding to a different geometrical design optimum case. The same rule is noticeable for the three considered alternatives. It arises from the wall channel combinations a remarkable feature that a three-dimensional converging rotor cross-sectional area is not a necessary and sufficient condition to increase the relative kinetic energy.

Nomenclature

D_2	Mean diameter at rotor inlet
b_2	Blade height at rotor inlet
δ_2	Cone angle at rotor inlet
D_3	Exducer hub diameter
D_{3S}	Exducer tip diameter
X_1	Length of the rotor
θ	Camber angle
θ_{ref}	Reference camber angle
x_{ref}	Reference axial distance of the blade
β_{2b}	Mean blade angle at rotor inlet
R_{0h}	The radius at the tip rotor inlet.
x_{0h}	The axial distance for the initial point of the hub.
D_3	Exducer root mean square diameter
X	Axial polar variable
r	Radial polar variable
u	variable between 0 and 1

References

- Hamel, M., Hamidou, M. K., Cherif, H. T., Abidat, M., Litim, S. A. (2008). Design and flow analysis of radial and mixed flow turbine volutes. *ASME Turbo Expo*. ASME, New York. Vol. 1(PART C), pp. 2329-2333, doi: 10.1115/GT2008-50503.
- Ali, L. S., Mohammed, H., Kamel, H. M. (2017). The number of blade effects on the performance of a mixed turbine rotor. *Engineering Review*, Vol. 37(3), pp. 349-360.
- Meghaine, M. A., Hamidou, M. K., Hamel, M. (2017). Influence of the volute cross-sectional shape on mixed inflow turbine performances. *Advances in Mechanical Engineering*, Vol. 9(7), pp. 1-15, doi: 10.1177/1687814017708174.
- Hamel, M., Bencherif, M. M., Hamidou, M. K. (2017). Investigation of a twin entry mixed flow turbine volute, benefits with regard to the eco-system. *Materials Physics and Mechanics*, Vol. 32(1), pp. 31-42.
- Omar, Z. K., Mohammed, H., Kamel, H. M. (2017). Computational aerodynamic performance of mixed-flow turbine blade design. *Engineering Review*, Vol. 37(2), pp. 201-213.
- Leonard, T., Spence, S., Filsinger, D., Starke, A. (2020). Design and performance analysis of mixed flow turbine rotors with extended blade chord. *Journal of Turbomachinery*, Vol. 142(12), 121003. doi: 10.1115/1.4047894.
- Lee, S. P., Barrans, S. M., Nickson, A. K. (2021). The impact of volute aspect ratio and tilt on the performance of a mixed flow turbine. *Proceedings of the Institution of Mechanical Engineers, Part A: Journal of Power and Energy*, Vol. 235(6), pp. 1435-1450, doi: 10.1177/0957650921998228.
- Bencherif, M. M., Hamidou, M. K., Hamel, M., Abidat, M. (2016). Study of unsteady performance of a twin-entry mixed flow turbine. *Journal of Applied Mechanics and Technical Physics*, Vol. 57(2), pp. 300-307, doi: 10.1134/S0021894416020139.
- Rajeevalochanam, P., Sunkara, S. N. A., Mayandi, B., Banda, B. V. G., Chappati, V. S. K., Kumar, K. (2016). Design of highly loaded turbine stage for small gas turbine engine. *ASME Turbo Expo 2016: Turbomachinery Technical Conference and Exposition, GT 2016*. Seoul, South Korea, Vol. 2C-2016, 123972, doi: 10.1115/GT2016-56178.

10. Chen, H., Abidat, M., Baines, N. C., Firth, M. R. (1992). The effects of blade loading in radial and mixed flow turbines. *ASME 1992 International Gas Turbine and Aeroengine Congress and Exposition, GT 1992*, Cologne, Germany, Vol. 1, 111210, doi: 10.1115/92-GT-092.
11. Kononenko, S., Dobrotvorskiy, S., Basova, Y., Gasanov, M., Dobrovolska, L. (2019) Deflections and frequency analysis in the milling of thin-walled parts with variable low stiffness. *Acta Polytechnica*, Vol. 59(3), pp. 283-291, doi: 10.14311/AP.2019.59.0283.
12. Dobrotvorskiy, S., Kononenko, S., Basova, Y., Dobrovolska, L., Edl, M. (2021). Development of optimum thin-walled parts milling parameters calculation technique. *4th International Conference on Design, Simulation, Manufacturing: The Innovation Exchange, DSMIE 2021*, Lviv, Ukraine, Vol.2021, pp. 343-352, doi: 10.1007/978-3-030-77719-7_34.
13. Abidat, M., Hamidou, M. K., Hachemi, M., Hamel, M., Litim, S. A. (2008). Performance prediction of a mixed flow turbine. *Mecanique et Industries*, Vol. 9(1), pp. 71-79, doi: 10.1051/meca:2008009.
14. Chelabi, M. A., Hamidou, M. K., Hamel, M. (2017). Effects of cone angle and inlet blade angle on mixed inflow turbine performances. *Periodica Polytechnica Mechanical Engineering*, Vol. 61(3), pp. 225-233, doi: 10.3311/PPme.9890.
15. Lee, S. P., Jupp, M. L., Barrans, S. M., Nickson, A. K. (2019). Analysis of leading edge flow characteristics in a mixed flow turbine under pulsating flows. *Proceedings of the Institution of Mechanical Engineers, Part A: Journal of Power and Energy*, Vol. 233(1), pp. 78-95, doi: 10.1177/0957650918778661.
16. Rajoo, S., Martinez-Botas, R. (2008). Mixed flow turbine research: A review. *Journal of Turbomachinery*, Vol. 130(4), 044001, doi: 10.1115/1.2812326.
17. Palfreyman, D., Martinez-Botas, R.F. (2002). Numerical study of the internal flow field characteristics in mixed flow turbines. *American Society of Mechanical Engineers, International Gas Turbine Institute, Turbo Expo (Publication) IGTI*, Vol. 5(A), pp. 455-472, doi: 10.1115/GT2002-30372.
18. Whitfield, A., Baines, N.C. (1990). *Design of radial turbomachines* (1st ed.). Harlow, Essex, England: Longman Scientific and Technical, Wiley, New York, USA.
19. Watson, N., Janota, M. S. (1982). *Turbocharging the Internal Combustion Engine* (1st ed.). Palgrave, Kent. doi: 10.1007/978-1-349-04024-7.
20. Pesiridis, A. (2007). *Turbocharger Turbine Unsteady Aerodynamics with Active Control*. PhD Thesis, Imperial College, London, UK.
21. Pesiridis, A., Martinez-Botas, R. F. (2007). Experimental evaluation of active flow control mixed-flow turbine for automotive turbocharger application. *Journal of Turbomachinery*, Vol. 129(1), pp. 44-52, doi: 10.1115/1.2372778.
22. Pesiridis, A., Martinez-Botas, R. F. (2006). Active control turbocharger for automotive application: An experimental evaluation. *Conference: 8th International Conference on Turbocharging and Turbochargers*, CRC Press, London, pp. 223-232, doi: 10.1016/B978-1-84569-174-5.50020-8.
23. Pesiridis, A., Martinez-Botas, R. F. (2005). Experimental evaluation of active flow control mixed-flow turbine for automotive turbocharger application. *ASME Turbo Expo 2005 - Gas Turbine Technology: Focus for the Future*, Reno-Tahoe, Nevada, USA, Vol. 6(B), GT2005-68830, pp. 881-895, doi: 10.1115/GT2005-68830.
24. Wallace, F. J., Blair, G. P. (1965). The pulsating-flow performance of inward radial-flow turbines. *ASME 1965 Gas Turbine Conference and Products Show*, Vol. 1-A, 113390, doi: 10.1115/65-GTP-21.
25. Yamaguchi, H., Nishiyama, T., Horiai, K., Kasuya, T. (1984). High performance Komatsu KTR150 turbocharger. *SAE*, 840019, doi: 10.4271/840019.
26. Ketata, A., Driss, Z. (2017). Numerical study of a vanned mixed flow turbine operating in various steady flow conditions. *International Journal of Mechanics and Applications*, Vol.7(1), pp. 24-30, doi: 10.5923/j.mechanics.20170701.03.
27. Leonard, T., Spence, S., Early, J., Filsinger, D. (2013). Numerical study of a vanned mixed flow turbine operating in various steady flow conditions. *6th International Conference on Pumps and Fans with Compressors and Wind Turbines, ICPF 2013*, Beijing, China, 52(TOPIC 4), 042012, doi: 10.1088/1757-899X/52/4/042012.
28. Luddecke, B., Filsinger, D., Ehrhard, J. (2012). On mixed flow turbines for automotive turbocharger applications. *International Journal of Rotating Machinery*, Vol. 2012, 589720, doi: 10.1155/2012/589720.
29. Padzillah, M. H., Rajoo, S., Martinez-Botas, R. F. (2015). Experimental and numerical investigation on flow angle characteristics of an automotive mixed flow turbocharger turbine. *Jurnal Teknologi*, Vol. 77(8), pp. 7-12, doi: 10.11113/jt.v77.6148.
30. Abidat, M., Chen, H., Baines, N. C., Firth, M. R. (1992). Design of a highly loaded mixed flow turbine. *Proceedings of the Institution of Mechanical Engineers, Part A: Journal of Power and Energy*, Vol. 206(2), pp. 95-107, doi: 10.1243/PIME_PROC_1992_206_016_02.



Verbovyi A., Khomenko V., Neamtu C., Pavlenko V., Cherednyk M., Vashyst B., Pavlenko I. (2021). Parameter identification of nonlinear bearing stiffness for turbopump units of liquid rocket engines considering initial gaps and axial preloading. *Journal of Engineering Sciences*, Vol. 8(2), pp. D8-D11, doi: 10.21272/jes.2021.8(2).d2

Parameter Identification of Nonlinear Bearing Stiffness for Turbopump Units of Liquid Rocket Engines Considering Initial Gaps and Axial Preloading

Verbovyi A.¹[0000-0002-7805-4733], Khomenko V.¹, Neamtu C.²[0000-0003-0899-0451], Pavlenko V.¹, Cherednyk M.¹, Vashyst B.¹, Pavlenko I.¹[0000-0002-6136-1040]

¹ Sumy State University, 2 Rymaskogo-Korsakova St., 40007 Sumy, Ukraine;

² Technical University of Cluj-Napoca, 28 Memorandumului St., 400114 Cluj-Napoca, Romania

Article info:

Submitted:

August 12, 2021

Accepted for publication:

December 3, 2021

Available online:

December 9, 2021

*Corresponding email:

a.verbovoy@omdm.sumdu.edu.ua

Abstract. This article is devoted to developing a mathematical model of nonlinear bearing supports for turbopump units of liquid rocket engines considering initial gaps and axial preloading. In addition to the radial stiffness of the bearing support, this model also considers the stiffness of the bearing cage, the rotational speed of the rotor, axial preloading of the rotor (due to which the inner cage shifts relative to the outer, changing the radial stiffness of the support), as well as radial gaps between contact elements of the bearings. This model makes it possible to calculate the stiffness of the bearing supports more accurately. The proposed model is realized using both the linear regression procedure and artificial neural networks. The model's reliability is substantiated by the relatively small discrepancy of the obtained evaluation results with the experimental data. As a result, this model will allow determining the critical frequencies of the rotor with greater accuracy. The results have been implemented within the experience of designing turbopump units for State Company "Yuzhnoye Design Office".

Keywords: bearing support, axial force, radial gap, regression analysis, artificial neural networks.

1 Introduction

One of the reasons for the deterioration of the vibration reliability of pumping units is increased vibrations due to the entry of the machine into resonance, which in turn arises mainly from the coincidence of the operating speed of the rotor with its eigenfrequency.

The radial stiffness of the bearing supports directly affects the natural frequencies of the rotor. At the same time, the bearing housings in which the clips lie have their own stiffness. Thus, the rotor support is a system of two consecutive stiffnesses.

In addition, the stiffness of the bearing is affected by the degree of axial compression of the rotor and the frequency of its rotation, as well as the gap between contact parts.

Therefore, the purpose of this work is to develop an approach for determining the equivalent stiffness of bearing supports considering initial gaps and axial preloading.

For achieving this aim, the following objectives have been formulated. Firstly, a mathematical model of

nonlinear bearing stiffness should be proposed considering axial preloading and radial gaps in contact parts.

Secondly, the regression dependencies for the identification of unknown coefficients should be achieved.

Finally, the proposed approach should be substantiated by comparison with the experimental data.

2 Literature Review

To ensure the vibration reliability of the turbopump rotor, it is necessary to turn to the already existing scientific publications devoted to studying individual influences on the dynamics of the rotor of any of the previously mentioned factors.

Particularly, Sharma et al. [1] presented a review of different models in the analysis of the nonlinear behavior of rotor systems. Xu et al. [2] made an overview of bearings for the next generation of reusable liquid rocket turbopumps.

Bai et al. [3] studied the impact of flexible support stiffness on rotor systems' dynamic characteristics and stability. Xu et al. [4] investigated the impact of bearing

stiffness on the nonlinear dynamics of shafts in drive systems.

Du and Liang [5] evaluated the dynamic performance of hydrostatic bearings. As a result, a better understanding of the performance of water-lubricated hydrostatic bearings was provided. Cao [6] carried out a transient analysis of flexible rotors with nonlinear bearings.

Study [7] describes rotor dynamics of the rotation of moving parts and the compliance of bearing support elements. This article also describes an approach to studying nonlinear reactions in rotor supports. The design model of the rotating rotor considers the rotation of the shaft, which manifests itself in the form of centrifugal inertia forces acting on the inner cage of the rolling bearing. After numerical simulation in ANSYS, diagrams of the dependence of the movements of the inner cage on the force applied to it in the radial direction were constructed from the calculated points. Thus, the authors of this article propose a more advanced method for determining the nonlinear stiffness characteristics of bearing supports.

In the article [8], using the example of the oxidizer rotor of a liquid rocket engine, it is shown how to consider the gaps in the rolling bearing, as well as the axial compression of the shaft when modeling the dynamics of the rotor, which directly affects the rigidity of rolling bearings due to the displacement of the inner cage relative to the outer one. The simulation was carried out using the multi-purpose ANSYS software package. In work, contact spots were obtained between the rolling elements, the contact angle was determined. The authors propose nonlinear stiffness as the tangent of the angle of inclination of the curve diagram of the relationship between radial load and radial displacement. Thus, the “radial load – radial displacement” graph was constructed according to the calculated points because of numerical simulation. Also, because of approximation, analytical expressions describing this dependence were determined.

The article [9] is devoted to a general approach to the use of neural networks to determine the parameters that affect the dynamics of the rotor. The neural networks described by the authors allow us to consider the nonlinear regression dependences of the stiffness of radial bearings on the speed of rotation of the rotor. Thus, it was possible to develop algorithms for identifying the stiffness of bearings based on previously known critical frequencies of the system.

The work described in the article [10] is devoted to considering such factors as the nonlinear weakening of the support during operation and the nonlinearity of the stiffness of the support.

Finally, numerical methods for calculating the stiffness of elements of arbitrary shape are described in [11, 12].

Overall, the described approaches to the calculation process in this article allow for modal analysis of the system, harmonic, and allow for virtual balancing without the need to have a significant time to prepare the source data and allow you to significantly reduce the machine time of the account, having an insignificant loss an accuracy. Nevertheless, a comprehensive approach to determining

the equivalent stiffness of bearing supports should be developed to eliminate recent publications’ advantages.

3 Research Methodology

3.1 A regression model of the bearing stiffness

Considering an experience of designing turbopump units ordered by the State Company “Yuzhnoye Design Office” (Dnipro, Ukraine), the equivalent bearing stiffness can be described by the following dependence:

$$c(\omega, r, F_a) = c_0 + \alpha\omega^2 + \beta r + \gamma F_a, \quad (1)$$

where c_0 – initial stiffness, N/m; ω – rotational speed, rad/s; r – radial displacement of a rotor, m; F_a – axial preloading of a rotor, N; α , β , γ – unknown coefficients, $N \cdot s^2/m$, N/m^2 , and m^{-1} , respectively.

The corresponding design scheme is presented in Figure 1.

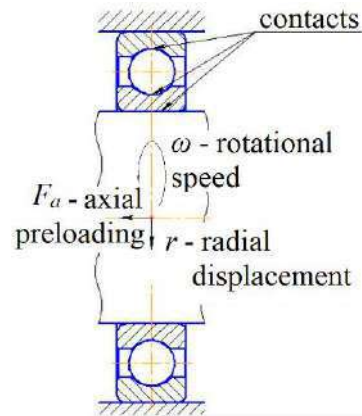


Figure 1 – The design scheme of the bearing support

This nonlinear model significantly improves the quasilinear model proposed previously in [8]. Its identification is now based on evaluating unknown parameters α , β , and γ .

For finding these coefficients, they can be presented as independent variables of the following error function $R(\alpha, \beta, \gamma)$, compiled according to the least-squares method:

$$R(\alpha, \beta, \gamma) = \sum_{i=1}^n (c_0 + \alpha\omega_i^2 + \beta r_i + \gamma F_{ai} - c_i)^2, \quad (2)$$

where i – a current number of experimental points; n – the total number of experimental points.

The value of this error function should be minimal ($R \rightarrow \min$). In this case, the following conditions can be written:

$$\begin{cases} \frac{\partial R}{\partial \alpha} = 2 \sum_{i=1}^n (c_0 + \alpha\omega_i^2 + \beta r_i + \gamma F_{ai} - c_i)\omega_i^2 = 0; \\ \frac{\partial R}{\partial \beta} = 2 \sum_{i=1}^n (c_0 + \alpha\omega_i^2 + \beta r_i + \gamma F_{ai} - c_i)r_i = 0; \\ \frac{\partial R}{\partial \gamma} = 2 \sum_{i=1}^n (c_0 + \alpha\omega_i^2 + \beta r_i + \gamma F_{ai} - c_i)F_{ai} = 0, \end{cases} \quad (3)$$

that can be reduced to the following linear equation:

$$[K]\{A\} = \{C\}, \quad (4)$$

where $[K]$ – symmetrical quadratic 3×3 matrix; $\{C\}$ – 3×1 column-vector; $\{A\} = \{\alpha, \beta, \gamma\}^T$ – 3×1 column-vector of evaluated parameters.

Elements of quadratic matrix $[K]$ and column-vector $\{C\}$ take the following forms:

$$\begin{aligned} K_{11} &= \sum_{i=1}^n \omega_i^4; K_{12} = K_{21} = \sum_{i=1}^n \omega_i^2 r_i; \\ K_{13} &= K_{31} = \sum_{i=1}^n \omega_i^2 F_{ai}; K_{22} = \sum_{i=1}^n r_i^2; \\ K_{23} &= K_{32} = \sum_{i=1}^n r_i F_{ai}; K_{33} = \sum_{i=1}^n F_{ai}^2; \end{aligned} \quad (5)$$

$$\begin{aligned} C_1 &= \sum_{i=1}^n (c_i - c_0) \omega_i^2; C_2 = \sum_{i=1}^n (c_i - c_0) r_i; \\ C_3 &= \sum_{i=1}^n (c_i - c_0) F_{ai}. \end{aligned} \quad (6)$$

Based on the transverse matrix approach, the column-vector of the evaluated parameters is determined as follows:

$$\{A\} = [K]^{-1} \{C\}. \quad (7)$$

Then, after determining the obtained coefficients α , β , and γ and substituting them into expression (1), and analytical dependence of the equivalent stiffness can be obtained considering the rotational speed of the rotor, radial gaps in the bearing support, and axial preloading.

3.2 The use of artificial neural networks

The above-described algorithm for determining equivalent stiffness assumes the linear bearing stiffness model. However, artificial neural networks can be applied if a linear mathematical model is not suitable (especially if there are more factors affecting the equivalent stiffness). The corresponding comprehensive approach for such modeling is presented in [9].

Particularly, for the considered case study, an artificial neural network architecture is presented in Figure 2.

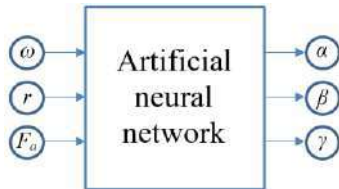


Figure 2 – An architecture of the artificial neural network

4 Results and Discussion

The design scheme of the rotor of the oxidizer turbopump of the liquid rotor engine is presented in Figure 3 [7].

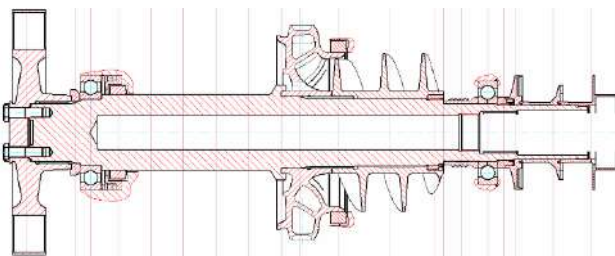


Figure 3 – An architecture of the artificial neural network

For this case study, the experimental results data is presented in Table 1 for bearings of types 45-216 and 45-276214.

Table 1 – Experimental data for different types of bearings

i	ω_i , rad/s	r_i , 10^{-6} m	F_{ai} , 10^3 N	Bearing stiffness, 10^8 N/m	
				45-216	45-276214
1	0	0	0	1.88	2.10
2	1100			1.90	2.10
3	1963			1.93	2.12
4	2215			1.94	2.13
5	0	95	4	2.02	2.25
6	1100			2.04	2.26
7	1963			2.07	2.27
8	2215			2.08	2.27

As a result of numerical calculation, the following values for elements of quadratic matrix (5) have been obtained:

$$K_{11} = 8.077 \cdot 10^{13}; K_{12} = K_{21} = 9.471 \cdot 10^2;$$

$$K_{13} = K_{31} = 3.988 \cdot 10^{10}; K_{22} = 3.610 \cdot 10^{-8};$$

$$K_{23} = K_{32} = 1.520; K_{33} = 6.400 \cdot 10^7.$$

Additionally, for the bearing 45-216, the column-vector (6) is as follows:

$$C_1 = 2.418 \cdot 10^{14}; C_2 = 6.555 \cdot 10^3; C_3 = 2.760 \cdot 10^3,$$

and for the bearing 45-276214:

$$C_1 = 1.931 \cdot 10^{14}; C_2 = 6.080 \cdot 10^3; C_3 = 2.560 \cdot 10^3.$$

After considering the regression dependence (7), the unknown parameters α , β , and γ have been evaluated and summarized in Table 2.

Table 2 – The evaluated parameters

Bearing	α , $N \cdot s^2/m$	β , N/m^2	γ , m^{-1}	Maximum error, %
45-216	0.72	$1.37 \cdot 10^{11}$	4100	7.0
45-276214	0.05	$1.37 \cdot 10^{11}$	0	1.8

Comparison of the data presented in Table 1 with the proposed mathematical model (1) for the data presented in Table 2 substantiates the reliability of the proposed approach. Particularly, the relative error of the parameter identification does not exceed 7 % for the bearing 56-216 and 2 % for the bearing 45-276214.

5 Conclusions

In this article, the analysis of existing studies on the influence of various factors on the equivalent stiffness of rolling bearings and various methods of considering these factors when developing a reliable mathematical model was carried out.

Based on these studies, an algorithm for evaluating the equivalent stiffness has been developed. The proposed model considers the impact of the rotational speed of the shaft, radial gaps, and axial preloading of the shaft.

The reliability of the proposed method is proved by the fact that the relative error of the parameter identification

does not exceed 7 % for the bearing 56-216 and 2 % for the bearing 45-276214.

In the case of large nonlinearities (e.g., for the bearing 56-216), a different approach based on artificial neural networks has allowed developing a reliable mathematical model considering other factors affecting the equivalent stiffness of the bearing support instead of determining the coefficients of influence.

6 Acknowledgments

The central part of the results has been obtained within the project “Fulfillment of tasks of the perspective plan of development of a scientific direction “Technical sciences” Sumy State University” funded by the Ministry of Education and Science of Ukraine (State reg. no. 0121U112684).

The research was partially supported by the Research and Educational Center for Industrial Engineering (Sumy State University) and International Association for Technological Development and Innovations.

References

1. Sharma, A., Upadhyay, N., Kankar, P. K., Amarnath, M. (2018). Nonlinear dynamic investigations on rolling element bearings: A review. *Advances in Mechanical Engineering*, Vol. 10(3), doi:10.1177/1687814018764148.
2. Xu, J., Li, C., Miao, X., Zhang, C., Yuan, X. (2020). An overview of bearing candidates for the next generation of reusable liquid rocket turbopumps. *Chinese Journal of Mechanical Engineering*, Vol. 33(1), 26, doi: 10.1186/s10033-020-00442-6.
3. Bai, C., Xu, Q., Wang, J. (2011). Effects of flexible support stiffness on the nonlinear dynamic characteristics and stability of a turbopump rotor system. *Nonlinear Dynamics*, Vol. 64(3), pp. 237-252, doi: 10.1007/s11071-010-9858-4.
4. Xu, J., Lei, W., Luo, W. (2016). Influence of bearing stiffness on the nonlinear dynamics of a shaft-final drive system. *Shock and Vibration*, Vol. 2016, 3524609, doi: 10.1155/2016/3524609.
5. Du, J., Liang, G. (2020). Dynamic coefficients and stability analysis of a water-lubricated hydrostatic bearing by solving the uncoupled Reynolds equation. *Chinese Journal of Aeronautics*, Vol. 33(8), pp. 2110-2122, doi: 10.1016/j.cja.2019.09.030.
6. Cao, J. (2012). *Transient Analysis of Flexible Rotors with Nonlinear Bearings, Dampers and External Forces*. Ph.D. Thesis in Mechanical and Aerospace Engineering. University of Virginia, Charlottesville, VA, USA.
7. Pavlenko I., Simonovskiy V., Pitel J., Demianenko M., Verbovyi A. (2018). Investigation of non-linear reactions in rotors' bearing supports of turbo-pump units for liquid rocket engines. *Journal of Engineering Sciences*, Vol. 5(1), pp. D6-D14., doi: 10.21272/jes.2018.5(1).d2.
8. Pavlenko I., Demyanenko M., Edl M., Simonovskiy V., Pitel J., Pavlenko V., Verbovyi A. (2018). Comprehensive approach for identification of nonlinear stiffness characteristics of bearing supports for the oxidizer turbopump of the liquid rocket engine. *Journal of Engineering Sciences*, Vol. 5(2), pp. D6-D14.
9. Pavlenko, I., Neamtu, C., Verbovyi, A., Pitel, J., Ivanov, V., Pop, G. (2019) Using computer modeling and artificial neural networks for ensuring the vibration reliability of rotors. *2nd International Workshop on Computer Modeling and Intelligent Systems. CMIS 2019. CEUR Workshop Proceedings*, Vol. 2353, pp. 702-716, <http://ceur-ws.org/Vol-2353/paper56.pdf>.
10. Zhang, H., Lu, K., Zhang, W., Fu, C. (2022). Investigation on dynamic behaviors of rotor system with looseness and nonlinear supporting. *Mechanical Systems and Signal Processing*, Vol. 166, 108400, doi: 10.1016/j.ymsp.2021.108400.
11. Gorodetsky, O. S., Barabash, M. S., Filonenko, Y. B. (2019). Numerical methods for determining stiffness properties of a bar cross-section. *Cybernetics and Systems Analysis*, Vol. 55(2), pp. 329-335, doi: 10.1007/s10559-019-00138-3.
12. Ding, F., Wang, Z., Qin, F. (2015). Two kinds of neural network fusion of aero-engine rotor vibration signal fault diagnosis. *4th International Conference on Mechatronics, Materials, Chemistry and Computer Engineering, Atlantis Press, Springer Nature*, doi: 10.2991/icmmce-15.2015.295.



Onysko O., Karabegović I., Dašić P., Penderetskyi M., Melnyk O. (2021). The stress state of compact mechatronic satellites of a cycloidal reducer. *Journal of Engineering Sciences*, Vol. 8(2), pp. D12-D17, doi: 10.21272/jes.2021.8(2).d3

The Stress State of Compact Mechatronic Satellites of a Cycloidal Reducer

Onysko O.^{1*}[0000-0002-6543-9554], Karabegović I.²[0000-0001-9440-4441], Dašić P.^{3,4}[0000-0002-9242-274X], Penderetskyi M.¹, Melnyk O.¹

¹ Ivano-Frankivsk National Technical University of Oil and Gas, 15, Karpatska St., 76000 Ivano-Frankivsk, Ukraine;

² Academy of Sciences and Arts of Bosnia and Herzegovina, 7, Bistrik St., 71000 Sarajevo, Bosnia and Herzegovina;

³ SaTCIP Publisher Ltd., 36210 Vrnjačka Banja, Serbia;

⁴ Faculty of Information Technology and Engineering (FITI), 11070 Novi Beograd, Serbia

Article info:

Submitted:

September 3, 2021

Accepted for publication:

December 6, 2021

Available online:

December 11, 2021

*Corresponding email:

onysko.oleg@gmail.com

Abstract. One of the urgent problems of mechanics is to design a lightweight, compact and precise reducer with high efficiency since it is an essential part of the robot actuators. The manufacture of modern toy robots made as Pet-models requires highly efficient and very compact drives. A topical part of the drive is the cycloidal reducer required to provide the torque appropriate for the effective movement of the toy. The article proposes a three-dimensional model of a cycloidal reducer designed for a four-legged walking robot toy. The outer diameter of the reducer is 56 mm. If its most significant parts are plastic, the weight does not exceed more than 0.2 kg. The obtained results of the analysis of stresses arising between the disk and the rollers indicate the complete suitability of the selected materials of polyamide and steel on their mechanical characteristics for use in the reducer of the robot actuator.

Keywords: slow speed shaft roller, cycloidal disk, bearing, finite end method.

1 Introduction

Nowadays, legged robots are becoming very popular among different groups of modern human society. They belong to one of these groups, and a pet simulated robot can be trendy shortly. Most of the natural pets are small: dogs and cats. But they are brisk, so the pet simulated robots must be prompt too. Therefore, robotics engineering deals with those types of toys and has to solve many problems of strength materials and compact and lightweight actuators for ones. One of the complex problems is to design an ultra-lightweight and high-efficiency compact cycloidal reducer.

2 Literature Review

The cycloidal planetary transmissions are widely used in mechanical efficiency automatic wheels and multi-legged platforms [1].

The article [2] describes a humanoid robotics platform and describes the design criteria, hardware, software framework, and experimental testing of the platform. But it does not offer the reducer design.

The paper [3] shows the general trends in the engines of humanoid robots, which of course, involve the use of structures of light drives.

In [4], authors developed a highly efficient compact cycloidal gearbox for legged robots, which uses needle roller bearings in all parts where there is contact during the power transfer process inside the gearbox, which significantly improves efficiency compared to a cycloidal gearbox using free rollers. The paper proposes the sub-carrier structure that distributes the load and allows the cycloidal gear to respond reliably to shocks that may occur while the robot is moving on its feet. But it weighs 766 g, so it can be used for legged robots but not for little pet-robot.

The paper [5] investigated the CBR is a one-stage reducer with a compact structure and a wide range of installation size. But it includes only CBR bearings.

Moreover, a number of scientific works are devoted to the problem of designing mechatronic satellites [6–9] and cycloidal reducers [10–12].

Therefore, it is relevant to design an ultra-lightweight and compact cycloidal reducer.

3 Research Methodology

3.1 Designs of electrical motor and cycloidal reducer

The cycloidal reducers have a high reduction ratio, high efficiency, high stiffness, and compact size compared to conventional reduction gears, so they are attractive candidates for tight spaces and precise applications such as small pet simulated four-legged robots. Therefore, it is essential to design a device consisting of a modern mini brushless direct current electrical motor and very short sizes stage single-reducer available to operate together with the output motor shaft (Figure 1).

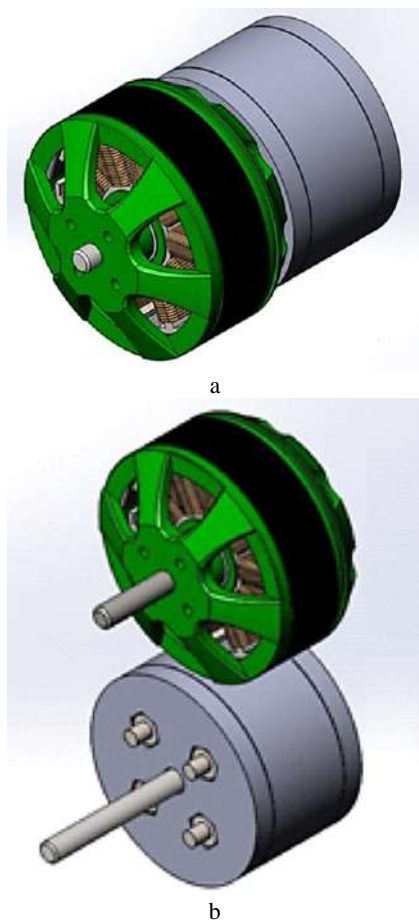


Figure 1 – Assembly of the BLDC electrical motor (a) and the cycloidal reducer (b)

Motor Multistar Elite 3508-268 KV Multirotor is usable for realizing it. Their weight is 78.6 g, the diameter is 41.8 mm, and the shaft diameter is 4.0 mm.

3.2 Usual cycloidal reducer

Figure 2 shows the development environment system information (SolidWorks) about the cycloidal disk designed by the authors.

On the diagram (Figure 2) and the reducer exploded view (Figure 3), numbers indicate the following parts: 1 –

brushless DC electric motor; 2, 9 – carriers; 3, 11 – output bearings; 4, 14 – cycloidal disk bearings; 5, 15 – cycloidal disks; 6 – input shaft (crank or eccentric shaft); 7, 17 – crank bearings; 8 – bolts; 10 – slow speed shaft rollers (four pieces); 12 – internal pins wheel (output slow speed shaft); 13, 16 – bushings; 18 – four nuts (for screws and motor-reducer connecting).

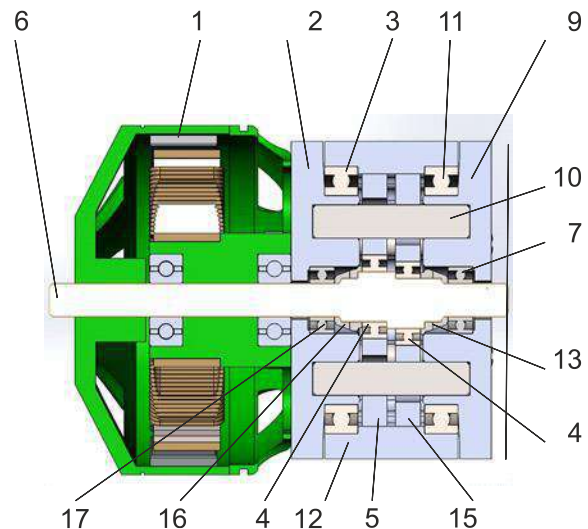


Figure 2 – Assembly axial-section sketch of the BLDC electrical motor and cycloidal reducer developed

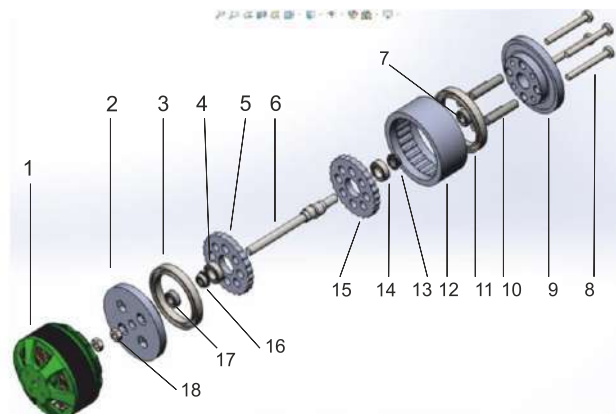


Figure 3 – Exploded view of the usual cycloidal reducer

Detailed development every of ones permit to receive their small sizes and compact assembly of reducer model design as a result.

The assembly allows putting the final design of the compact device. The essential data determined by this are the major diameter, length, and weight of the reducer. The model includes two equal cycloidal disks: parts 5 and 15, because it minimizes the vibration and improves the gear's wear resistance (Figure 3).

3.3 Minimized cycloidal reducer

Figure 4 shows the development environment system information (SolidWorks) about cycloidal disk major diameter of 32 mm.

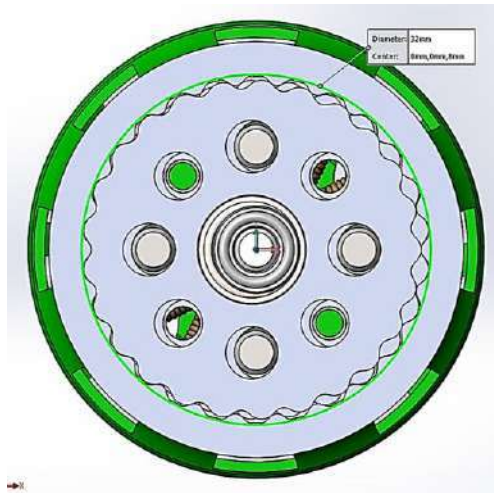


Figure 4 – Assembly cross-section sketch of the compact cycloidal reducer developed by authors

One of the essential dimensions of the reducer is the outer diameter of 38 mm (Figure 5).

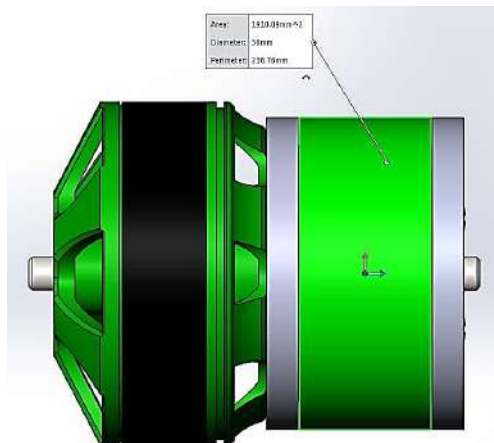


Figure 5 – Assembly drawing plan of the BLDC electrical motor and very compact cycloidal reducer developed by authors

This cycloidal reducer model predicts that the weight will not exceed 350 g if the device is made of steel parts and not more than 120 g if its biggest parts are made of plastic.

3.4 High-efficiency compact cycloidal reducer for a pet robot

It is essential to consider this value to calculate the number of cycloidal teeth and slow-speed shaft rollers.

This compact reducer includes more shaft rollers than before. There are ten rollers in its design (Figure 7). Therefore, the cycloidal disks include ten holes (Figures 7, 8).

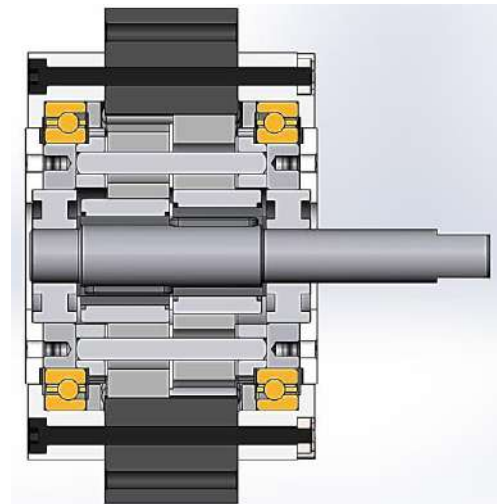


Figure 6 – View of assembly cross-section sketch of the high-efficiency compact cycloidal reducer developed by authors

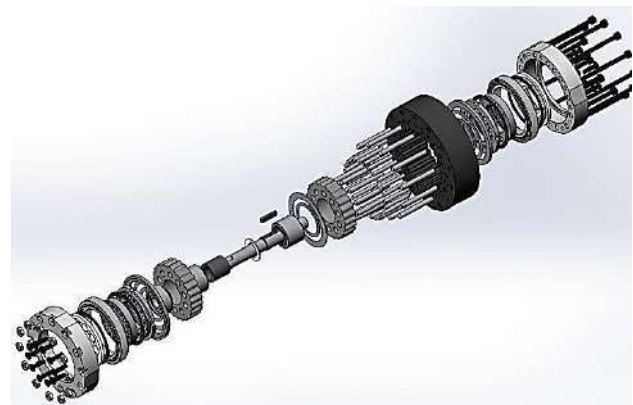


Figure 7 – Exploded view of the high-efficiency very compact cycloidal reducer developed by authors

Parameters of a reducer consider elements intended for fastening a reducer to a robot frame (Table 1).

Table 1 – Reducer parameters

Parameter	Value	Dimension
Mass	189.5	g
Diameter	56	mm
Length	41	mm
Ratio	26	–

The input shaft of the reducer is made from steel. One of the essential reducers is cycloidal disks made from plastic and slow-speed shaft rollers made from steel. Therefore, it is necessary to research the interaction between them. So the aim of the study is to receive the analysis of the stress state in a contact zone between cycloidal disks and slow-speed shaft rollers (Figure 8).

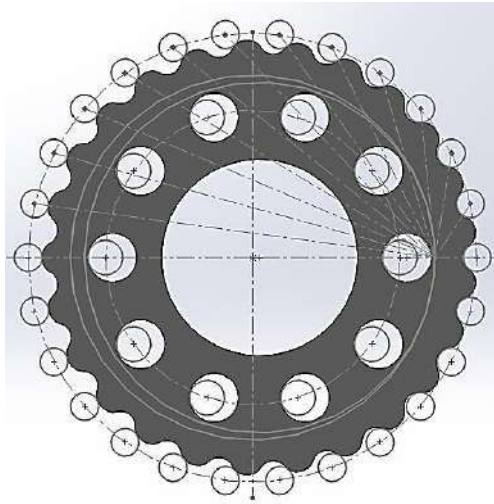


Figure 8 – Schema of interaction between cycloidal disk and slow speed shaft rollers

3.5 Computational model

Since the forces acting on the cycloid disk have a complex configuration, it is necessary to use the finite element method to determine the stresses in this part.

The stress in rollers is also easier to determine with this method due to the static uncertainty of the ones.

To speed up the calculations, simplification of the model is needed. For this reason, holes, chamfers and fillets that do not affect the result were removed. Bearings and rigid clamps were replaced with the appropriate restrictions.

Figure 9 with green arrows shows the rigid clamp, which replaced the press-fit in the carrier. The blue cones show the surfaces to which the bearing restriction has been applied.

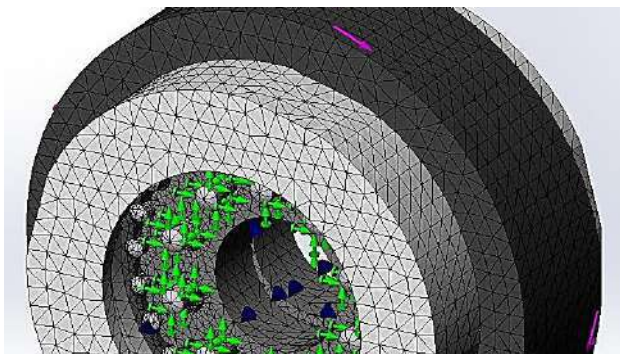


Figure 9 – applied FEM to reducer assembly

To increase the accuracy of the result, grid control was used by selecting the surfaces on which the stresses are to be determined and setting the dimensions of the grid elements on them, the sides of which are 0.5 mm. For the rest of the parts, a grid was used, the dimensions of which depend on the curvature of the surfaces with the largest elements, the dimensions of the sides of which are 2 mm.

The total number of nodes is $3.1 \cdot 10^5$. The number of elements is $2.0 \cdot 10^5$. The number of Jacobian points is 4. Solver – FFEPlus.

The contact “node to the surface” is used for the parts between which the engagement occurs. This is because the contact between the cycloid disk and the rollers looks like a line. This type of contact is better suited for such part engagement (Figure 10).



Figure 10 – Cycloid disk with FEM grid control applied

The output link of the gearbox was loaded with a torque of 28 N·m. In Figure 9, the moment is shown by purple arrows.

The materials are selected from the SolidWorks Simulation material libraries (Tables 2, 3).

Table 2 – Characteristics of caprolon (PA Type 6) – a material selected for cycloidal disks

Property	Value	Dimension
Yield strength	108.65	MPa
Density	1120	kg/m ³
Elastic modulus	2620	MPa
Shear modulus	970.4	MPa
Poisson's ratio	0.34	–
Tensile strength	90	MPa

Table 3 – Characteristics of steel SP15 - a material selected for slow speed shaft rollers disks

Property	Value	Dimension
Yield strength	390	MPa
Density	7812	kg/m ³
Elastic modulus	$2.1 \cdot 10^5$	MPa
Shear modulus	$0.8 \cdot 10^5$	MPa
Poisson's ratio	0.31	–
Tensile strength	595	MPa

Slow speed shaft rollers with applied FEM grid control are presented in Figure 11.



Figure 11 – Slow speed shaft rollers with FEM grid control applied

4 Results

The diagrams of the stresses in the rollers in cross section next to the satellite are shown at the base of the rollers. Stresses are caused by the reaction of the torque (Figures 12, 13).

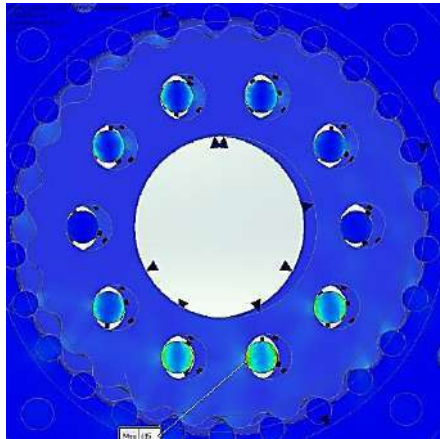


Figure 12 – Diagram of stress distribution in slow-speed shaft rollers

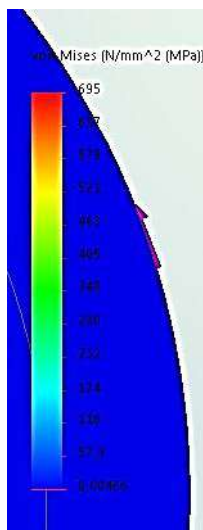


Figure 13 – The legend of the equivalent stress distribution in slow-speed shaft rollers (von Mises)

The maximum value is 695 MPa. The strength limit for steel SH15, from which the rollers are made, is 2160 MPa.

Figures 14 and 15 show the stress diagrams of the cycloid disk.

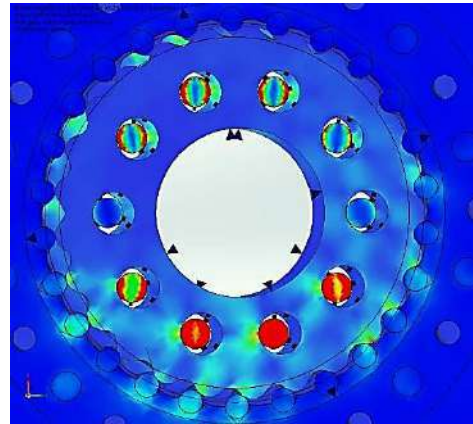


Figure 14 – Diagram of stress distribution in cycloidal disk

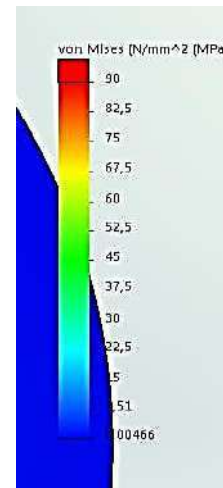


Figure 15 – The legend of equivalent stress distribution in cycloidal disk (von Mises)

Tensile stress for graphite's saturated polyamide is 75 MPa, with relative compression strain of 135 MPa.

The maximum stress in the cycloid disk is about 90 MPa. It occurs in contact with the most loaded rollers near the surface, it is the compressive stress.

The offset of the point lying on the surface at a distance of 0.391 mm of the reducer on a radius of 28 mm is 0.8° (Figures 16).

The cycloid type of engagement selected for the stepper robot reducer allows you to design a compact and lightweight engine capable of withstanding relatively heavy loads.

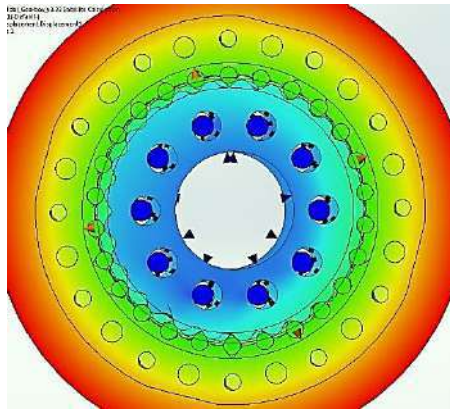


Figure 16 – Deformation diagram in a zone of the cycloidal disk

5 Conclusions

The Diameter and Length of the developed cycloidal reducer are small enough and correct to use with modern BLDC electrical motors.

The predicted weight of the developed cycloidal reducer is 180 g only.

The lightweight and compact cycloidal reducer model is developed and can be suggested as a drive for a pet simulated four-legged robot.

The obtained results of the analysis of stresses arising between the disk and the rollers indicate the complete suitability of the selected materials of polyamide and steel on their mechanical characteristics for use in the reducer of the robot activator.

Analysis of the predicted deformation of the disk demonstrates the need to use an output shaft position sensor to ensure high accuracy in determining the robot's position.

References

1. Bednarczyk, S. (2021). Analysis of the cycloidal reducer output mechanism while taking into account machining deviations. *Proceedings of the Institution of Mechanical Engineers, Part C: Journal of Mechanical Engineering Science*, Vol. 235(23), pp. 7299-7313, doi: 10.1177/09544062211016889.
2. Jung, T., Lim, J., Bae, H., Lee, K. K., Joe, H.-M., Oh, J.-H. (2018). Development of the humanoid disaster response platform DRC-HUBO+. *IEEE Transactions on Robotics*, Vol. 34(1), pp. 1-17, doi: 10.1109/TRO.2017.2776287.
3. Sensinger, J. W., Lipsey, J. H. (2012). Cycloid vs. harmonic drives for use in high ratio, single stage robotic transmissions. *The International Conference on Robotics and Automation*, Vol. 606(11), pp. 4130-4135.
4. Lee, K. K., Hong, S., Oh, J.-H. (2020). Development of a lightweight and high-efficiency compact cycloidal reducer for legged robot. *International Journal of Precision Engineering and Manufacturing*, Vol. 21, pp. 415-425.
5. Sun, X. X., Han, L. (2019). A new numerical force analysis method of CBR reducer with tooth modification. *Journal of Physics: Conference Series*, Vol. 1187, 032053, doi: 10.1088/1742-6596/1187/3/032053.
6. Qi, M., Wu, D., Zhang, S., Yao, R., Zhang, P., Han, T., Chang, J. (2018). Structural design and development of a mechatronic flywheel for miniature satellites. *Advances in the Astronautical Sciences*, Vol. 165, pp. 2219-2228.
7. Rasouli, K., Shahbazi, H., Ariaei, A., Malekzadeh, M. (2017). Mechatronic design and construction of a five axes satellite simulator. *4th RSI International Conference on Robotics and Mechatronics, ICRoM 2016*, pp. 210-215, doi: 10.1109/ICRoM.2016.
8. Li, R., Guo, F., Yu, C., He, Y., Ye, Z., Yuan, S. (2017). Development and validation of a mechatronic solar array drive assembly for mini/micro-satellites. *Acta Astronautica*, Vol. 134, pp. 54-64, doi: 10.1016/j.actaastro.2017.01.047.
9. Mendoza-Bárceñas, M. A., Vicente-Vivas, E., Rodríguez-Cortés, H. (2014). Mechatronic design, dynamic modeling and results of a satellite flight simulator for experimental validation of satellite attitude determination and control schemes in 3-axis. *Journal of Applied Research and Technology*, Vol. 12(3), pp. 370-383, doi: 10.1016/S1665-6423(14)71619-0.
10. Xie, F., Li, L., Zhang, G., Hu, X. (2021). Application of cycloidal pin wheel planetary reducer in the design of digging machine. *2021 International Conference on Electronics, Circuits and Information Engineering, ECIE 2021*, pp. 153-156, doi: 10.1109/ECIE52353.2021.00039.
11. Kormin, T. G., Tsumbu, J.-D. B. (2020). Cycloidal reducer with rotation external ring gear. *IOP Conference Series: Materials Science and Engineering*, Vol. 971(4), doi: 10.1088/1757-899X/971/4/042072.
12. Huang, J.-T., Li, C.-W. (2020). The high-payload manipulator development based on novel two-stage cycloidal speed reducers and hub motors. *Journal of Physics: Conference Series*, Vol. 1583(1), doi: 10.1088/1742-6596/1583/1/012002.



sustainability

an Open Access Journal by MDPI

IMPACT
FACTOR
3.251

CITESCORE
3.9
SCOPUS

Industry 4.0 Technologies for Sustainable Asset Life Cycle Management

Guest Editors

Dr. Malgorzata Jasiulewicz-Kaczmarek, Prof. Dr. Katarzyna Antosz, Dr. Chao Zhang,
Prof. Dr. Vitalii Ivanov

Deadline

15 March 2022

Special Issue

mdpi.com/si/93508

Invitation to submit

Topics and themes of this Special Issue can include but are not limited to:

- Drivers and barriers for the implementation of Industry 4.0 technologies for sustainability in ALCM;
- Intelligent decision support systems for sustainability in ALCM;
- Digitalization and Industry 4.0 for supporting the ALCM;
- Mapping of technologies and capabilities for adoption and implementation of Industry 4.0 for ALCM;
- Role of competences for successful adoption and implementation of Industry 4.0 technologies for ALCM;
- Digital product–service system for sustainability in ALCM;
- The impact of digitalization on ALCM;
- Modeling and simulation in ALCM;
- Big data analytics implementation for sustainable ALCM;
- Digital-twin-driven intelligent ALCM for sustainability;
- IoT solutions in ALCM for sustainability;
- Data-driven maintenance and ALCM systems;
- Risk-based approaches in ALCM;
- Causes and effects of implementing Industry 4.0 technologies for sustainable ALCM.



Real Power Loss Reduction by Enhanced RBS Algorithm

Kanagasabai L.

Department of EEE, Prasad V. Potluri Siddhartha Institute of Technology, Kanuru, Vijayawada, 520007 Andhra Pradesh, India.

Article info:

Submitted:

July 20, 2021

Accepted for publication:

December 3, 2021

Available online:

December 8, 2019

*Corresponding email:

gklenin@gmail.com

Abstract. In this paper enhanced red-breasted sapsucker (ERBS) algorithm has been proposed to solve the power loss lessening problem. RBS algorithm is designed on the copulate actions of RBS. Male RBS (MRBS) will attract the female with an exclusive tone. Concerning the concentration of the tone female RBS (FMBS) will progress in the direction of the MRBS. Various tone engendered by MRBS will catch the fancy of FRBS, and this action is analogous to data contribution in Evolutionary techniques. Naturally, so many MRBS will put huge efforts simultaneously to attract the FRBS for copulate. RBS has been integrated with the sine-cosine algorithm (SCA) and opposition-based learning (OBL). SCA process shifts resourcefully from exploration to exploitation by acclimatizing the functions. Solutions are frequently streamlined to the premium solution and optimization of the premium region of the exploration zone. OBL is one of the significant optimization procedures to improve the convergence pace of different optimization procedures. The successful execution of the OBL holds the assessment of the opposite population and present population in the analogous generation to find out the better contender solution. The proposed enhanced RBS (ERBS) algorithm is corroborated in IEEE 30 bus test systems. Power discrepancy compressed, power reliability amplified, and power loss condensed.

Keywords: optimal, reactive, transmission, sine-cosine algorithm, opposition.

1 Introduction

Power loss lessening is a fundamental problem in Electrical power systems. Bountiful numeric procedures [1-6] and evolutionary approaches [9-19] solved the real power loss lessening problem. Carpentier [1] done the work on contribution to “à l’étude du dispatching économique” problem. Dommel et al. [2] researched optimal power flow solutions.

Takapoui et al. [3] did work on a simple, effective heuristic for embedded mixed-integer quadratic programming. Abaci et al. [4] solved optimal reactive-power dispatch using a differential search algorithm. Pulluri et al. [5] worked on an enhanced self-adaptive differential evolution-based solution methodology for multiobjective optimal power flow. Sahli et al. [10] applied a hybrid PSO-tabu search to solve the problem.

Mouassa et al. [11] used an ant lion optimizer for solving the optimal reactive power problem. Using quasi-oppositional teaching learning-based optimization, Mandal et al. [12] solved optimal reactive power dispatch. Tran et al. [14] researched optimal reactive

power dispatch solutions by using a novel improved stochastic fractal search optimization algorithm.

Polprasert et al. [15] solved optimal reactive power dispatch using improved pseudo-gradient search particle swarm optimization. Muhammad et al. [26] found a solution of optimal reactive power dispatch with FACTS devices. Das et al. [27] solved the optimal reactive power dispatch problem considering load uncertainty using a modified JAYA algorithm.

Das et al. [28] integrated the PV system with optimal reactive power dispatch for voltage security using the JAYA algorithm. Muhammad et al. [29] designed fractional evolutionary processing for reactive power planning with FACTS devices. Shanono et al. [30] did a bibliometric analysis of optimal reactive power dispatch.

Tudose et al. [31] solved single- and multi-objective optimal reactive power dispatch problems using an improved Salp swarm algorithm. Balancing the exploration and exploitation is essential in the progress of the algorithms. Few algorithms are good in exploration, but exploitation property will be poor. Then some algorithms are worthy of exploitation, but it has deprived performance in exploration.

The optimal solution cannot be reached when both exploration and exploitation are not balanced [21-25]. In this article, the ERBS algorithm has been proposed to solve the power loss lessening problem. RBS algorithm is designed on the copulate actions of RBS. MRBS will attract the female with an exclusive tone. Various tone engendered by MRBS will catch the fancy of FRBS, and this action is analogous to data contribution in Evolutionary techniques.

Naturally, so many numbers of MRBS will put huge efforts simultaneously to attract the FRBS for copulate. Mainly, there will be tone variation among MRBS, which subsequently modifies the FRBS direction of movement towards males concerning the concentration of the tone. MRBS and FRBS are considered populations. Initially, MRBS will be in mammoth quantity and the duration of the preliminary stage of copulate – the amount of MRBS diminish owing to copulate.

When iteration increases precisely, the population diminishes. Exploration will be there initially, and regular exploitation will be followed. In the initial phase, FRBS will get fascinated with reverence to the concentration of tone.

However, at the concluding phase, it will be fascinated in the direction of the most excellent MRBS. FRBS only listens to a single MRBS tone, and at the concluding phase, it is a seal to the FRBS and most excellent concentration tone. RBS is at variance based on the objective function.

MRBS is the most excellent position established in the exploration space, and FRBS is the main investigate representative. The location of the FRBS is entirely grounded on the MRBS. When an enhanced contender solution is attained, subsequently, there will be modernization of the MRBS. RBS arbitrarily instigates, and each RBS is performing as a contender solution. The population and fitness value of RBS is appraised. Most excellent MRBS is considered as ME-population, and it will be mainly striking MRBS, progressively FRBS shift near to particular MRBS.

In the proposed ERBS algorithm, SCA and OBL algorithm has been integrated with the RBS algorithm. SCA process shifts resourcefully from exploration to exploitation by adapting the functions. Solutions are frequently streamlined to the premium solution and optimization of the premium region of the exploration zone. OBL is one of the significant optimization procedures to improve the convergence pace of different optimization procedures.

The successful execution of the OBL holds the assessment of the opposite population and present population in the analogous generation to find the better contender solution. The proposed ERBS algorithm is corroborated in IEEE 30 bus test systems. Power discrepancy compressed, power reliability amplified, and power loss condensed.

2 Research Methodology

2.1 Problem formulation

Power loss minimization is defined by:

$$\text{Min } \overline{OBF}(\bar{r}, \bar{u}), \quad (1)$$

subjected to:

$$L(\bar{r}, \bar{u}) = 0; \quad (2)$$

$$M(\bar{r}, \bar{u}) = 0; \quad (3)$$

$$r = [VLG_1, \dots, VLG_{N_g}; QC_1, \dots, QC_{N_c}; T_1, \dots, T_{N_T}]; \quad (4)$$

$$u = \left[\begin{array}{c} PG_{slack}; VL_1, \dots, VL_{N_{Load}}; \\ QG_1, \dots, QG_{N_g}; SL_1, \dots, SL_{N_T} \end{array} \right]. \quad (5)$$

The fitness function (F_1, F_2, F_3) is designed for power loss (MW) reduction, Voltage deviation, voltage stability index (L-index) is defined by:

$$F_1 = P_{\text{Minimize}} = \text{Minimize} \left[\sum_m^{NTL} G_m [V_i^2 + V_j^2 - 2 * V_i V_j \cos \theta_{ij}] \right]; \quad (6)$$

$$F_2 = \text{Minimize} \left[\sum_{i=1}^{N_{LB}} |V_{Lk} - V_{Lk}^{desired}|^2 + \sum_{i=1}^{N_g} |Q_{Gk} - Q_{LG}^{Lim}|^2 \right]; \quad (7)$$

$$F_3 = \text{Minimize } L_{\text{Maximum}}; \quad (8)$$

$$L_{\text{Maximum}} = \text{Maximum} [L_j]; j = 1; N_{LB}; \quad (9)$$

$$\begin{cases} L_j = 1 - \sum_{i=1}^{NPV} F_{ji} \frac{V_i}{V_j}; \\ F_{ji} = -[Y_1]^{-1} [Y_2]; \end{cases} \quad (10)$$

$$L_{\text{Maximum}} = \text{Maximum} \left[1 - [Y_1]^{-1} [Y_2] \times \frac{V_i}{V_j} \right]. \quad (11)$$

Equality constraints are:

$$0 = PG_i - PD_i - V_i \sum_{j \in N_B} V_j \times \left[G_{ij} \cos[\theta_i - \theta_j] + B_{ij} \sin[\theta_i - \theta_j] \right]; \quad (12)$$

$$0 = QG_i - QD_i - V_i \sum_{j \in N_B} V_j \times \left[G_{ij} \sin[\theta_i - \theta_j] + B_{ij} \cos[\theta_i - \theta_j] \right]. \quad (13)$$

Inequality constraints are:

$$P_{gslack}^{minimum} \leq P_{gslack} \leq P_{gslack}^{maximum}; \quad (14)$$

$$Q_{gi}^{minimum} \leq Q_{gi} \leq Q_{gi}^{maximum}, i \in N_g; \quad (15)$$

$$VL_i^{minimum} \leq VL_i \leq VL_i^{maximum}, i \in N_L; \quad (16)$$

$$T_i^{minimum} \leq T_i \leq T_i^{maximum}, i \in N_T; \quad (17)$$

$$Q_c^{minimum} \leq Q_c \leq Q_c^{maximum}, i \in N_c; \quad (18)$$

$$|SL_i| \leq S_{L_i}^{maximum}, i \in N_{TL}; \quad (19)$$

$$VG_i^{minimum} \leq VG_i \leq VG_i^{maximum}, i \in N_g. \quad (20)$$

Multi objective fitness:

$$MOF = F_1 + r_i F_2 + u F_3 = F_1 + \left\{ \sum_{i=1}^{NL} x_v [VL_i - VL_i^{min}]^2 + \sum_{i=1}^{NG} r_g [QG_i - QG_i^{min}]^2 \right\} + r_f F_3; \quad (21)$$

$$VL_i^{minimum} = \begin{cases} VL_i^{max}, & VL_i > VL_i^{max}; \\ VL_i^{min}, & VL_i < VL_i^{min}; \end{cases} \quad (22)$$

$$QG_i^{minimum} = \begin{cases} QG_i^{max}, & QG_i > QG_i^{max}; \\ QG_i^{min}, & QG_i < QG_i^{min}. \end{cases} \quad (23)$$

2.2 RBS algorithm

RBS algorithm is designed on the copulate actions of RBS. MRBS will attract the female with an exclusive tone. Concerning the concentration of the tone FRBS will progress in the direction of the MRBS.

Modulation in the tone will vary with time, and this tone concentration induces the FRBS to progress gradually in the direction of the MRBS for copulating.

Various tones engendered by MRBS will catch the fancy of FRBS, and this action is analogous to data contribution in Evolutionary techniques.

Naturally, so many male RBSs will put huge efforts simultaneously to attract the FRBS for copulate. There will mainly be tone variation among MRBS, which subsequently modifies the FRBS direction of movement towards males concerning the concentration of the tone.

Tone concentration (TC) is defined as:

$$TC = \frac{\text{Tone supremacy}}{\text{zone}}. \quad (24)$$

Proliferation velocity of the tone mathematically described as:

$$TC = \frac{\text{source of Proliferation velocity}}{4\pi r^2}. \quad (25)$$

Based on the space Concentration of the Tone is calculated by

$$\text{Space} = ||\text{Tone location } (Z_{tl}) - \text{Location of RBS which hear the tone } (Z^h)|| \quad (26)$$

Concerning tone concentration, fascination will occur between males and females, leading to copulation. RBS fitness value has been calculated. FRBS will get fascinated by the most excellent MRBS, and the prettiness is considered to be similar to fitness value. Tone source is essential because minor space will augment tone strength, which is similar to sound emission. Expanse amplifies; subsequently, the pace of concentration of tone diminishes. MRBS and FRBS are considered populations. Initially, MRBS will be in mammoth quantity, and in the duration of the preliminary stage of copulating, the amount of MRBS will diminish owing to copulate. When iteration increases precisely, the population diminishes. Exploration will be there initially, and regular exploitation will be followed. In the initial phase, FRBS will get fascinated with reverence to the concentration of tone. However, at the concluding phase, it will be fascinated in the direction of the most excellent

MRBS. FRBS only listens to a single MRBS tone, and at the concluding phase, it is a seal to the FRBS and most excellent concentration tone. RBS is at variance based on the objective function.

Male RBS is the most excellent position established in the exploration space, and FRBS is the main investigate representative. The location of the FRBS is entirely grounded on the MRBS. When an enhanced contender solution is attained, subsequently, there will be modernization of the MRBS. RBS arbitrarily instigates, and each RBS is performing as a contender solution. The population and fitness value of RBS is appraised. Most excellent MRBS is considered as ME-population, and it will be mainly striking MRBS, progressively FRBS shift near to particular MRBS.

Progress of the RBS is modernized by:

$$z_i^{t+1} = z_i^t + R \frac{\mu_i^t}{2} \times \left[(z_{ME_{pop}}^t - z_i^t) + \gamma_{mrsj} * (z_{mrsj}^t - z_i^t) \right], \quad (27)$$

where z_i^t – the preceding location of RBS; $z_{ME_{pop}}^t$ indicates the location of most excellent RBS; z_{mrsj}^t specifies the location of MRBS; μ_i^t is coefficient of RBS in t -th iteration; R is random:

$$\mu_i^t = R \times \text{Factor value}, \quad (28)$$

where the factor is 0.79 to 0 during the iterations.

$\mu_i^t > 1$ and $\mu_i^t \leq 1$ specify the location of FRBS which attaining the MRBS:

$$\gamma = \frac{1}{1 + \text{Tone concentration}_j^t}, \quad (29)$$

where γ signifies the lure possibility grounded on the tone concentration with reverence to location (close to or remote); γ possesses enormous consequence over the exploitation segment.

Tangent sigmoid T_s is employed in the procedure:

$$E = T_s \left(1 - \frac{\text{present iter. no}}{\text{max no of iter.}} \right). \quad (30)$$

Quantity of MRBS in the iteration is defined as:

$$\text{Quantity of Male Red – breasted sapsucker} = \left\{ \text{Ring} \left[\frac{\text{max quantity of Red-breasted sapsuckersapsucker}}{2} \times \left(1 - \frac{\text{present iter. no}}{\text{max no of iter.}} \right) \right] + 1 \right\} \quad (31)$$

The most excellent MRBS based on ME-population is described as:

$$z_i^{t+1} = z_i^t + R * \mu_i^t * (z_{ME_{pop}}^t - z_i^t) + \gamma_{ME_{pop}} \quad (32)$$

Alteration in the path and location is based on the concentration of stone, and in addition, if some danger brings into being from others, then RBS will shift from the position:

$$T_\gamma = 0.8 \frac{\sum_{n=1}^{n-1} \gamma_{ME_{pop}}^n}{n-1}, \quad (33)$$

where T_γ indicates the threshold:

$$z_{shift}^i = LB - (LB - UB)R, \quad (34)$$

where LB, UB are lower and upper bound:

Based on tone adaptableness, the RBS locate, and as soon as there is an elevated concentration of tone from the most excellent MRBS subsequently the FRBS will progress towards it:

$$P_{ME-pop.Progress\ rate} = \beta \left(1 - \frac{present\ iter.\ no}{max\ no\ of\ iter.}\right), \quad (35)$$

where $P_{ME-pop.Progress\ rate}$ specifies the possibility of RBS population progress:

$$ME_{pop.Progress\ rate} = \begin{cases} 1 & \text{if } space \leq P_{ME-pop.\ progress\ rate}; \\ 0 & \text{otherwise.} \end{cases} \quad (36)$$

Subsequently, the location of FRBS is described as

$$z_{ME_{pop.progress\ rate}}^i = z_i^t + ME_{pop.progress\ rate} \times \{(z_{ME\ pop}^t - z_{space})R\}. \quad (37)$$

The corresponding procedure is as follows:

- a. Start
- b. RBS population initialized
- c. Red-breasted sapsucker fitness value computed
- d. Calculate T_γ
- e. **while** ($iter < max\ no\ of\ iter$)
- f. The quantity of MRBS is calculated by $Quantity\ of\ Male\ Red - breasted\ sapsucker = \frac{max\ quantity\ of\ Red - breasted\ sapsuckersapsucker}{2} \times \left(1 - \frac{present\ iter.\ no}{max\ no\ of\ iter.}\right) + 1$.
- g. Categorize the RBS
- h. For every RBS; decide MRBS
- i. $\gamma = \frac{1}{1 + Tone\ concentration_j^i}$.
- j. $\mu_i^t = R \times Factor\ value$.
- k. Location of the RBS modernized by $z_i^{t+1} = z_i^t + R \frac{\mu_i^t}{2} \times \left[\left(z_{ME_{pop}}^t - z_i^t \right) + \gamma_{mrsj} * \left(z_{mrsj}^t - z_i^t \right) \right]$,
- l. Calculate the progression of RBS $ME_{pop.Progress\ rate} = \begin{cases} 1 & \text{if } space \leq P_{ME-pop.\ progress\ rate}; \\ 0 & \text{otherwise.} \end{cases}$
- m. $z_{ME_{pop.progress\ rate}}^i = z_i^t + ME_{pop.progress\ rate} \times \{(z_{ME\ pop}^t - z_{space})R\}$.
- n. End if
- o. Modify the location of FRBS
- p. Once the most excellent solution is established, subsequently modernize ME_{pop}
- q. End for
- r. $iter = iter + 1$
- s. End while
- t. End
- u. End
- v. Revisit the ME_{pop}

In the proposed ERBS algorithm, SCA and OBL algorithms have been integrated with RBS.

SCA [32] processes shift resourcefully from exploration to exploitation by adapting the functions. Solutions are frequently streamlined to the premium solution and optimization of the premium region of the exploration zone.

$$\vec{Z}_i^{m+1} = \vec{Z}_i^m + R_1 \sin(R_2) |R_3 \times E_i^m - \vec{Z}_i^m|; \quad (38)$$

$$\vec{Z}_i^{m+1} = \vec{Z}_i^m + R_1 \cos(R_2) |R_3 \times E_i^m - \vec{Z}_i^m|; \quad (39)$$

$$\vec{Z}_i^{m+1} = \begin{cases} \vec{Z}_i^m + R_1 \sin(R_2) |R_3 E_i^m - \vec{Z}_i^m| & R_4 < 0.50; \\ \vec{Z}_i^m + R_1 \cos(R_2) |R_3 E_i^m - \vec{Z}_i^m| & R_4 \geq 0.50, \end{cases}; \quad (40)$$

where \vec{Z}_i^m is the present position at m -th iteration with E_i^m population.

OBL [33] is one of the significant optimization procedures to improve the convergence pace of different optimization procedures. The successful execution of the OBL holds the assessment of the opposite population and present population in the analogous generation to find out the better contender solution.

Fix ON ($ON \in [g, h]$) by an actual number and ON^o (opposite number) is described as follows:

$$N^o = g + h - ON. \quad (41)$$

Exploration augmented by:

$$ON_i^o = g_i + h_i - ON_i, \quad (42)$$

where (ON_1, ON_2, \dots, ON_d) is a spot in “ d ” exploration space; $N_i \in [x_i, y_i]; i \rightarrow \{1, 2, 3, \dots, d\}$.

The corresponding procedures are as follows:

- a. Start
- b. Initialize parameters
- c. Engender opposite population; For $j = 1$; population size: for $i = 1$; umber of control variables
- d. $ON_i^o = g_i + h_i - ON_i$
- e. Categorize the present and opposite population from most excellent to poor
- f. RBS population initialized
- g. RBS fitness value computed
- h. Calculate T_γ
- i. $T_\gamma = 0.8 \frac{\sum_{n=1}^{n-1} \gamma_{ME_{pop}}^i}{n-1}$
- j. **while** ($iter < max\ no\ of\ iter$)
- k. The quantity of RBS is calculated by $Quantity\ of\ Male\ Red - breasted\ sapsucker = \frac{max\ quantity\ of\ Red - breasted\ sapsuckersapsucker}{2} \times \left(1 - \frac{present\ iter.\ no}{max\ no\ of\ iter.}\right) + 1$.
- l. Categorize the RBS
- m. For every RBS; decide MRBS
- n. $\gamma = \frac{1}{1 + Tone\ concentration_j^i}$
- o. $\mu_i^t = R \times Factor\ vaue$

l. Location of the RBS modernized by

$$z_i^{t+1} = z_i^t + R \frac{\mu_i^t}{2} \times$$

- m. $\times \left[\left(z_{ME_{pop}}^t - z_i^t \right) + \gamma_{mrsj} * \left(z_{mrsj}^t - z_i^t \right) \right]$,
n. $\vec{Z}_i^{m+1} = \vec{Z}_i^m + R_1 \sin(R_2) |R_3 \times E_i^m - \vec{Z}_i^m|$
o. $\vec{Z}_i^{m+1} = \vec{Z}_i^m + R_1 \cos(R_2) |R_3 \times E_i^m - \vec{Z}_i^m|$
p. $\vec{Z}_i^{m+1} = \begin{cases} \vec{Z}_i^m + R_1 \sin(R_2) |R_3 E_i^m - \vec{Z}_i^m| R_4 < 0.50; \\ \vec{Z}_i^m + R_1 \cos(R_2) |R_3 E_i^m - \vec{Z}_i^m| R_4 \geq 0.50, \end{cases}$
q. Calculate the progression of RBS
 $ME_{pop,progress\ rate} =$
r. $= \begin{cases} 1 \text{ if } space \leq P_{ME-pop, progress\ rate}; \\ 0 \text{ otherwise.} \end{cases}$
s. $z_{ME_{pop,progress\ rate}}^i = z_i^t + ME_{pop,progress\ rate} \times$
 $\times \{ (z_{ME_{pop}}^t - z_{space}) R \}$.
t. End if
u. Modify the location of FRBS
v. Once the most excellent solution is established,
subsequently modernize ME_{pop}
w. End for
x. $iter = iter + 1$
y. End while
z. End
aa. Revise the ME_{pop}

3 Results

Projected RBS and ERBS algorithms have been corroborated in IEEE 30 bus system [20].

Table 1 shows the loss appraisal, Table 2 – the voltage aberration evaluation, and Table 3 – the L-index assessment.

Table 1 – Assessment of entire power loss

Technique	Power loss, MW
Basic PSO-TS [10]	4.52
Standard TS [10]	4.68
Basic PSO [10]	4.69
Ant LO [11]	4.59
Basic QO-TLBO [12]	4.56
Standard TLBO [12]	4.56
Standard GA [13]	4.94
Basic PSO [13]	4.92
HAS [13]	4.91
Standard FS [14]	4.58
IS-FS [14]	4.51
Standard FS [16]	4.53
RBS	4.50
ERBS	4.50

Figures 1–3 give the graphical appraisal of the methods. MSO and EMSO abridged the power loss efficiently.

Table 2 – Comparison of voltage aberration

Technique	Voltage deviancy, PU
Basic PSO-TVIW [15]	0.104
Basic PSO-TVAC [15]	0.206
Standard PSO-TVAC [15]	0.135
Basic PSO-CF [15]	0.129
PG-PSO [15]	0.120
SWT-PSO [15]	0.161
PGSWT-PSO [15]	0.154
MPG-PSO [15]	0.089
QO-TLBO [12]	0.086
TLBO [12]	0.091
Standard FS [14]	0.122
ISFS [14]	0.089
Standard FS [16]	0.088
RBS	0.086
ERBS	0.085

Table 3 – Appraisal of voltage constancy

Technique	Voltage constancy L-index, PU
Basic PSO-TVIW [15]	0.126
Basic PSO-TVAC [15]	0.150
Standard PSO-TVAC [15]	0.127
Basic PSO-CF [15]	0.126
PG-PSO [15]	0.126
SWT-PSO [15]	0.149
PGSWT-PSO [15]	0.139
MPG-PSO [15]	0.124
QO-TLBO [12]	0.119
Standard TLBO [12]	0.118
ALO [11]	0.116
ABC [11]	0.116
Standard GWO [11]	0.124
Basic BA [11]	0.125
Standard FS [14]	0.125
IS-FS [14]	0.125
Standard FS [16]	0.101
RBS	0.100
ERBS	0.100

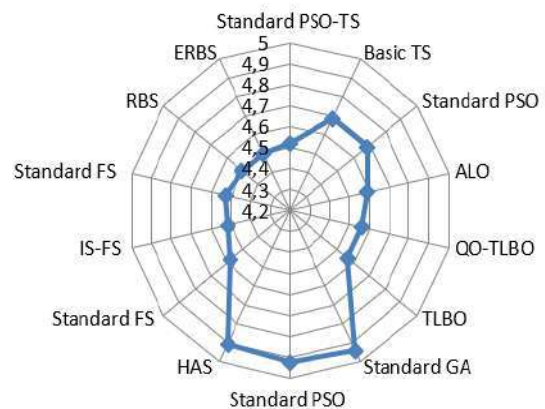


Figure 1 –Assessment of power loss, MW

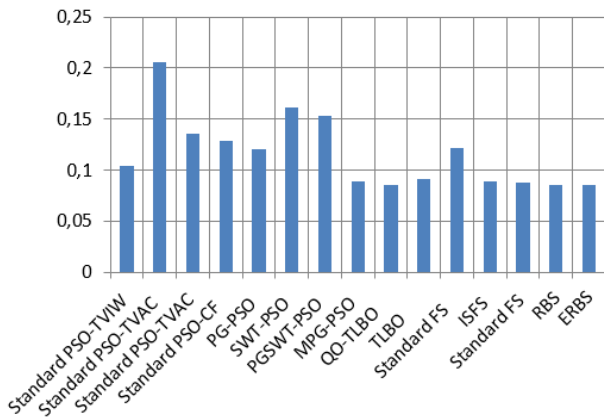


Figure 2 – Appraisal of voltage aberration, PU

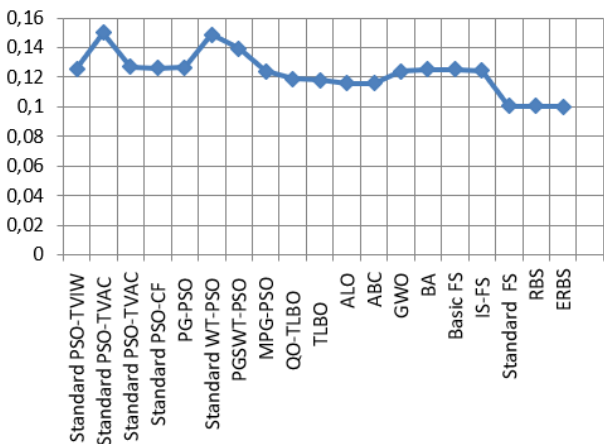


Figure 3 – Assessment of voltage constancy index, PU

Appraisal of loss has been done with PSO, adapted PSO, enhanced PSO, comprehensive learning PSO, Adaptive genetic algorithm, Canonical genetic algorithm, enhanced genetic algorithm, Hybrid PSO-Tabu search (PSO-TS), Ant lion (ALO), quasi-oppositional teaching learning-based (QOTBO), enhanced stochastic fractal search optimization algorithm (ISFS), harmony search (HS), upgraded pseudo-gradient search particle swarm optimization and cuckoo search algorithm. Power loss abridged competently, and the proportion of the power loss lessening has been enhanced. Predominantly voltage constancy augmentation attained with minimized voltage deviancy.

Then Projected RBS and ERBS algorithm substantiated in IEEE 14, 30, 57, 118, and 300 bus test systems [19] deprived of L-index. Loss appraisal is shown in Tables 4–8.

Figures 4–8 give a graphical comparison between the approaches with orientation to power loss. Proposed RBS and ERBS are compared with Adapted PSO, PSO, EP, SARGA, CGA, AGA, EPSO, CLPSO, AGA, FEA, and CSO.

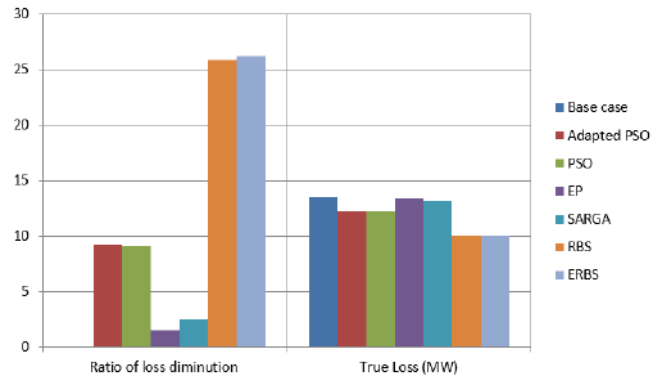


Figure 4 – Power loss appraisal (IEEE 14 bus system)

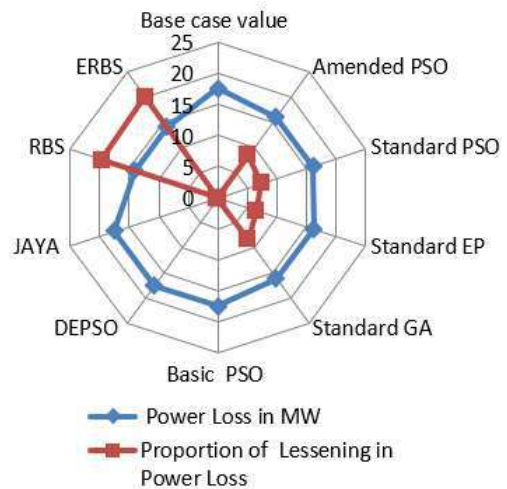


Figure 5 – Appraisal of power loss (IEEE 30 bus system)

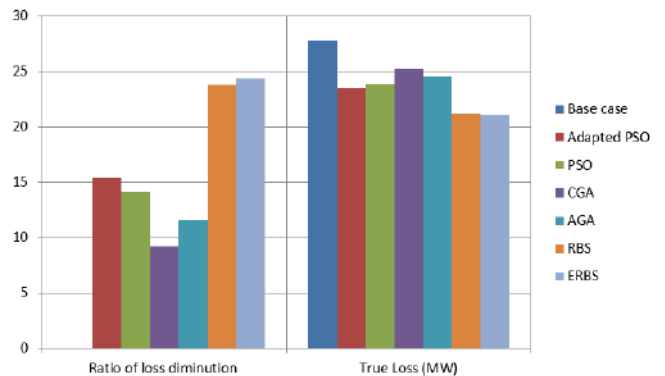


Figure 6 – Power loss appraisal (IEEE 57 bus system)

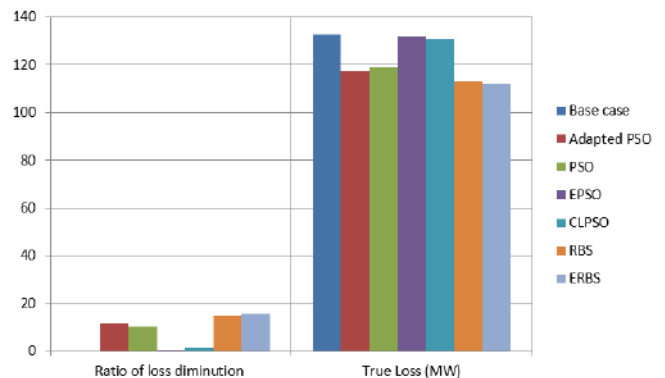


Figure 7 – Power loss appraisal (IEEE 118 bus system)

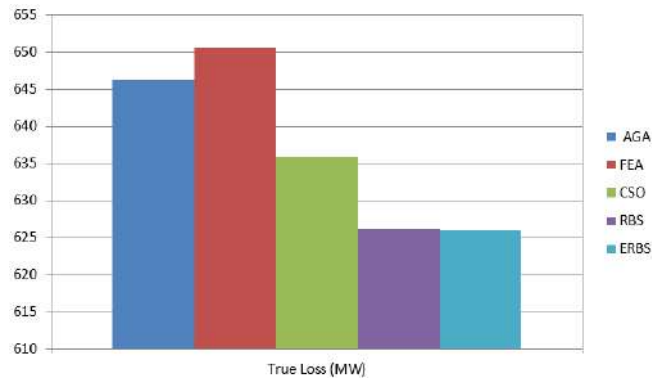


Figure 8 – Power loss appraisal (IEEE 300 bus system)

Table 4 – Assessment of results (IEEE 14 bus system)

Parameter	Base case [24]	Adapted PSO [24]	PSO [23]	EP [23]	SARGA [22]	RBS	ERBS
Ratio of loss diminution	0.000	9.2000	9.1000	1.500	2.500	25.892	26.169
True Loss (MW)	13.550	12.293	12.315	13.346	13.216	10.029	10.004

Table 5 – Appraisal of loss (IEEE 30 bus system)

Parameter	Actual power loss, MW	The proportion of lessening in power loss
Base case value [24]	17.5500	0.000
M-PSO [24]	16.0700	8.400
Basic-PSO [23]	16.2500	7.400
EP [21]	16.3800	6.600
S-GA [22]	16.0900	8.300
PSO [25]	17.5246	0.145
DEPSO [25]	17.52	0.171
JAYA [25]	17.536	0.080
RBS	14.100	19.658
ERBS	14.034	20.034

Table 6 – Assessment of parameters (IEEE 57 bus system)

Parameter	Base case [24]	Adapted PSO [24]	PSO [23]	CGA [22]	AGA [22]	RBS	ERBS
Ratio of loss diminution	0.00	15.40	14.10	9.20	11.60	23.76	24.33
True loss, MW	27.80	23.51	23.86	25.24	24.56	21.20	21.04

Table 7 – Assessment of results (IEEE 118 bus system)

Parameter	Base case [24]	Adapted PSO [24]	PSO [23]	EPSO [21]	CLPSO [21]	RBS	ERBS
Ratio of loss diminution	0.00	11.70	10.10	0.60	1.30	14.97	15.56
True loss, MW	132.80	117.19	119.34	131.99	130.96	112.92	112.14

Table 8 – Power loss appraisal (IEEE 300 bus system)

Parameter	AGA [35]	FEA [35]	CSO [34]	RBS	ERBS
True loss, MW	646.30	650.60	635.89	626.15	626.09

4 Discussion

Projected RBS and ERBS algorithms compressed the power loss resourcefully. With and devoid of power stability index, proposed algorithms performed well. The ratio of power loss diminution improved sufficiently, and assessment has been done with other standard reported algorithms.

At first, the projected RBS and ERBS algorithm was substantiated in IEEE 30 bus system with considering voltage stability. Appraisal of loss has been done with

PSO, adapted PSO, enhanced PSO, comprehensive learning PSO, Adaptive genetic algorithm, Canonical genetic algorithm, enhanced genetic algorithm, Hybrid PSO-Tabu search (PSO-TS), Ant lion (ALO), quasi-oppositional teaching learning-based (QOTBO), enhanced stochastic fractal search optimization algorithm (ISFS), harmony search (HS), upgraded pseudo-gradient search particle swarm optimization and cuckoo search algorithm.

Then Projected RBS and ERBS algorithm was substantiated in IEEE 14, 30, 57, 118, and 300 bus test

systems deprived of L-index. Loss appraisal and graphical comparison between the approaches with orientation to power loss are reported. Proposed RBS and ERBS are compared with Adapted PSO, PSO, EP, SARGA, CGA, AGA, EPSO, CLPSO, AGA, FEA, and CSO. The ratio of power loss reduction has been improved.

5 Conclusions

ERBS algorithm condensed the power loss with amplifying of power constancy. MRBS and FRBS are considered populations. Initially, MRBS will be in mammoth quantity and the duration of the preliminary stage of copulate – the amount of MRBS diminish owing to copulate.

When iteration increases precisely, the population diminishes. Exploration will be there initially, and regular exploitation will be followed. In the initial phase, FRBS will get fascinated with reverence to the concentration of tone; however, at the concluding phase, it will be fascinated in the direction of the most excellent MRBS. FRBS only listens to a single MRBS tone, and at the concluding phase, it is a seal to the FRBS and most excellent concentration tone. RBS is at variance based on the objective function. MRBS is the most excellent position established in the exploration space, and FRBS is the main investigate representative. The location of the FRBS is entirely grounded on the MRBS.

When an enhanced contender solution is attained, subsequently, there will be modernization of the MRBS. RBS arbitrarily instigates, and each RBS is performing as a contender solution. The population and fitness value of RBS is appraised. Most excellent MRBS is considered ME-population, and it will be mainly striking MRBS, progressively FRBS shift near to particular MRBS.

In the proposed ERBS algorithm, SCA and OBL algorithm has been integrated with RBS. SCA process shifts resourcefully from exploration to exploitation by

adapting the functions. Solutions are frequently streamlined to the premium solution and optimization of the premium region of the exploration zone.

OBL is one of the significant optimization procedures to improve the convergence pace of different optimization procedures. The successful execution of the OBL holds the assessment of the opposite population and present population in the analogous generation to find the better contender solution. ERBS and RBS algorithms are verified in IEEE 30 bus test system with and devoid of L-index.

Both algorithms commendably reduced the power loss, and the percentage of real power loss lessening has been enhanced. Convergence characteristics show the better performance of the proposed optimization algorithms. The comparison of power loss has been made with other standard reported algorithms.

Nomenclature

OBJ – minimization of the objective function;
 r – consist of control variables;
 Q_c – reactive power compensators;
 T – dynamic tap setting of transformers;
 V_g – level of the voltage in the generation units;
 u – consist of dependent variables;
 PG_{slack} – slack generator;
 V_L – voltage on transmission lines;
 Q_G – generation unit's reactive power;
 S_L – apparent power;
 N_{TL} – number of the transmission line;
 V_{Lk} – load voltage in k -th load bus;
 $V_{Lk}^{desired}$ – voltage desired;
 Q_{GK} – reactive power;
 Q_{KG}^{Lim} – reactive power limitation;
 N_{LB}, N_g – number load and generating units;
 T – transformer tap.

References

1. Carpentier, J. (1962). Contribution à l'étude du dispatching économique. *Bull. de la Société Française des Electriciens*, Vol. 3, pp. 431-447.
2. Dommel, H. W., Tinney, W. F. (1968). Optimal power flow solutions. *IEEE Trans. Power Appar. Syst.*, Vol. PAS-87, pp. 1866-1876.
3. Takapoui, R., Möhle, N., Boyd, S., Bemporad, A. (2017). A simple effective heuristic for embedded mixed-integer quadratic programming. *International Journal of Control*, pp. 1-11, doi: 10.1080/00207179.2017.1316016.
4. Abaci, K., Yamaçlı, V. (2017). Optimal reactive-power dispatch using differential search algorithm. *Electrical Engineering*, Vol. 99(1), pp. 213-225.
5. Pulluri, H., Naresh, R., Sharma, V. (2017). An enhanced self-adaptive differential evolution based solution methodology for multiobjective optimal power flow. *Applied Soft Computing*, Vol. 54, pp. 229-245.
6. Heidari, A., Abbaspour, R. A., Jordehi, A. R. (2017). Gaussian barebones water cycle algorithm for optimal reactivepower dispatch in electrical power systems. *Applied Soft Computing*, Vol. 57, pp. 657-671.
7. Keerio, M. U., Ali, A., Saleem, M., Hussain, N., Hussain, R. (2020). Multi-objective optimal reactive power dispatch considering probabilistic load demand along with wind and solar power integration. *2nd International Conference on Smart Power and Internet Energy Systems (SPIES), Bangkok, Thailand, 2020*, pp. 502-507, doi: 10.1109/SPIES48661.2020.9243016.
8. Roy, R., Das, T., Mandal, K. K. (2020). Optimal reactive power dispatch for voltage security using JAYA algorithm. *International Conference on Convergence to Digital World - Quo Vadis (ICCDW), Mumbai, India, 2020*, pp. 1-6, doi: 10.1109/ICCDW45521.2020.9318700.
9. Mugemanyi, S., Qu, Z., Rugema, F. X., Dong, Y., Bananeza, C., Wang, L. (2020). Optimal reactive power dispatch using chaotic bat algorithm. *IEEE Access*, Vol. 8, pp. 65830-65867, doi: 10.1109/ACCESS.2020.2982988.

- 10.Sahli, Z., Hamouda, A., Bekrar, A., Trentesaux, D. (2014). Hybrid PSO-tabu search for the optimal reactive power dispatch problem. *Proceedings of the IECON 2014-40th Annual Conference of the IEEE Industrial Electronics Society, Dallas, TX, USA, 2014*, pp. 3536-3542, doi: 10.1109/IECON.2014.7049024.
- 11.Mouassa, S., Bouktir, T., Salhi, A. (2017). Ant lion optimizer for solving optimal reactive power dispatch problem in power systems. *Engineering Science and Technology, an International Journal*, Vol. 20(3), pp. 885-895.
- 12.Mandal, B., Roy, P. K. (2013). Optimal reactive power dispatch using quasi-oppositional teaching learning based optimization. *International Journal of Electrical Power and Energy Systems*, Vol. 53, pp. 123-134.
- 13.Khazali, H., Kalantar, M. (2011). Optimal reactive power dispatch based on harmony search algorithm. *International Journal of Electrical Power and Energy Systems*, Vol. 33(3), pp. 684-692.
- 14.Tran, H. V., Pham, T. V., Pham, L. H., Le, N. T., Nguyen, T. T. (2019). Finding optimal reactive power dispatch solutions by using a novel improved stochastic fractal search optimization algorithm. *Telecommunication Computing Electronics and Control*, Vol. 17(5), pp. 2517-2526.
- 15.Polprasert, J., Ongsakul, W., Dieu, V. N. (2016). Optimal reactive power dispatch using improved pseudo-gradient search particle swarm optimization. *Electric Power Components and Systems*, Vol. 44(5), pp. 518-532.
- 16.Duong, T. L., Duong, M. Q., Phan, V.-D., Nguyen, T. T. (2020). Optimal reactive power flow for large-scale power systems using an effective metaheuristic algorithm. *Hindawi Journal of Electrical and Computer Engineering*, Vol. 2020, 6382507, doi: 10.1155/2020/6382507.
- 17.Muhammad, Y., Rahimdad, R., Muhammad, A., Farman, C., Naveed I., He, Y. (2020). Solution of optimal reactive power dispatch with FACTS devices: A survey. *Energy Reports*, Vol. 6, pp. 2211-2229, doi: 10.1016/j.egyr.2020.07.030.
- 18.Mukherjee, A., Mukherjee, V. (2015). Solution of optimal reactive power dispatch by Chaotic Krill Herd algorithm. *IET Generation, Transmission and Distribution*, Vol. 9(15), pp. 2351-2362.
- 19.MATPOWER 4.1 IEEE 30-bus and 118-bus test system. Available online: <http://www.pserc.cornell.edu/matpower>.
- 20.Illinois Center for a Smarter Electric Grid (ICSEG). Available online: <https://icseg.iti.illinois.edu/ieee-30-busssystem>.
- 21.Dai, C., Chen, W., Zhu, Y., Zhang, X. (2009). Seeker optimization algorithm for optimal reactive power dispatch. *IEEE T. Power Syst.*, Vol. 24(3), pp. 1218-1231.
- 22.Subbaraj, P., Rajnarayan, P. N. (2009). Optimal reactive power dispatch using self-adaptive real coded genetic algorithm. *Electr. Power Syst. Res.*, Vol. 79(2), pp. 374-38.
- 23.Pandya, S., Roy, R. (2015). Particle swarm optimization based optimal reactive power dispatch. *Proceeding of the IEEE International Conference on Electrical, Computer and Communication Technologies (ICECCT)*, pp: 1-5, doi: 10.1109/ICECCT.2015.7225981.
- 24.Hussain, A. N., Abdullah, A. A., Neda, O. M. (2018). Modified particle swarm optimization for solution of reactive power dispatch. *Research Journal of Applied Sciences, Engineering and Technology*, Vol. 15(8), pp. 316-327, doi: 10.19026/rjaset.15.5917.
- 25.Mini Vishnu, Sunil Kumar, T. K. (2020). An improved solution for reactive power dispatch problem using diversity-enhanced particle swarm optimization. *Energies*, Vol. 13, 2862, doi: 10.3390/en13112862.
- 26.Muhammad, Y., Rahimdad, R., Muhammad, A., Farman, C., Naveed I., He, Y. (2020). Solution of optimal reactive power dispatch with FACTS devices: A survey. *Energy Reports*, Vol. 6, pp. 2211-2229, doi: 10.1016/j.egyr.2020.07.030.
- 27.Das, T., Roy, R., Mandal, K. (2021). Solving optimal reactive power dispatch problem with the consideration of load uncertainty using modified JAYA algorithm. *International Conference on Advances in Electrical, Computing, Communication and Sustainable Technologies (ICAECT), 2021*, pp. 1-6, doi: 10.1109/ICAECT49130.2021.9392508.
- 28.Das, T., Roy, R., Mandal, K. K. (2021). Integrated PV system with optimal reactive power dispatch for voltage security using JAYA algorithm. *7th International Conference on Electrical Energy Systems (ICEES), 2021*, pp. 56-61, doi: 10.1109/ICEES51510.2021.9383711.
- 29.Muhammad, Y., Akhtar, R., Khan, R. et al. (2021). Design of fractional evolutionary processing for reactive power planning with FACTS devices. *Sci Rep*, Vol. 11, 593, doi: 10.1038/s41598-020-79838-2.
- 30.Shanono, I. H., Muhammad, A., Abdullah, N. R. H. et al. (2021). Optimal reactive power dispatch: A bibliometric analysis. *Journal of Electrical Systems and Inf Technol*, Vol. 8(1), doi: 10.1186/s43067-020-00024-5.
- 31.Tudose, A. M., Picioroaga, I. I., Sidea, D. O., Bulac, C. (2021). Solving single- and multi-objective optimal reactive power dispatch problems using an improved salp swarm algorithm. *Energies*, Vol. 14(5), 1222, doi: 10.3390/en14051222.
- 32.Gholizadeh, S., Sojoudizadeh, R. (2019). Modified sine-cosine algorithm for sizing optimization of truss structures with discrete design variables. *Iran Univ. Sci. Technol.*, Vol. 9(2), pp. 195-212.
- 33.Tizhoosh, H. R. (2005). Opposition-based learning: a new scheme for machine intelligence. *International Conference on Computational Intelligence for Modelling, Control and Automation and International Conference on Intelligent Agents, Web Technologies and Internet Commerce (CIMCA-IAWTIC'06), 2005*, pp. 695-701, doi: 10.1109/CIMCA.2005.1631345.
- 34.Reddy, S. S. (2017). Optimal reactive power scheduling using cuckoo search algorithm. *International Journal of Electrical and Computer Engineering*, Vol. 7(5), pp. 2349-2356.
- 35.Reddy, S. S. (2014). Faster evolutionary algorithm based optimal power flow using incremental variables. *Electrical Power and Energy Systems*, Vol. 54, pp. 198-210.



MANUFACTURING 2022

7th International Scientific-Technical Conference

MANUFACTURING 2022

May 16-19, 2022 | Poznan, Poland

Special Session SS_08

Smart Manufacturing Systems

- Smart Manufacturing
- Collaborative Robotics
- Digital Twin
- Vision Systems
- Radio Frequency Identification
- Industrial Internet of Things
- Micro-Electro-Mechanical Systems
- Computational Intelligence, Soft Computing
- Edge Computing
- Big Data, Cloud Computing



ORGANIZERS SS_08

Sławomir Luściński
Kielce University of Technology, Poland
slawomir.luscinski@tu.kielce.pl

Ivan Pavlenko
Sumy State University, Ukraine
i.pavlenko@omdm.sumdu.edu.ua

Ján Piteľ
Technical University of Košice, Slovakia
jan.pitel@tuke.sk

Kamil Židek
Technical University of Košice, Slovakia
kamil.zidek@tuke.sk

<https://manufacturing.put.poznan.pl/>



Kozii I. S., Plyatsuk L. D., Hurets L. L., Volnenko A. A. (2021). Capturing aerosol particles in a device with a regular pulsating nozzle. *Journal of Engineering Sciences*, Vol. 8(2), pp. F1-F5, doi: 10.21272/jes.2021.8(2).f1

Capturing Aerosol Particles in a Device with a Regular Pulsating Nozzle

Kozii I. S.¹[0000-0003-0402-6876], Plyatsuk L. D.¹[0000-0003-0095-5846], Hurets L. L.¹[0000-0002-2318-4223], Volnenko, A. A.²[0000-0001-6800-9675]

¹ Sumy State University, 2, Rymskogo-Korsakova St., 40007, Sumy, Ukraine;

² M. Auezov South Kazakhstan State University, 5, Taukekhan Ave., 160012, Shymkent, Kazakhstan

Article info:

Submitted: August 25, 2021
 Accepted for publication: November 5, 2021
 Available online: November 10, 2021

*Corresponding email:

i.koziiy@ecolog.sumdu.edu.ua

Abstract. The paper is dedicated to reducing the technogenic impact on the environment of using highly efficient apparatus for the complex exhaust gas treatment, operating in the advanced turbulence regime – an apparatus with a regular pulsating nozzle (RPN). Devices with on-load tap-changers are characterized by high efficiency of capturing solid particles of different dispersion (e.g., fog, dust, and smoke), the possibility of self-cleaning of contact elements from sticky dust, low material consumption, and high reliability in operation. Purpose of the study – to obtain analytical solutions for assessing the efficiency of capturing polydisperse aerosols in an apparatus with an on-load tap-changer due to diffusion and inertial mechanisms. The paper proposes a new solution for the minimum effective diameter of aerosol particles that can be captured in devices with an on-load tap-changer and can be used for a wide range of diameters of absorbing liquid droplets and their number in the volume of the apparatus. The calculations allow us to say that the minimum effective diameter of aerosol particles captured by liquid drops in an apparatus with an on-load tap-changer is less than 0.3 microns.

Keywords: high-efficiency equipment, environment, dust and gas emissions, phase contact surface, movable plug, drop, condensation.

1 Introduction

Nowadays, environmental problems of the atmosphere, which is polluted by gas emissions with fine particulate matter (aerosols), at various industrial facilities, are among the most important issues [1]. Conventional particulate removal equipment (electrostatic precipitators, cyclones, and others) is ineffective for fine particles less than a micron in size.

One of the ways to intensify the process of diffuse-inertial deposition based on the technology of “wet” gas cleaning from different types of aerosols (e.g., dust, smoke, and fog) is to carry out these processes in the advanced turbulence regime [2]. Its realization is possible in devices with a regular pulsating nozzle (RPN) [3]. Devices with regular pulsating nozzle are characterized by high efficiency of capturing aerosols of different dispersion, the ability to self-clean contact elements from various adhesive inclusions, low material consumption, and high reliability, making them effective for widespread use.

2 Literature Review

Wet dust collectors are usually used to remove fine dust particles [4]. In this case, the capture of particles is realized through various mechanisms [5]. Dust particles smaller than 0.1 μm can be effectively trapped by a diffusion deposition mechanism (Brownian diffusion). The inertial mechanism and the gripping mechanism play an essential role in removing solid particles larger than 1 micron. To a large extent, the efficiency of dust collection depends on the size of liquid droplets [6–8].

Consequently, there are particles size of 0.1 – 1.0 microns, for the effective capture of which should be considered different deposition mechanisms and the efficiency of capturing particles of different dispersed composition has a minimum value, which is called the “minimum effective catching diameter” of particles [9, 10].

The efficiency of capturing fine particles (aerosols) in wet cleaning devices is calculated by considering the pattern of behavior of a single drop, the fraction of particles that were absorbed by the volume of the

considered drop during the operation of the device, and the subsequent summation of all drops per unit volume of the gas flow. The efficiency of this interaction can be determined by solving the Navier-Stokes equation for airflow around a liquid droplet. However, it is complicated to obtain a theoretical solution to the Navier-Stokes equation due to the complex flow structure considering the internal circulation of the droplets. Therefore, the approach of determining the effectiveness of the interaction of liquid droplets and solid particles of a pollutant by considering various mechanisms of particle deposition in the apparatus is of interest [11].

3 Research Methodology

3.1 General formulation

The physicochemical parameters of aerosol particles and the nature of the gas flow, which generates specific turbulent flows and pulsations in the apparatus, are one of the determining factors affecting the deposition efficiency of aerosol particles.

The droplet formation mechanism was considered in [4], where an equation was obtained to calculate the diameter of absorbing liquid droplets formed during the interaction of a vapor-gas-liquid flow in wet cleaning devices.

Based on the data of [12], for aerosol particles with a diameter of more than $0.05 \mu\text{m}$, the overall efficiency of capturing aerosol particles in wet dust collection devices can be represented as the sum of the capturing efficiencies due to the diffusion mechanism, the particle capture mechanism, and the inertial interaction mechanism:

$$\eta_{\text{tot}} = 1 - (1 - \eta_d) \cdot (1 - \eta_{\text{int}}) \cdot (1 - \eta_{\text{imp}}), \quad (1)$$

where η_d – the collection efficiency due to the diffusion mechanism; η_{int} – the efficiency of capturing due to the mechanism of capturing particles by a drop of liquid; η_{imp} – collection efficiency due to the inertial mechanism.

The equation describing the capture of polydisperse aerosol particles in wet cleaning devices can be represented by the following expression [13]:

$$\frac{\partial n(d_p, t)}{\partial t} = -n(d_p, t) \int_{D_{d \min}}^{D_{d \max}} \beta(d_p, D_d) n_d(D_d) dD_d, \quad (2)$$

where $n(d_p, t)$ – the aerosol particle size distribution function in the apparatus volume during t ; d_p – diameter of aerosol particles, m ; $n_d(D_d)$ – the function of the size distribution of the absorbing liquid droplets; D_d – diameter of droplets typical for a particular turbulent flow, m ; β – mass transfer coefficient, m/s .

The equation can represent the interaction of drops of absorbing liquid and aerosol particles:

$$\beta(d_p, D_d) = \frac{\pi D_d^2}{4} U(D_d) \eta(d_p, D_d), \quad (3)$$

where U – the speed of motion of a drop of absorbing liquid in apparatus volume, m/s ; $\eta(d_p, D_d)$ – the efficiency of interaction of aerosol particles d_p with drops of absorbing liquid D_d .

3.2 Laboratory installation

Based on the general rules and laws of heuristic modeling [10], a direct flow column-type apparatus with a regular structure of the turbulizing elements is developed, which complies with the well-known principles of longitudinal sectioning and is designed to clean aerosol from gases (Figure 1).

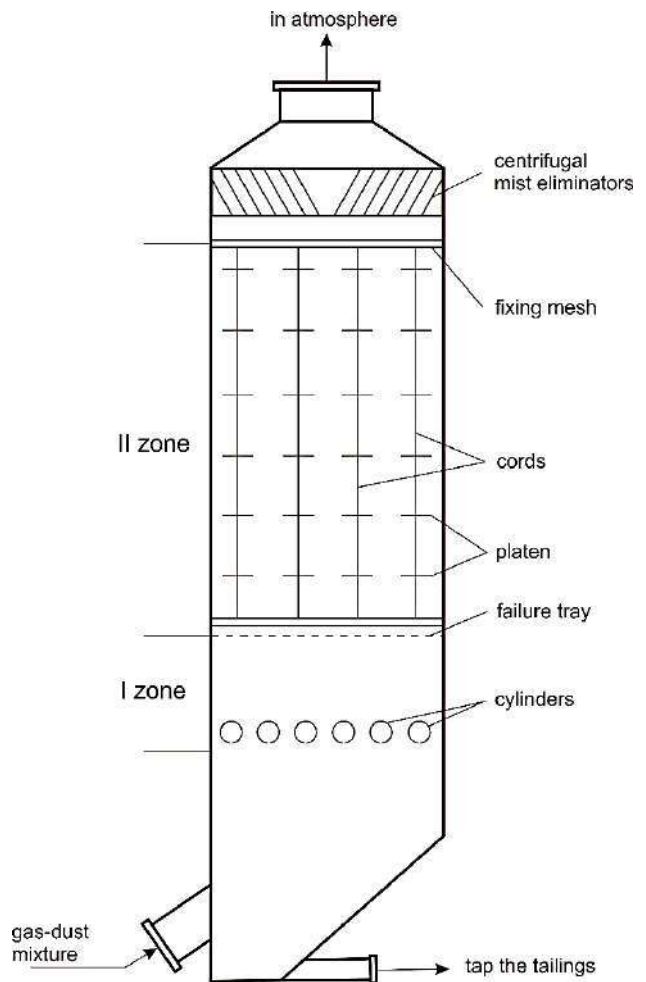


Figure 1 – Scheme of the investigated direct-flow apparatus with a regular arrangement of turbulizing elements.

The contact zone of the apparatus under study consists of two sequentially connected zones for cleaning exhaust gases from fine impurities.

In the lower part (zone I), there is an enlargement of aerosol particles captured from the gas stream due to the mechanism of condensation-coagulation deposition. The lower zone consists of a package of plane-parallel channels with turbulizing elements in the form of hollow cylinders. The cylinders have perforations in the lower part, which performs the function of steam channels (a vapor-liquid mixture is supplied). The two zones of the apparatus are

separated by a failing plate, which has a hole diameter of $d_o = 20$ mm and a free cross-sectional area of 45 %, which ensures the maintenance of a uniform dust-gas-liquid flow into the second zone of the apparatus.

The top of the unit (zone II), intended for capturing aerosols, is a packing layer in the form of strings evenly spaced over the section of the apparatus body with plates fixed on them.

The nature of the flow and turbulent eddies during the movement of the gas flow with aerosol particles in the direct-flow apparatus, the efficiency of the interaction of the gas and liquid phases (considering the joint flow with steam), make it possible to determine the general hydrodynamic picture in the apparatus.

The movement of aerosol particles in the second zone of the apparatus after flowing around the plates occurs with pulsations and oscillations, which are inherent in the separated stream of the gas flow. In addition, during the movement of a polydisperse aerosol in the zone of a single vortex, a redistribution of aerosol fractions occurs in the vortex volume. Thus, the coarse fraction of particles under the action of centrifugal forces by inertia tends to the periphery of the vortex, and the fine inertial fraction of particles rotates in the region of the axial zone of the vortex. Thus, the vortex flow and its detached (pulsated) nature of motion largely contribute to the intensification of the enlargement processes and further sedimentation of aerosol particles.

4 Results

Let us analyze the components of equation (3).

The results obtained in [14] assert that the secondary components of the efficiency of capturing aerosol particles are insignificant and simplify expression (1). The equation can represent the efficiency of interaction due to diffusion of aerosol particles:

$$\eta_d(d_p, D_d) = 2 \left(\frac{\sqrt{3}\pi D_{diff}}{4D_d U(D_d)} \right)^{2/3} \left[\frac{(1-\alpha)(3\sigma+4)}{J+\sigma K} \right]^{1/3}, \quad (4)$$

where the density of the absorbing medium α is defined as the volume fraction of droplets; σ is the ratio of the viscosity of the liquid-absorbing medium to the gas phase;

$$J = 1 - \frac{6}{5}\alpha^{1/3} + \frac{1}{5}\alpha^2; \quad K = 1 - \frac{9}{5}\alpha^{1/3} + \alpha + \frac{1}{5}\alpha^2.$$

Aerosol particle diffusion coefficient D_d :

$$D_d = \frac{k_B T K_C(d_p)}{3\pi\mu d_p}, \quad (5)$$

where k_B – the Boltzmann constant; T – the absolute temperature, K; μ – viscosity of the gas phase, kg/(m·s); K_C – Cunningham slip correction factor, which is applied in the case when aerosol particles are less than 15 microns, otherwise it is taken equal to 1.

In the case of an aerosol particle moving along a conventional trajectory towards a liquid drop, at the

moment of approaching it at a distance not less than the particle radius, a mechanism for the capture of this particle by a liquid drop is possible. The efficiency of particle sedimentation due to the capture effect [7] will be:

$$\eta_{int}(d_p, D_d) = \left(\frac{D_d + d_p}{D_d} \right). \quad (6)$$

Under the described conditions [13], the efficiency of the capture of aerosol particles by a liquid drop due to the capture mechanism is determined by the equation:

$$\eta_{int}(d_p, D_d) = \frac{1-\alpha}{J+\sigma K} \left[\frac{R}{1+R} + \frac{1}{2} \left(\frac{R}{1+R} \right)^2 (3\sigma+4) \right], \quad (7)$$

where $R = d_p/D_d$.

By quantifying the size of particles and liquid droplets in the apparatus, it can be determined that the efficiency of the capture mechanism $\eta_{int}(d_p, D_d) = 0.4$ % at $d_p = 1$ μ m, $D_d = 2 \cdot 10^{-3}$ m and the characteristic size of the plates in the vortex formation zone is 0.05 m.

For aerosol particles larger than 1 μ m in size, the key mechanism for their removal in an apparatus with RPN an on-load tap changer is inertial deposition [4]. A dimensionless quantity that describes the properties of the inertial interaction of particles - the Stokes number:

$$Stk = \frac{\rho_p d_p^2 U(D_d)}{18\mu D_d}, \quad (8)$$

where d_p – the density of particles.

To estimate the efficiency of collision of aerosol particles with liquid droplets due to the inertial mechanism, one can use the equation in [15]:

$$\eta_{imp}(d_p, D_d) = \left(\frac{Stk}{Stk + 0,35} \right)^2. \quad (9)$$

The overall efficiency of the interaction of aerosol particles with a drop of absorbing liquid, considering the mechanism of diffusion, interception, and inertia, can be represented by the sum of equations (4), (6), and (8). It should be clarified that the solution of the sum of these equations is a complex mathematical problem, which makes it impossible to obtain analytical dependences for aerosols of different dispersed compositions. Therefore, the primary task is to allow several approximations to assess the effectiveness of the interaction of aerosol particles and drops of absorbing liquid.

The speed of motion of drops of an absorbing liquid, considering the works [16, 17], can be determined as:

$$U(D_d) = c_1 D_d^{c_2}, \quad (10)$$

where c_1, c_2 – constants that consider the operational and design parameters of the apparatus and are determined experimentally.

In [13], a study was carried out to compare the effectiveness of interaction due to three mechanisms,

depending on the diameter of aerosol particles. Based on the graphical dependencies, for larger particles ($d_p > 10 \mu\text{m}$), the inertial interaction mechanism prevails, for smaller ones ($d_p < 5 \mu\text{m}$) – the diffusion mechanism.

Considering the data of [18], a promising approach to solving the problem of effective interaction of the system of an aerosol particle – an absorbing liquid droplet is to consider the diffusion and inertial mechanisms. In this case, the capture mechanism of aerosol particles of different dispersed compositions can be neglected due to the insignificant contribution to the total deposition efficiency.

There is a particle size for which neither diffusion nor inertial collision effectively allows the removal of particles – the minimum particle diameter for effective interaction with a droplet of absorbing liquid. To determine the minimum diameter of aerosol particles, we use the data on the deposition efficiency due to the diffusion and inertial mechanisms.

To clarify the efficiency of the diffusion interaction, we use the approximation of the Cunningham slip correction coefficient by the following equation:

$$K_C = \text{Max} \left[1,664 \left(\frac{2\lambda}{d_p} \right), 2,609 \sqrt{\frac{2\lambda}{d_p}} \right]. \quad (11)$$

Using this approximation, in [18], an analytical solution was obtained for particles of various dispersed compositions in wet cleaning devices with a predominantly fine particle size (diffusion interaction mechanism).

To assess the effectiveness of the mechanism of inertial interaction, we use the approximation from [2]:

$$\eta_{imp}(d_p, D_d) = \text{Min} [3, 4Stk^{9/5}, 1]. \quad (12)$$

Substituting equations (4)–(6), (10), and (11) into equation (2), we get a dependence for assessing the interaction of liquid droplets with aerosol particles, for which the diffusion mechanism prevails:

$$\beta_d(d_p, D_d) = Ad_p^{-1} D_d^{(4+c_2)/3}, \quad (13)$$

where

$$A = \frac{\pi}{2} \left[\frac{c_1 \lambda (1-\alpha)(3\sigma+4)}{24(J+\sigma K)} \right]^{1/3} \left(\frac{2,609 k_B T}{\mu} \right)^{2/3}. \quad (14)$$

Substituting equations (7), (9), and (11) into equation (2), we obtain a dependence for assessing the interaction of liquid droplets with aerosol particles, for which the inertial mechanism prevails:

$$\beta_{imp}(d_p, D_d) = Bd_p^{18/5} D_d^{(1+14c_2)/5}, \quad (15)$$

where

$$B = \frac{3,4\pi c_1^{14/5}}{4} \left(\frac{\rho_p}{18\mu} \right)^{9/5}. \quad (16)$$

To determine the minimum effective diameter of a particle that can interact with a liquid drop, it is necessary to consider the diffusion and inertial mechanisms. The interaction of the above aerosol particles and droplets can be represented by the sum of equations (12) and (14):

$$\beta(d_p, D_d) = Ad_p^{-1} D_d^{(4+c_2)/3} + Bd_p^{18/5} D_d^{(1+14c_2)/5}. \quad (17)$$

Let us consider Eq. (16) as a homogeneous differential one and, having solved it, we obtain the dependence for determining the minimum effective diameter of the interaction of aerosol particles and a droplet:

$$d_{p \min} = \left(\frac{5A}{18B} \right)^{5/23} D_d^{(17-37c_2)/69}. \quad (18)$$

The resulting dependence (17) makes it possible to determine the value of the minimum diameter of an aerosol particle that can be captured by a liquid drop in devices with an on-load tap changer and can be used for a wide range of the diameter of absorbing liquid drops and their number in the volume of the device. To select the values of c_1 and c_2 , the characteristics of the experimental stands of wet cleaning devices were taken [19]. The calculation results for different equilibrium droplet diameters characteristic for different turbulent flow in the apparatus ($D_d = 1-7 \text{ mm}$) and irrigation density of the absorbing liquid are presented in (Figure 2).

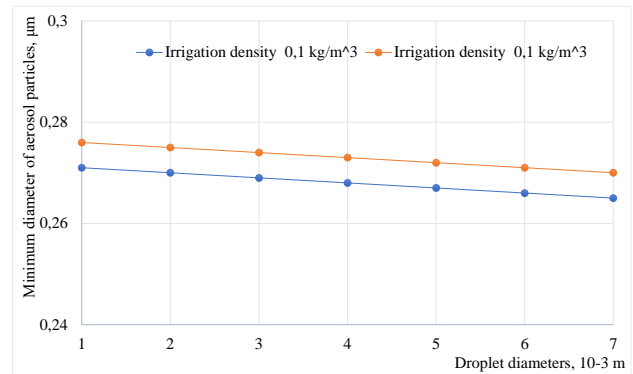


Figure 2 – The minimum diameter of aerosol particles for different droplet diameters and irrigation density of the absorbing liquid

5 Conclusions

In this work, studies of various mechanisms of deposition of aerosols capable of being captured by liquid droplets in an apparatus with RPN on-load tap changer, depending on the particle size distribution parameters of aerosols carried out.

The choice of particle deposition's diffusion and inertial mechanisms, as prevailing in the apparatus with RPN on-load tap changer, has been substantiated.

The calculations made allow us to say that the minimum effective diameter of aerosol particles that will be captured by liquid droplets in an apparatus with RPN on-load tap-changer, without considering the effects in the first zone of the apparatus, is not less than 0.3 microns, which indicates the possibility of working with fine aerosol emissions from industry.

References

1. Hurets, L. L., Kozii, I. S., Miakaieva, H. M. (2017). Directions of the environmental protection processes optimization at heat power engineering enterprises. *Journal of Engineering Sciences*, Vol. 4(2), pp. G12-G16, doi: 10.21272/jes.2017.4(2).g12.
2. Neira, M. (2016). *Ambient Air Pollution: A Global Assessment of Exposure and Burden of Disease*. WHO Document Production Services. Geneva, Switzerland.
3. Tronvil, P. (2008). Developing standards: Global standards for air cleaning equipment. *Filtration and Separation*, Vol. 45, no. 9, pp. 28-31.
4. Kozii, I. S., Plyatsuk, L. D., Hurets, L. L. (2021). Distribution of the Dispersed Phase in the Gas Cleaning Equipment with Pulsating Plug. *Problemele Energeticii Regionale*, Vol. 1(49), pp. 29-38, doi: 10.52254/1857-0070.2021.1-49.05.
5. Phillips, H. W. (2000). Select the proper gas cleaning equipment. *Chemical Engineering Progress*, Vol. 96(9), pp. 19-38.
6. Sutherland, K. (2007). Choosing equipment: Cleaning air and gas. *Filtration and Separation*, Vol. 44(1), pp. 16-19.
7. Aliyev, G. M. (1986). *Technique of Dust Collection and Purification of Industrial Gases*. Metallurgy, Moscow.
8. Cuia, L., Songa, X., Lia, Y., Wangb, Y., Fenga, Y., Yana, L., Dong, Y. (2018). Synergistic capture of fine particles in wet flue gas through cooling and condensation. *Applied Energy*, Vol. 225, pp. 656-667, doi: 10.1016/j.apenergy.2018.04.084.
9. Sun, J., Liu, B. Y-H., McMurry, P. H., Greenwood, S. (1994). A method to increase control efficiencies of wet scrubbers for submicron particles and particulate metals. *Air and Waste*, Vol. 44, pp. 184-185, doi: 10.1080/1073161X.1994.10467248.
10. Sui, Z. F., Zhang, Y. S., Peng, Y. (2016). Fine particulate matter emission and size distribution characteristics in an ultra-low emission power plant. *Fuel*, Vol. 185, pp. 863-871, doi: 10.1016/j.fuel.2016.08.051.
11. Xu, Y. S., Liu, X. W., Cui, J. (2016). Field measurements on the emission and removal of PM_{2.5} from coal-fired power stations: PM removal performance of wet electrostatic precipitators. *Energy Fuel*, Vol. 30(9), pp. 7465-7473.
12. Kim, H. T., Jung, C. H., Oh, S. N., Lee, K. W. (2001). Particle removal efficiency of gravitational wet scrubber considering diffusion, interception, and impaction. *Environmental Engineering Science*, Vol. 18, pp. 125-136.
13. Park, S. H., Jung, C. H., Jung, K. R., Lee, B. K., Lee, K.W. (2005). Wet scrubbing of polydisperse aerosols by freely falling droplets. *Aerosol Science*, Vol. 36, pp. 1444-1458, doi: 10.1016/j.jaerosci.2005.03.012.
14. Jung, C. H., Lee, K. W. (1998). Filtration of fine particles by multiple liquid drop and gas bubble systems. *Aerosol Science and Technology*, Vol. 29, pp. 389-401.
15. Calvert, S. (1984). Particle control by scrubbing. *Handbook of Air Pollution Technology*. Wiley, New York, pp. 215-248.
16. Kessler, E. (1969). *On the Distribution and Continuity of Water Substance in Atmospheric Circulations*. Meteorological Monograph, Vol. 32.
17. Mircea, M., Stefan, S. (1998). A theoretical study of the microphysical parameterization of the scavenging coefficient as a function of precipitation type and rate. *Atmospheric Environment*, Vol. 32, pp. 2931-2938.
18. Lee, K.W., Liu, B.Y. H. (1980). On the minimum efficiency and the most penetrating particle size for fibrous filters. *Journal of the Air Pollution Control Association*, Vol. 30, pp. 377-381.
19. Jung, C. H., Kim, Y. P., Lee, K. W. (2002). Analytic solution for polydispersed aerosol dynamics by a wet removal process. *Journal of Aerosol Science*, Vol. 33, pp. 753-767.



Kun T., Jie H. W., Markovych S., Wang Y. (2021). Dimet Laval nozzle expansion section analysis and optimization. *Journal of Engineering Sciences*, Vol. 8(2), pp. F6-F10, doi: 10.21272/jes.2021.8(2).f2

Dimet Laval Nozzle Expansion Section Analysis and Optimization

Kun T.^{1*}, Jie H. W.¹, Markovych S.¹, Wang Y.²

¹ National Aerospace University “Kharkiv Aviation Institute”, 17, Chkaloova St., 61000 Kharkiv, Ukraine;

² Commercial Aircraft Corporation of China, Ltd., 1027, Changning Rd., 200050 Shanghai, China

Article info:

Submitted:
Accepted for publication:
Available online:

August 5, 2021
November 18, 2021
November 23, 2021

*Corresponding email:

tankun09@126.com

Abstract. The cold spray technology mainly accelerates the powder in the Laval nozzle by gas, ensuring that the powder has a greater velocity at the exit of the Laval nozzle, and achieving high-efficiency deposition on the substrate, thereby obtaining a better performance of the deposition coating. The article uses numerical simulation to study the influence of the length of the expansion section of the Dimet Laval nozzle on the acceleration effect of Al powder. The results show that the length of the expansion section of the nozzle is an essential factor affecting the velocity of the Al powder at the nozzle outlet. Through analysis, it can be known that the pressure inlet range of the Dimet Laval nozzle is 1.0 MPa, and the length of the expansion section is about 210 mm, which can ensure that the Al powder has a better acceleration effect in the nozzle and has a better velocity at the nozzle outlet. It is recommended that the joints between the small sections of the nozzle expansion section should be kept as smooth as possible so that the accelerating effect of the accelerating gas on the Al powder is more uniform and stable.

Keywords: cold spray nozzle, turbulence, velocity, Laval nozzle, numerical simulation.

1 Introduction

There are many turbulence models used to simulate the compressible flow inside the Laval nozzle. For example, the S-A turbulence model was proposed by Spalart and Allmaras in 1992. It is believed that the S-A turbulence model is often used for the numerical simulation of large gradient, near-wall gas flow [1]. The k-ε turbulence model is mainly proposed for high Reynolds number flows [2]. Yuan scholars believe that the k-ω turbulence model has a small amount of calculation and the processing of boundary conditions is straightforward [3].

First, the three turbulence models of S-A, k-ε, and k-ω can be compared in terms of convergence velocity, mass flow error, Mach number error, to provide a reference for choosing a turbulence model that simulates the flow of cold spray technology particles in a Laval nozzle [4].

In the simulation of the internal flow channel of the Laval nozzle, the three commonly used turbulence models are the S-A model, k-ε model, and k-ω model.

Yang [5, 6] scholars have shown that the k-ω turbulence model is compared with the S-A turbulence model. The k-ε turbulence model can better represent the flow law of the internal flow channel of the Laval nozzle; compare the residual diagram, the k-ω turbulence model has a better convergence velocity; compare the mass flow

error, the k-ω turbulence model has the smallest mass flow error; compare the Mach number Error, the Mach number error of the k-ω turbulence model is the smallest ((theoretical calculated Mach number-numerical simulation maximum Mach number)/theoretical Mach number × 100 %). Therefore, the turbulence model is used when simulating the internal flow passage of the Dimet Laval nozzle [4].

Analyze the influence of the length of the expansion section of the cold spray nozzle on the outlet velocity of the powders.

2 Research Methodology

2.1 The governing equation

The compressible two-dimensional axisymmetric flow satisfies the N-S equation in the cylindrical coordinate system [5].

According to this scheme, the angles are calculated by formulas [15]:

$$\frac{\partial Q}{\partial t} + \frac{\partial E_u}{\partial x} + \frac{\partial F_u}{\partial r} + \frac{\partial E_v}{\partial x} + \frac{\partial F_v}{\partial r} + \frac{H}{r} = 0 \quad (1)$$

2.2 The turbulence models

The specific description of the turbulence model is as follows:

$$\rho \frac{D\vec{v}}{Dt} = G_v + \frac{1}{\sigma_v} \left\{ \frac{\partial}{\partial x_j} \left[\left(\mu + \rho \vec{v} \right) \frac{\partial \vec{v}}{\partial x_j} \right] + C_{b2} \rho \left[\frac{\partial \vec{v}}{\partial x_j} \right]^2 \right\} - Y_v \quad (2)$$

Among them, \vec{v} represents the turbulent motion viscosity coefficient, ν represents the molecular motion viscosity coefficient; G_v is the generation term, and Y_v is the destruction term.

k- ϵ Turbulence Model [6] is as follows:

$$\frac{\partial \rho \kappa^m}{\partial t} + \frac{\partial \rho u_i \kappa^m}{\partial x} + \frac{\partial \rho v_i \kappa^m}{\partial r} = \frac{\partial}{\partial r} \left[\frac{\mu_i r^m}{\sigma_k} \frac{\partial \kappa}{\partial r} \right] + r^m (P\kappa - \rho \epsilon) \quad (3)$$

$$\frac{\partial \rho \epsilon^m}{\partial t} + \frac{\partial \rho u_i \epsilon^m}{\partial x} + \frac{\partial \rho v_i \epsilon^m}{\partial r} = \frac{\partial}{\partial r} \left[\frac{\mu_i r^m}{\sigma_\epsilon} \frac{\partial \epsilon}{\partial r} \right] + r^m (C_1 P\kappa - C_2 \rho \epsilon) \frac{\epsilon}{\kappa} \quad (4)$$

Also, the k- ω Turbulence Model [6] is as follows:

$$\frac{\partial \rho \kappa^m}{\partial t} + \frac{\partial \rho u_i \kappa^m}{\partial x} + \frac{\partial \rho v_i \kappa^m}{\partial r} = \frac{\partial}{\partial r} \left[\frac{\mu_i r^m}{\sigma_k} \frac{\partial \kappa}{\partial r} \right] + r^m (P\kappa - C_D \rho \kappa \omega^{0.5}) \quad (5)$$

$$\frac{\partial \rho \omega^m}{\partial t} + \frac{\partial \rho u_i \omega^m}{\partial x} + \frac{\partial \rho v_i \omega^m}{\partial r} = \frac{\partial}{\partial r} \left[\frac{\mu_i r^m}{\sigma_\omega} \frac{\partial \omega}{\partial r} \right] + r^m (C_1 P\kappa - C_2 \rho \kappa \omega^{0.5}) \frac{\omega}{\kappa} \quad (6)$$

2.3 Experimental setup

The cold spray Dimet Laval nozzle is used is to be chosen, as shown in Figure 1 a, and the detailed design parameters of the Dimet Laval nozzle are shown in Figure 1 b [7]; After that, the internal flow channel of the Dimet Laval nozzle is obtained by 3D modeling software. The gas inlet of the Dimet Laval nozzle and the inlet of Al powder are perpendicular to each other, and the powder inlet is located at the throat of the Dimet Laval nozzle.

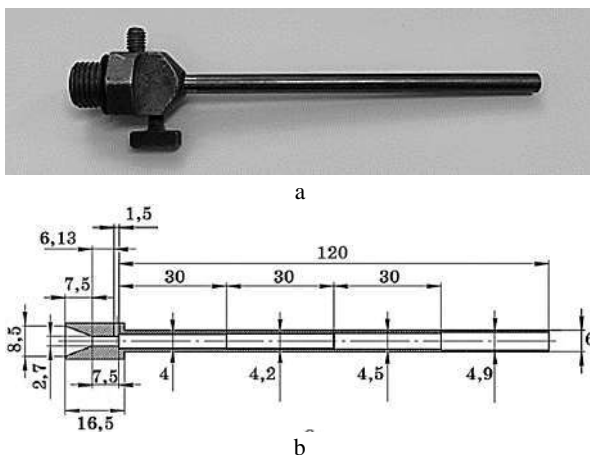


Figure 1 – Dimet Laval nozzle (a) and its design parameters (b)

Many technical parameters affect the gas and powder flow velocity in the Dimet Laval nozzle, such as temperature (powder, gas, or substrate), powder size, spraying distance, gas pressure, Laval nozzle structure. Tan summarized the influence of technical parameters on cold spray technology [8–10]. The length of the

expansion section of the Dimet Laval nozzle is an essential factor that affects the acceleration of the powders in the Dimet Laval nozzle. If the expansion section is too short, it will not accelerate the powders in the Dimet Laval nozzle fully. If the expansion section is too long, there will be possible that the powder has already begun to decelerate in the Dimet Laval nozzle; therefore, it is essential to research the influence of the length of the expansion section on the velocity of the powder at the nozzle outlet.

In the article, the pressure inlets are 0.8 MPa, 1.0 MPa, and 1.2 MPa, and the length of the expansion section of the Dimet Laval nozzle is 120 mm, 150 mm, 180 mm, 210 mm, and 240 mm. The velocity distribution of Al powder at the outlet of Dimet Laval nozzle is researched. The gas is air, the total inlet temperature is 900 K, and the powder is made of spherical Al powder with a diameter of 25 μm .

3 Results

3.1 Analysis of Al powder velocity at the same pressure

Solidworks simulate the velocity distribution of Al powder in the Dimet Laval nozzle. Firstly, research the velocity distribution of the Al powder in the expansion section of the Dimet Laval nozzle with different lengths under the same pressure inlet; secondly, research the velocity distribution of Al powder in the nozzle at different pressure inlets of the expansion section of the Dimet Laval nozzle of the same length.

Analyze the expansion section of different lengths under the same pressure inlet conditions, the acceleration of the Al powder in the Dimet Laval nozzle, and the velocity at the nozzle outlet; respectively simulate the pressure inlets at 0.8 MPa, 1.0 MPa, and 1.2 MPa; As shown in Figure 2, the pressure inlet is 0.8 MPa, and the velocity distribution of Al powder in the expansion section of different lengths.

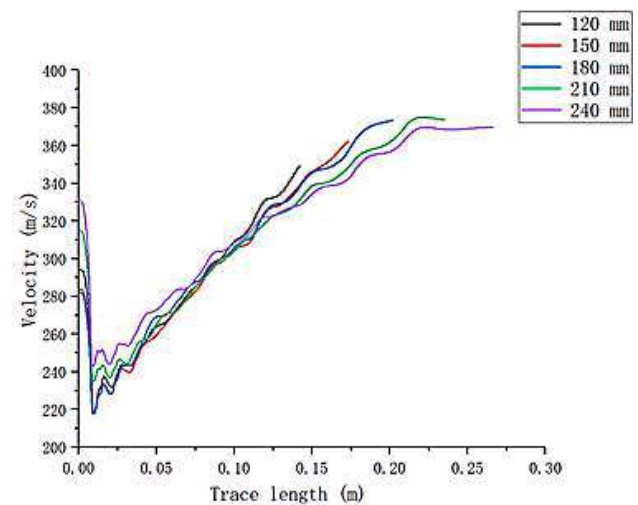


Figure 2 – The pressure inlet is 0.8 MPa, the velocity distribution of Al powder in the expansion section of different lengths

It can be seen from Figure 2 that when the pressure inlet is 0.8 MPa, the Al powder has been accelerated near the expansion section of the nozzle 220 mm, so the expansion section length is 120 mm, 150 mm, and 180 mm nozzles, the Al powder is still in a state of acceleration before the nozzle exit.

Expansion section length of 210 mm and 240 mm nozzles, Al powder, has been accelerated before the nozzle exit, and the Al powder decelerates in the nozzle; five different lengths of expansion section nozzles, The Al powder has reached the critical velocity of spraying, which can meet the deposition on the substrate.

As shown in Figure 3, the pressure inlets are 1.0 MPa and 1.2 MPa, respectively, and the velocity distribution of Al powder in the expansion section of different lengths.

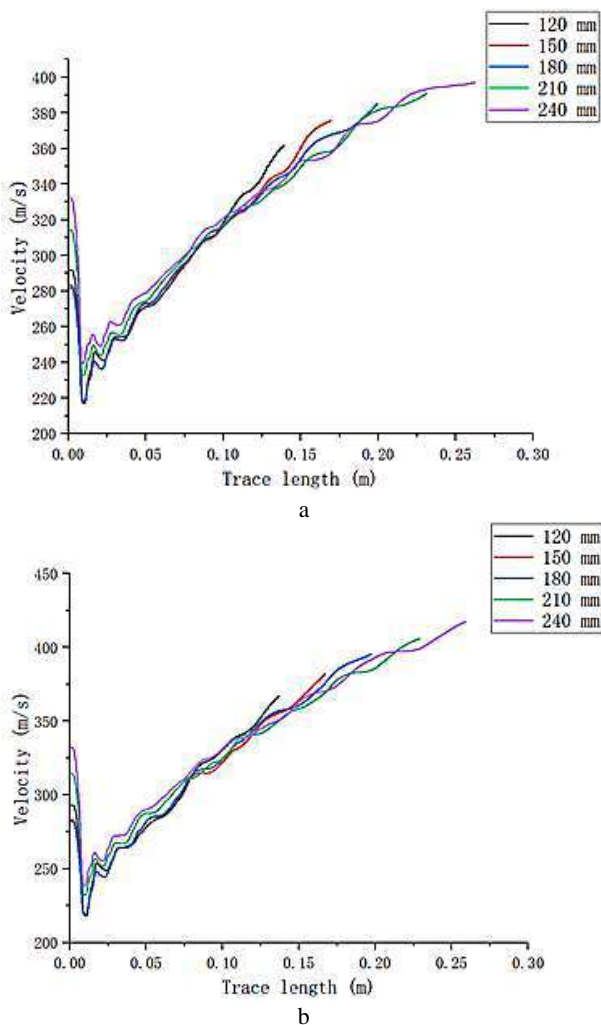


Figure 3 – The pressure inlets are 1.0 MPa (a) and 1.2 MPa (b), the velocity distribution of Al powder in the expansion section of different lengths

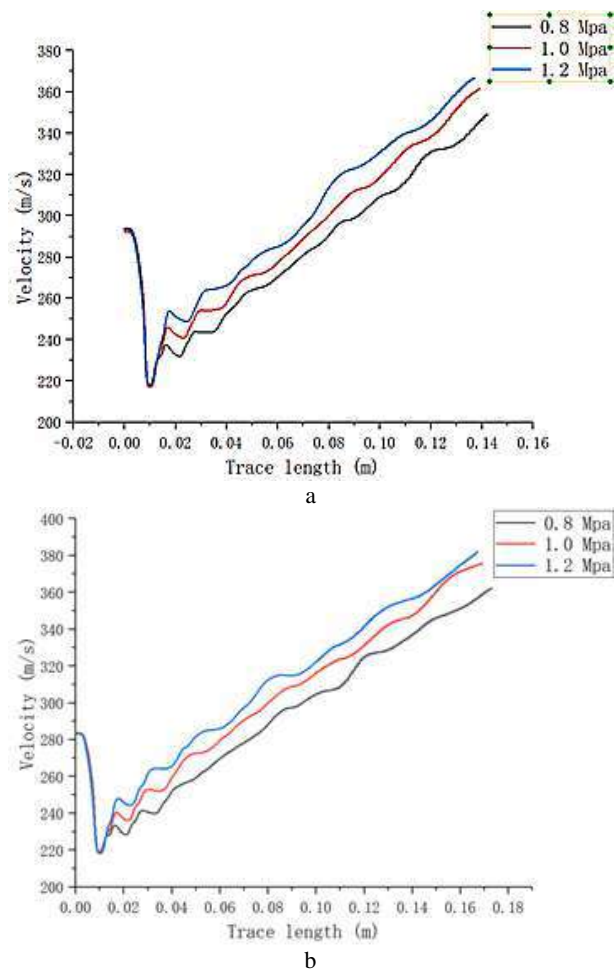
Figure 3 a shows that when the pressure inlet is 1.0 MPa. For nozzles with an expansion section length of 120 mm, 150 mm, 180 mm, and 210 mm, the Al powder is still accelerating in the nozzle; for nozzles with an expansion section length of 240 mm, the velocity of Al powder in the nozzle slowly stabilizes. In Figure 3, the curvature of the curve represents the acceleration of the

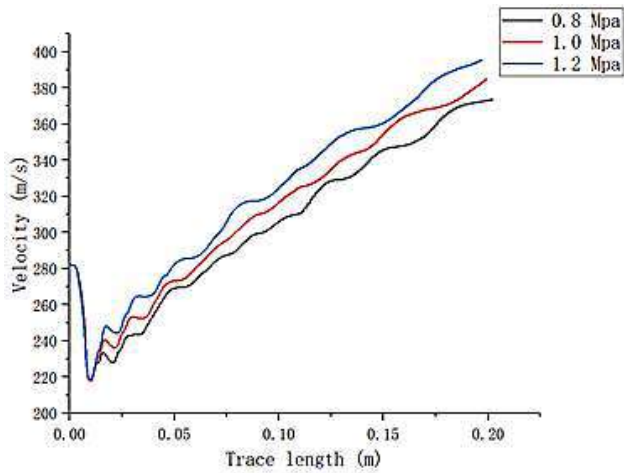
Al powder. Combined with the curvature analysis of the five curves, as the length of the expansion section increases, the curvature gradually becomes smaller, indicating that the acceleration of the Al powder inside the nozzle becomes smaller as the length of the expansion section increases.

It can be seen from Figure 3 b that when the pressure inlet is 1.2 MPa, the Al powder in the nozzles of the five different length expansion sections is still accelerating. This is because the pressure inlet is increased. Combined with the five curves in Figure 3 b, it can also be seen that as the length of the expansion section increases, the curvature gradually becomes smaller, indicating that the acceleration effect of the Al powder in the nozzle is gradually weakened.

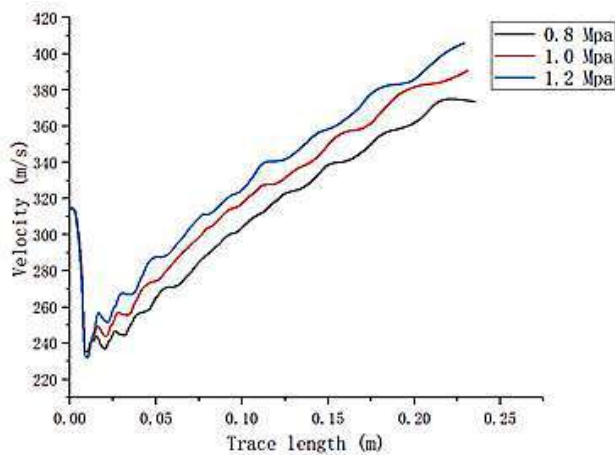
3.2 Analysis of Al powder velocity in the same expansion section length

Under the condition of equal expansion section length, analyze the inlet of the different pressure, the acceleration of Al powder in the Dimet Laval nozzle, and the velocity at the nozzle outlet; through simulation, the expansion section length of the nozzle is 120 mm, 150 mm, 180 mm, 210 mm, and 240 mm the Al powder velocity distributions. As shown in Figure 4, the velocity distribution of the Al powder in the nozzles of the expansion section of different lengths when the pressure inlets are 0.8 MPa, 1.0 MPa, and 1.2 MPa.

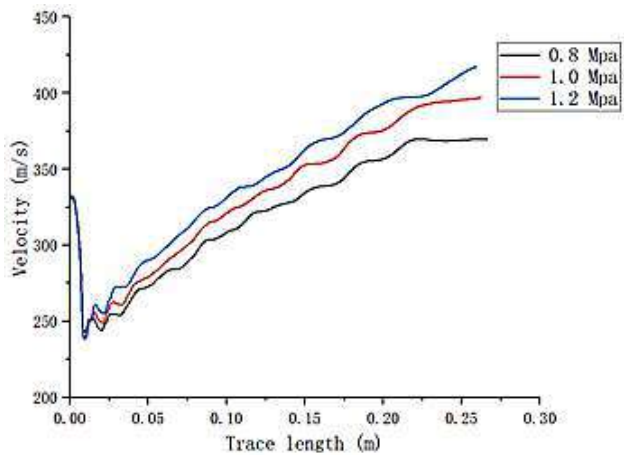




c



d



e

Figure 4 – The length of the expansion section is 120 mm (a), 150 mm (b), 180 mm (c), 210 mm (d), and 240 mm (e), the Al powder velocity distribution under different pressure inlets conditions

From Figures 4 a–c, the pressure inlets are an essential factor determining the velocity of Al powder acceleration in the nozzle. The higher the pressure inlet, the shorter the acceleration time of the Al powder; the expansion section the length of the Al powder is also an influencing factor that affects the acceleration velocity of the Al powder in the nozzle.

The expansion nozzle is within a specific length range. As the length of the expansion section increases, the faster the Al powder can obtain in the nozzle.

It can be seen from Figures 4 d–e, when the length of the expansion section of the nozzle reaches a particular value, the acceleration effect of Al powder is reduced; The expansion nozzle of the same length can improve the acceleration effect of the Al powder in the nozzle, and can appropriately increase the pressure inlet. When the pressure inlet is 0.8 MPa, the velocity of Al powder in the nozzle increases first and then decreases; when the pressure inlet is 1.0 MPa, the acceleration effect of Al powder in the nozzle is weakened. By comparing the slopes of all the velocity curves in Figure 4, as the length of the expansion section increases, the curvatures of the different pressure curves have been decreasing, indicating that the acceleration effect of Al powder is gradually weakening.

Therefore, the pressure inlet is too small, and the nozzle expansion section is too short, which is not conducive to the acceleration of the Al powder in the nozzle.

It is essential to choose the proper length of the expansion nozzle in the proper pressure range; increasing the pressure inlet to increase the velocity of the Al powder or increasing the expansion section length to obtain a more significant outlet velocity will increase the spraying cost. Therefore, in the pressure inlet range of 1.0 MPa, the length of the expansion section of the nozzle is about 210 mm, which can ensure that the Al powder has a better acceleration effect in the nozzle and has a good exit velocity at the nozzle outlet, to ensure smooth completion on the substrate deposition.

4 Conclusions

The length of the Dimet Laval nozzle is an essential factor affecting the Al powder outlet velocity. Therefore, a better Al powder outlet velocity can be obtained by changing the length of the expansion section of the Dimet Laval nozzle.

Through analysis, the pressure inlet range of the Dimet Laval nozzle is 1.0 MPa, and the length of the expansion section is about 210 mm, which can ensure that the Al powder has a better acceleration effect in the nozzle has a better exit velocity at the nozzle outlet.

Dimet Laval nozzle expansion section is divided into four parts in total. Each part is 30 mm; it is recommended that the joint between each part be rounded so that the accelerated gas will not produce excessive gas backflow at the joint. This ensures that the velocity of the gas in the entire nozzle remains uniform and stable, thereby ensuring that the velocity of the sprayed material has a better acceleration effect.

5 Acknowledgments

The author would like to thank the China Scholarship Council for its support (No. 201908360307).

References

1. Jameson, A., Schmidt, W., Turkel, E. (2012). Numerical solution of the Euler equations by finite volume methods using Runge Kutta time stepping schemes. 14th Fluid and Plasma Dynamics Conference, Palo Alto, CA, USA, doi: 10.2514/6.1981-1259.
2. Fujun, W. (2004). *Computational Fluid Dynamics Analysis*. Tsinghua University Press, Beijing, China.
3. Xin, Y. (1998). Choice of two-equation turbulence model in compressible viscous flow. *Journal of Engineering Thermophysics*, Vol. 19(4), pp. 427-432. doi: 10.1109/ISIC.1999.796628.
4. Yang, Z., Xin, Z., Xie, H. (2010). The comparison of turbulence model of cfd in the numerical simulation of nozzle flow field numerical simulation. *Journal of Heilongjiang Bayi Agricultural University*, Vol. 22(5), pp. 36-38, doi: 10.1016/j.euromechflu.2013.11.006.
5. He, F., Xie, J., Hao, P., Yao, Z. (2001). Computation of axisymmetric jet flow with Spalart-Allmaras turbulence model. *Journal of Propulsion Technology*, Vol. 22(1), pp. 43-46.
6. Zhenyu, H., Wencan, X. (1999). Numerical simulation of turbulent jets. *Journal of Beijing Institute of Technology*, Vol. 19(6), pp. 691-695, doi: 10.3969/j.issn.1001-0645.1999.06.007.
7. Dolmatov, A. I., Bilchuk, O. V. (2019). Simulation of process of solid particles sputtering with Dimet nozzle. *Metallofizika i Noveishie Tekhnologii*, Vol. 41(7), pp. 927-940, doi: 10.15407/mfint.41.07.0927.
8. Kun, T., Markovych S., Hu, W. (2021). On the characteristics of cold spray technology and its application in aerospace industries. *IOP Conference Series: Earth and Environmental Science*, Vol. 719(3), 032023, doi: 10.1088/1755-1315/719/3/032023.
9. Kun, T., Markovych, S., Hu, W. (2021). Review of application and research based on cold spray coating materials. *Aerospace Technic and Technology*, Vol. 1, pp. 47-59, doi: 10.32620/akt.2021.1.05.
10. Kun, T., Markovych, S., Hu, W. (2020). Review of manufacturing and repair of aircraft and engine parts based on cold spraying technology and additive manufacturing technology. *Aerospace Technic and Technology*, Vol. 3, pp. 53-70, doi: 10.32620/akt.2020.3.06.



Javanbakht T. (2021). Comparative study of rheological properties of polyvinyl alcohol and polyethylene glycol. *Journal of Engineering Sciences*, Vol. 8(2), pp. F11-F18, doi: 10.21272/jes.2021.8(2).f3

Comparative Study of Rheological Properties of Polyvinyl Alcohol and Polyethylene Glycol

Javanbakht T.

Department of Chemistry and Biochemistry, Department of Physics, Concordia University,
Richard J. Renaud Science Complex, 7141 Sherbrooke Street West, Montreal, Quebec, Canada

Article info:

Submitted:

Accepted for publication:

Available online:

September 3, 2021

December 9, 2021

December 14, 2021

*Corresponding email:

taraneh.javanbakht@concordia.ca

Abstract. Hydrogels are promising biomaterials for diverse applications that require studying their rheological properties. While some properties of hydrogels have been investigated, their comparative analysis for a deeper understanding of their rheological properties is required to determine their mechanical behavior. Polyvinyl alcohol (PVA) and polyethylene glycol (PEG) are among the hydrogels with diverse applications in engineering. This study aims to provide comparative data on their rheological properties. Both PVA and PEG showed steady shear viscosity as their viscosity did not show a huge change with time. Their shear viscosity increased with shear strain. PEG showed more shear thickening behavior than PVA. While the shear viscosity of PVA reached a plateau, that of PEG continued to increase. This was attributed to the sensitivity of PEG to its deformation because of the junction separations after the application of mechanical force on the polymer. Furthermore, the slow increase in the shear viscosity of both polymers was observed with the increase of the shear rate. This increase was 2.4 % for PVA and 8.7 % PEG, respectively. As these polymers are among the candidates for the preparation of nanocomposites, the results of this study can provide the required information for their applications in engineering.

Keywords: rheology, hydrogels, polyvinyl alcohol, polyethylene glycol, mechanical engineering.

1 Introduction

Polyvinyl alcohol (PVA) and polyethylene glycol (PEG) are among the polymers that absorb water during their preparation. These hydrogels are transparent materials that can be prepared by dissolving in water [1–4] and contain a lot of water in their total mass due to their hydrophilic functional groups attached to their backbone [5–8]. The biocompatibility of PVA and PEG has made them excellent candidates for medical applications for drug delivery systems and tissue engineering [9–14].

Three types of hydrogels are used in engineering based on their chemical composition: natural, synthetic and hybrid hydrogels [10]. This classification is made based on the cross-linking in the hydrogels [15, 16]. The type and degree of crosslinking determine swelling, elastic modulus, and transport of molecules in hydrogels [17]. Further classification of hydrogels depends on their ionic charge, structure, and preparation methods [16, 17]. Their network structure should be controlled to get an appropriate design and characterization, which impact the degradation of hydrogel scaffolds, diffusion of bioactive

molecules, and migration of cells through the network [16, 17].

Freezing without chemical crosslinking is an appropriate method for the preparation of PVA hydrogels. Ring-opening polymerization of ethylene oxide cyclic monomers, radiation crosslinking of PEG, or free radical polymerization of PEG macromers are common methods for preparing PEG-based hydrogels [18–20].

Diverse methods have been applied for the functionalization of hydrogels. Three-component reaction, polyelectrolyte multilayer microencapsulation, and microwave-assisted functionalization have been applied to functionalize PEG and PVA hydrogels [21–23].

Chain polymerization of hydrogels is used for the preparation of heterogeneous network structures containing dense crosslinking regions [9]. For performing the step-growth polymerization, a crosslinker or comonomer is used to react with the terminal functional groups of the hydrogel macromers to produce greater network structure homogeneity [9].

The applications of PVA and PEG are numerous in engineering. These hydrogels are appropriate candidates for coating nanomaterials in order to reduce their natural reactivity and maintain their physical properties [24]. The coating has two advantages: it can shield the nanomaterial from the surrounding environment and help functionalize the nanomaterial by attaching chemical groups to its surface [25].

Superparamagnetic iron oxide nanoparticles and graphene oxide nanoribbons are among the nanomaterials studied, previously [26–31]. These nanomaterials can be coated with hydrogels. Previous studies have shown that the physicochemical properties of these nanomaterials could be modified because of their coating [27, 30, 32]. The obtained nanocomposites have various applications in engineering. Therefore, their coating with PEG and PVA was performed in previous studies.

In this study, we compare the rheological properties of PVA and PEG. We investigate herein the variation of rheological parameters of these hydrogels. The consideration of the hydrophilic networks of these polymers allow for a better understanding of their rheological properties. To our knowledge, no comparative study has been carried out on the rheological properties of these hydrogels.

2 Research Methodology

2.1 Chemicals

PVA (Mw 89,000-98,000) and PEG (Mw 8000) were purchased from Sigma Aldrich and ThermoFisher Scientific, respectively.

2.2 Preparation of hydrogels

The hydrogel solutions were prepared as described previously [27, 30]. Briefly, a total of 0.4 g of PVA was dissolved in deionized water (10 mL) and mixed during heating at 90 °C for 2 h and at 140 °C for 4 h [27].

A total of 4.8 g of PEG was dissolved in deionized water (20 mL) and mixed during 15 minutes at room temperature [30].

2.3 Rheological measurements

The rheological properties of the solutions of PVA and PEG in millipore water were studied using an Anton Paar MCR-302 rheometer.

5 mL of each sample were used for rheological assessments. The circular rheological measurements were performed in triplicate at room temperature [27].

2.4 Statistical analysis

The QtiPlot software was used for the data analysis. The mean values and standard deviations were obtained for the calculations with this software [7].

The statistical significance of data was checked after the calculations [28]. As the obtained data were close to each other, their standard deviation values were small.

3 Results

Figure 1 shows the viscosity of PVA and PEG versus shear rate. The shear rate was measured between 0 and 1 000 s⁻¹.

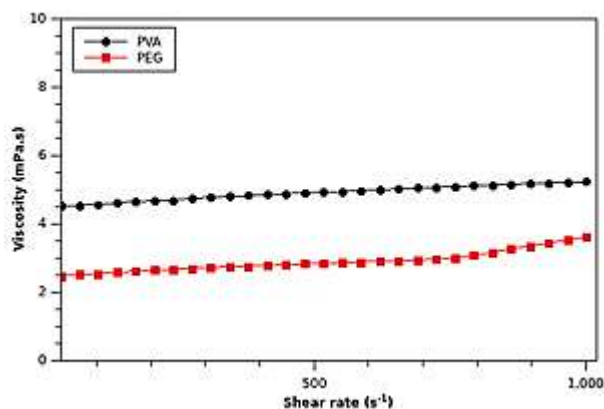


Figure 1 – Viscosity of PVA and PEG versus shear rate

As shown in Figure 1, the viscosity of PVA and PEG increased slowly with the increase of shear rate. Moreover, the increase of viscosity for PEG was more than that of PVA. The first polymer had an increase of 8.7 % in viscosity, whereas the second one had an increase of 2.4 % at shear rate of 1 000 s⁻¹.

Figure 2 shows the change of viscosity of both polymers versus shear strain.

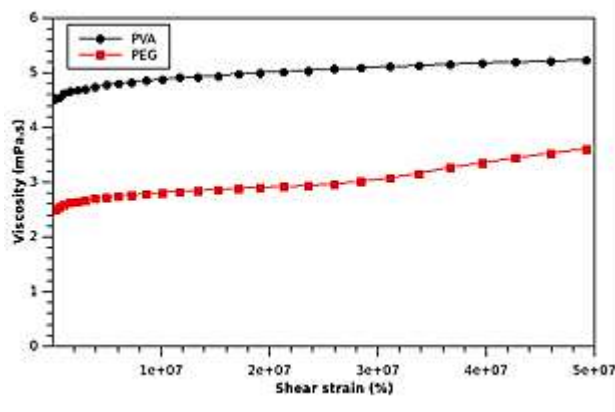


Figure 2 – Viscosity of PVA and PEG versus shear strain

As seen in this figure, the viscosity of PVA and PEG increased with shear strain. The shear-thickening behavior of PEG was more than that of PVA. The viscosity of both polymers reached a plateau. However, PEG reached to the plateau at lower shear strains than PVA. Moreover, PEG showed a second increase of viscosity at high shear strains, whereas PVA did not significantly increase after the plateau. This was attributed to the sensitivity of PEG to its deformation because of the junction separations after the application of mechanical force on the polymer.

The viscosity of PVA and PEG versus time curves are displayed in Figure 3.

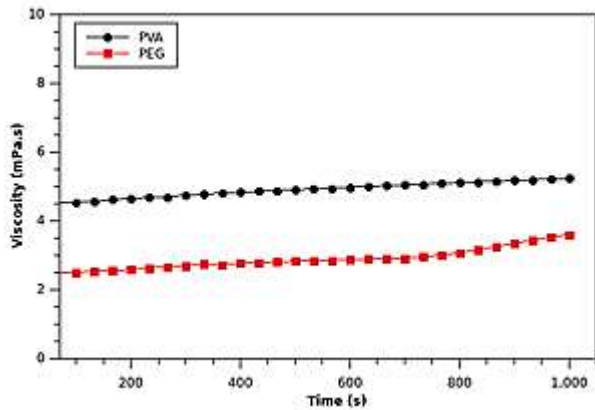


Figure 3 – Viscosity of PVA and PEG versus time

As shown in this figure, the viscosity of both polymers increased with time. Although the viscosity increase of PVA with time was small and reached a plateau, that of PEG was significant and continued at 1 000 s. This shows that when shear stress is applied on these polymers, the effect of the viscosity increase with time for PEG is more than that of PVA. This may be attributed to the difference of the position of the hydrophilic OH group in the structures of these polymers. The presence of this functional group bound to the chain of PEG makes a hindrance for the application of high shear stress on the polymer, whereas this effect is much less in PVA because its OH group is inside its chain, which makes less increase of the viscosity of this second polymer when more shear stress is applied with the increase of time.

The viscosity values of PVA and PEG versus time are presented in Table 1.

Table 1 – Viscosity of PVA and PEG (mPa·s) versus time

Polymer	Time, s		
	200	600	1 000
PVA	4.66 ± 0.03	4.98 ± 0.01	5.24 ± 0.02
PEG	2.62 ± 0.04	2.89 ± 0.02	3.61 ± 0.01

Comparing the results presented in the above table, the increase values of 0.32 mPa·s and 0.26 mPa·s in viscosity were observed for PVA between 600 seconds and 200 s, and between 1 000 s and 600 s, respectively. Whereas in the second time span more viscosity, which was 0.72 mPa·s was observed for PEG compared to the increase of viscosity in the first time span, which was 0.27 mPa·s. This result showed that the viscosity of PEG at higher shear stress in the second time span increased more than its viscosity at lower shear stress in the first time span, whereas PVA showed the inverse effect in these time spans. These results were consistent with the presented figures.

Figure 4 shows torque versus shear strain.

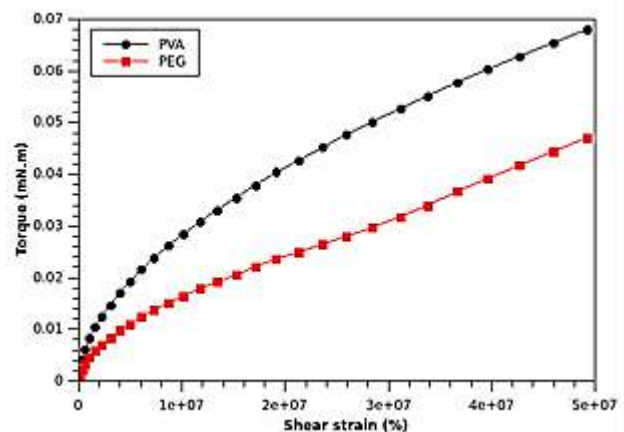


Figure 4 – Torque versus shear strain

The torque values increased with time for both polymers. This was due to their high elasticity that made the torque increase with time. It is worth noting that at the same shear strain, the torque value was more for PVA than PEG. This was consistent with the fact that the initial viscosity of PVA as shown in Figure 2 was more than that of PEG.

The changes in the torque values for PVA and PEG versus time are displayed in Figure 5.

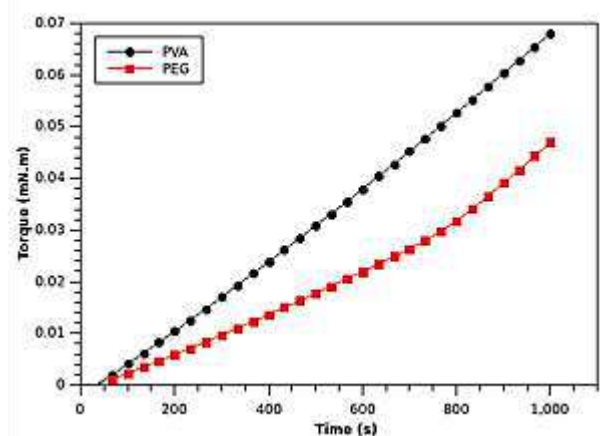


Figure 5 – Torque versus time

This figure shows that the torque values increased with time for both polymers. However, the torque increase was more rapid for PVA than for PEG. This indicates that the torque changes versus time for PVA and PEG were not the same as the first polymer showed a steeper line compared to the second one.

Comparing the torque changes for PVA and PEG versus time showed that this change for the first polymer was linear, whereas it was a curve for the second one. In other words, the torque values when applied for PEG did not change linearly with time. This could correspond to the difference in the structures of these polymers.

Figure 6 shows the shear stress versus shear rate curves of PVA and PEG.

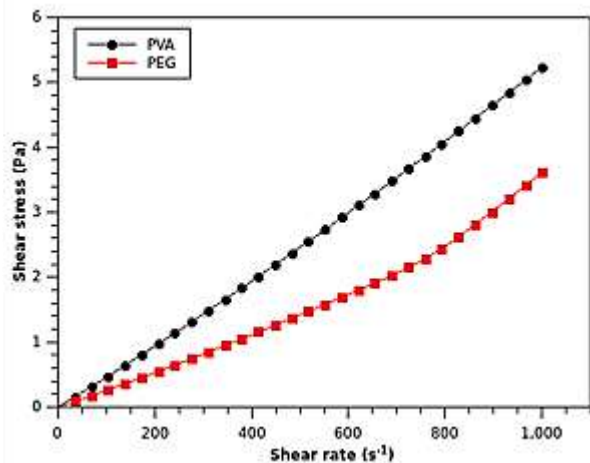


Figure 6 – Shear stress of PVA and PEG versus shear rate

As observed in this figure, the same shear stress corresponds to a greater shear rate for PEG than PVA. This is because the flow velocity gradient in PEG is more than that of PVA when the same shear stress is applied to each polymer solution.

Figure 7 shows the shear stress versus shear strain curves of both polymers.

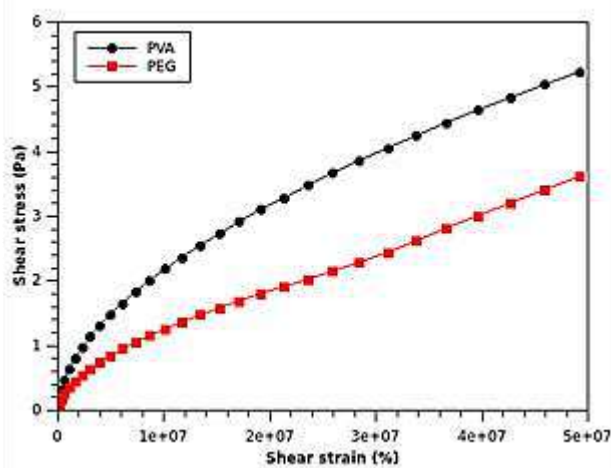


Figure 7 – Shear stress of PVA and PEG versus shear strain

As shown in this figure, less shear stress is required for the same quantity of the deformation of PEG in comparison with that of PVA. In other words, the deformation of PEG is easier than that of PVA as more shear stress is required for the deformation of the second polymer in comparison with the first one. This is attributed to the differences in these polymers' chemical structures and molecular weights.

The shear stress values of PVA and PEG versus shear strain are presented in Table 2.

The data in the above table show that the shear strain increase of polymers from $1 \cdot 10^6$ to $2 \cdot 10^7$ would require more shear stress on PVA than that on PEG.

Table 2 – Shear stress (Pa) of PVA and PEG versus shear strain

Polymer	Shear strain, %		
	$1 \cdot 10^6$	$2 \cdot 10^7$	$4 \cdot 10^7$
PVA	0.64 ± 0.01	3.29 ± 0.01	4.84 ± 0.02
PEG	0.36 ± 0.01	1.91 ± 0.01	3.21 ± 0.01

The same phenomenon was observed for the shear strain increase from $2 \cdot 10^7$ to $4 \cdot 10^7$. This is attributed to the differences in these hydrogels' molecular weights and structures that can determine the shear effect [33]. These comparative data can be used to improve the mechanical properties of these materials for the preparation of blends and composites.

4 Discussion

The results presented in this paper provide important new insights to the comparative rheological properties of PVA and PEG. Previous investigations on the rheological properties of these polymers showed that up to certain shear rates, these polymers would behave as Newtonian liquids. These studies indicated that at high shear rates, viscosity instant flow cessation occurred in these polymers [34–37]. However, no study has reported the comparative analysis of the rheological properties of these polymers.

Shear modulus is a parameter that reflects the ability of polymer to withstand the force applied and resist to the deformation. This parameter is obtained from the division of shear stress by shear strain [38, 39]. In the current paper, the shear modulus values of both PVA and PEG were very small and they decreased with time for both polymers. We expect to observe that this parameter would decrease with the increase of temperature as the deformation of polymers could happen by applying less amount of shear stress with the increase of temperature. In a further investigation, we will study the effect of temperature on the rheological properties of these polymers.

The molecular weight and chain branching are the structural factors that can impact the rheological behavior of polymers. Low molecular weight polymers display Newtonian behavior due to a tumbling or sliding of the molecules over one another during applying a shear stress [40]. Moreover, the ratio of the response time of the polymer to observation or experimental time depends on the molecular weight of the sample and the temperature [40]. The physicochemical properties of some of the materials that were applied in engineering were investigated previously [41–45]. More investigations are required to determine the effect of PVA and PEG on these materials regarding their preparation with polymers.

The composites of PVA and PEG with metals and non-metals are of significant interest in engineering as these hydrogels can improve materials' workability and water retention [46–50]. It has been observed that the viscosity of gel would increase with increasing the concentration of metals when a constant concentration of PEG was used in the samples. An investigation showed that the reduction of the gel viscosity was necessary in

order to control the concentration of metal ions in water-glycol solutions [34]. The rheological properties of dried composite membranes can provide information on the mechanical resistance and tolerance to pressure applied during preparing materials with hydrogels [50]. The structural recovery tests can be conducted by applying different shear rates for getting information on the sample preparation after deposition conditions of mixtures and the change in their viscosity [51]. Some compositions can influence pH, particularly those obtained in a weakly alkaline environment with higher values of relative viscosity [52]. Crosslinking in the composites can improve light shielding, visible light transparency, better mechanical and water vapor barrier properties, and thermal stability [53]. Rheological and electrical assessments of PVA-based composites can give information on the formation of ordered liquid-crystal structures in the polymer matrix [54]. When dimethyl sulfoxide with water is used to dissolve PEG, the system could become more heterogeneous because of the hydrogel structure produced by weakly bonded water molecules. The network structure impacts the rheological properties as the reorganization of hydrogen bonding could contribute to the transitions of the macroscopic viscoelasticity [55].

The rheological properties of PVA and PEG are of interest when they are mixed with other materials in composites. The non-Newtonian behavior of PVA is maintained when it is mixed with graphene oxide nanoribbons [27]. It has been shown that the rheological properties of nanocomposites of PVA and cellulose nanocrystals had limited molecular weight dependence [56]. Lactose-filled PEG composites were also studied concerning their processing temperature. It was reported that decreasing the process temperature could lead to an increase in shear viscosity. Moreover, the temperature dependence of shear viscosity decreased with the increase of shear rate [57]. Another study revealed that introducing silica nanoparticles into PEG-based composites that are used as membranes for separating gases could affect their rheological properties [58, 59]. The study of the viscoelastic behavior of PEG-poly(lactic acid) composites showed that these materials could have a higher magnitude of storage modulus than pure polymers [60]. Another study showed the increase of viscosity due to loading additives in the biphasic polymer solution, which did not change in further growth of the filler concentration [61]. The addition of clay to PEG could change its Newtonian flow behavior to thixotropic shear thinning when its structure broke down by mechanical shearing, and its viscosity decreased with time under conditions of constant shear rate [62].

Blends also are of interest in engineering. A study showed that the viscosity of pure PVA solutions would increase slowly as they age, and the aging of the PVA/PEG blends would be much faster than those of pure polymers [50]. Another study revealed that a blend having viscoelastic behavior could remain stable upon storage [51]. It has been shown that long polymers could interconnect several particles, acting as cross-links which

could explain the mechanism of the enhancement of viscosity [52]. The physical crosslinking methods have been widely applied in materials science because there has been no need to introduce new chemicals, complicating their use in the biomedical environment [53]. Another important aspect of the preparation of blends concerns the phase separation. A study revealed that the presence of PEG forces the PVA solution to separate phase. The authors proposed that this phenomenon could help the formation of gel [63]. Crosslinking has a positive impact on the preparation of PVA and PVA-PEG blends as their rheological properties could reveal their viscoelastic behavior and stability upon storage [64, 65]. Adding PEG to PVA can counteract the reduction of the water content in the polymer matrix to make the blend more appropriate for biomedical applications [66].

The other important issues in preparing materials with PVA and PEG hydrogels are discussed below. The presence of gel with abnormal rheological properties in the glycol regeneration systems is a problem for this purpose because it may cause filters to clog at critical shear rates [35]. High molecular weight PEG can increase the elasticity and stability of shear thickening fluids [67–69]. It is worth noting that the interchain hydrogen bonds and shear-induced orientation can affect the rheological properties of PEG solutions in water. The application can break the intrachain and interchain hydrogen bonds of shear stress, and new interchain hydrogen bonding can be created simultaneously. The viscoelasticity of these systems depends on the reorganization of hydrogen bonding [70–73].

As discussed above, temperature and crosslinking can impact the rheological properties of PVA and PEG. More investigations are required to determine the impact of these factors on the comparative analysis of the rheological properties of these hydrogels for the preparation of composites and blends.

5 Conclusions

This study shows that the rheological properties of PVA and PEG are similar to each other at low shear rates. However, at high shear rates, they behave differently. Moreover, the increase in the shear strain values requires more shear stress on PVA than on PEG.

These results are attributed to the differences in these polymers' network structures and molecular weights. Some issues, such as the viscoelasticity of PVA and PEG and the temperature change that affect the drug delivery output when these hydrogels are used for coating drug vectors, must be addressed in further studies for the development of their biomedical applications.

These investigations will allow better control of the physicochemical properties of these hydrogels for these applications.

6 Acknowledgments

The author gratefully acknowledges Professor Ingo Salzmann for the provision of polymers.

References

1. Hou, Y., Liu, K., Tu, Y., Zhang, L. (2015). Preparation of PVA hydrogel with high-transparence and investigations of its transparent mechanism, *RSC Advances*, Vol. 5(31). <https://doi.org/10.1039/C5RA01280E>.
2. Shulyak, I. V. ; Grushova, E. I. ; Semenchenko, A. M. Rheological properties of aqueous solutions of polyethylene glycols with various molecular weights, *Russian Journal of Physical Chemistry A*, Vol. 85(3), pp. 419–422. <https://doi.org/10.1134/S0036024411030265>.
3. Liu, P., Chen, W., Liu, C., Tian, M., Liu, p. (2019). A novel poly (vinyl alcohol)/poly(ethylene glycol) scaffold for tissue engineering with a unique bimodal open-celled structure fabricated using supercritical fluid foaming, *Scientific Reports*, Vol. 9, 9534. <https://doi.org/10.1038/s41598-019-46061-7>.
4. Falqi, F.H., Bin-Dahman, O.A., Hussain, M., Al-Harathi, M.A. (2018). Preparation of miscible PVA/PEG blends and effect of graphene concentration on thermal, crystallization, morphological, and mechanical properties of PVA/PEG (10 wt%) Blend, *International Journal of Polymer Sciences*, 2018, 8527693. <https://doi.org/10.1155/2018/8527693>.
5. Ahmed, E.A. (2015). Hydrogel: Preparation, characterization, and applications: A review, *Journal of Advanced Research*, Vol. 6(2), pp. 105–121. <https://doi.org/10.1016/j.jare.2013.07.006>.
6. Bahram, M., Mohseni, N., Moghtader, M. (2016). An introduction to hydrogels and some recent applications, in *Emerging Concepts in Analysis and Applications of Hydrogels*, Ed. S. B. Majee, IntechOpen Book Series: London, UK, 2016; ISBN 978-953-51-6668-9, <https://doi.org/10.5772/64301>.
7. Bustamante-Torres, M., Romero-Fierro, D., Arcentales-Vera, B., Palomino, K., Magaña, H., Bucio, E. (2021). Hydrogels classification according to the physical or chemical interactions and as stimuli-sensitive materials, *Gels*, Vol. 7, 182. <https://doi.org/10.3390/gels7040182>.
8. Javanbakht, T., Bérard, A., Tavares, J. R. (2016). Polyethylene glycol and poly (vinyl alcohol) hydrogels treated with photo-initiated chemical vapor deposition. *Canadian Journal of Chemistry*, Vol. 94(9), pp. 744–750. <https://doi.org/10.1139/cjc-2016-0229>.
9. Lin, C.-C., Anseth, K.S. (2009). PEG hydrogels for the release of biomolecules in regenerative medicine, *Pharmaceutical Research*, Vol. 26(3), pp. 631–643. <https://doi.org/10.1007/s11095-008-9801-2>.
10. Lin, C. C., Metters, A.T. (2006) Hydrogels in controlled release formulations: Network design and mathematical modeling. *Adv. Drug Deliv. Rev.*, Vol. 58, pp. 1379–1408. <https://doi.org/10.1016/j.addr.2006.09.004>.
11. Peppas, N.A., Hilt, J.Z., Khademhosseini, A., Langer, R. (2006). Hydrogels in biology and medicine: From molecular principles to bionanotechnology. *Adv. Mater.*, Vol. 18, pp. 1345–1360. <https://doi.org/10.1002/adma.200501612>.
12. Mellott, M.B., Searcy, K., Pishko, M.V. (2001). Release of protein from highly cross-linked hydrogels of poly(ethylene glycol) diacrylate fabricated by UV polymerization. *Biomaterials*, Vol. 22, pp. 929–941. [https://doi.org/10.1016/S0142-9612\(00\)00258-1](https://doi.org/10.1016/S0142-9612(00)00258-1).
13. Hunt, N.C., Grove, L.M. Cell encapsulation using biopolymer gels for regenerative medicine, *Biotechnol. Lett.* Vol. 32(6), pp. 733–742. <https://doi.org/10.1007/s10529-010-0221-0>.
14. Zhu, J. Bioactive modification of poly(ethylene glycol) hydrogels for tissue engineering, *Biomaterials*, Vol. 31(17), pp. 4639–4656. <https://doi.org/10.1016/j.biomaterials.2010.02.044>.
15. Chung, H. J., Park, T. G. (2009). Self-assembled and nanostructured hydrogels for drug delivery and tissue engineering, *Nano Today*, Vol. 4 (5), pp. 429–437. <https://doi.org/10.1016/j.nantod.2009.08.008>.
16. Slaughter, B. V., Khurshid, S. S., Fisher, O. Z., Khademhosseini, A., Peppas, N. A. Hydrogels in regenerative medicine, *Adv. Mater.*, 2009, Vol. 21 (32–33), pp. 3307–3329. <https://doi.org/10.1002/adma.200802106>.
17. Hoffman, A.S. (2012). Hydrogels for biomedical applications, *Advanced Drug Delivery Reviews*, Vol. 64, pp. 18–23. <https://doi.org/10.1016/j.addr.2012.09.010>.
18. Li, C., She, M., She, X., Dai, J., Kong, L. (2013). Functionalization of polyvinyl alcohol hydrogels with graphene oxide for potential dye removal, *J. Appl. Polym. Sci.*, Vol. 131(3), 39872. <https://doi.org/10.1002/app.39872>.
19. Zhu, J., Marchant, R.E. (2011). Design properties of hydrogel tissue-engineering scaffolds, *Expert Med. Dev. Devices*, Vol. 8(5), pp. 607–626. <https://doi.org/10.1586/erd.11.27>.
20. Varshney, S., Zhu, J. (2001)., Heterofunctional polyethylene glycol and polyethylene oxide, process for their manufacture, Patent, US20030027929A1.
21. Li, L., Kan, X.-W., Deng, X.-X., Song, C.-C., Du, F.-S., Li, Z.-C. (2013). Simultaneous dual end-functionalization of peg via the passerini three-component reaction for the synthesis of ABC miktoarm terpolymers, *J. Polym. Sci. Part Polym. Chem.* Vol. 51(4), pp. 865–873. <https://doi.org/10.1002/pola.26443>.
22. Zhu, H., Mcshane, M.J. (2006). Synthesis and functionalization of monodisperse poly(ethylene glycol) hydrogel microspheres within polyelectrolyte multilayer microcapsules, *Chemical Communications*, Vol. 2, pp. 153–155. <https://doi.org/10.1039/B513292D>.
23. Van Hove, A.H., Wilson, B.D., Benoit, D.S. (2013). Microwave-assisted functionalization of poly(ethylene glycol) and on-resin peptides for use in chain polymerizations and hydrogel formation, *J. Vis. Exp.*, Vol. 80, 50890. <https://doi.org/10.3791/50890>.
24. Solar, P., González, G., Vilos, C., Herrera, N., Juica, N., Moreno, M., Simon, F., Velásquez, L. (2015). Multifunctional polymeric nanoparticles doubly loaded with SPION and ceftiofur retain their physical and biological properties. *Journal of Nanobiotechnology*, Vol. 13(14), pp. 14–25. <https://doi.org/10.1186/s12951-015-0077-5>.

25. Andrade, A., Ferreira, R., Fabris, J., Domingues, R. (2011). Coating Nanomagnetic Particles for Biomedical Applications. *Biomedical Engineering - Frontiers and Challenges*, North Dakota, University of North Dakota.
26. Javanbakht, T., Laurent, S., Stanicki, D., Frenette, M. (2020). Correlation between physicochemical properties of superparamagnetic iron oxide nanoparticles and their reactivity with hydrogen peroxide. *Canadian Journal of Chemistry*, Vol. 98(10), pp. 601–608. <https://doi.org/10.1139/cjc-2020-0087>.
27. Javanbakht, T., David, E. (2020). Rheological and physical properties of a nanocomposite of graphene oxide nanoribbons with polyvinyl alcohol. *Journal of Thermoplastic Composite Matererials*, 0892705720912767. <https://doi.org/10.1177/0892705720912767>.
28. Javanbakht, T., Laurent, S., Stanicki, D., Salzmann, I. (2021). Rheological properties of superparamagnetic iron oxide nanoparticles, *Journal of Engineering Sciences*, Vol. 8(1), pp. C29–C37. [https://doi.org/10.21272/jes.2021.8\(1\).c4](https://doi.org/10.21272/jes.2021.8(1).c4).
29. Heo, J., Tanum J., Park, S., Choi, D., Jeong, H., Han, U., Hong, J. (2020). Controlling physicochemical properties of graphene oxide for efficient cellular delivery, *Journal of Industrial and Engineering Chemistry*, Vol. 88, pp. 312–318. <https://doi.org/10.1016/j.jiec.2020.04.030>.
30. Smith, A.T., LaChance, A.M., Zeng, S., Liu, B., Sun, L. (2019). Synthesis, properties, and applications of graphene oxide/reduced graphene oxide and their nanocomposites, *Nano Materials Science*, Vol. 1(1), pp. 31–47. <https://doi.org/10.1016/j.nanoms.2019.02.004>.
31. Javanbakht, T., Laurent, S., Stanicki, D., David, E. (2019). Related physicochemical, rheological, and dielectric properties of nanocomposites of superparamagnetic iron oxide nanoparticles with polyethyleneglycol. *Journal of Applied Polymer Science*, Vol. 137(3), pp. 48280–48289. <https://doi.org/10.1002/app.48280>.
32. Javanbakht, T., Hadian, H., Wilkinson, K. J. (2020). Comparative study of physicochemical properties and antibiofilm activity of graphene oxide nanoribbons. *Journal of Engineering Sciences*, Vol. 7(1), pp. C1–C8. [https://doi.org/10.21272/jes.2020.7\(1\).c1](https://doi.org/10.21272/jes.2020.7(1).c1).
33. Naiko, R. (1959). Shear dependence of the viscosity of PVA solution, *Kobunshi Kagaku, J-Stage*, Vol. 16(174), pp. 579–58. <https://doi.org/10.1295/koron1944.16.579>.
34. Brikov, A.V., Markin, A.N., Sukhoverkhov, S.V. (2015). Rheological properties of polyethylene glycol solutions and gels, *Industrial Chemistry*, Vol. 1(1), 1000102. <https://doi.org/10.4172/2469-9764.1000102>.
35. Clapp, L. (2020). Rheological properties of glycol solutions and gels, *Short Communication*, Vol. 6(1), 1–3.
36. Lewandowska, K., Dąbrowska, A., Kaczmarek, H. (2012). Rheological properties of pectin, poly(vinyl alcohol) and their blends in aqueous solutions, *e-Polymers*, Vol 12(1), pp. 15–27. <https://doi.org/10.1515/epoly.2012.12.1.160>.
37. Lewandowska, K. (2009). Progress on chemistry and application of chitin and its derivatives, (ed.: Jaworska M.), *Polish Chitin Society, Lodz*, Vol 14, pp. 41–47.
38. Van Oosten, A.S.G., Vahabi, M., Licup, A.J., Sharma, A., Galie, P.A., MacKintosh, F.C., Janmey, P.A. (2016). Uncoupling shear and uniaxial elastic moduli of semiflexible biopolymer networks: compression-softening and stretch-stiffening, *Sci Rep.*, Vol. 6, 19270. <https://doi.org/10.1038/srep19270>.
39. Deegan, D.B. (2015). Effects of liver extracellular matrix gel stiffness on primary hepatocyte function, PhD thesis, Wake Forest University, Winston-Salem, North Carolina, p. 75.
40. Wilkes, G.L. (1981). An overview of the basic rheological behavior of polymer fluids with an emphasis on polymer melts, *Journal of Chemical Education*, Vol. 58(11), pp. 880–892. <https://doi.org/10.1021/ed058p880>.
41. Javanbakht, T., Ghane-Motlah, B., Sawan, M. (2020). Comparative study of antibiofilm activity and physicochemical properties of microelectrode arrays. *Microelectronic Engineering*, Vol. 229, 111305. <https://doi.org/10.1016/j.mee.2020.111305>.
42. Ghane-Motlagh, B., Javanbakht, T., Shoghi, F., Wilkinson, K. J., Martel, R., Sawan, M. (2016). Physicochemical properties of peptide-coated microelectrode arrays and their in vitro effects on neuroblast cells. *Materials Science and Engineering C*, Vol. 68, pp. 642–650. <https://doi.org/10.1016/j.msec.2016.06.045>.
43. Djavanbakht, T., Carrier, V., André, J. -M., Barchewitz, R., Troussel, P. (2000). Effets d'un chauffage thermique sur les performances de miroirs multicouches Mo/Si, Mo/C et Ni/C pour le rayonnement X mou. *Journal de Physique IV France*, Vol. 10, pp. 281–287. <https://doi.org/10.1051/jp4:20001031>.
44. Javanbakht, T., Sokolowski, W. (2015). Thiol-ene/acrylate systems for biomedical shape-memory polymers in *Shape Memory Polymers for Biomedical Applications* (Ed. L'H Yahia), pp. 157–166, Sawston, Cambridge, Woodhead Publishing. <https://doi.org/10.1016/B978-0-85709-698-2.00008-8>.
45. Djavanbakht, T., Jolès, B., Laigle, A. (2000). Intracellular stability of antisense oligonucleotides protected by the d(GCGAAGC). *Biomedical Society Transactions*, Vol. 28, p. A201. <https://doi.org/10.1042/bst028a201c>.
46. Liu, F., Wang, B., Xing, Y., Zhang, K., Jiang, W. (2020). Effect of polyvinyl alcohol on the rheological properties of cement mortar, *Molecules*, Vol. 25, 754. <http://doi.org/10.3390/molecules25030754>.
47. Kim, J.H., Robertson, R.E., Naaman, A.E. (1999). Structure and properties of poly(vinyl alcohol)- modified mortar and concrete. *Cement and Concrete Research*, Vol. 29(3), pp. 407–415. [https://doi.org/10.1016/S0008-8846\(98\)00246-4](https://doi.org/10.1016/S0008-8846(98)00246-4).
48. Kim, J.H., Robertson, R.E. (1997). Prevention of air void formation in polymer-modified cement mortar by pre-wetting, *Cement and Concrete Research*, Vol. 27, pp. 171–176. [https://doi.org/10.1016/S0008-8846\(97\)00001-X](https://doi.org/10.1016/S0008-8846(97)00001-X).
49. Allahverdi, A., Kianpur, K., Moghbeli, M.R. (2010). Effect of polyvinyl alcohol on flexural strength and some important physical properties of Portland cement paste. *Iran. J. Mater. Sci. Eng.*, 7, pp. 1–6.
50. Remiš, T. (2017). Rheological properties of poly(vinyl alcohol) (PVA) derived composite membranes for fuel cells, *J. Phys.: Conf. Ser.*, Vol. 790, 012027. <https://doi.org/10.1088/1742-6596/790/1/012027>.

51. Schulte, J., Kilic, U., Ma, J., Ozbulut, O.E. (2021). Rheological and buildability characterization of PVA fiber-reinforced cementitious composites for additive construction, *Proceedings*, Vol. 11589. <https://doi.org/10.1117/12.2588770>.
52. Krasinskyi, V., Suberlyak, O., Antonuk, V., Jachowicz, T. (2017). Rheological properties of compositions based on modified polyvinyl alcohol, *Adv. Sci. Technol. Res. J.*, Vol. 11(3), pp. 304–309. <https://doi.org/10.12913/22998624/76584>.
53. Bai, H., Sun, Y., Xu, J., Dong, W., Liu, X. (2015). Rheological and structural characterization of HA/PVA-SbQ composites film-forming solutions and resulting films as affected by UV irradiation time, *Carbohydr. Polym.*, Vol. 115, pp. 422–31. <http://doi.org/10.1016/j.carbpol.2014.08.103>.
54. Lazareva, T.G., Yakovleva, O.V., Shinkareva, E.V. (2002). Rheological and electrical characteristics of polyvinyl alcohol composites with phosphoric acid, *Russian Journal of Applied Chemistry*, Vol. 75, pp. 965–968. <https://doi.org/10.1023/A:1020349132315>.
55. Le Song, S., Kim, B.C. (2004). Characteristic rheological features of PVA solutions in water-containing solvents with different hydration states, *Polymer*, Vol. 45(7), pp. 2381–2386. <https://doi.org/10.1016/j.polymer.2004.01.057>.
56. Meree, C.E., Schueneman, G.T., Meredith, J.C., Shofner, M.L. (2016). Rheological behavior of highly loaded cellulose nanocrystal/poly(vinyl alcohol) composite suspensions, *Cellulose*, Vol. 23(5), pp. 3001–3012. <https://doi.org/10.1007/s10570-016-1003-1>.
57. Li, Y., He, H., Ma, Y., Geng, Y., Tan, J. (2019). Rheological and mechanical properties of ultrahigh molecular weight polyethylene/high density polyethylene/polyethylene glycol blends, *Advanced Industrial and Engineering Polymer*, Vol. 2(1), pp. 51–60. <https://doi.org/10.1016/j.aiepr.2018.08.004>.
58. Bahramian, B., Motlagh, G.H., Majidi, S., Kaffashi, B., Nojoomi, S.A., Haririan, I. (2013). Evaluation of melt rheology of lactose-filled polyethylene glycol composites by means of capillary rheometry, *Pharm. Dev. Technol.*, Vol. 18(1), pp. 98–105. <http://doi.org/10.3109/10837450.2011.640685>.
59. Salahshoori, I., Nasirian, D., Rashidi, N., Hossain, K., Hatami, A., Hassanzadeganroodsari, M. (2021). The effect of silica nanoparticles on polysulfone–polyethylene glycol (PSF/PEG) composite membrane on gas separation and rheological properties of nanocomposites, *Polymer Bulletin*, Vol. 78, pp. 3227–3258. <https://doi.org/10.1007/s00289-020-03255-8>.
60. Mohapatra, A.K., Mohanty, S., Nayak, S.K. (2014). Properties and characterization of biodegradable poly(lactic acid) (PLA)/poly(ethylene glycol) (PEG) and PLA/PEG/organoclay: A study of crystallization kinetics, rheology, and compostability, *Journal of Thermoplastic Composite Materials*, Vol. 29(4), pp. 443–463. <https://doi.org/10.1177/0892705713518812>.
61. Vasilyev, G.B., Makarova, V.V., Picken, S.J., Rebrov, A.V., Kulichikhin, V.G. (2010). Extension rheology of liquid-crystalline solution/layered silicate hybrids, *Polymer Engineering and Science*, Vol. 50(4), pp. 789–799. <https://doi.org/10.1002/pen.21586>.
62. Nojoomi, A., Tamjid, E., Simchi, A., Bonakdar, S., Stroeve, P. (2016). Injectable polyethylene glycol-laponite composite hydrogels as articular cartilage scaffolds with superior mechanical and rheological properties, *International Journal of Polymeric Materials and Polymeric Biomaterials*, Vol. 66(3), pp. 105–114. <https://doi.org/10.1080/00914037.2016.1182914>.
63. Yang, N., Hutter, J.L., de Bruyn, J.R. (2013). Rheology and structure of poly(vinyl alcohol)-poly(ethylene glycol) blends during aging, *Journal of Rheology*, Vol. 57, 1739. <https://doi.org/10.1122/1.4824428>.
64. Ahmed, A.S., Mandal, U.K., Taher, M., Susanti, D., Jaffri, J. (2017). PVA-PEG physically cross-linked hydrogel film as a wound dressing: Experimental design and optimization, *Pharmaceutical Development and Technology*, Vol. 23(8), pp. 1–25. <https://doi.org/10.1080/10837450.2017.1295067>.
65. Riedo, C., Caldera, F., Poli, T., Chantore, O. (2015). Poly(vinylalcohol)-borate hydrogels with improved features for the cleaning of cultural heritage surfaces, *Heritage Science*, 3, 23. <https://doi.org/10.1186/s40494-015-0053-2>.
66. Wan, W., Bannerman, A.D., Yang, L., Mak, H. (2014). Poly(vinyl alcohol) cryogels for biomedical applications, in *Polymeric Cryogels: Macroporous gels with remarkable properties*, Ed. O. Okay, *Advances in Polymer Science*, 263, Springer.
67. Singh, M., Verma, S.K., Biswas, I., Mehta, R. (2018). Effect of molecular weight of polyethylene glycol on the rheological properties of fumed silica-polyethylene glycol shear thickening fluid, *Materials Research Express*, Vol. 5, 055704. <https://doi.org/10.1088/2053-1591/aac25c>.
68. Ghosh, A., Majumdar, A., Butola, B.S. (2020). Modulating the rheological response of shear thickening fluids by variation in molecular weight of carrier fluid and its correlation with impact resistance of treated p-aramid fabrics, *Polymer Testing*, Vol. 91, 106830. <https://doi.org/10.1016/j.polymertesting.2020.106830>.
69. Kordani, N., Vanini, A.S. (2016). Investigation of penetration into woven fabric specimens impregnated with shear thickening fluid, *Science and Engineering of Composite Materials*, Vol. 25(1), 205–212. <https://doi.org/10.1515/secm-2015-0202>.
70. Gao, H.-W., Yang, R.-J., He, J.-Y., Yang, L. (2010). Rheological behaviors of PVA/H₂O solutions of high-polymer concentration, *Journal of Applied Polymer Science*, Vol. 116, 1459–1466. <https://doi.org/10.1002/app.31677>.
71. Lewis, C.L., Stewart, K., Anthamatten, M. (2014). The influence of hydrogen bonding side-groups on viscoelastic behavior of linear and network polymers, *Macromolecules*, Vol. 47(2), 729–740. <https://doi.org/10.1021/ma402368s>.
72. Vereroudakis, E., Vlassopoulos, D. (2021). Tunable dynamic properties of hydrogen-bonded supramolecular assemblies in solution, *Progress in Polymer Science*, Vol. 112, 101321. <https://doi.org/10.1016/j.progpolymsci.2020.101321>.
73. Sun, M., Qiu, J., Lu, C., Jin, S., Zhang, G., Sakai, E. (2020). Multi-sacrificial bonds enhanced double network hydrogel with high toughness, resilience, damping, and notch-insensitivity, *Polymers*, Vol. 12(10), 2263. <https://doi.org/10.3390/polym12102263>.



Challenges of Fuel Cell Technologies for the Needs of the Energy Transition to a Zero-carbon Technology

Ostroverkh A. S.^{1*}[0000-0002-1602-7510], Solonin Yu. M.¹, Bezdorozhev O. V.¹[0000-0002-0026-6031], Ostroverkh Y. M.¹[0000-0001-6831-8734], Shcherbatiuk O. M.²[0000-0002-8634-2209], Dubau M.³, Kovalenko L. L.⁴

¹ Frantsevich Institute for Problems of Materials Science of the National Academy of Science of Ukraine, 3, Krzhyzhanovsky St., Kyiv, 03142, Kyiv, Ukraine;

² Hydrogen Systems Engineering LLC, 4/19, P. Bolbochana Str., 01014, Kyiv, Ukraine;

³ Department of Surface and Plasma Science, Charles University, 2, V Holešovičkách St., CZ-18000 Prague 8, Czech Republic;

⁴ Vernadsky Institute of General and Inorganic Chemistry of the National Academy of Science of Ukraine, 32/34, Palladina Ave., 03142 Kyiv, Ukraine

Article info:

Paper received:

August 18, 2021

The final version of the paper received:

December 9, 2021

Paper accepted online:

December 14, 2021

*Corresponding email:

anna.ostroverkh84@gmail.com

Abstract. The study focuses on the challenges of implementing fuel cell technologies and materials to achieve efficient use of green hydrogen and zero CO₂ emissions. It is shown that only identifying the optimal parameters for each fuel cell component and technology and testing the system will help achieve the planned output-specific power. The thorough structure optimization of the membrane-electrode complex and testing in actual operating conditions will accelerate the implementation of fuel cell technologies. An example of structural optimization and improvement of catalytic activity of electrodes and electrolytes is shown. The current density of 0.36 μA/cm² was obtained at a voltage of 0.6 V and a temperature of 500 °C for the fuel cell with 75–80 μm thick ZnO electrolyte and without membrane electrode assembly optimization. It is shown that the fuel cell electrodes' catalytic activity depends on the modeling profile and structure of the catalytic layer, which was verified by testing in real fuel cell operating conditions.

Keywords: fuel cells, electrolysis cell, material science, hydrogen energy, decarbonization.

1 Introduction

The modern world is moving away from a fossil fuel-based economy, as CO₂ emissions are at the root of climate change and the critical environmental situation. There is an urgent need to introduce environmentally friendly fuel sources that use fuel cells and green hydrogen technologies, which allows the fuel cell system to enter the market as zero-emission technologies [1]. The significant event in the world is the first implemented hydrogen law, which entered into force on February 5, 2021, in South Korea to promote the development of the hydrogen economy. The law has become the main piece of legislation governing the hydrogen industry, while the RES (renewable energy source) law will be used in matters not covered by the fundamental law. Currently, in Ukraine, the main steps are forming the hydrogen strategy and implementing strategic research works in the scientific field through fundamental research projects of

NAS of Ukraine [2]. The work is devoted to studying the peculiarities of the development of fuel and cell technologies in decarbonization and transition to a zero-emission economy, which consists of developing fuel and cell technologies and achieving maximum electrical efficiency of electrochemical conversion of 1 kg of hydrogen.

2 Literature Review

With a growing population and, as a result, growing energy needs, environmental problems, and climate change are becoming the challenges for our other existence [3].

According to the World Health Organization, every 9 out of 10 people breathe polluted air. This means that almost 91 % of the world's population does not have access to clean air, and high levels of pollutants cause the deaths of more than 8 million people annually [4, 5].

According to the AQLI (the air quality life index), polluted air is the greatest threat to reducing life expectancy, compared to smoking, alcohol dependence, polluted water consumption, road accidents, diseases, and terrorism. It is becoming clear that implementing policies to combat pollution can allow people to live longer and healthier today. The UN Framework Convention on Climate Change, to which Ukraine is a party, aims to preserve the environment by stabilizing greenhouse gas concentrations in the atmosphere at a level that would not allow dangerous anthropogenic impacts on the climate system (Law No. 435/96-VR dated by 29.10.96, BBP, 1996, No. 50, p. 277).

The main steps to overcome this global problem are the energy transition to clean energy sources and decarbonization processes (Paris Agreement from 2015 adopted under the UN Framework Convention on Climate Change to avoid dangerous climate change by limiting global warming to well below 2 °C and pursuing efforts to limit it to 1.5 °C). Reducing fossil fuel consumption and switching to renewable energy sources are steps in the global decarbonization agenda and meet the goals of sustainable development [6].

- goal 7: ensure access to affordable, reliable, sustainable, and modern energy for all;
- goal 12: ensure sustainable consumption and production patterns;
- goal 13: Take urgent action to combat climate change and its impacts.

The main stages of decarbonization include 3 levels of energy transition:

- an increase of efficiency (energy efficiency) - 1st level of decarbonization, get more power from fuel;
- hybridization/fuel transition – 2nd level of decarbonization, use of low carbon fuel;
- deep decarbonization – 3rd of decarbonization, hydrogen fuel, and carbon capture technologies are key factors in “zero” CO₂ emissions.

Implementation of the first level of decarbonization is a set of measures aimed at reducing energy consumption by transport, buildings, and factories. Examples include improving the energy efficiency of buildings, reducing the fuel consumption of vehicles, and optimizing fuel supply. Everything that will contribute at all levels and in all possible ways to reduce energy consumption by the population and any production aspect.

To implement the second level of decarbonization, the international community, especially developed countries, is setting a time frame until 2030. There is a gradual transition from natural gas to biomethane, distributed through the existing gas infrastructure. It is also projected to increase the share of renewable energy and develop infrastructure for hydrogen fuel. The following main measures can be identified to ensure the 2nd level of decarbonization [6].

The transition from the second level of decarbonization to the final level is limited to 2030–2050. This period is characterized by hydrogen fuel, CO₂ capture, and hydrogen and CO₂ storage technologies and has the potential for deeper decarbonization of fossil

fuels. These technologies should significantly change the ability of the oil and gas industry to reduce carbon emissions. It is also planned to significantly increase the share of renewable electricity for green hydrogen production, which will come directly to the infrastructure of the distribution network. The transition between decarbonization levels 2 and 3 is schematically shown in Figure 1.

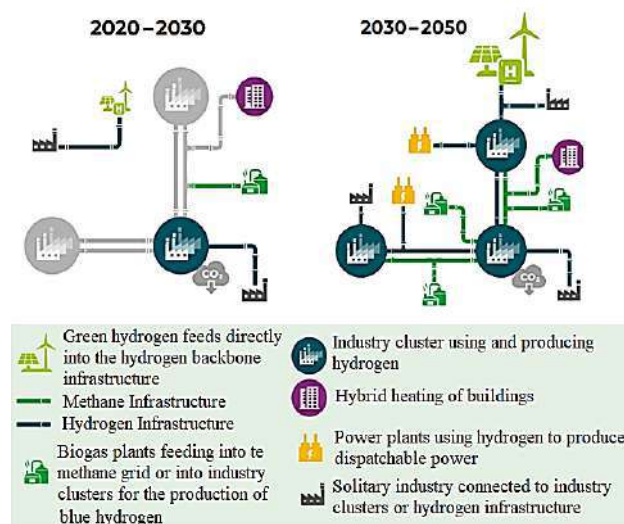


Figure 1 – Development of energy infrastructure in the periods 2020-2050 in terms of decarbonization steps, adapted from [7]

The main advantage of using hydrogen as a fuel is the significant compensation during intermittent energy production from renewable energy sources, which consists of the production and storage of hydrogen (closed cycle of green energy) [8]. Simultaneously, the primary purpose of using hydrogen as a carrier of clean environmental energy is the production of electricity and heat.

Currently, hydrogen is produced by steam reforming from natural gas, although biomethane can significantly reduce carbon emissions during hydrogen production (blue hydrogen). Pure hydrogen production is possible using the reverse mode of fuel cells (FCs) or electrolytic fuel cells.

FC is the most energy-efficient device for generating electricity, which consumes hydrogen as a fuel and oxygen (from the air) as an oxidant. Such devices can be used in all areas of electricity consumption with distributed stationary production of electricity in heavy vehicles and cars. Therefore, issues related to the operation of such energy sources are relevant today.

That is why the implementation of available and known chemical and electrochemical reactions for energy production by using FCs, when chemical energy contained in fuels (hydrocarbons or pure hydrogen) directly and in an energy-efficient way converts into electrical and thermal energy, gives priority in current conditions of planetary pollution over fossil fuel combustion.

The transition from a fossil energy economy to a hydrogen-based economy, if the technologies are available, requires the widespread use of renewable energy sources, including hydrogen production and storage to stabilize electricity supply by regulating renewable energy intermittent; for the production and storage of hydrogen (the so-called buffer to increase the stability of the energy system of a country or region) [9].

One of the most straightforward production processes of pure hydrogen is its production from water by electrolysis, which can be carried out using electricity from other renewable energy sources, such as wind energy, solar energy, or water energy. In such cases, there are two additional benefits in obtaining hydrogen. The first one is that hydrogen can be used to supplement and adjust electricity generation (so-called intermittent production) when there is a shortage of water, wind, sun, or ocean activity, but there is an electricity demand. Hydrogen, which is already extracted and accumulated, can be easily converted into electricity by FCs (Figure 2). Another valuable property of hydrogen accumulation manifests itself in increasing the resilience of the entire energy system of a country or region, stabilizing the regional electricity distribution network.

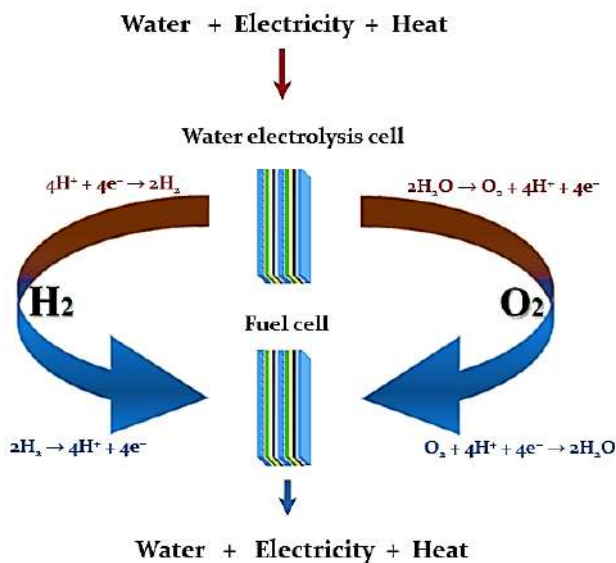


Figure 2 – Process of electrochemical conversion of hydrogen fuel and oxidant to water in the fuel cell system and components of the battery of two fuel cells

Finally, and most importantly, it is clean energy that meets all the possible demands of decarbonization to improve social and environmental needs, and therefore the goals of sustainable development, to which Ukraine has joined. Decarbonization reduces or eliminates carbon dioxide from the energy production process. According to the World Economic Forum, complete decarbonization of our energy systems is the only solution to stabilize the climate. Thus, in practice, achieving zero emissions requires a transition to clean energy sources and a complete transition from fossil fuels to electricity from clean sources.

The most efficient technology for obtaining hydrogen is electrolysis (water electrolysis cell), and the reverse mode of conversion of hydrogen (with oxidant) into water is provided by highly efficient fuel cell technology.

A fuel cell is a device that directly converts chemical energy into electricity by electrochemical oxidation of fuel (e.g., hydrogen, methanol). The operation principle of a fuel cell stack and its constituent elements is schematically shown in Figure 3.

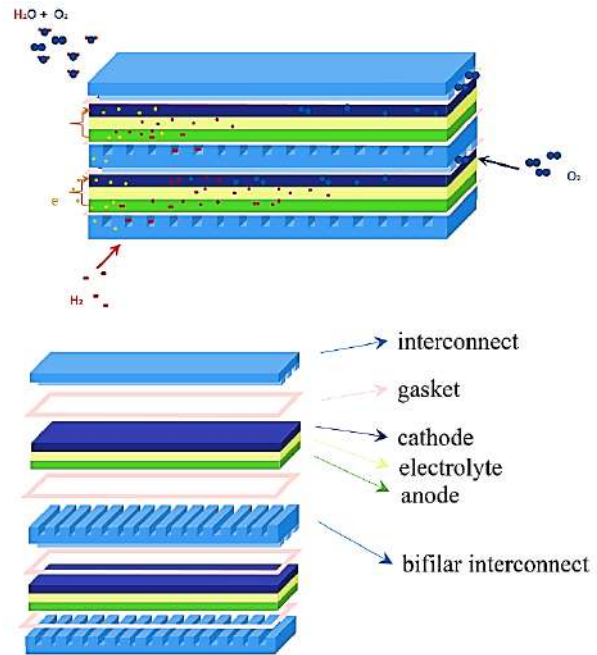


Figure 3 – Electrochemical conversion of hydrogen fuel and oxygen to water in the fuel cell system and components of the stack of two cells.

The fuel cell consists of an electrolyte layer located between two porous electrodes (anode and cathode). Hydrogen and oxygen molecules enter the porous structure of the anode and cathode, respectively, through gas channels on the plate (interconnect), connected by a dense electrolyte material. The anode, electrolyte, and cathode form a membrane-electrode complex of the fuel cell, in which the electrochemical process takes place. Hydrogen molecules on the catalytic component of the anode material dissociate into protons that pass through the anode, which contains the electrolyte material, and the electrolyte to the cathode, which also contains electrolyte material, and electrons along the outer circuit and electrical conductor (anode and cathode material) transfer to the cathode. As a result of the oxygen reduction reaction on the catalytic material of the cathode, water is formed. This type of fuel cell is proton-conducting, and the main characteristic of the electrolyte material is the proton conductivity.

In terms of electrolytes, FCs can be classified into many types, such as alkaline (usually KOH) FCs (AFCs), phosphate FCs (PAFCs), molten carbonate FCs (MCFCs), where a mixture of Li_2CO_3 and K_2CO_3 is used, solid oxide or ceramic FCs (SOFCs, commercial SOFCs

usually uses yttrium stabilized zirconia electrolyte) and proton-exchange membrane FCs (PEMFCs). SOFCs and PEMFCs can be divided by their operating temperature: high-temperature (800–1 000 °C for SOFCs with a ceramic electrolyte and 110–180 °C for HTPEMFCs with a polymer electrolyte) and low-temperature (500–600 °C for LTSOFCs and 40–80 °C for PEMFCs) fuel cells. Low-temperature PEMFCs are most widely used due to the low operating temperature of the electrolyte (and a system as a whole), but in Ukraine, the research is focused on SOFCs. In terms of application for transport and mobile devices, the advantages of PEMFCs are low operating temperature, high specific power, fast start, high efficiency, easy and safe operation. The comparison of the main FC types that have the most significant potential for implementation or have already been implemented (PEMFC) is presented in Table 1.

Table 1 – Comparison of different types of fuel cells

Fuel cell	Membrane	Fuel	T, °C	Efficiency, %	Charge carrier
PEM	Nafion	H ₂ MeOH	60–80	40–60	H ⁺
HT PEM	PBI	H ₂ MeOH	110–180	50–60	H ⁺
SOFC	(Y ₂ O ₃) _x (ZrO ₂) _{1-x}	CH ₄ MeOH H ₂	800–1 000	55–65	O ²⁻
LT SOFC	CeO ₂ -based	CH ₄ MeOH H ₂	550–600	55–65	O ²⁻

Among the energy conversion devices that use hydrogen, FC technology occupies a unique place. Hydrogen-containing methanol (MeOH) fuel is available for widespread use without significant infrastructure costs, which is an ideal hydrogen carrier for transportation because it is liquid at room temperature and ambient pressure. The hydrogen release from the methanol molecule's bound state is more accessible than in other liquid fuels. Moreover, methanol fuel does not contain sulfur, which is harmful to FCs, and the high ratio of hydrogen to carbon in methanol makes it a promising fuel for the hydrogen economy. Methanol is an example of hydrocarbon-containing fuel for the transition period to achieve an economy with zero CO₂ emissions.

Electrolytic FCs can be similarly divided according to their operation principle and characteristics. As for SOFC, the high temperatures (700–900 °C) of the ceramic electrolysis cell (SOEC) provide high efficiency, namely up to 98 %. There are other electrolyze technologies of this type on the market [10]. Like the fuel cells, electrolyzers can be divided by the type of electrolyte. In the case of the alkaline electrolyzer cell (AEC), the electrolyte is a liquid solution of NaOH or KOH, so that OH⁻ becomes a conductor of ionic charges. This technology uses carbon, transition, or precious metals as catalytically active materials, electrodes, and connectors and operates at temperatures of 40–90 °C. Electrolyser based on proton exchange membrane (FC with polymer electrolyte) has an electrolyte consisting of hydrated polymer membrane and conducts protons

through the membrane. The electrode mainly contains carbon, platinum, and iridium-based materials. The operating temperature of the electrolyzer ranges from 20 °C to 150 °C. The main characteristics of the most common electrolyzers are summarized in Table 2.

Table 2 – Comparison of two electrolyzer cell technology

Electrolysis cell type	PEMWE	SOEC
Electrolyte	PEM	Ceramics
Charge carrier	H ⁺ , H ₃ O ⁺	O ²⁻
Cathode reaction	2H ⁺ + 2e ⁻ → H ₂	H ₂ O + 2e ⁻ → H ₂ + O ²⁻
Anode reaction	H ₂ O → ½O ₂ + 2H ⁺ + 2e ⁻	O ²⁻ → ½O ₂ + 2e ⁻
Electrode materials	C	Ceramics
Catalytic materials	Pt, Ir	Ni, LSM, LSCF
Interconnect	Carbon / metal	Modification of stainless steel/metal ceramics
Operation temp., °C	20–150	600–900

The electrochemical process of the closed cycle of green hydrogen (Figure 2) takes place in the membrane electrode assembly of the fuel or electrolysis cells, namely in the anode-electrolyte-cathode structure (Figure 3). It is a process that consists of producing H₂ as an energy source from the splitting of water, and the subsequent use of such energy, which relies on four elementary reactions, i.e., hydrogen evolution reaction (HER), hydrogen oxidation reaction (HOR), oxygen evolution reaction (OER) and oxygen reduction reaction (ORR).

The main goal is to recommend systematic protocols for measuring the activity of these four reactions and reference actions in real electrochemical transformation systems, which is critical to facilitate research and development of new materials with high activity and stability in FC and electrolytic FC electrodes.

Detailed information on the electrochemical tuning of FCs and electrolysis FCs, measurement, and analysis of data used to quantify the processes of reverse systems in acidic and basic solutions, are given as examples of the latest specific and mass activity of catalytic materials. Experiments should be performed correctly, and general recommendations for appropriate reactions should be provided, including cell design, electrode structure, selection of catalytic and electrolyte materials. It is essential to develop experimental protocols, including data collection and processing, such as ohmic and background correction and surface evaluation of catalytic materials, materials with different electrolyte conductivity, the practicality of tests, and comparison of different classes of materials for hydrogen energy. Finally, it is necessary to qualitatively assess some modern catalysts' specific and mass activity to facilitate comparison and interpretation of catalyst activity for these four reactions in different laboratories because different types of fuel cells require different operating temperatures. Figure 4 schematically illustrates the composition of materials included in the membrane electrode assembly.

Catalytically active materials are needed to increase the kinetics of these reactions and thus meet the practical demand to increase the efficiency of electrochemical conversion in FC and electrolytic FC and reduce energy loss during the entire cycle. Scientists are trying to discover and establish the principles of designing catalysts with more significant activity through systematic experimental and computational studies [11–13], some of them focus on increasing the mass-specific surface area of catalytically active materials by designing and creating new structures of catalytic layers/electrodes [14, 15].

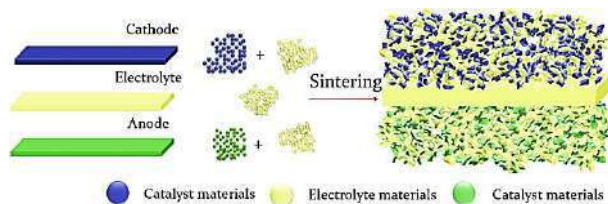


Figure 4 – Materials for the membrane electrode assembly (anode-electrolyte-cathode)

Understanding the mechanisms of reactions, obtaining the maximum possible values of specific activity of catalytic materials, and identifying active sites for catalyzing URFC (unitized reversible fuel cell) processes are studied systematically. The results are often associated with a clear definition of material surfaces, such as single crystal faces [16, 17]. The development of highly active electrocatalysts for practical use is associated with specific methodologies of electrochemical measurements [18, 19] and comparative evaluation with modern electrocatalysts [20]. Unfortunately, today a careful comparison of such studies in real FC devices and electrolytic FCs in most cases only allows assessing the performance of the whole device. Unfortunately, there are often cases when electrocatalytic material was unpromising, although electrochemical tests for electrocatalysis were successful. In the case of high-temperature SOFCs, precious metals are not used as catalytic materials, so the catalytic material in the structure of the electrodes acts as an electrical conductor.

A complex electrochemical process characterizes the fuel cell system with one type of conductivity, while each component of the fuel cell should meet specific requirements, meeting which does not always guarantee high efficiency in actual conditions [21, 22].

Therefore, it is reasonable to assume that in the case of analysis of the process kinetics at each of the FC electrodes or the efficiency of an electrochemical reaction in the system with mixed conductivity, the task becomes much more complex. Thus, it is obvious to perform structural optimization of each element of the fuel or electrolysis cell and test new materials and structures in real conditions of electrochemical transformation.

An essential characteristic for electrolyte materials is the ionic conductivity of materials, which in most cases is regulated by nanostructural or morphological features, such as the shape and size of ionic domains and their

interaction. Therefore, oscillations either in the nanostructure/orientation or in the transport mechanism can change the activation energy of conductivity. Recent studies have shown that the nanostructure and morphology of the thin layers of Nafion electrolyte, the most commercialized membrane for PEMFC, differ from the thick Nafion layers [23]. It is noted that the conductivity of the thin Nafion layers becomes dependent on the humidity, which is not observed for thick membranes.

One of the main reasons is the high interfacial area ratio and volume of thin layers. As a result, the substrate causes interfacial and configurational effects when the morphology and properties of thin films predominate [24].

Ceramics with ionic conductivity are used as electrolytes in high-temperature and low-temperature SOFCs. Thus, high ionic conductivity (more than 0.1 S/cm), density, mechanical properties, minimum thickness, stability in real conditions of electrochemical reactions are required. The oxygen ion conductivity in ZrO₂- and CeO₂-based ceramics, commercialized in SOFC technology, is well studied and governed by grain boundary and defects concentration (typically dislocations or differently oriented domains) [25]. However, using semiconductor materials leads to more complicated kinetics processes and mixed conductivity when the electrolyte has both ion and proton conductivity [26–28].

A breakthrough in micro-energy technologies is required to cover the increasing demand for embedded, personal, or local use of power. Due to their miniaturization capabilities, solid-state energy devices are promising candidates to play a significant role in this new era. However, improving their performance while downscaling their size can only be achieved by looking for disruptive concepts in materials capabilities [29].

Achieving the requirements for electrolyte materials and FC electrodes should ensure high process efficiency, namely the high specific power of the fuel system [30], which is currently not achieved in real conditions.

3 Research Methodology

The morphology and structure of the ZnO-based electrolyte were examined using a scanning electron microscope (SEM) Superprobe 733 (JEOL, Japan).

The chemical composition and structure of the powders were determined by spectral analysis and X-ray phase analysis.

For the morphological investigation of the catalytic layer, a scanning electron microscope (SEM) TESCAN MIRA3 was used. The measurement was carried out in the secondary-electron-mode using primary electrons with 30 keV energy.

The porosity of the samples was measured by hydrostatic weighing.

The electrolyte tests in real operation conditions of the fuel cell were carried out on a new stand for studying the efficiency of materials for hydrogen energy (IPM NAS of

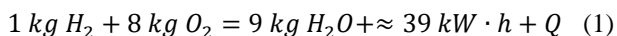
Ukraine). Hydrogen and oxygen were obtained from a polymer-type electrolysis battery. The anode and cathode of the fuel cell were formed using a platinum-rhodium grid (12217, AlfaAesar). The temperature range was set from room temperature to 650 °C.

To form a multilayered electrolyte with a thickness up to 80 μm, a mixture of ZnO nanopowder and polymer with the ratio of 90:10 and 92:8 was used, which was preliminarily homogenized for 4–8 hours in 30 % aqueous-alcohol solution (isopropanol and deionized water). The mass fraction of solid components in the solution was 1 mg per 10 ml of solution.

4 Results and Discussion

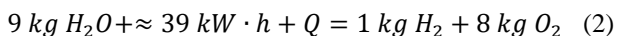
4.1 Chemical reactions

The overall chemical reaction in the fuel cell is characterized as follows:



According to the state-of-the-art technology and materials, the generation of 39 kW·h of electricity by SOFCs with an efficiency of 85%, where the rest is released as heat, is achievable. While the overall efficiency of PEMFCs reaches 70 %. Note that the thermodynamic efficiency calculated as efficiency from the ratio of Gibbs function for total reaction (1) gave 83 % for ideal FC. That means 39 kW·h value of electrical energy will be much higher.

In the case of the reversed electrochemical reaction, namely electrolysis, the reaction can be written as follows:



PEMWE electrolysis technology has an efficiency of 75–93 %, and the total energy consumption reaches 45–53 kW·h. At the same time, the efficiency of SOEC is higher and reaches 90–98 %. In state-of-the-art production, energy costs for SOEC technology require 34–37 kW·h of electricity and 6–11 kW·h of thermal energy.

To approximately estimate the consumption and price of hydrogen, we present the following data:

- 1 kW·h PEMWE produces 0.016-0.018 kg/h H₂
- 1 kW·h SOEC produces 0.022-0.028 kg/h H₂
- 1 kW·h PEMFC consumes 0.069 kg/h H₂ [31]
- 1 kW·h SOFC consumes 0.0534 kg/h H₂ [32]

In 2020 the cost of hydrogen varied as follows: 2.50–6.80 USD/kg for green H₂; 1.40–2.40 USD/kg for blue H₂ (biofuel), and 1.00–1.80 USD/kg for gray H₂ (from hydrocarbons).

The strategy for the transition to technologies with zero CO₂ emissions involves using blue and green hydrogen, and fuel cell technologies are at the forefront of different development strategies of many countries (Hydrogen Road Maps). To reach high efficiency

(reactions (1)–(2)), scientists are focusing on the development of new materials and improving their properties. However, above all, it is necessary to ensure the efficiency of the whole FC system to achieve better performance for FC materials and complete structural optimization of all fuel cell elements and technologies.

4.2 Structural optimization

According to DOE, the catalytic layer's percentage of catalytically active platinum is less than 50 %. Figure 5 schematically shows the catalytic layer, which consists of platinum particles on a carbon carrier, and schematically shows the catalytic layer in actual FC operation conditions, when the amount of catalytically active material is reduced significantly.

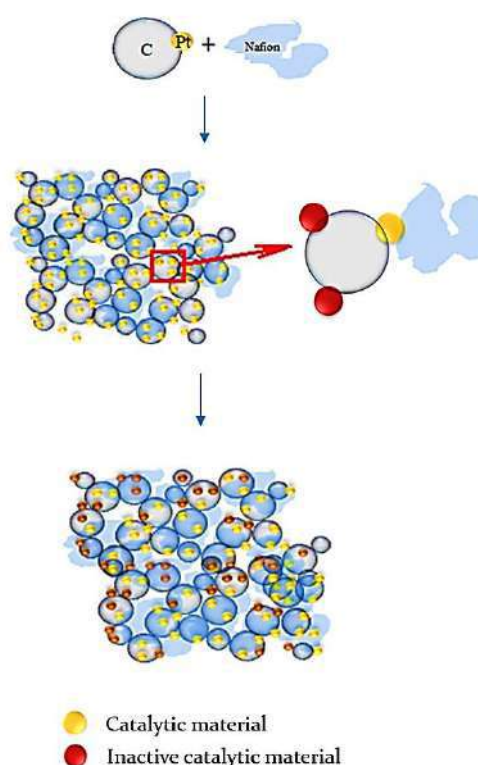


Figure 5 – Catalytic layer of PEMFC: catalytically active Pt (yellow), inactive Pt (brown), carbon (gray), polymer component (Nafion™)

Stable electrochemical conversion on FC electrodes is ensured by a constant flow of semi-cellular redox reactions, which begin on the surface of the catalytic material with constant removal of protons and electrons to the polymer electrolyte (Nafion™) and electronic conductor (carbon particles). The catalytically active platinum is depicted by a yellow color, while platinum which does not contribute to the efficiency of electrochemical conversion, is depicted by brown color.

The content of one of the components or adding other structural changes to the whole catalytic layer is varied. Therefore the study of FC processes in conditions of low content of catalytically active material is a difficult task with many uncertainties and complexities. Solid platinum

[22] is usually used as a reference for non-Pt systems, especially concerning activity, but it is proven theoretically and experimentally that platinum activity can be significantly improved by doping with other metals. Thus, the efficiency of the modified Pt systems becomes a reference point for implementing hydrogen conversion technology into electricity. In energy conversion devices, weight and efficiency play an important role, and the amount of catalyst in fuel cells for fuel conversion, in general, can be a critical parameter.

The magnetron sputtering was used for the controlled deposition of the catalyst material. To obtain a highly dispersed substance by magnetron sputtering, a surface with high specific area [22]. Usually, the catalytic layer is made of catalytic ink and is applied on the surface of the electrode with the presence or absence of a hydrophobic microporous layer. In our case, the adapted catalytic ink method was used to form a surface with an active support layer for platinum catalyst. For obtaining a standard PEMFC catalytic layer, the catalytic ink contained a catalyst material (catalyst nanoparticles or carbon-supported catalyst nanoparticles), proton-conductor membrane ionomer dispersion, and the aqueous-alcoholic solution used. Since the catalyst material was obtained by magnetron sputtering, the catalyst material was absent in the prepared ink. The microporous layer was formed from a mixture of carbon carrier (nanoparticles of size 20–50 nm), 5 % Nafion ionomer dispersion or polytetrafluoroethylene dispersion, isopropyl alcohol, and water. Figure 6 shows the microporous carbon-based surface and Nafion ionomer images before and after hot pressing. This technique is applied to obtain a sandwich-like catalyst, the details, and parameters described in [33, 34]. Hot pressing is usually used to form a membrane complex of the fuel cell with improved proton conductivity at the interfaces between the membrane and catalytic layers of the anode and cathode.

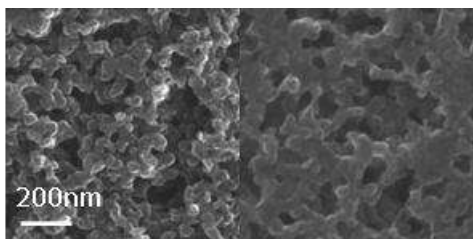


Figure 6 – SEM image of the surface of microporous layer based on carbon nanoparticles and Nafion ionomer (25 %) before and after hot pressing

During the formation of the catalytic layer by magnetron sputtering on this type of surface (Figure 1), the thickness of the deposition film should not exceed 50–60 nm in the case of pure platinum since a further increase in thickness does not increase the fuel cell efficiency [22]. The catalytic layer can be deposited on the surface of the electrode (anode/cathode) or the surface of the membrane during magnetron sputtering. In the latter case, hot pressing is used, and the amount of the active catalyst can be increased during a deposition of a

sandwich-like structure of the catalyst material for direct and reverse FC [34]. The catalytic layer is shown in Figure 7. In the near-membrane catalytic layer (Figure 7 a), the catalyst material is deposited by magnetron sputtering on the surface of the microporous layer and transferred to the surface of the membrane by hot pressing. When the catalytic layer is located on the support (Figure 7 b), the catalyst material is deposited by magnetron sputtering on the surface of the microporous layer, which was transferred to the membrane by hot pressing.

Performed studies on the catalytic activity of the anode and cathode materials in real FC operation conditions resulted in developing a layered structure of the anode and cathode with a polymer electrolyte and ultra-low platinum content [21].

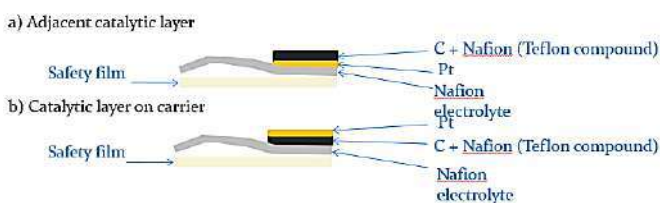


Figure 7 – Model of catalytic layer deposition: a – in-orientation or adjacent catalytic layer; b – top-orientation or catalytic layer on the carrier

The amount of platinum can be reduced to 1–10 $\mu\text{g}/\text{cm}^2$ on the hydrogen electrode (anode) and up to 40–60 $\mu\text{g}/\text{cm}^2$ on the cathode by deposition the catalytic layer on the surface of the electrode with a hydrophobic microporous layer [22]. Further reduction in the amount of the catalyst is possible by carbon doping [35].

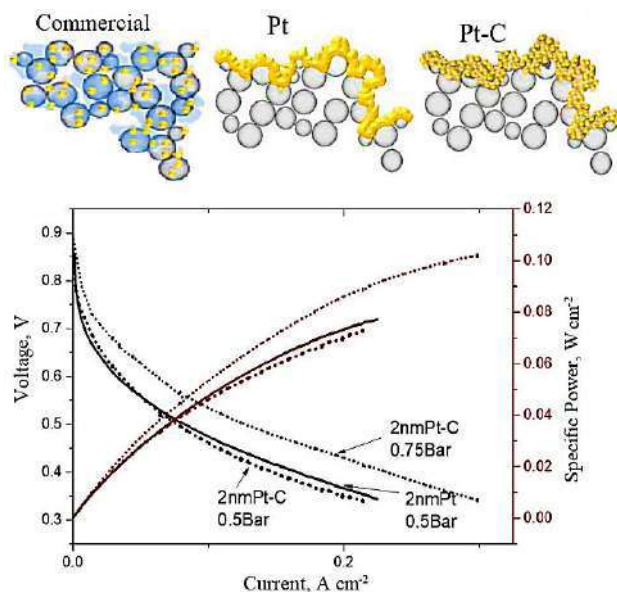


Figure 8 – VA curves for Pt and Pt-C thin films with a thickness of 2 nm on the cathode side of the FC (anode 300 $\mu\text{g}/\text{cm}^2$ Pt, Nafion 212)

Figure 8 also schematically represents the formation of a pure platinum catalytic layer on a carbon carrier and porous structure during the simultaneous deposition of platinum and carbon by magnetron sputtering. By replacing the “bulk” Pt catalytic layer with Pt-C composite, we reduce the amount of Pt in the catalytic layer, while the catalyst dispersion is improved due to the roughness of the surface. The FC tests showed that the samples had almost the same initial characteristic (Figure 8) when the catalyst layer on the cathode was pure Pt and Pt-C (11 % Pt) with an equivalent thickness of 2 nm. However, the porous structure of the Pt-C composite has an advantage in the case of increased pressure inside the FC. The efficiency of the FC increases by only 20–25 % for pure Pt thin films with increasing pressure, and then the efficiency decreases. The evolution of the development of new material is shown in Figure 8 (top).

According to this technique, the content of precious metal in the membrane complex of FC can be significantly reduced without loss of initial characteristics and long-term stability of FC compared to the conventional catalysts on carbon carriers.

The effect of pressure was used to control ionic conductivity in SOFC electrolyte materials based on zinc oxide.

4.3 Structural optimization of electrolyte

Zinc oxide can be used in SOFCs as a primary or alloying material to increase ionic conductivity, reduce sintering temperature, improve the mechanical properties of the electrolyte, and reduce the operating temperature of the cell.

After the literature analysis on the application of ZnO in SOFCs, we studied the effect of forming pressure (84–336 MPa) on the sintering of zinc oxide ceramics.

According to SEM fractography, the fracture of ZnO ceramics is brittle [24]. As for its micromechanism, the fractographic analysis indicated that all samples obtained at different pressures and a sintering temperature of 1 100 °C show chipping.

Data on the electrical properties of ZnO ceramics after being formed under different pressures and sintered at various temperatures are presented in Arrhenius coordinates in Figure 9. The linear dependencies in wide temperature ranges correspond to the ceramics with zero porosity, and nonlinear curves are referred to the porous samples. Analysis of electrical conductivity data concludes that the ionic conductivity can be adjusted by changing the forming pressure of the powders. Red (sintered at 1 100 °C and pressed at 336 MPa) and green (sintered at 1 200 °C and pressed at 168 MPa) curves clearly indicate the possibility of reducing the sintering temperature when the pressure is doubled to achieve similar ionic conductivity values, which gives the possibility to develop materials with different alloying elements and properties.

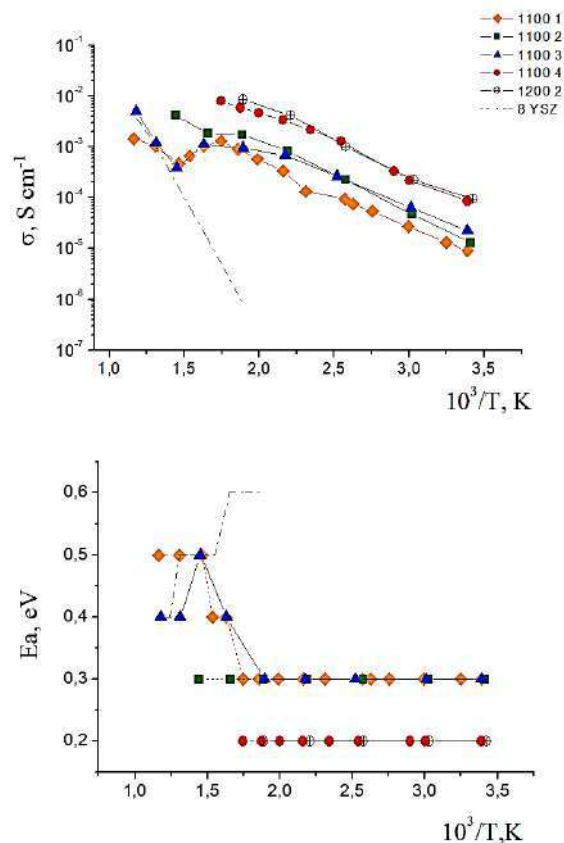


Figure 9 – Electrical conductivity and activation energy of ZnO ceramics pressed at different pressures and sintered in the range of 1 100–1 200 °C: 1 – 84 MPa; 2 – 168 MPa; 3 – 252 MPa; 4 – 336 MPa

Comparing the activation energies of zinc oxide and yttria-stabilized zirconia (marked as 8YSZ, dashed line at Figure 9) materials in the temperature range from room temperature to 600 °C, the decrease of E_a value with temperature is observed for zinc oxide. Such behavior is attributed to zero porosity of ZnO ceramics (red lines). The activation energy increases by 0.1–0.2 eV with the porosity and depends on the temperature in the range from 300 °C and above, which should be considered when forming the porous structure of the electrodes. In the case of 8YSZ-based ceramics with only oxygen conductivity, the activation energy increases with decreasing temperature. ZnO electrolyte with a thickness of 75–85 μm and diameter of 13–15 mm after sintering at 1 100–1 200 °C was used for testing in real fuel cell operation conditions without structural optimization membrane-electrode complex. The open-circuit voltage of 1.07 V was obtained at 450 °C.

Platinum-rhodium grid, which has a limited catalytic surface (catalytic layer), was used as electrodes. The current density of 0.36 $\mu\text{A}/\text{cm}^2$ was obtained at a voltage of 0.6 V and a temperature of 500 °C [26, 28]. The obtained results confirm the effectiveness of using the method for materials characterization without structural optimization of membrane-electrode complex and can be used to search for promising fuel cell materials. The sensitivity of the test system is 2.5 pA.

5 Conclusions

It can be concluded that the application of zinc oxide in fuel cells is a promising area of research. However, the complexity of the processes occurring in the electrode-membrane complex requires step-by-step analysis of each element (anode, cathode, and electrolyte), structural and chemical composition optimization, and tests at real FC operation conditions. The small number of studies on using pure zinc oxide as the SOFC electrolyte opens opportunities for thorough analysis and determination of optimal technological parameters that will accelerate the implementation of SOFCs with operating temperatures below 600 °C. As follows from the review of ZnO-based materials for SOFC, the materials with mixed conductivity and low sintering temperatures are the most promising and effective for electrochemical conversion in real FC operation conditions. Moreover, the structure optimization of the membrane-electrode complex and

testing in real operation conditions will accelerate the implementation of fuel cell technologies to achieve a zero-carbon target. The method for analysis of promising materials without structural optimization was investigated. The current density of 0.36 $\mu\text{A}/\text{cm}^2$ was obtained for the fuel cell with 75–80 μm thick ZnO electrolyte and without membrane electrode assembly optimization at a voltage of 0.6 V and a temperature of 500 °C.

The paper presents the steps of increasing the catalytic activity of the fuel cell electrodes, which are useful in modeling the profile of the catalytic layer and its subsequent verification in real conditions.

6 Acknowledgments

The authors are grateful to NRFU - under the project 2020.02 / 0301 “Research support leading and young scientists” (2020-2022) and Charles University for access to infrastructure.

References

1. Staffell, D. I., Scamman, A. V., Abad, P., Balcombe, P. E., Dodds, P., Ekins, N., Shahd, K., Ward, R. (2019). The role of hydrogen and fuel cells in the global energy system. *Energy and Environmental Science*, Vol. 12, pp. 463–491.
2. Solonin, Yu. M. (2019). On the implementation of the target comprehensive program scientific research of NAS of Ukraine “Fundamental Aspects of Renewable Hydrogen Energy and Fuel-clear Technologies”. *Bulletin of the National Academy of Science of Ukraine*, Vol. 4, pp. 37–41.
3. Owusu, P. A., Asumadu-Sarkodie, S. (2016). A review of renewable energy sources, sustainability issues and climate change mitigation. *Cogent Engineering*, Vol. 3(1), 1167990, doi: 10.1080/23311916.2016.1167990.
4. Cox, L. A. (2019). Communicating more clearly about deaths caused by air pollution. *Global Epidemiology*, Vol. 1(100003), pp. 1–7.
5. Sweileh, W. M., Al-Jabi, S. W., Zyoud, S. H., Sawalha, A. F. (2018). Outdoor air pollution and respiratory health: A bibliometric analysis of publications in peer-reviewed journals (1900 – 2017). *Multidisciplinary Respiratory Medicine*, Vol. 13(15) pp. 1–12, doi: 10.1186/s40248-018-0128-5.
6. Meschede, C. (2020). The Sustainable development goals in scientific literature: A bibliometric overview at the meta-level. *Sustainability*, Vol. 12, 4461.
7. Sun, T., Ocko, I. B., Sturcken, E., Steven, P. H. (2021). Path to net zero is critical to climate outcome. *Scientific Reports*, Vol. 11, 22173.
8. Xiong, P., Peng, X., Taie, Z., Liu, J., Zhang, Y., Peng, X., Regmi, Y. N., Fornaciari, J. C., Capuano, C., Binny, D., Kariuki, N. N., Myers, D. J., Scott, M. C., Webe, A. Z., Danilovic, N. (2020). Hierarchical electrode design of highly efficient and stable unitized regenerative fuel cells (URFCs) for long-term energy storage. *Energy and Environmental Science*, Vol. 13, pp. 4872–4881.
9. Egeland-Eriksen, T., Hajizadeh, A., Sartori, S. (2021). Hydrogen-based systems for integration of renewable energy in power systems: Achievements and perspectives. *International Journal of Hydrogen Energy*, Vol. 46(63), pp. 31963–31983, doi: 10.1016/j.ijhydene.2021.06.21.
10. Bianchi, F. R., Bosio, B. (2021). Operating principles, performance and technology readiness level of reversible solid oxide cells. *Sustainability*, Vol. 13, 4777, doi: 10.3390/su13094777.
11. Hong, W. T., Stoerzinger, K. A., Lee, Y.-L., Giordano, L., Grimaud, A., Johnson, A. M., Hwang, J., Crumlin, E. J., Yang, W., Shao-Horn, Y. (2017). Charge-transfer-energy-dependent oxygen evolution reaction mechanisms for perovskite oxides. *Energy and Environmental Science*, Vol. 10, pp. 2190–2200.
12. Calle-Vallejo, F., Tymoczko, J., Colic, V., Vu, Q. H., Pohl, M. D., Morgenstern, K., Loffreda, D., Sautet, P., Schuhmann, W., Bandarenka, A. S. (2015). Finding optimal surface sites on heterogeneous catalysts by counting nearest neighbors. *Science*, Vol. 350, pp. 185–190, 2015.
13. Escudero-Escribano, M., Malacrida, P., Hansen, M. H., Vej-Hansen, U. G., Velázquez-Palenzuela, A., Tripkovic, V., Schiøtz, J., Rossmeisl, J., Stephens, I. E. L., Chorkendorff, I. (2016). Tuning the activity of Pt alloy electrocatalysts by means of the lanthanide contraction. *Science*, Vol. 352, pp. 73–76.
14. Chen, C., Kang, Y., Huo, Z., Zhu, Z., Huang, W., Xin, H. L., Snyder, J. D., Li, D., Herron, J. A., Mavrikakis, M., Chi, M., More, K. L., Li, Y., Markovic, N. M., Somorjai, G. A., Yang, P., Stamenkovic, V. R. (2014). Highly crystalline multimetallic nanoframes with three-dimensional electrocatalytic surfaces. *Science*, Vol. 343, pp. 1339–1343.

15. Li, M., Zhao, Z., Cheng, T., Fortunelli, A., Chen, C.-Y., Yu, R., Zhang, Q., Gu, L., Merinov, B. V., Lin, Z., Zhu, E., Yu, T., Jia, Q., Guo, J., Zhang, L., Goddard, W. A., Huang, Y., Duan, X. (2016). Ultrafine jagged platinum nanowires enable ultrahigh mass activity for the oxygen reduction reaction. *Science*, Vol. 354, pp. 1414–1419.
16. Kuo, D.-Y., Kawasaki, J. K., Nelson, J. N., Kloppenburg, J., Hautier, G., Shen, K. M., Schlom, D. G., Suntivich, J. (2017). Influence of surface adsorption on the oxygen evolution reaction on IrO₂ (110). *Journal of the American Chemical Society*, Vol. 139, pp. 3473–3479.
17. Jensen, K. D., Tymoczko, J., Rossmeisl, J., Bandarenka, A. S., Chorkendorff, I., Escudero-Escribano, M., Stephens, I. E. L. (2018). Elucidation of the oxygen reduction volcano in alkaline media using a copper-platinum (111) alloy. *Angewandte Chemie International Edition*, Vol. 57, pp. 2800–2805.
18. Chen, J. G., Jones, C. W., Linic, S., Stamenkovic, V. R. (2017). Best practices in pursuit of topics in heterogeneous electrocatalysis. *ACS Catalysis*, Vol. 7(9), pp. 6392–6393
19. Stevens, M. B., Enman, L. J., Batchellor, A. S., Cosby, M. R., Vise, A. E., Trang, C. D. M., Boettcher, S. W. (2017). Measurement techniques for the study of thin film heterogeneous water oxidation electrocatalysts. *Chemistry of Materials*, Vol. 29(1), pp. 120–140.
20. McCrory, C. C. L., Jung, S., Ferrer, I. M., Chatman, S. M., Peters, J. C., Jaramillo, T. F. (2015). Benchmarking hydrogen evolving reaction and oxygen evolving reaction electrocatalysts for solar water splitting devices. *Journal of the American Chemical Society*, Vol. 137, pp. 4347–4357.
21. Ostroverkh, A., Dubau, M., Kúš, P., Haviar, S., Václavů, M., Šmíd, B., Fiala, R., Yakovlev, Y., Ostroverkh, Y., Johánek, V. (2020). Durable ultra-low-platinum ionomer-free anode catalyst for hydrogen proton exchange membrane fuel cell. *International Journal of Energy Research*, Vol. 44(6), pp. 4641–4651, doi: 10.1002/er.5245.
22. Ostroverkh, A., Johánek, V., Dubau, M., Kúš, P., Khalakhan, I., Šmíd, B., Fiala, R., Václavů, M., Ostroverkh, Y., Matolín, V. (2019). Optimization of ionomer-free ultra-low loading Pt catalyst for anode/cathode of PEMFC via magnetron sputtering. *International Journal of Hydrogen Energy*, 2019, Vol. 44(35), pp. 19344–19356, doi: 10.1016/j.ijhydene.2018.12.206.
23. Paul, D. K., McCreery, R., Karan, K. (2014). Proton transport property in supported Nafion nanothin films by electrochemical impedance spectroscopy. *Journal of The Electrochemical Society*, Vol. 161(14), pp. F1395–F1402.
24. Choi, P., Jalani, N. H., Datta, R. (2005). Thermodynamics and proton transport in Nafion: II. Proton diffusion mechanisms and conductivity. *Journal of the Electrochemical Society*, Vol. 152(3), E123.
25. Rajeswari, K., Buchi Suresh, M., Hareesh, U. S., Rao, Y. S., Das, D., Johnson, R. (2011). Studies on ionic conductivity of stabilized zirconia ceramics (8YSZ) densified through conventional and non-conventional sintering methodologies. *Ceramics International*, Vol. 37(8), pp. 3557–3564, doi: 10.1016/j.ceramint.2011.05.151.
26. Qiao, Z., Xia, C., Cai, Y., Afzal, M., Wanga, H., Qiaod J., Zhu, B. (2018). Electrochemical and electrical properties of doped CeO₂-ZnO composite for low-temperature solid oxide fuel cell applications. *Journal of Power Sources*, Vol. 392, pp. 33–40, doi: 10.1016/j.jpowsour.2018.04.096.
27. Paydar, S., Akbar, N., Shi, Q., Wu, Y. (2021). Developing cuprospinel CuFe₂O₄-ZnO semiconductor heterostructure as a proton conducting electrolyte for advanced fuel cells. *International Journal of Hydrogen Energy*, Vol. 46(15), pp. 9927–9937, doi: 10.1016/j.ijhydene.2020.04.198.
28. Chen, X., Dong, B., Islam, Q. A., Song, H., Wu, Y. (2021). Semiconductor-ionic properties and device performance of heterogeneous La-doped CeO₂-ZnO nanocomposites. *International Journal of Hydrogen Energy*, Vol. 46(15), pp. 9968–9975, doi: 10.1016/j.ijhydene.2020.04.174.
29. Garbayo, I., Baiutti, F., Morata, A., Tarancón, A. (2018). Engineering mass transport properties in oxide ionic and mixed ionic-electronic thin film ceramic conductors for energy applications. *Journal of the European Ceramic Society*, Vol. 39(2-3), pp. 101–114, doi: 10.1016/j.jeurceramsoc.2018.09.004.
30. Lim, D., Im, H., Song, S. (2016). Spatial distribution of oxygen chemical potential under potential gradients and theoretical maximum power density with 8YSZ electrolyte. *Scientific Reports*, Vol. 6, 18804, doi: 10.1038/srep18804.
31. Yousefkhani, M. B., Ghadamian, H., Daneshvar, K., Alizadeh, N., Troconis, B. C. R. (2020). Investigation of the fuel utilization factor in PEM fuel cell considering the effect of relative humidity at the cathode. *Energies*, Vol. 13, 6117, doi: 10.3390/en13226117.
32. Zhang, L., Xing, Y., Xu, H., Wang, H., Zhong, J., Xuan, J. (2017). Comparative study of solid oxide fuel cell combined heat and power system with multi-stage exhaust chemical energy recycling: modeling, experiment and optimization. *Energy Conversion and Management*, Vol. 139(1), pp. 79–88, doi: 10.1016/j.enconman.2017.02.045.
33. Kúš, P., Ostroverkh, A., Ševčíková, K., Khalakhan, I., Fiala, R., Skála, T., Tsud, N. (2016). Magnetron sputtered Ir thin film on TiC-based support sublayer as low-loading anode catalyst for proton exchange membrane water electrolysis. *International Journal of Hydrogen Energy*, Vol. 41(34), pp. 15124–15132, doi: 10.1016/j.ijhydene.2016.06.248.
34. Kúš, P., Ostroverkh, A., Khalakhan, I., Fiala, R., Kosto, Y., Šmíd, B., Lobko, Y., Yakovlev, Y., Nováková, J., Matolínová, I., Matolín, V. (2019). Magnetron sputtered thin-film vertically segmented Pt-Ir catalyst supported on TiC for anode side of proton exchange membrane unitized regenerative fuel cells. *International Journal of Hydrogen Energy*, Vol. 44(31), pp. 16087–16098.
35. Ostroverkh, A., Dubau, M., Johánek, V., Václavů, M., Šmíd, B., Veltruská, K., Ostroverkh, Y., Fiala, R., Matolín, V. (2018). Efficient Pt-C MEA for PEMFC with low platinum content prepared by magnetron sputtering. *Fuel Cells*, Vol. 18(1), 137, doi: 10.1002/fuce.201700137.



Onyeka V. O., Nwobi-Okoye C. C., Okafor O. C., Madu K. E., Mbah O. M. (2021). Estimation of global solar radiation using empirical models. *Journal of Engineering Sciences*, Vol. 8(2), pp. G11-G19, doi: 10.21272/jes.2021.8(2).g2

Estimation of Global Solar Radiation Using Empirical Models

Onyeka V. O.¹, Nwobi-Okoye C. C.¹, Okafor O. C.^{2*}, Madu K. E.¹, Mbah O. M.³

¹Chukwuemeka Odumegwu Ojukwu University, Uli, Anambra State, Nigeria;

²Grundtvig Polytechnic, Oba, Anambra State, Nigeria;

³Federal University Oye, Ekiti State, Nigeria

Article info:

Paper received:

September 7, 2021

The final version of the paper received:

December 10, 2021

Paper accepted online:

December 15, 2021

*Corresponding email:

okaforobiorac@gmail.com

Abstract. The dearth of solar radiation data availability has necessitated the development of several mathematical models for estimating global solar radiation (GSR) of regions using the readily available meteorological data of the region. This study was centered on estimating the GSR of the Ihiala region in Sub-Saharan Africa using empirical models. For the last ten years, meteorological data from the Nigerian Meteorological Agency (NIMET) were used. The sunshine-based equation, temperature-based equation, and multivariate polynomial equations were the empirical models employed to estimate the GSR of the region. The performance of the seven models was determined using statistical measures. From the results obtained, the seven models had their respective P-values all less than 5 % significant level for a confidence interval of 95 %. Thereby attesting their suitability for GSR estimation of the region is needed. Also, from the other statistical tools employed, the considered multivariate model had better estimation performance than the other models. Therefore, the considered multivariate model is suitable for estimating the GSR of the Ihiala region in Sub-Saharan Africa.

Keywords: renewable energy, global solar radiation, artificial neural network, statistical tests.

1 Introduction

Solar energy is a primary source of energy and is non-polluting and inexhaustible. According to [1], solar energy can be harnessed using three different methods, namely: using photocells or photovoltaic cells for converting solar energy to electrical one directly; converting solar energy into thermal energy through the application of suitable devices which may be subsequently converted into mechanical, chemical, or electrical energy; through photosynthesis in which plant trap the solar energy and it is converted to chemical energy- biomass energy.

Solar energy is ultimately harnessed using solar cells to convert the solar energy that falls on it into electricity. Research [2] argues that renewable and clean energy, such as solar energy, is needed to maintain quality of life and the environment. The use of solar energy, like any other natural resource, requires detailed information on the total number of cases of solar radiation on the earth's surface. The total solar radiation incident on the earth's surface is called global solar radiation (GSR). GSR data are necessary for various design, engineering, simulation,

and performance evaluation of any project utilizing solar energy. Most recent technologies are hinged principally on solar energy applications. These technologies are seen in the invention of solar cars, solar heaters, solar pumps, solar refrigerators, solar air conditioners etc. Though, some designed solar cars are hybrid systems that still employ internal combustion (IC) engines in their operations.

Owing to the broad areas of application of solar technologies, the knowledge of the intensity of global solar radiation of a geographical location is imperative. Also, the intensity of GSR is influenced by seasonal changes, geographical location, and collector position [3]. Thereby the need for frequent measurement of GSR parameters is created. Therefore, there is a need to develop mathematical models using empirical equations to estimate the GSR of a region of interest.

Therefore, this study estimated the GSR of the Ihiala region in Sub-Saharan Africa using empirical models. The meteorological data employed in the study were obtained from the Nigerian Meteorological Agency (NIMET). The estimation performance of all the models was validated using some statistical tools, such as mean

bias error (MBE), mean percentage error (MPE), and root mean square error (RMSE).

2 Literature Review

Ihiala is a city in Sub-Saharan Africa, located in the southern part of Anambra state at latitude 5.85 N, longitude 6.86 E, and altitude 146 m above sea level and has long served as the Local Government Area of the region. The Local Government Area has a population of about 87,796 persons.

The frequent measurement of GSR of a region of interest due to seasonal changes and the position of collectors [3] has thus called the attention of researchers to develop mathematical models for estimating the GSR of a geographical location. In [4], a linear regression model used in correlating the GSR data with relative sunshine duration was developed using the Angstrom type model. [5] studied the correlation between the measurement data on global solar radiation and meteorological parameters using solar radiation, average daily maximum temperature, average daily relative humidity, average daily sea level pressure, average daily vapor pressure, and many hours of bright sunshine obtained from different parts of Egypt.

Also, [6] developed two decomposition-based models that predict atmospheric transmittance using temperature and relative humidity data of Petronas city in India. [7], developed a mathematical model for estimating global solar radiation using Angstrom's formulation equation for the Himalayas region, Nepal. The statistical analysis results proved that the model was suitable for estimating global solar radiation parameters of the region. Furthermore, [8] examined and compared the results of three isotropic sky models (Liu and Jordan, Badescue and Koronakis model) with experimental data for global solar radiation estimation in eastern Nigeria. Scilab computational software tool was used in implementing the models. Statistical tools were used to determine the accuracy of the models. It was observed that Liu and Jordan's model gave the most negligible value of mean bias error and t-stat of $0.0127 \text{ W}\cdot\text{h}/\text{m}^2$ and 3.3947 respectively. In addition, [9] compared anisotropic sky models with experimental data for solar radiation estimation on tilted surfaces in the Sub-Saharan African climate. The models considered were the Perez model and Hay, Davies, Klucher, and Reindl (HDKR) models. The result showed that the Perez model recorded the least mean bias error ($0.05 \text{ W}\cdot\text{h}/\text{m}^2$) and root mean square error ($0.02 \text{ W}\cdot\text{h}/\text{m}^2$) than the HDKR model.

3 Research Methodology

3.1 Data processing

The meteorological data of the Ihiala region was retrieved from the Nigerian Meteorological Agency (NIMET), Awka, during the last ten years. The climatic data collected were: monthly mean daily sunshine duration, monthly mean daily hours of bright sunshine, monthly mean minimum and maximum temperatures,

monthly mean global solar radiation, monthly mean relative humidity, and monthly mean extraterrestrial global solar radiation of the Ihiala region.

The following characteristics are used:

– monthly mean global solar radiation H_m – the monthly mean of total short-wave radiation of the sky falling on the horizontal surface of the earth. It includes both direct sunlight and scattered radiation resulting from the reflected or scattered sun's energy;

– monthly mean extraterrestrial global solar radiation H_o – defined as the monthly mean of the total short-wave radiation from the sky before reaching the atmosphere, where its reflection, absorption, scattering, and diffusion occurs;

– monthly mean minimum temperature T_{min} – the monthly average of the minimum temperature of an area under study;

– monthly mean maximum temperature T_{max} – gives the monthly average of the maximum temperatures of an area being studied;

– monthly mean sunshine duration/day length N – gives the mean of the day length during the sunshine period for a month;

– monthly mean relative humidity R_H – the average amount of water vapor present in the air as a percentage of the maximum airflow at a given temperature for a month. The relative humidity is the actual water vapor pressure ratio to the saturation vapor pressure;

– monthly average hours of bright sunshine n – the average of all the daily hours of bright sunshine for a month.

MINITAB 2020 software was used to determine the correlation coefficient between the region's measured and estimated global solar radiation values. It was also employed in deriving the mathematical models using the formulation equations proposed by other researchers. Microsoft Excel 2020 was used to simplify and compute the model terms.

The estimation of global solar radiation of the Ihiala region was done by employing Angstrom-PreScott (sunshine-based), Hargreaves-Samani (temperature-based), and various multivariate (polynomial-based) formulation equations. The estimation performance of the models was validated using some standard statistical tools, such as root mean square error (RMSE), mean bias error (MBE), mean percentage error (MPE), the coefficient of correlation (r), Nash-Sutcliffe model (NSE), R-square value, and t-statistic test. The best suitable model for estimating global solar radiation of the Ihiala region was obtained through the confirmatory results of the statistical tests. The methodical procedures employed in this study are further elucidated in the preceding sections.

3.2 Applied formulation models

According to the Angstrom-PreScott model, the first correlation proposed for estimating the monthly mean daily global solar radiation on a horizontal surface using sunshine duration [10] and clear sky radiation data was

first developed by Angstrom. The correlation is shown thus:

$$\frac{H_m}{H_c} = a + b \left(\frac{n}{N}\right). \quad (1)$$

However, due to the problems usually encountered in The new model, the Angstrom-PreScott model or sunshine model. In [12, 13], it was stated that many researchers have equally employed this concept.

According to the Hargreaves-Samani model, the temperature-based model used to estimate global solar radiation is used. The model is based on the temperature difference of the experimental site and is shown thus:

$$H = a \cos \phi + b \cos n + c T_{max} + d \left(\frac{n}{N}\right) + e \left(\frac{T_{max}}{R.H}\right) + f \left(\frac{T_{max}}{R.H}\right)^2 + g \cos \phi \cdot \cos n + h; \quad (3)$$

$$H = a \cos \phi + b \cos n + c T_{max} + d \left(\frac{n}{N}\right) + e \left(\frac{T_{max}}{R.H}\right) + f \left(\frac{T_{max}}{R.H}\right)^4 + g \cos \phi \cdot \cos n + h \frac{T_{max}}{\cos \phi} + i; \quad (4)$$

$$H = a \cos \phi + b \cos n + c T_{max} + d \left(\frac{n}{N}\right) + e \left(\frac{n}{N}\right)^3 + f \left(\frac{T_{max}}{R.H}\right) + g \left(\frac{T_{max}}{R.H}\right)^2 + h \left(\frac{T_{max}}{R.H}\right)^2 + i \left(\frac{T_{max}}{R.H}\right)^3 + j \cos \phi \cdot \cos n + k \left(\frac{T_{max}}{\cos \phi}\right) + l \cos^2 n + m; \quad (5)$$

$$H = a \cos \phi + b \cos n + c T_{max} + d \left(\frac{n}{N}\right) + e \left(\frac{n}{N}\right)^3 + f \left(\frac{T_{max}}{R.H}\right) + g \left(\frac{T_{max}}{R.H}\right)^2 + h \left(\frac{T_{max}}{R.H}\right)^3 + i \left(\frac{T_{max}}{R.H}\right)^4 + j \cos \phi \cdot \cos n + k \left(\frac{T_{max}}{\cos \phi}\right) + l \cos^2 n + m; \quad (6)$$

$$H = a \cos \phi + b \cos n + c T_{max} + d \left(\frac{n}{N}\right) + e \left(\frac{T_{max}}{R.H}\right) + f(R.H) + g \cos \phi \cdot \cos n + h \left(\frac{T_{max}}{\cos \phi}\right) + i \left(\frac{T_{max}}{R.H}\right)^2 + j \left(\frac{n}{N}\right)^2 + k \cos^2 n + l, \quad (7)$$

where ϕ – location latitude, degrees; n – the monthly mean sunshine hours; N – maximum sunshine duration or day length; T_{max} – maximum monthly mean temperature, °C; n – day number in the year, R_H – monthly mean relative humidity; a – m – correlation coefficients or constants; n/N – the relative sunshine ratio; H – the monthly mean global solar irradiance value.

According to [14, 15], an approximate equation for determining the declination angle is as follows:

$$\delta = 23.45 \sin \left(360 \frac{284+n}{365}\right). \quad (8)$$

$$H_o = \frac{24 \times 3600 G_{sc}}{10^6 \pi} \left(1 + 0.033 \cos \frac{360n}{365}\right) \left(\cos \phi \cos \delta \sin \omega_s + \frac{\pi \omega_s}{180} \sin \phi \sin \delta\right), \quad (11)$$

where $G_{sc} = 1367 \text{ W/m}^2$ – the solar constant; ϕ – the area's latitude considered, degrees; δ – solar declination angle, degrees; ω_s – sunset hour angle, degrees.

3.3 Validation of the models

Validations of the models has been carried out based on the calculation of the following characteristics.

The mean bias error (MBE) is determined using the following relation [15]:

$$MBE = \frac{1}{n} \sum_{i=1}^n (H_{ical} - H_{imeas}). \quad (12)$$

The mean percentage error (MPE) is computed with the equation expressed by [16]:

$$MPE(\%) = \frac{1}{n} \sum_{i=1}^n \left(\frac{H_{ical} - H_{imeas}}{H_{imeas}}\right) \times 100. \quad (13)$$

$$\frac{H_m}{H_o} = K_r (T_{max} - T_{min})^{\frac{1}{2}}, \quad (2)$$

where K_r – an empirical coefficient.

Moreover, the multivariate model development involves applying multivariate regression analysis to model climatic data having two or more independent variables. The presence of many predictors in a multivariate model enhances its estimation performance. The five multivariate formulation equations are of the form indicated in the following equations [12]:

According to [14], the sunset hour angle is computed using the relation:

$$\omega_s = \cos^{-1}(-\tan \phi \tan \delta). \quad (9)$$

Monthly mean daily sunshine duration N is computed using:

$$N = \frac{2}{15} \cos^{-1}(-\tan \phi \tan \delta) = \frac{2}{15} \omega_s. \quad (10)$$

Monthly mean daily extraterrestrial global solar radiation H_o is determined using the relation:

This is the relation used in the computation of MPE. A percentage error in a range from -10 % to +10 % is sufficient.

The smaller the root mean square error (RMSE), the better the model's estimation strength and accuracy. Its computational formula is given by [17]:

$$RMSE = \left[\frac{1}{n} \sum_{i=1}^n (H_{ical} - H_{imeas})^2\right]^{\frac{1}{2}}, \quad (14)$$

where H_{imeas} , H_{ical} , n – the i -th measured values and i -th calculated values of daily global solar radiation and the number of values, respectively.

According to [18], a model is more efficient only when the Nash-Sutcliffe equation (NSE) is closer to 1.0:

$$NSE = 1 - \frac{\sum_{i=1}^n (H_{imeas} - H_{ical})^2}{\sum_{i=1}^n (H_{imeas} - \bar{H}_{meas})^2} \quad (15)$$

where H_{imea} – the mean measured global solar radiation.

Also, Karl Pearson's method was used in this work, and the relation is given as:

$$r = \frac{\sum XY}{\sqrt{(\sum X^2)(\sum Y^2)}}, \quad (16)$$

where X is the difference between the measured global radiation and the mean of the measured global radiation; Y is the difference between the estimated global radiation and the mean of the estimated global radiation.

According to the t-statistic test, at a confidence interval of 95 % and significance level of 5 %, the t-statistics test was carried out to determine how small its value was based on the fact that the smaller the value, the better the performance of the model. The formula used to compute it is given by the following equation:

$$t = \left[\frac{(n-1)(MBE)^2}{(RMSE)^2 - (MBE)^2} \right]^{\frac{1}{2}}, \quad (17)$$

where the smaller t , the better its estimation performance.

According to the R-squared method, models with R2 closer to one are considered the best model. The formula used to compute its value is given as follows:

$$R^2 = \frac{\sum_{i=0}^n (H_{imea} - \bar{H}_{imea})^2}{\sum_{i=0}^n (H_{imea} - \bar{H}_{ical})^2}, \quad (18)$$

where H_{imea} – the mean measured global solar radiation; H_{ical} – the mean of calculated global solar radiation.

4 Results and Discussion

4.1 Sunshine-based model

With the aid of the sunshine-based formulative equation, the following equation was obtained:

$$\frac{H_m}{H_o} = 0.397 + 0.421 \left(\frac{n}{N} \right), \quad (19)$$

where H_m – measured global solar radiation; H_o – extraterrestrial global solar radiation; n/N – relative sunshine or fraction of sunshine.

The significance level of each model term and the entire regression model were ascertained from the performed analysis of variance (ANOVA). The results are presented in Tables 1, 2.

Table 1 – The significance level of the model terms

Predictor	Coef	SE Coef	T	P
Constant	0.397	0.024	16.56	0.000
n/N	0.421	0.057	7.38	0.000

S = 0.0818436 R-Sq = 31.6 % R-Sq(adj) = 31.0 %

From Table 1, each of the model terms was all significant as their respective p-values are far less than the chosen α -value of 0.05 for a confidence interval of 95 %. The values of these statistical parameters: S, R-Sq,

and R-Sq(adj.), show the level of accuracy of the model in fitting data. The small values of R-Sq and R-Sq(adj.) explain that the model's predicted strength is poor. The small value of S implies that the model's data fitting ability is not too strong.

Table 2 – Analysis of variance (ANOVA)

Source	DF	SS	MS	F	P
Regression	1	0.365	0.365	54.48	0.000
Residual error	118	0.790	0.007	–	–
Total	119	1.155	–	–	–

The p-value of 0.000 for the regression model attests that the model is statistically significant. In other words, the model's degree of accuracy is only justified by using other statistical and analytical tools employed in this work.

4.2 Temperature-based model

This model was solely based on the temperature difference of the test site- Ihiala region. The model is given thus:

$$\frac{H_m}{H_o} = 0.236 + 0.106(T_{max} - T_{min})^{\frac{1}{2}}. \quad (20)$$

The statistical significance is presented in Table 3.

Table 3 – The significance level of the model terms

Predictor	Coef	SE Coef	T	P
Constant	0.236	0.057	4.10	0.000
n/N	0.106	0.018	5.79	0.000

S = 0.0873280 R-Sq = 22.1 % R-Sq(adj) = 21.5 %

From Table 3, it is quite vivid that each of the model terms is significant as their respective p-values are less than the significant level (α) of 0.05.

Therefore, the model's response predictors or independent variables are all essential. In addition, the smaller values of R-Sq and R-Sq(adj) imply a poor predicting strength of the temperature model since their higher values connote a better-predicting strength of models.

Further, on the model's statistical analysis, the ANOVA result shown in Table 4 proves that the temperature model is statistically suitable for response prediction since the p-value is less than α -value of 0.05.

Table 4 – Analysis of variance (ANOVA)

Source	DF	SS	MS	F	P
Regression	1	0.255	0.255	33.50	0.000
Residual error	118	0.890	0.008	–	–
Total	119	1.155	–	–	–

4.3 Multivariate models

The following multivariate models were developed using the polynomial models given in equations (3)–(7).

The response predictors or independent variables which are not significant have been removed from all the models.

- 1) multivariate model 1:

$$H_m = -8.85 - 0.922\cos n + 0.768T_{max} + 6.25\frac{\bar{n}}{N} + 1.9\frac{T_{max}}{R.H} - 1.6\left(\frac{T_{max}}{R.H}\right)^2. \quad (21)$$

The ANOVA analysis for multivariate model 1 is shown in Table 5.

From Table 5, the p-value of the regression model is much less than the α -value of 0.05 at a confidence interval of 95 %. Hence, the model is statistically significant for response prediction (global solar radiation) of the Ihiala region.

2) multivariate model 2:

$$H_m = -7.65 - 0.910\cos n + 0.716T_{max} + 6.19\frac{\bar{n}}{N} + 2.51\frac{T_{max}}{R.H} - 1.94\left(\frac{T_{max}}{R.H}\right)^4 \quad (22)$$

The ANOVA analysis for multivariate model 2 is shown in Table 6.

Table 6 reveals that the model is statistically significant as the p-value of the model is far less than the α -value of 0.05 for a confidence interval of 95 %.

3) multivariate model 3:

$$H_m = 2.07 - 0.670\cos n + 0.691T_{max} + 6.41\frac{\bar{n}}{N} + 1.28\left(\frac{\bar{n}}{N}\right)^3 - 50.2\frac{T_{max}}{R.H} + 88.0\left(\frac{T_{max}}{R.H}\right)^2 - 46.9\left(\frac{T_{max}}{R.H}\right)^3 + 1.58\cos^2 n. \quad (23)$$

The ANOVA analysis for multivariate model 3 is shown in Table 7.

The p-value of the multivariate regression model 3 is less than the 0.05 value of the significant level (α). This proves that the model is suitable for response prediction.

4) multivariate model 4:

$$H_m = -7.4 - 0.646\cos n + 0.686T_{max} + 6.20\frac{\bar{n}}{N} + 1.76\left(\frac{\bar{n}}{N}\right)^3 + 18\frac{T_{max}}{R.H} - 85\left(\frac{T_{max}}{R.H}\right)^2 + 139\left(\frac{T_{max}}{R.H}\right)^3 - 71\left(\frac{T_{max}}{R.H}\right)^4 + 1.58\cos^2 n. \quad (24)$$

The ANOVA analysis for multivariate model 4 is shown in Table 8.

The p-value of the multivariate regression model 4 is less than the 0.05 value of the significant level (α). This proves that the model is suitable for response prediction.

5) multivariate model 5:

$$H_m = -1.0 - 0.631\cos n + 0.633T_{max} + 1.3\frac{\bar{n}}{N} + 6.1\left(\frac{\bar{n}}{N}\right)^2 + 18\frac{T_{max}}{R.H} - 85\left(\frac{T_{max}}{R.H}\right)^2 + 139\left(\frac{T_{max}}{R.H}\right)^3 - 71\left(\frac{T_{max}}{R.H}\right)^4 + 1.58\cos^2 n. \quad (25)$$

The ANOVA analysis for multivariate model 5 is shown in Table 9.

Table 9 reveals that the model is statistically significant as the p-value of the model is far less than the α -value of 0.05 for a confidence interval of 95 %.

Table 5 – Analysis of variance (ANOVA) for model 1

Source	DF	SS	MS	F	P
Regression	5	719.72	143.94	18.89	0.000
Residual error	114	868.72	7.62	–	–
Total	119	1588.44	–	–	–

S = 2.76050 R-Sq = 45.3 % R-Sq(adj) = 42.9 %

Table 6 – Analysis of variance (ANOVA) for model 2

Source	DF	SS	MS	F	P
Regression	5	721.23	144.25	18.96	0.000
Residual error	114	867.21	7.61	–	–
Total	119	1588.44	–	–	–

S = 2.75810 R-Sq = 45.4 % R-Sq(adj) = 43.0 %

Table 7 – Analysis of variance (ANOVA) for model 3

Source	DF	SS	MS	F	P
Regression	8	775.45	96.93	13.23	0.000
Residual error	111	812.98	7.32	–	–
Total	119	1588.44	–	–	–

S = 2.70632 R-Sq = 48.8 % R-Sq(adj) = 45.1 %

Table 8 – Analysis of variance (ANOVA) for model 4

Source	DF	SS	MS	F	P
Regression	9	776.28	86.25	11.68	0.000
Residual error	110	812.16	7.38	–	–
Total	119	1588.44	–	–	–

S = 2.71721 R-Sq = 48.9 % R-Sq(adj) = 44.7 %

Table 9 – Analysis of variance (ANOVA) for model 5

Source	DF	SS	MS	F	P
Regression	8	768.59	96.07	13.01	0.000
Residual error	111	819.85	7.39	–	–
Total	119	1588.44	–	–	–

S = 2.71772 R-Sq = 48.4 % R-Sq(adj) = 44.7 %

From the ANOVA results, it is evident that the values of R-Sq. and R-Sq. (adj.) for all the multivariate models were more significant than sunshine and temperature-based models. This implies that the multivariate models have better estimation performance than the sunshine and temperature models for the region under study.

4.4 Graphical plots of the models

To visually compare and contrast the measured and estimated global solar radiation values of the Ihiala region, the following figures show the respective graphical plots for each model.

Figure 1 shows the plot of measured global solar radiation and global solar radiation values estimated using the sunshine-based model.

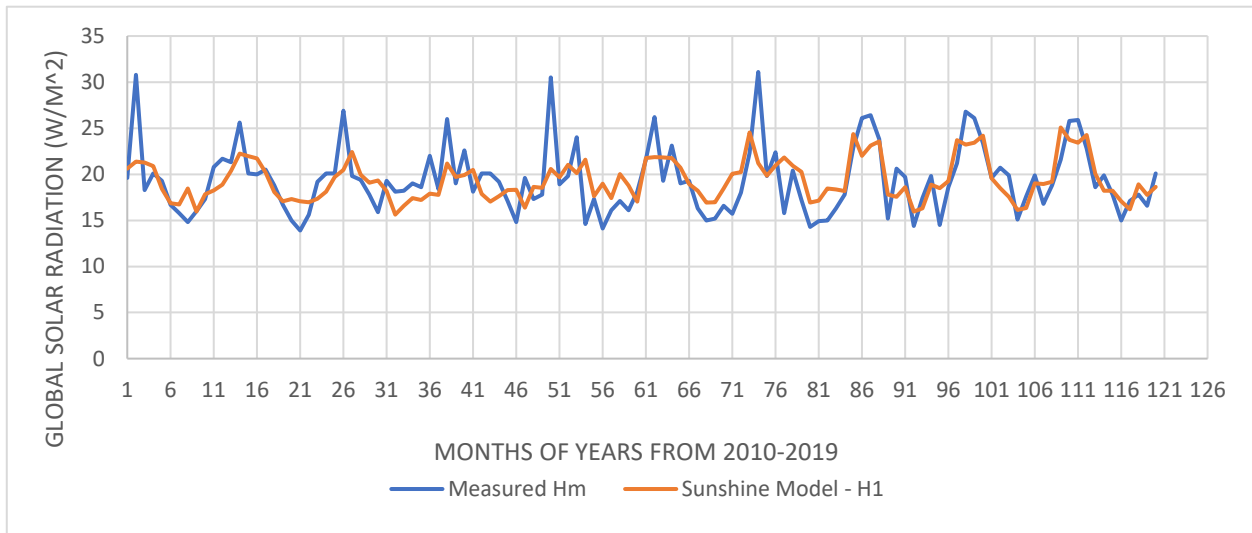


Figure 1 – Comparison of measured and estimated values of global solar radiation using sunshine-based model

From Figure 1, it could vividly be seen that the sunshine-based model did not reasonably estimate the global solar radiation (GSR) data. This is justified because estimated data are dispersed from the measured GSR, as observed in Figure 1.

Figure 2 depicts the graphical plot of the measured and estimated values of GSR using the temperature-based model.

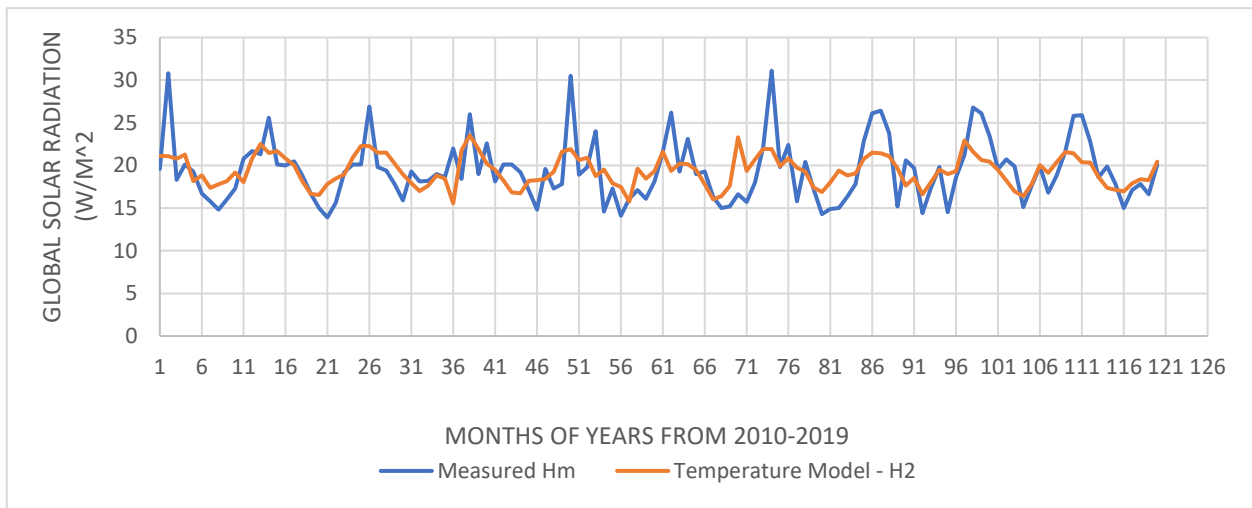


Figure 2 – Comparison of measured and estimated values of global solar radiation using temperature-based model

From Figure 2, the model failed to fit the GSR data well, and as such, the correlative associativity of both data points is reasonably good. The sunshine and temperature models performed poorly in estimating GSR values because they only considered a few regressors/response predictors/independent variables in their respective model formulations. The regressors considered in the Angstrom-Prescot model were only the

sunshine index and the extraterrestrial global solar radiation. While in the temperature-based model, the global extraterrestrial solar radiation and the temperature difference were the model's regressors.

Figures 3–7 show the graphical plots of the measured GSR and estimated GSR using the multivariate models (MVM 1, MVM 2, MVM 3, MVM 4, and MVM 5, respectively).

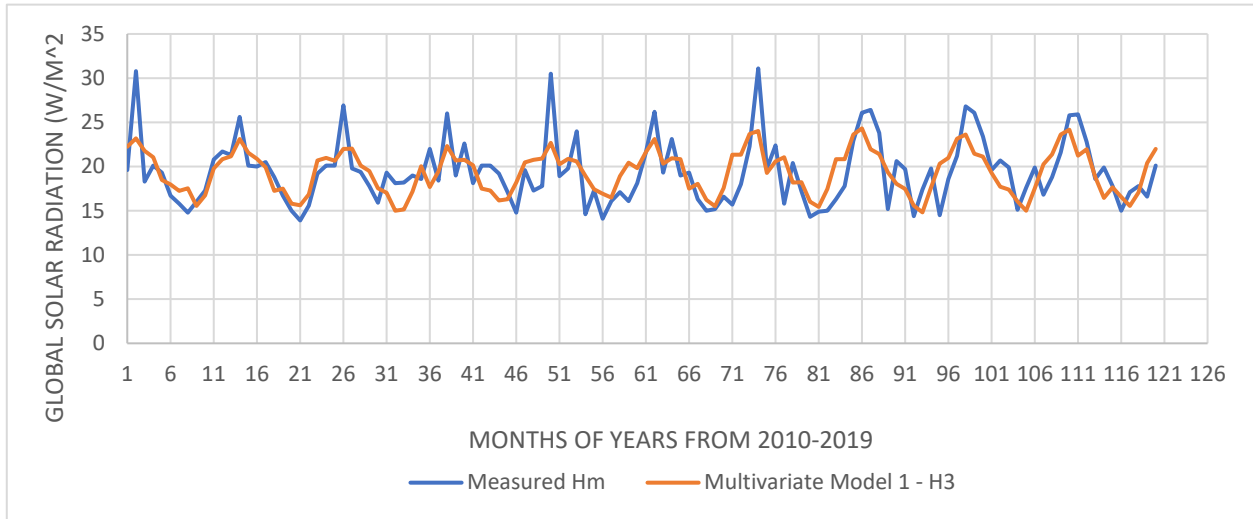


Figure 3 – Comparison of measured and estimated values of global solar radiation using multivariate model 1

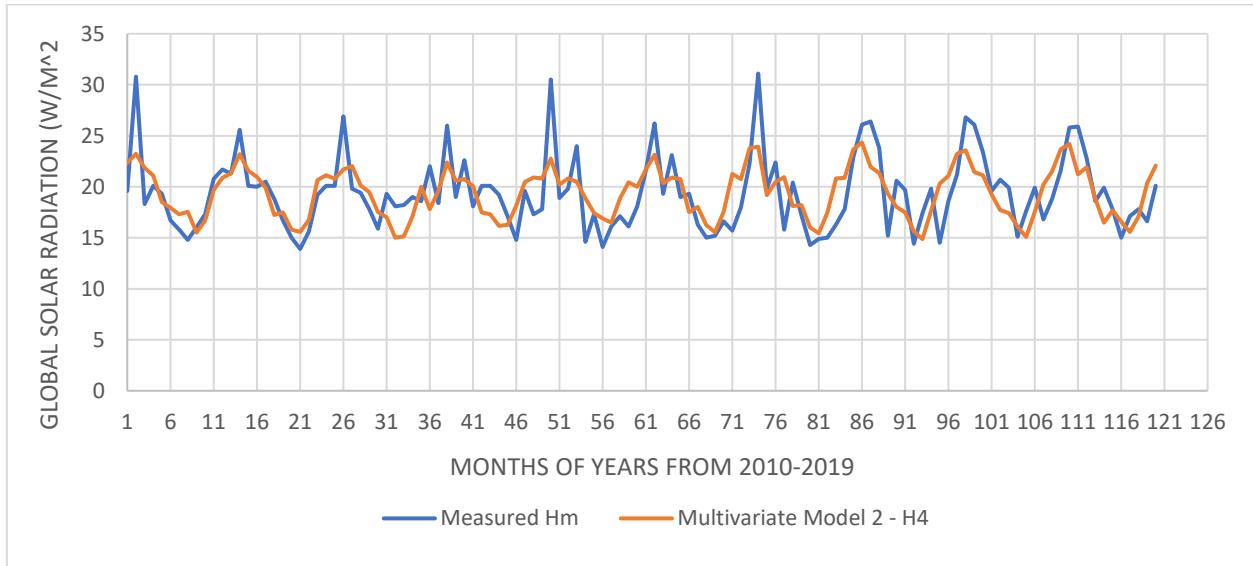


Figure 4 – Comparison of measured and estimated values of global solar radiation using multivariate model 2

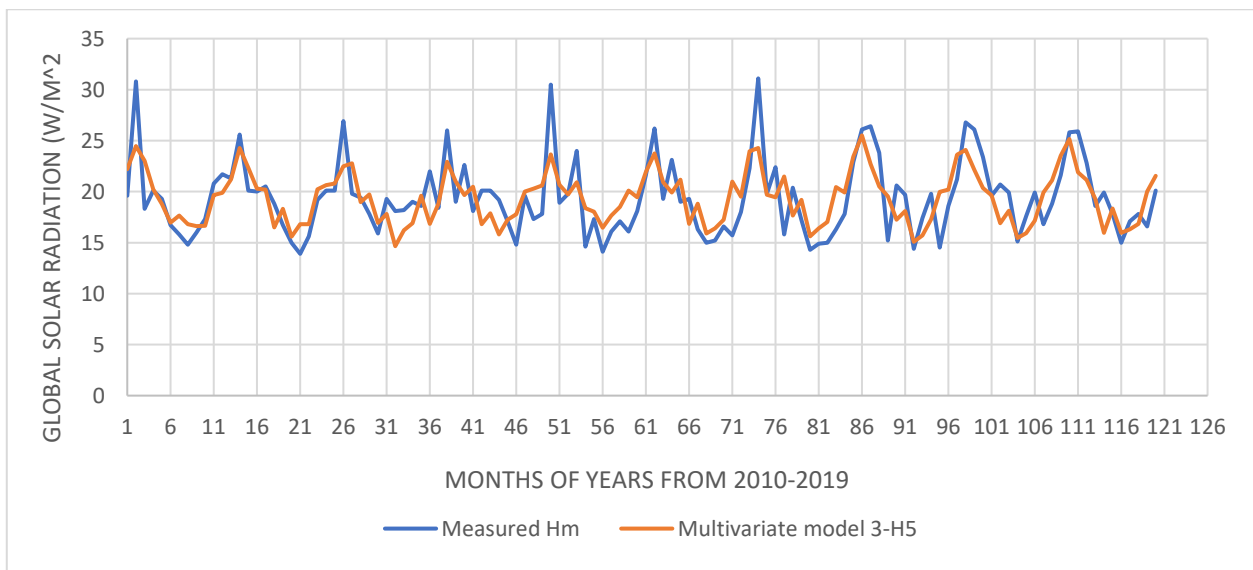


Figure 5 – Comparison of measured and estimated values of global solar radiation using multivariate model 3

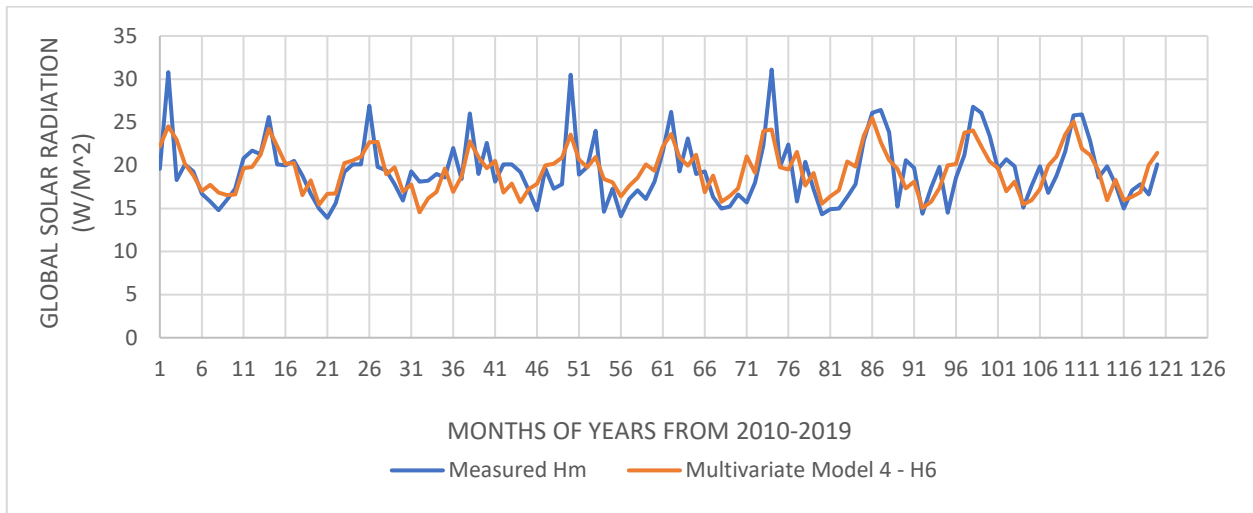


Figure 6 – Comparison of measured and estimated values of global solar radiation using multivariate model 4

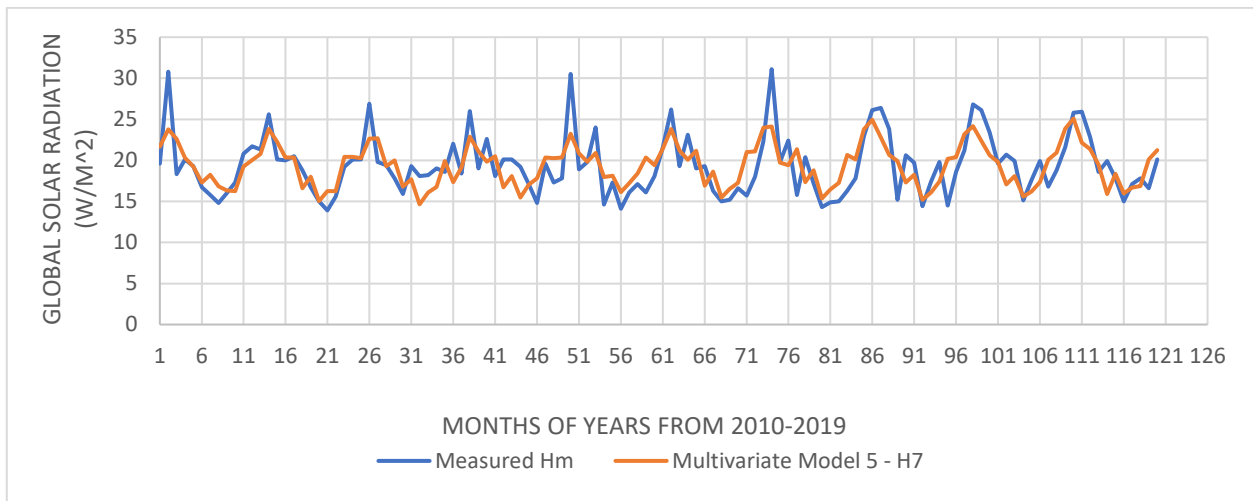


Figure 7 – Comparison of measured and estimated values of global solar radiation using multivariate model 5

From Figures 3–7, it is evident that the estimated and measured values of GSR are more correlated than those of Figures 1, 2. This could be observed from the sequential rise and fall of the data points in the figures.

Figure 6 depicts a greater degree of correlation between the measured and estimated values of GSR gotten using the multivariate model 4. This was because

multivariate model 4 had more regressors/ response predictors than the other models.

Table 10 shows the result of the employed statistical validation tools that aided in deciding the best model out of the seven applied empirical equations for estimating the GSR of the Ihiala region.

Table 10 – Statistical validation of the models

Models	MBE	MPE, %	RMSE	NSE	r	t-statistic	R-Square, %
SM	-0.007	1.910	2.819	0.400	0.633	0.026	0.316
TM	-0.021	2.162	2.998	0.321	0.572	0.075	0.221
MVM1	$-3.553 \cdot 10^{-16}$	1.731	2.691	0.453	0.673	$1.44 \cdot 10^{-15}$	0.453
MVM2	$8.333 \cdot 10^{-7}$	1.726	2.688	0.454	0.674	$3.381 \cdot 10^{-6}$	0.454
MVM3	$4.167 \cdot 10^{-6}$	1.649	2.603	0.488	0.697	$1.746 \cdot 10^{-5}$	0.488
MVM4	$3.333 \cdot 10^{-6}$	1.644	2.602	0.489	0.699	$1.398 \cdot 10^{-6}$	0.489
MVM5	$-4.293 \cdot 10^{-16}$	1.647	2.614	0.484	0.696	$1.792 \cdot 10^{-15}$	0.484

The acronyms used in Table 10 to represent the model names are expressed thus: SM – sunshine-based model; TM – temperature-based model; MVM1–MVM5 – the multivariate models.

Table 10 attests that the multivariate model 4 (MVM 4) performed better than the other models as it

best satisfied five (5) out of the seven (7) stated standard statistical tools for model validation:

- 1) MBE value is lower than those of the other models except MVM2;
- 2) MPE percentage falls within ± 10 , and it is the smallest;

- 3) RMSE is smaller than those of the other models;
- 4) NSE value is closer to one;
- 5) coefficient of correlation is higher than those of the other models;
- 6) T-statistics test is smaller than those of the other models except MVM5 and MVM1;
- 7) R-Square value is higher than those of the other models.

5 Conclusions

Under using empirical models, the study focused on estimating GSR of the Ihiala region, Anambra state in Sub-Saharan Africa. A total of seven mathematical models were derived using the formulated equations of sunshine, temperature, and multivariate polynomial equations. The obtained regression models were all statistically significant as attested by their respective p-

values that were less than the chosen significance level of 5 % for a confidence interval of 95 %.

Despite the models being statistically significant, the multivariate model 4 had a better estimation performance than the other models based on the statistical error indices employed, MBE, MPE, RMSE, NSE. This implies that the multivariate model 4 is suitable for the estimation/prediction of global solar radiation of Ihiala in Sub-Saharan Africa.

6 Acknowledgments

The authors appreciate the Nigerian Meteorological Agency (NIMET), Awka, for providing all the meteorological data employed in this study despite the hurdles encountered during the process. Special thanks to Prof. C. H. Achebe for his invaluable insights that contributed significantly to the success of this scientific article.

References

1. Appelbaum, J. (2001). *Photovoltaics: Present and Future, a Seminar Series*. Katholieke Universiteit, Leuven, Belgium.
2. Mandalia, H. C., Jain, V. K., Pattanaik, B. N. (2012). Application of Super-molecules in solar energy conversion: A review. *Research Journal of Chemical Science*, Vol. 2(1), pp. 89-102.
3. Abdulrahim, A. T., Diso, I. S., El-Jumma, A.M. (2011). Solar concentrators' developments in Nigeria: A review. *Continental Journal of Engineering Sciences*, Vol. 6(3), pp. 30-37.
4. Page, J. K., (1964). The estimation of monthly mean values of daily total short-wave radiation on vertical and inclined surfaces from sunshine records. *Proceeding of the UN Conference on New Sources of Energy*, p. 98.
5. Trabea, A. A., Shaltout M. A., (2000). Correlation of global solar-radiation with meteorological parameters over Egypt. *Renewable Energy*, Vol. 21, pp. 297-308.
6. Dimas, F. A. R., Syed, I. U. H. G., Mohd, S. A. (2011). Hourly solar radiation estimation using ambient temperature and relative humidity data. *International Journal of Environment Science and Development*, Vol. 2(3), pp. 188-193.
7. Khem, P. N., Bhattarai, B. K., Sapkota, B., Kjeldstad, B. (2012). Estimation of global solar radiation using sunshine duration in Himalaya region. *Research Journal of Chemical Sciences*, Vol. 2(11), pp. 20-25.
8. Mbah, O. M., Ozor, P., Mgbemene, C., Enibe, S. O., Mbohwa, C. (2018). Comparison of experimental data and isotropic sky models for global solar radiation estimation in Eastern Nigeria. *World Congress on Engineering, WCE 2018*, paper no. ICME_107.
9. Mbah, O. M., Ozor, P., Mgbemene, C., Enibe, S. O., Mbohwa, C. (2018). Comparative analysis of anisotropic sky models and experimental data in estimating solar radiation on tilted surface in Sub-Saharan African climate. *IEOM Conference. IEOM 2018*, pp. 592-598.
10. Aruna, R. K., Janarthanan, B. (2014). Study of clearness and cloudiness index at tropical locations. *International Journal of Scientific and Engineering Research*, Vol. 5(2), 161.
11. Prescott, J. A. (1940). Evaporation from a water surface in relation to solar radiation. *Journal of Energy Technology*, Vol. 64, pp. 114-148.
12. Page, J. K. (1961). The estimation of monthly mean values of daily total short wave radiation on vertical and inclined surface from sunshine records for latitude 40N-40S. *Proceedings of UN Conference on New Sources of Energy*, Vol. 4(598), pp. 378-390.
13. Cohen, J., Cohen, P., West, S. G., Aiken, L. S. (2003). *Applied Multiple Regression/Correlation Analysis for the Behavioral Sciences*. Lawrence Erlbaum Associates, New Jersey, USA, pp. 168-174.
14. Cooper, P. I., (1969). The absorption of radiation in solar stills. *Solar Energy*, Vol. 12(3), pp. 333-346.
15. Duffie, J. A., Beckman, W. A. (2013). *Solar Engineering of Thermal Processes*. John Wiley and Sons, New York, USA.
16. Robaa, S. M. (2008). Evaluation of sunshine duration from cloud data in Egypt. *Energy*, Vol. 33, pp. 785-795.
17. Glover, J., McCulloch, J. S. (1958). The empirical relation between solar radiation and hours of sunshine. *Journal of Royal Meteorological Society*, Vol. 84, pp. 172-175.
18. Chen, R., Ersi, K., Yang, J., Lu, S., Zhao, W. (2004). Validation of five global radiation models with measured daily data in China. *Energy Conversion and Management*, Vol. 45, pp. 1759-1769.



machines



an Open Access Journal by MDPI

Editor-in-Chief

Prof. Dr. Antonio J. Marques
Cardoso
CISE - Electromechatronic
Systems Research Centre,
Department of Electromechanical
Engineering, University of Beira
Interior, Calçada Fonte do
Lameiro, P - 6201-001 Covilhã,
Portugal






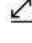

Message from the Editor-in-Chief

Machines is an international, peer reviewed journal on machinery and engineering. It publishes research articles, reviews, short communications and letters.

Our aim is to encourage scientists to publish their experimental and theoretical results in as much detail as possible. There is no restriction on the length of the papers. Full experimental and/or methodical details must be provided.

There are, in addition, unique features of this journal: Manuscripts regarding research proposals and research ideas will be particularly welcomed; Electronic files or software regarding the full details of the calculation and experimental procedure - if unable to be published in a normal way can be deposited as supplementary material.

Author Benefits

-  **Open Access** Unlimited and free access for readers
-  **Thorough Peer-Review**
-  **Discounts on Article Processing Charges (APC)** If you belong to an institute that participates with the MDPI Institutional Open Access Program
-  **High Visibility** SCIE-Science Citation Index Expanded (Clarivate Analytics), Scopus (Elsevier), ESCI-Web of Science (Clarivate Analytics), INSPEC (IET)
-  **No Space Constraints, No Extra Space or Color Charges** No restriction on the length of the papers, number of figures or colors
-  **Rapid Publication** manuscripts are peer-reviewed and a first decision provided to authors approximately 16.7 days after submission; acceptance to publication is undertaken in 2.9 days (median values for papers published in this journal in the second half of 2021)
-  **Journal Rank** JCR - Q2 (*Engineering, Mechanical*) / CiteScore - Q1 (*Mechanical Engineering*)



Alekseevsky D. G., Chernysh Ye. Yu., Shtepa V. N. (2021). Formalization of the task of creating a mathematical model of combined wastewater treatment Processes. *Journal of Engineering Sciences*, Vol. 8(2), pp. H1-H7, doi: 10.21272/jes.2021.8(2).h1

Formalization of the Task of Creating a Mathematical Model of Combined Wastewater Treatment Processes

Alekseevsky D. G.¹[0000-0002-5787-6092], Chernysh Ye. Yu.^{2,3*}[0000-0003-4103-4306], Shtepa V. N.^{3,4}[0000-0002-2796-3144]

¹Zaporizhzhya National University, 66, Zhukovskogo St., 69600, Zaporizhzhya, Ukraine;

²Sumy State University, 2, Rymkogo-Korsakova St., 40007, Sumy, Ukraine;

³International Innovation and Applied Center "Aquatic Artery", 2, Rymkogo-Korsakova St., 40007, Sumy, Ukraine;

⁴Polissya State University, 23, Dneprovskoy Flotilii St., 225710, Minsk, Belarus

Article info:

Submitted: August 31, 2021
Accepted for publication: November 3, 2021
Available online: November 8, 2021

*Corresponding email:

e.chernish@ssu.edu.ua

Abstract. This paper focuses on the formation approach to formalize the mathematical modeling of wastewater treatment processes for further forming decision support systems for wastewater treatment facilities management on such a theoretical basis. To create an experimental model of formalization of modeling problems, research was conducted on activated sludge from municipal sewage treatment facilities by introducing an oxidant (H₂O₂) during standard operation of wastewater treatment facilities and introducing a toxicant (sulfur compounds). It was determined that under conditionally standard conditions, the influence of the oxidant is negative: exceeding technological standards of the concentration of dissolved oxygen in water solutions (3.0–13.7 mg/l), low water column transparency (1.4–1.6 cm), higher concentrations of ammonia nitrogen and phosphorus. With the appearance of a toxicant in the form of reduced sulfur compounds (sulfide ions and hydrogen sulfide 1.4–2.8 mg/l), on the contrary, the positive effect of H₂O₂ on biological water treatment processes was determined: the concentration of dissolved oxygen increases to 3.4 mg/l and the swelling of activated sludge stops. In this case, using a simplified scheme of expert evaluation as a global quality criterion of the biological stage management process of water treatment for rapid assessment of the vitality of activated sludge is justified. As parameters available for direct automatic measurement, it was proposed to use ORP and pH approximated by the regression equation. Also, a conditional scheme of the decision support system for water treatment management was proposed, which will provide two-level hierarchical control: situational and operational in real-time with a preventive response to emergencies; tactical with daily, at least daily, forecasting of the treatment plants.

Keywords: formalization, mathematical model, activated sludge, toxicant, wastewater treatment, biological stage.

1 Introduction

Analyzing the composition of technical regulations and peculiarities of functioning of water treatment equipment, we can conclude that the key and most difficult tasks in the implementation of technological regulations directly at the production are [1]:

- control of the parameters of technological processes, characteristics of the equipment of treatment facilities;
- technological analysis of equipment operation according to operational production indices, resource consumption, cleaning efficiency according to regulations and established criteria and indices.

Even more complicated situation with technical devices capable of operating in real-time (RT) in industrial conditions – and they are essential for monitoring

compliance with regulatory requirements for water treatment efficiency [2].

Accordingly, justification of approaches to formalizing mathematical modeling of water treatment processes with further creation of an appropriate decision support system (DSS) is a relevant and promising scientific and applied task.

2 Literature Review

The combination of physical and mathematical modeling in a single instrumental engineering complex will integrate the approaches' strengths, minimizing the weaknesses. When creating such tools and complexes, it is advisable to take into account as much as possible the possibility of emergencies (ES) - expanding their area of

effective practice-oriented use [2]. At the same time, the operation of the activated sludge system at high values of its retention time in the aeration tanks contributes to endogenous respiration of biomass, which increases the amount of chemical oxygen demand (COD) oxidized to CO₂ and reduces the total production of sludge biomass [3]. It is essential to control the influx of electron donors to the system for different groups of microorganisms. Thus, limiting the concentration of reduced sulfur compounds in wastewater is associated with their toxic effects on biota and the fact that they are energy donors for aerobic bacteria of the genus *Thiobacillus* [4]. The ratio of microbial groups affects the qualitative and quantitative yield of greenhouse gases and the efficiency of the oxidation process of organic pollutants in wastewater, which also requires an efficient mathematical apparatus to describe this process in practice. Baresel et al. (2016) calculated nitrous oxide emissions from a conventional biological treatment process using mathematical modeling while monitoring dissolved N₂O in the aqueous phase using a sensor [5], which was necessary for monitoring system automation. Monitoring the structure, size, and morphology of aerobic pellets is increasing in importance and can be used for operation and process control purposes. For example, Leal et al. (2021) verified a sampling technique to estimate pellet and flocculus biomass using quantitative image analysis in the presence of biochemically active compounds [6].

Dychko et al. (2020) presented a methodology for environmental monitoring of natural and engineered wastewater treatment systems, including determining the dichotomous fractal structure of the measuring network, the boundaries of the polygon, and the density of pollution by Peano and Koch curves [7]. Modeling is also essential in assessing the effectiveness of biological treatment processes using activated sludge (AS). Thus, the work of Mir-Tutusaus et al. (2020) evaluated the combination of advanced oxidation processes (AOPs) based on UV/H₂O₂ treatment in combination with biological treatment (aerobic activated sludge or fungal enzyme-based treatment). Twenty-two PhACs (a pharmacological drug) were found in wastewater and were effectively removed (93–95 %) by a combination of biological treatments followed by UV/H₂O₂ treatment [8]. Spina et al. (2020) studied the enzymatic degradation of micropollutants in real, unmodified municipal wastewater with modeling of process optimization criteria [9].

The study by Breithaupt and Wiesmann (1998) used Haldane kinetics to mathematically model the biodegradation of organics in an anaerobic wastewater treatment system. The model took into account all local parameters (pH value, acetic acid concentration, biomass, and ion activity) and showed the influence of ion activity, which also requires refinement of the dispersion model [10].

Thus, previous studies presented the experimental modeling of treatment plant operation systems according to existing regulations, using the parameters of microbial growth kinetics. However, the systematization of

parameters of influence on the efficiency of activated sludge in biological treatment systems with the formation of an adequate mathematical model of the process remains an unsolved problem.

This study aims to substantiate approaches to the formalization of mathematical modeling of wastewater treatment processes using different ways of removing pollutants from municipal wastewater for further formation of decision support systems for the management of wastewater treatment facilities on such a theoretical basis.

3 Research Methodology

To create an experimental basis for formalizing the tasks of mathematical modeling, we used active sludge (AS) of biological treatment facilities of Baranovich city (Belarus) and additionally added oxidant H₂O₂ (one of the approaches of AOPs) according to the following sequence:

1) a revolving AS of the functioning sewage treatment plants was taken;

2) a zero sample (initial AS) was settled, and its qualitative indices were assessed: water column transparency, the concentration of dissolved oxygen, phosphorus, ammonia nitrogen, assessment of species composition;

3) different doses of oxidizer H₂O₂ (concentration of 3 %) were added to a zero sample (initial AS), the solution was retained, and its qualitative indicators were evaluated: transparency of water column [11]; concentration of dissolved oxygen was determined by an electrochemical method [12]; concentration of total dissolved phosphorus was determined by a photometric method after combustion with persulfate [13]; concentration of ammonium nitrogen by persulfate photometric method with Nessler reagent [14]; the species composition was assessed [11].

Also, the presence of sulfide ions and hydrogen sulfide at the treatment plant's inlet and its effect on the AS was investigated in a passive experiment mode. The results were analyzed to build mathematical models and form a hierarchical structure for solving such a complex problem. The basis of such conclusions justified the "global" criterion of quality of the management process of combined pollutant removal processes.

4 Results and Discussion

4.1 Experimental study

Three doses of H₂O₂ (3 %) were introduced into the activated sludge of the treatment plant: 0.5, 1.0, and 1.5 ml/l. Comparison of dissolved oxygen concentration in the aqueous solution of activated sludge was performed at intervals equal to 2 hours (Figure 1). The influence of various toxicants leads to a disturbance of the flocculation process and the destruction of floccules, which are already formed. This entails an increase in the amount of finely dispersed suspended fraction and, accordingly, a decrease in the transparency of supernatant (Figure 2).

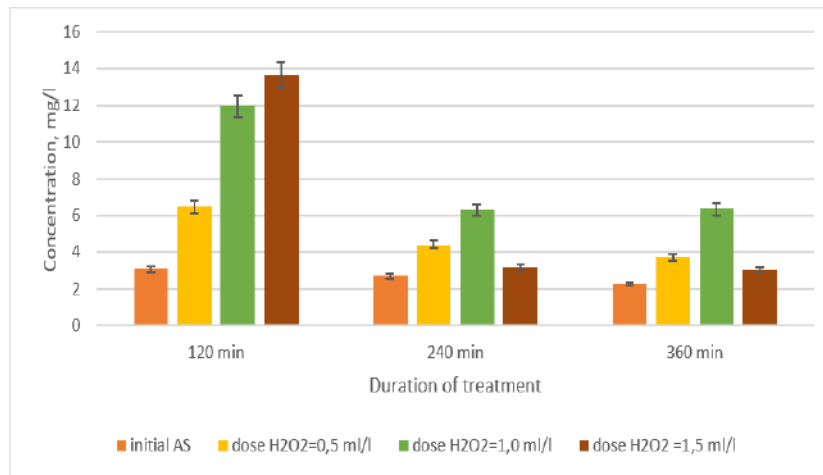


Figure 1 – The concentration of dissolved oxygen in the activated sludge of wastewater treatment plants and after adding different doses of hydrogen peroxide to AS (3 % concentration)

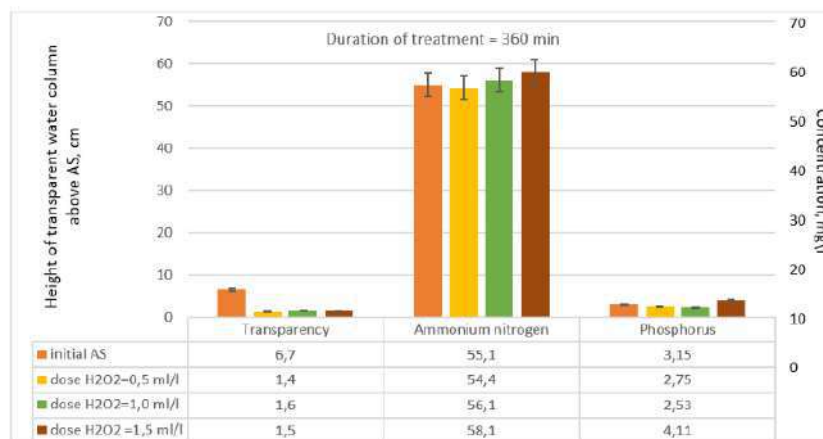


Figure 2 – Wastewater quality control by indicators of water column transparency over AS, the concentration of ammonia nitrogen and phosphorus when treated with different doses of hydrogen peroxide (3 % concentration)

The degree of biological treatment is satisfactory if the water transparency is at least 12 cm. In this case, it was initially (in the initial AS) was 8 cm. When applying different doses of hydrogen peroxide, it decreased. Other indices, in particular the concentration of ammonia nitrogen and phosphorus, did not vary significantly from the initial AS without adding hydrogen peroxide (3% solution), but still higher concentrations of ammonia nitrogen and phosphorus were observed in the series of experiments.

After 6 hours from the start of the experiments, an analysis of the species composition of AS was performed (Table 1).

The results obtained (Figures 1–2, Table 1) allow us to formulate the following conclusions about the conditionally standard modes of operation of biological wastewater treatment systems:

- in general, the initial AS, functioning treatment plants (without adding additional oxidant H_2O_2), more consistent with the technological objectives of wastewater treatment in terms of “Concentration of dissolved oxygen”, “Transparency”, “Concentration of phosphorus”,

“Concentration of ammonium nitrogen”, the species composition;

- additional oxidizer H_2O_2 has a negative impact on the AS by the indicators mentioned above.

At the same time to the inlet of sewage treatment plants after a certain period began to arrive sewage with an impermissibly high concentration of reduced sulfur compounds (the total concentration of sulfide ions and hydrogen sulfide 1.4–2.8 mg/l) - as a result, began to swell the AS, reducing the concentration of dissolved oxygen in the water solution, reducing the transparency of the water column above the silt. Following the rules for the reception of industrial wastewater in the sewer system of settlements, the maximum allowable concentration of hydrogen sulfide in the effluent sent for biological treatment should not exceed 1 mg/l. At $pH < 10$, the content of sulfide ions can be neglected, at $pH = 7$ the content of H_2S and HS^- is approximately the same, at $pH = 4$ H_2S is almost entirely (99.8 %) in the form of H_2S .

At the same time introduction of an additional oxidizer H_2O_2 promptly stabilized the technological situation (Table 2).

The results obtained (Table 2) demonstrate the positive technological effect of using AOPs approaches in biological water treatment – the process of swelling of AS was stopped, and its regeneration began.

At the same time several other solutions can be used to prevent bloating of AI: when the concentration of dissolved oxygen in the aerobic zones of the aeration tank is less than 1.0 mg/l – to use the maximum available capacity of the aeration system and ensure a dissolved oxygen concentration not lower than 1.0 mg/l; when pH values of sludge mixture are less than 6.0–6.5 – provide the possibility of pH regulation; when volley discharge of toxic substances and/or oil products to the treatment plant – increase the air supply to the aeration tanks to ensure the concentration of dissolved oxygen in the tank.

However, all such operations require maximum automation of the process, taking into account normal and abnormal situations, and to date, the wastewater treatment process using activated sludge is uncontrollable (very poorly controlled) in real-time. In the design of sewage treatment plants, this process is considered self-organizing. At the same time, with the emergence of new factors that lead to the death of AS, the natural process of self-regulation can not, in some cases, ensure the survival of activated sludge.

Accordingly, there is a problem with creating a process control system. And, in modern conditions, the primary process in this system must be an automatic control system (ACS).

Table 1 – Species composition of AS before and after application of H₂O₂ (3 % solution)

Active peroxide treatment (3 % concentration)		Species composition of the initially AS
Active peroxide treatment (3 % concentration)	Species composition after peroxide application (3 % concentration)	
0.5	<p>Nitrous; Opercularia sp; Vorticella; Aspidisca; Carchesium (singular); Amoeb shell cysts</p> <p>In the silt, Vorticella, attached colonials are mainly present. Vagrants are observed. Protozoa cysts are present.</p> <p>Cottonwood of moderate size, dark brown color</p>	<p>Nitrous; Carchesium; Opercularia sp; Vorticella (разнообразные); Pamphagus; Aspidisca.</p> <p>A relatively large number of attached infusoria, solitary forms, and colonial forms are observed. The activity of the attached ones is satisfactory. The number of bacteria not associated with the active sludge is moderate. Gastropod infusoria appeared occasionally. Small filamentous are present in sludge flakes. Diversity in attached infusoria. Sludge flake of moderate size</p>
1.0	<p>Nitrous; Opercularia; Vorticella; Carchesium.</p> <p>Sludge flakes are finer, the number of attached ones decreased, single attached (Vorticella) jug-shaped, attached infusoria are smaller. The number of filamentous bacteria not associated with activated sludge flakes has decreased. No other species diversity was observed</p>	<p>Nitrous; Euglypha; Opercularia (with a closed eyelash disc); Oligohymenophora; large free-floating infusoria; Vorticella; several species are found in the mud funnel-shaped and with a narrow peristome; Carchesium (colonial infusoria); Opercularia coarctata.</p> <p>Cotton silt of moderate size, pervaded by many small filamentous bacteria. Little diversity of protozoa by species. The silt is dominated by attached infusoria</p>
1.5	<p>Small filamentous;</p> <ul style="list-style-type: none"> - Carchesium; - Opercularia; - Vorticella; - Shell corneocytes; -Equal-crested infusoria. <p>Attached are found in a depressed state. Protozoan cysts are found. The total number decreased, the cotton was more fragmented. Water over silt has non-sedimentary turbidity</p>	<p>Small filamentous; Archesium; Opercularia; Vorticella; Shell cornicles; Equinocular infusoria.</p> <p>Cottonwood silt of moderate size, a variety of attached infusoria both solitary and colonial forms is observed. Mostly moderately active, but there are also with a closed ciliated disk.</p> <p>Equiaceous ciliated infusoria appeared, shell amoebae - singularly.</p> <p>The number of free-floating bacteria decreased</p>

Table 2 - AS states at increased concentrations of reduced sulfur compounds and with the addition of an additional oxidizer H₂O₂

The total concentration of sulfide ions and hydrogen sulfide	Without hydrogen peroxide		After a dose of 1 ml/l of peroxide (3 % concentration)	
	Transparency, cm	Dissolved oxygen concentration, mg/l	Transparency, cm	Dissolved oxygen concentration, mg/l
2.80	0.7	1.3	6.8	2.3
1.36	1.1	1.5	5.1	3.4
2.06	0.9	1.1	7.1	2.5

4.2 Formalization of mathematical models

In the procedure of ACS synthesis, the first step is the synthesis of the mathematical model of the control object (CO). In this process, the control object is the AS itself, located inside the technological equipment.

Therefore, the following hierarchical structure of the solution of the complex problem is built.

– Problem 1 (global). Preventing the death of activated sludge at sewage treatment plants.

Solution of the problem 1. Creation of a process control system.

– Problem 2 (consequence). An adequate mathematical model of the process is needed to create the ACS.

Solution of problem 2. Studying the process, in the course of experimental researches, with its subsequent formalization.

– Problem 3. Formalization of the process implies the introduction of process quality criterion as a numerical expression of control objective.

Solution of problem 3. Formation of a control quality criterion by setting its physical meaning, designation, and scale.

– Problem 4. Both the study of the control object, to synthesize a mathematical model, and the control process require the automatic definition of a global criterion. The input quality criterion cannot be determined automatically by direct measurement.

The solution to Problem 4. Application of indirect measurement by determining the global quality criterion through the quantities available for direct automatic measurement.

– Problem 5. At present, no adequate models are defining the connection of global criterion with output parameters available for direct automatic measurement.

The solution to Problem 5. Carrying out experimental researches on the determination of relation of values available for direct automatic measurement and global criterion, with its further formalization in the form of a mathematical model.

A global criterion must be connected with a control purpose to solve a global problem. At the same time, it must be an adequate numerical expression of the goal, i.e., the assessment of the state of the AS biocenosis.

It should be noted that there are many techniques for assessing the viability of AS [11, 15–18]. They are based on studying the qualitative and quantitative composition of its biocenosis. The quantitative composition of

microorganisms has a direct relationship with the incoming wastewater flow rate. After counting all microfauna, the following is calculated: number of species, the ratio of attached microorganisms to free-floating (K coefficient), percentage of sensitive microorganisms to resistant ones, Cuba index (it contains information both on the number of species and their numerical distribution by species) and the number of microorganisms per dose of sludge. These quantitative indices serve to assess the biocenosis of activated sludge. For example, according to them, one can judge whether it has a good species composition if all the indices are normal [15, pp. 195–203].

Thus, in [16–18], approaches to the systematization of filamentous microorganisms are outlined. These techniques for assessing the AS biocenosis are rather labor-intensive. Therefore, we proposed to use a simplified expert evaluation scheme as a global criterion for the quality of the management process with the characteristics presented in Table 3 for express evaluation.

For example, it is proposed to use ORP (redox potential) and pH as parameters available for direct automatic measurement.

As a first approximation, the following regression equation for determining the global criterion for the wastewater treatment plants understudy is proposed:

$$\alpha = a_1 \cdot (ORP_1 - ORP_2) + a_2 \cdot (pH_1 - pH_2) + a_3 \cdot ((ORP_1 - ORP_2) \cdot (pH_1 - pH_2))$$

where a_1, a_2, a_3 – regression coefficients; ORP_1, ORP_2 – readings of potential redox sensors at the inlet and outlet of aeration tank (digester), respectively; pH_1, pH_2 – readings of pH sensors at the inlet and outlet of the aeration tank, respectively.

Accordingly, such a mathematical model can be included in decision support systems for wastewater treatment process management (Figure 3).

Such pattern will allow providing water treatment systems with two-level hierarchical control:

– situational-operational in real-time with preventive response to emergencies;

– tactical with daily, as a minimum, forecasting of treatment facilities operation.

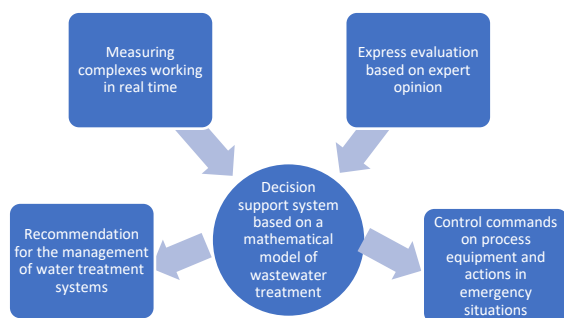


Figure 3 – Integration of the decision support system based on the proposed mathematical models with the existing water treatment system

5 Conclusions

The wastewater treatment plant is complex, multi-parameter, and non-linear to control the object, which is confirmed by the experimental studies on the effect on the activated sludge oxidant H_2O_2 (one of the approaches AOPs):

– under conditionally normal conditions, such influence is negative: exceeding technological standards of dissolved oxygen concentration in water solutions (3.04–13.68 mg/l), low transparency of the water column (1.4–1.6 cm), higher concentrations of ammonia nitrogen and phosphorus

– with the appearance of a toxicant in the form of reduced sulfur compounds (total concentration of sulfide ions and hydrogen sulfide 1.38–2.80 mg/l), for which measurements in real-time there are no effective measuring instruments, on the contrary, the effect of the oxidant H_2O_2 has a positive effect on the biological water treatment: the concentration of dissolved oxygen increases to 3.4 mg/l. It stops bloating of AI with further regeneration.

Using the global criterion (criterion of AS vitality) associated with the purpose of management, as a form of solving the global problem of automation of wastewater treatment plants, as a tool for formalizing mathematical models, will create an appropriate decision support system with the functionality of operational regulation and tactical prediction even in emergencies.

Further research should be aimed at forming a knowledge base for creating mathematical models and checking their adequacy and technological compliance.

References

- Shtepa, V. M. (2012). Rationale for the algorithm of experimental and analytical studies of modes of electrical wastewater treatment of agro-industrial facilities in order to build energy-efficient control systems. *Energy and Automation*, Vol. 1(11), pp. 62–71.
- Shtepa, V. M. (2014). Substantiation of the architecture of the management system of complex methods of wastewater treatment of industrial facilities. *Bulletin of Kharkiv National Technical University of Agriculture named after of Peter Vasylenko*, Vol. 154, pp. 48–50.
- Campos, J. L., Valenzuela-Heredia, A., Pedrouso, D., del Rio, D. V., Belmonte, M., Mosquera-Corral A. (2016). Greenhouse gases emissions from wastewater treatment plants: minimization, treatment, and prevention. *Journal of Chemistry*, Vol. 2016, 3796352, doi: 10.1155/2016/3796352.
- Kuldeyev, E. I., Tastanova, A. E., Bondarenko, I. V., Temirova, S. S., Nurlybayev, R. E., Botantayeva, B. S., M. Zaihidee, F. (2021). Complex alumina-ferrous coagulant for effective wastewater purification from hydrogen sulfide. *Advances in Materials Science and Engineering*, Vol. 2021, 5595599, doi: 10.1155/2021/5595599.
- Baresel, C., Andersson, S., Yang, J., Andersen, M. H. (2016). Comparison of nitrous oxide (N_2O) emissions calculations at a Swedish wastewater treatment plant based on water concentrations versus off-gas concentrations. *Advances in Climate Change Research*, Vol. 7(3), pp. 185–191.
- Leal, C., del Rio, A. V., Ferreira, E. C., Mesquita, D., Amaral, A. L. (2021). Validation of a quantitative image analysis methodology for the assessment of the morphology and structure of aerobic granular sludge in the presence of pharmaceutically active compounds. *Environmental Technology and Innovation*, Vol. 23, 101639, doi: 10.1016/j.eti.2021.101639.
- Dychko, A., Remez, N., Kyselov, V., Kraychuk, S., Ostapchuk, N., Kniazevych, A. (2020). Monitoring and biochemical treatment of wastewater. *Journal of Ecological Engineering*, 2020, Vol. 21(4), pp. 150–159, doi: 10.12911/22998993/119811.
- Mir-Tutusaus, J. A., Jaen-Gil, A., Barcelo, D., Buttiglieri, G., Gonzalez-Olmos, R., Rodriguez-Mozaz, S., Caminal, G., Sarra, M. (2021). Prospects on coupling UV/ H_2O_2 with activated sludge or a fungal treatment for the removal of pharmaceutically active compounds in real hospital wastewater. *Science of The Total Environment*, Vol. 773, 145374, doi: 10.1016/j.scitotenv.2021.145374.
- Spina, F., Gea, M., Bicchi, C., Cordero, C., Schiliro, T., Varese, G. C. (2020). Ecofriendly laccases treatment to challenge micropollutants issue in municipal wastewaters. *Environmental Pollution*, Vol. 257, 113579, doi: 10.1016/j.envpol.2019.113579.
- Breithaupt, T., Wiesmann, U. (1998). Konzentrationsprofile in rotationsscheibenreaktoren und deren modellierung am beispiel des anaeroben acetatabbaus mit experimenteller überprüfung. *Acta Hydrochimica et Hydrobiologica*, doi: 10.1002/(SICI)1521-401X(199809)26:5%3C288::AID-AHEH288%3E3.0.CO;2-X.
- Markevich, R. M., Grebenchikova, I. A., Rymovskaya, M. V., Flurik, E. A. (2009). Methodological guide to control the process of biological treatment of municipal wastewater. *Bulletin of Belarusian State Technical University*, Vol. 10, pp. 25–31.
- ISO 5814-2007 Water quality – Determination of dissolved oxygen – Electrochemical sensor method.

13. Semenov, A. D. (1977). *Guidebook on Chemical Analysis of Inland Surface Waters*. Hydrometeoizdat, Saint-Petersburg.
14. Collection of Measurement Procedures Approved for Use in Environmental Control Laboratories of Enterprises and Organizations of the Republic of Belarus. Minskizdat, Minsk, Belarus, 1997, pp. 167–174.
15. Dzhumagulova, N. T., Gavrilov, I. E., Dap, N. D. (2019). Study of the species composition of microorganisms involved in wastewater treatment. *Bulletin of the Tomsk Polytechnic University. Series "Geo Assets Engineering"*, Vol. 330(9), pp. 195–203.
16. PND F SB 14.1.92-96. Methods of Sanitary and Biological Control. Methodological Guidelines for Hydrobiological Control of Filamentous Microorganisms of Activated Sludge. Moscow, 1996, pp. 22–23.
17. Flores-Alsina, X., Ramin, E., Ikumi, D., Harding, T., Batstone, D., Brouckaert, C., Sotemann, S., Gernaey, K. V. (2021). Assessment of Sludge Management Strategies in Wastewater Treatment Systems Using a Plant-Wide Approach. *Water Research*, Vol. 15, 116714, doi: 10.1016/j.watres.2020.116714.
18. Spiller, M. (2017). Measuring adaptive capacity of urban wastewater infrastructure – Change impact and change propagation. *Science of Total Environment*, Vol. 601, pp. 571–579, doi: 10.1016/j.scitotenv.2017.05.161.



Chernysh Y., Plyatsuk L., Roubik H., Yakhnenko O., Skvortsova P., Bataltsev Y. (2021). Application of technological solutions for bioremediation of soils contaminated with heavy metals. *Journal of Engineering Sciences*, Vol. 8(2), pp. H8-H16, doi: 10.21272/jes.2021.8(2).h2

Application of Technological Solutions for Bioremediation of Soils Contaminated with Heavy Metals

Chernysh Y.^{1,2*}, Plyatsuk L.^{1,2}, Roubik H.^{2,3}, Yakhnenko O.¹, Skvortsova P.¹, Bataltsev Y.¹

¹ Sumy State University, 2, Rymkogo-Korsakova St., 40007 Sumy, Ukraine;

² International Innovation and Applied Center “Aquatic Artery”, 2, Rymkogo-Korsakova St., Sumy, 40007, Ukraine;

³ Czech University of Life Sciences Prague, Faculty of Tropical AgriSciences, 129, Kamycka St., 165 00 Prague, Czech Republic

Article info:

Submitted: September 2, 2021
 Accepted for publication: November 24, 2021
 Available online: November 29, 2021

*Corresponding email:

e.chernish@ssu.edu.ua

Abstract. This article focuses on studying biotechnologies for remediation of soils contaminated with heavy metals to determine further the most effective methods for cleaning soils from the action of toxicants with their subsequent implementation in practice. The soil restoration methods were analyzed, their advantages and disadvantages were identified, making it possible to establish that biological methods are the safest and most environmentally friendly. The expediency of using biological methods lies in the possibility of breeding strains of microorganisms that destroy soil toxicants. However, the efficiency of microbial cultures is not equally high due to a narrow range of favorable conditions for functioning, the risk of manifestation of the phenomenon of degeneration of microorganisms until the required level of soil purification is achieved. This confirms the prospects for the further development of this direction and the search for ways to eliminate certain disadvantages of biological methods. For an integrated biotechnological solution to soil remediation, a scheme of aerobic plants was developed, which is characterized by two stages: aerobic soil cultivation with biocomposite and a phytoremediation stage for additional purification and control of the content of toxicants in the soil.

Keywords: soil contamination, biotechnologies, remediation, heavy metals, biocomposite

1 Introduction

One of the most dangerous to human and animal health pollutants is heavy metals (HM). They do not decompose in the environment and accumulate in the tissues of living organisms [1]. Developing effective ways to preserve and protect the environment requires the definition and constant monitoring of the distribution of toxicants in the ecosystem, particularly in the edaphotope, according to their distribution by soil profile. At the same time, the need for comprehensive application of measures for their immobilization into immobile forms is of paramount importance. An ecologically safe method of soil decontamination is traditionally considered to be phytoremediation, due to which the process of removing toxicants occurs without destroying the soil structure and reducing its fertility [2, 3]. The latest biotechnological methods of detoxification and restoration of soil complexes of natural and anthropogenic landscapes are being developed.

Scientific and methodological issues of soil remediation and other components of the geological environment from toxic pollutants are being developed within a new scientific direction – geopurgology.

Among the measures to reduce the impact of pollutants on the soil should be identified primary: chemical, technological, mechanical, and biotechnological. The formed block diagram for these areas is shown in Figure 1.

Phytoremediation is considered the most promising and ecologically safe method of decontamination of contaminated soils. The purification mechanism is based mainly on the use of hyperaccumulator plants, which can remove toxicants from the environment in high concentrations and show tolerance to their action.

The main advantage of phytotechnologies is that removing pollutants occurs without destroying the soil structure and reducing its fertility.

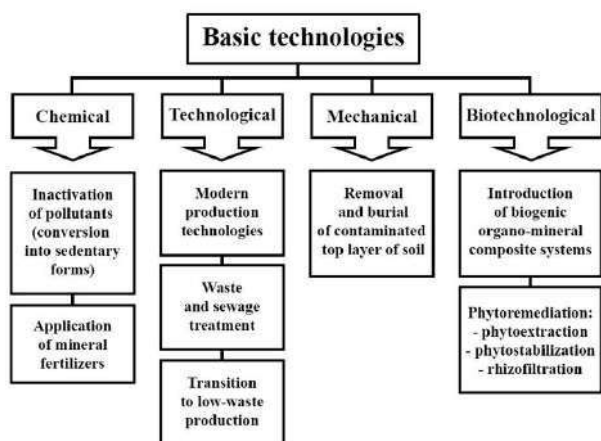


Figure 1 – Remediation technologies for contaminated soil

To remediate the soil from heavy metals used [4-6]: phytoextraction (absorption and accumulation of pollutants in the plant), phytostabilization (reduction of pollutant mobility and/or accumulation in the root system of the accumulating plant or in the rhizome) or rhizofiltration (metals are absorbed and bound in the root systems of phytore).

The work aims to study the influence of biotechnological tillage on the localization of HM in the soil complex.

To achieve this aim, the following tasks were solved:

- to study the processes of heavy metals in the soil complex concerning other components of the ecosystem;
- to determine the directions of soil bioremediation in the process of cleaning them from HM;
- development of a technological scheme for implementing complex biotechnology for remediation of soils contaminated with heavy metals.

2 Methodological approach to the processes of heavy metals fixation in soils using biotechnological techniques

Soil microorganisms can influence the bioavailability and absorption of heavy metals and can also promote growth and reduce the toxic effect of pollutants on plants. Approximately 80 % of aboveground plants have symbiotic associations of microorganisms. The ability to exist in an environment contaminated with heavy metals is characteristic of many species inhabiting the rhizosphere. The reason for the stability of the soil microbiota can be both innate and acquired mechanisms of adaptation.

Microorganisms (internal bioremediation) can be introduced into the contaminated soil or isolated from a specific environment and then into the contaminated one (bioaugmentation).

Bioaugmentation – the introduction (in the form of biological products) of specialized microorganisms, alien to the habitat, which has been previously isolated from natural sources or specially genetically modified and selected. There is the destruction of pollutants by different types of microorganisms due to the activation of aboriginal microflora or the introduction of certain cultures of microorganisms into the soil, the use of complex biological products and other methods to create an optimal environment for the development of certain groups microorganisms decompose pollutants. The soil becomes suitable for growing plants. Introduced microorganisms decompose the bulk of contaminants, reduce their negative impact on biota and thus stimulate self-cleaning processes [7].

Table 1 shows the results of the analysis of the properties of different types of organic fertilizers.

Table 1 – Advantages and disadvantages of different types of organic fertilizers

Name of organic fertilizer	Advantages	Disadvantages
Manure	Cheap and affordable organic fertilizer contains macro-and micronutrients in large quantities. The aftereffect of the applied fertilizer lasts 3-5 years. Contributes to the gradual humus formation and soil structure	The composition is not constant, it depends on the type of animal, its feed, litter and method of maintenance, storage of manure and its humidity. Requires special mechanisms for introduction. Requires determination of the concentration of substances to not provoke toxic effects. It may contain geohelminth eggs and cause additional biocontamination. Improper storage and application can cause contamination of soil, groundwater, and surface water with excessive amounts of nitrogen and phosphorus compounds. It may contain large amounts of dissolved salts, including chlorides and sulfates, which can cause secondary salinization of the soil.

Name of organic fertilizer	Advantages	Disadvantages
Digest	<p>It has a balanced composition of macro and micronutrients.</p> <p>It's an "environmentally friendly" fertilizer, because after the mesophilic mode, it does not contain components of pathogenic microflora, worm eggs, weed seeds.</p> <p>Promotes the development of typical soil microflora.</p> <p>It is a fermented material, quickly humified or mineralized depending on the soil conditions.</p> <p>Contributes to the structure of the soil.</p> <p>Increases soil moisture content.</p> <p>Stimulates the development of bacterial microflora and inhibits the development of actinomycetes and mycoflora.</p>	<p>The composition is not constant and depends on the raw material and the fermentation period.</p> <p>Productivity as a biofertilizer depends on humidity and depth of application.</p> <p>It has an alkaline pH, better have a stimulating effect on acidic soils.</p> <p>The liquid fraction of the digestate has a high concentration of certain nutrients (phosphorus, ammonia) and requires prior preparation before application (dilution with water).</p> <p>Does not have a selective inhibitory or stimulating effect concerning certain types of microorganisms.</p> <p>The digestate obtained during the fermentation of the sludge of treatment plants preliminarily requires laboratory chemical studies to prevent the ingress of contaminants into the soil in a mobile form.</p>
Vermicompost	<p>Contains 4–8 times more humus content Than regular compost.</p> <p>Easy to transport.</p> <p>Improves soil structure.</p> <p>Enriches with organic residues serve as a nutrient substrate for certain groups of soil microorganisms.</p>	<p>The need to dispose of biomass of live worms, to ensure that they do not enter natural ecosystems.</p> <p>The need to maintain certain conditions for the activity of worms.</p> <p>Have enough space for vermicomposting.</p>
Biofertilizers – micro-biological inoculants - specialized drugs based on microorganisms and enzymes	<p>Do not harm the soil ecosystem.</p> <p>Contain natural strains of microorganisms that can facilitate the assimilation of certain chemical elements in other members of the soil biota.</p> <p>Direct stimulation of growth through the synthesis of valuable substances for plants.</p> <p>Resistant to water leaching.</p> <p>Do not contain pathogenic microflora.</p> <p>Cause increased availability of nutrients, synthesis of growth hormones, decomposition of stress mediators.</p>	<p>Requires certain conditions during storage of the drug.</p> <p>They do not contain the necessary ready-made substances necessary for developing soil microflora or plants but only stimulate the chemical transformation of substances present in the soil.</p> <p>You can not accurately predict the speed of the result.</p> <p>They operate in certain climatic conditions and require a particular time of application (from spring to autumn, in a relatively warm period).</p>
Biopesticides – indirect stimulation of the development of certain crops due to the suppression and displacement of phytopathogens or bacteria that inhibit the growth of plants or beneficial microflora	<p>High efficiency.</p> <p>Non-toxic.</p> <p>Do not cause gradual resistance in the organism on which they act.</p> <p>Effective for different plant crops and in different soil and climatic conditions.</p> <p>Often compatible for use together with biofertilizers.</p>	<p>Have a short storage method.</p> <p>More expensive than conventional pesticides.</p> <p>Stop active action after a specific time.</p> <p>Requirements for deadlines.</p> <p>Have only a narrow focus on practical action.</p>

The expediency of their use is due to the lack of developed natural microbiological coenosis with pollution.

Advantages of use:

- selectivity;
- the possibility of removing strains of microorganisms that destroy soil toxicants.

Disadvantages of use:

- the efficiency of microbial cultures is not equally high due to the narrow range of favorable operating conditions;
- the risk of manifestation of the phenomenon of degeneration of microorganisms before reaching the required level of soil purification;
- the risk of violation of natural microbiocenoses with the use of microbial cultures.

Bacteria of the genera *Actinomyces*, *Arthrobacter*, *Thiobacterium*, *Desulfoiromaculum*, *Pseudomonas*, *Bacillus*, and other fungi with bacterial genes are used for purification. In complex cases of soil contamination, the most effective is its purification with complex biological products containing a range of crops and nutrients at the same time.

For the biodegradation of HM in soils, a method of their purification [8] has been developed by treatment with a culture of bacteria (strain *Bacillus fastidious* VKPM B-4368) in a liquid mineral nutrient medium containing carbohydrates. The bioleaching process is carried out until the pH value is equal to 4.0–6.0 with the consumption of the liquid component in the amount of 0.4–10.0 mass parts per 1 mass part of the cultivated soil. The method is effective but is material-intensive (bringing pH 2.8 to pH 4.0–6.0 requires a large amount of neutralizing substance, the cost of 0.4–10.0 mass parts of nutrient medium per 1 mass part of the soil is also resource-intensive) [9–10].

The efficiency of phytotechnology use is determined by the phytoavailability of heavy metals in the soil environment. Effectors are used to enhance remediation, mainly chelated compounds, but sometimes microorganisms are used. Common effectors are ethylenediaminetetraacetic acid, citric acid, diethylenetriaminepentaacetic acid, ethylene glycol tetraacetic acid, and others. Synthetic chelating compounds are considered more effective, but have a severe disadvantage of use – many soluble and mobile forms of metals [11–13].

Biosurfactants are amphiphilic compounds containing both hydrophilic and hydrophobic portions, referred to as head and tail. Compared with chemical surfactants, biosurfactants derived from plants and microorganisms have shown better performance considered suitable in removing heavy metal from contaminated soil. The mechanism of heavy metal removal from contaminated soil using ionic biosurfactants is shown in Figure 2.

[15] studied the effect of the sequence of addition of OH-Al species, protein molecules (albumin) and montmorillonite, and pH on the nature and properties of the final protein-OH-Al-montmorillonite complexes.

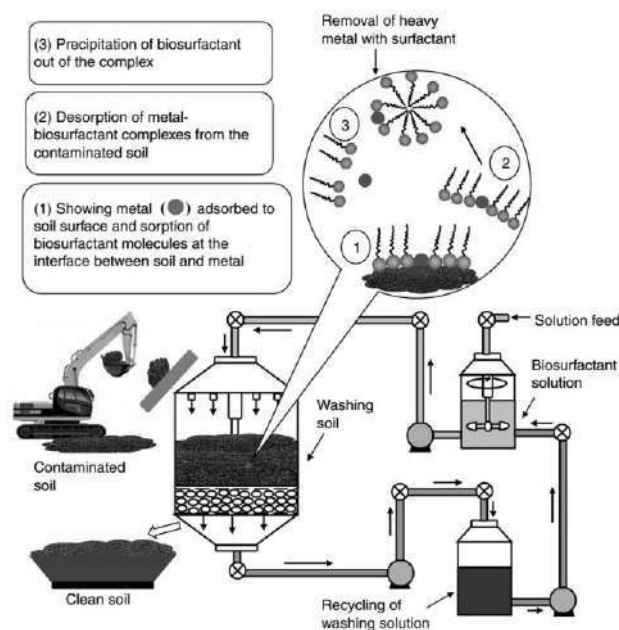


Figure 2 – Processing contaminated soil using biosurfactants for heavy metal removal [14]

Sorption of elements in cationic form onto soil components may be either enhanced or inhibited by the presence of organic acids (as oxalic, citric, malic, tartaric, malonic acid) and aminoacids through different processes, including alteration of surface charge, site competition, formation of different complexes in solution, ternary complex formed on the surfaces of soil components. Ternary surfaces complexes may be classified as type A, in which the metal ion is bonded to both the sorbent and the organic ligand, or type B, in which the ligand is bonded to the sorbent between the surface and the metal ion (Figure 3) [15].

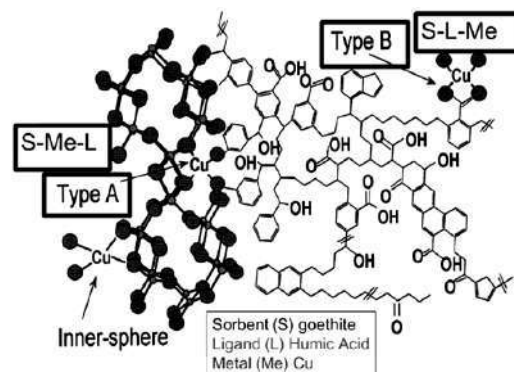


Figure 3 – Illustration of some possible bonding configurations of Cu (Me) on goethite (S)–organic matter (L) complexes: inner sphere complexation of Cu at goethite sites, and type-A-(S-Me-L) and B-(S-L-Me) ternary complexes [15]

The highly dispersed fraction consists of minerals with a layered crystalline structure, in which the layers are connected less firmly than the ions in the structures of clastic minerals.

Table 2 – Methods of soil biocleaning

The process of bio-remediation	Gist	Sort	Advantages	Disadvantages
Biodegradation of pollutants using microorganisms	Destruction or transformation of contaminants under the influence of enzymatic systems of microorganisms, decomposition of toxic forms of HM compounds to less toxic ones, transformation from active-mobile form of HM compounds into difficult or immobile inaccessible biota, or absorbed on the surface of secondary clay soil minerals.	Internal bioremediation due to naturally occurring species in this type of soil.	<p>The possibility of using artificially created to extract a particular type of toxicant strains.</p> <p>Specific selectivity of action on the toxicant.</p> <p>Relatively easy application in the absence of a developed natural microbiological coenosis.</p> <p>Can be used in situ and ex situ.</p> <p>The cleaning process can be carried out in the near-surface part of the soil using optional aerobes and anaerobes.</p> <p>Less depends on the seasonal phenomena of the atmosphere due to more stable conditions of the soil environment.</p>	<p>The efficiency of microbial cultures is not equally high due to the narrow range of favorable operating conditions.</p> <p>The risk of the phenomenon of degeneration of microorganisms to achieve the required level of soil purification, the need for constant monitoring of species composition.</p> <p>The need together with a specific strain of microorganisms to make additional nutrient medium (mineral or organic components) the risk of violation of natural microbiocenoses with introduced microbial cultures.</p>
		Bioaugmentation (introducing certain cultured or removed from another environment species of organisms).		
Phytoremediation	The use of hyperaccumulator plants that are tolerant to the action of HM and can remove certain toxicants from the environment in high concentrations, accumulating them in certain parts of the body.	Phytoextraction (absorption and accumulation of pollutants in the plant).	<p>Can be used in situ, without spending money on the transfer and return of soil after cleaning, are more environmentally friendly for the environment.</p> <p>It is possible, if necessary, to completely remove from the contaminated area of the plant, the body of which contains absorbed from the soil HM.</p> <p>After the death of the body of plants and transformation into a component of humus or the formation of organo-mineral complexes of soil with clay minerals, there is a binding of HM compounds in the stationary component, at the same time there is an improvement in the structural state of the soil, trophic and gas regimes, improvement of the properties of the soil system as a whole.</p>	<p>Do not show selective action only for a certain type of pollutant.</p> <p>Die with an exaggeration of a certain amount of toxicant due to violation of enzymatic regulatory systems.</p> <p>Cleansing occurs only during the growing season.</p> <p>Cleaning occurs primarily in the surface layers of the soil, where the root systems of plants reach.</p> <p>Long-term slow uncontrolled process, which depends on the state of the plant organism.</p>
		Phytostabilization (reduction of pollutant mobility and/or accumulation in the root system of the accumulating plant or in the rhizosphere).		
		Rhizofiltration (metals are absorbed and bound in the root systems of phytoremediaries)		

This feature of these minerals contributes to the sorption of scattered heavy metals, and their concentration in this fraction is higher than in fine-grained and in the soil as a whole [16].

A new direction of scientists' research is the use of alternative immobilizers and the evaluation of their effectiveness compared to traditional means.

Table 2 shows a comparative description of methods of biological soil treatment.

In the work of Adejumo Sifau et al. (2011) investigated the effect of inorganic fertilizer (NPK, 100 kgN/ha), compost from cassava (*Manihot utilissima* Pohl.), and tintonia (*Tithonia diversifolia*) at concentrations of 20 and 40 tn/ha on the process of immobilization of Pb in the soil in which corn was grown (*Zea mays* L.). It was found that the concentration of mobile lead in the soil environment with the use of compost from titanium and cassava in the amount of 40 tn/ha, decreased by 72 % and 67 %, and at 20 tn/ha – by 66 % and 49 %. The addition of compost helped to increase the height of the plant by 89–94 %, as well as the area of leaves and their number (especially when applying to the soil compost from titanium at a concentration of 40 tn/ha). Activation of biodegradation of pollutants by maintaining the optimal temperature is carried out by covering the contaminated soil with black polyethylene film in winter to increase the temperature. In summer – use a transparent film to reduce evaporation from the surface [11].

4 Results and Discussion

4.1 Technological intensification of soil bioremediation processes

Various bioreactor designs can be used for ex situ purification of contaminated soils and other materials, including fixed bed reactors (solid-phase bioreactor) and suspension with stirring (sludge bioreactor).

Suspension (sludge) reactors are mainly used for the biological treatment of contaminated soil (Figure 4). The amount of soil in suspension reactors with stirring can be up to 30 % of the total volume. Their advantages over solid-phase reactors are easier control, better process control, the ability to provide a higher level of aeration. They are not prone to siltation, which clogs with sediments, suspended particles, and excess biomass. But the design of suspension reactors is more complex, consumes more energy, and requires high costs for exhaust-air purification [18]. Aerobic biogeochemical barriers can be created by the migration of groundwater with high content of Sr^{2+} , Ba^{2+} , Fe^{2+} , Mn^{2+} . Due to the formation of carbonic acid during the oxidation by microorganisms of organic substrates introduced into the contact zone, there is a precipitation of carbonates and bioleaching processes [19]. The development of iron-oxidizing bacteria under aerobic conditions promotes the formation of Fe^{3+} , which interacts with phosphate to form insoluble compounds. The reduction of sulfate is accompanied by HM sulfides, which occur as follows [20]. CH_2O is organic carbon in these reactions, and Me^{2+} denotes the divalent cation HM (Figure 5).

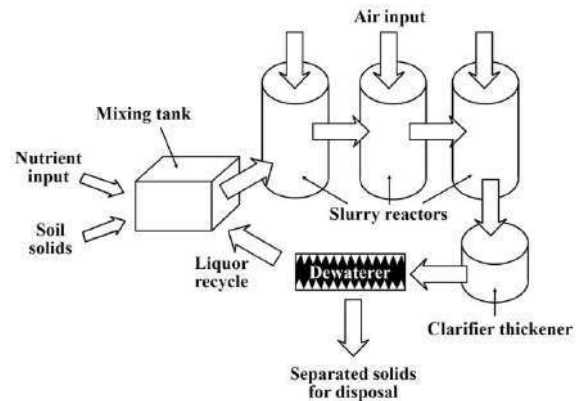


Figure 4 – Tillage using a sludge bioreactor

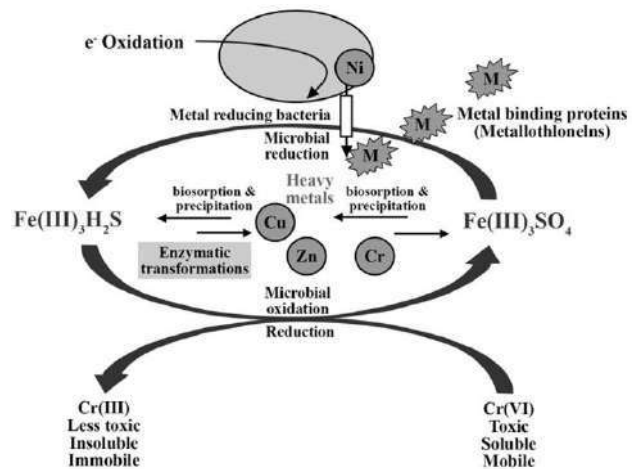


Figure 5 – Precipitation of metals from contaminated soil by microorganisms, based on [20]

The bioscreen can be organized by aerating a section of soil in a direction perpendicular to the movement of groundwater. The pollution can be biologically oxidized or desorbed by the airflow [21].

Methods of electrokinetic activation of biodegradation include the use of electric current, which provides the migration of microorganisms, with its charge, in the contaminated area and increase the speed, efficiency of uniform soil cleaning [22]. Ultrasound is used to activate biodegradation, which includes the destruction of large soil aggregates to increase the availability of contaminants to microorganisms [23].

Electrokinetic remediation is associated with the transmission of a direct electric current of low voltage (20–40 mA/cm²) with a potential difference of several volts through the ground for a specific time interval from 5–10 min to 120–150 min, which can be carried out in the place of contamination when the electrodes are installed in the soil in situ, or a specially equipped reactor [24].

Electrokinetics processes involve passing a low-intensity electric current between a cathode and an anode embedded in contaminated soil (Figure 6).

Ions and small charged particles, in addition to water, are transported between the electrodes. Anions move towards the positive electrode and cations towards the negative one. An electric gradient initiates movement by

electromigration (charged chemical movement), electro-osmosis (movement to fluid), electrophoresis (charged particle movement), and electrolysis (chemical reactions due to an electric field).

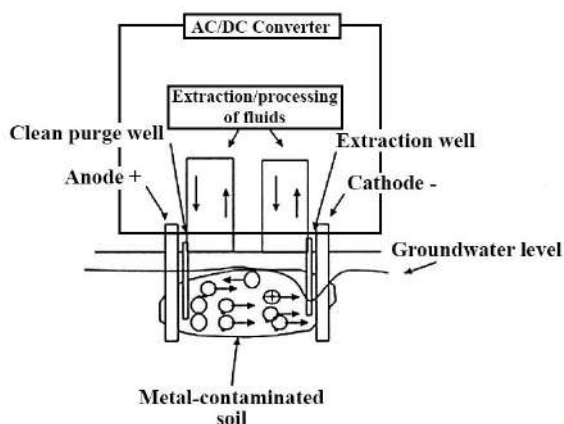


Figure 6 – Electrokinetic process for soil remediation (buffer solutions are added and removed by purge and extraction wells [25])

Improving soil aeration conditions also contributes to the biodegradation of soil contamination by blowing soils and groundwater with air at different pressures in combination with the introduction of nutrients through holes with air or spraying micro-particles of nutrient solutions.

A number of bioventilation screens are installed in the unsaturated zone. Air is blown in using a ventilator, and decomposition of the contamination is stimulated. Usually, a number of passive “air-emission screens” are located at appropriate distances depending on the characteristics of the contamination. Bioventilation stimulates biodegradation by blowing in the air, unlike soil vapor extraction, where contamination components are sucked out of the soil. The location of the contamination is significant. For example, this method should be considered where contamination is located under or close to a building (Figure 7).

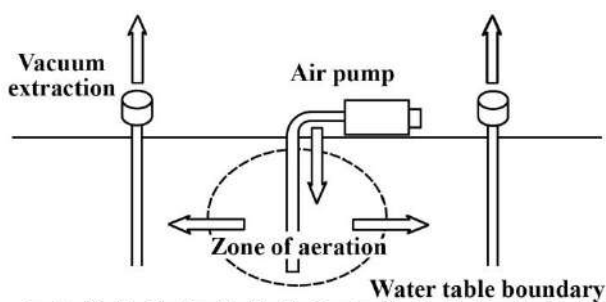


Figure 7 – Typical soil bioventilation system [26]

4.2 Development of a complex biotechnological solution for soil remediation

Previous studies [27] at the laboratory of Sumy State University modeled the mechanisms of influence of biogenic composite material based on sludge and phosphogypsum on soil protective functions and described the dynamics of soil microbial biome in the system “biotic component – biogenic product (digestate)– toxicant (HM)” with the stimulating effect of the biocomposite. This requires further determination of the ecological and biochemical aspects of the impact of organo-mineral bio-composite on the development of natural soil microorganisms and the process of formation of favorable biochemical conditions for the restoration of disturbed lands.

A clear and structured construction of the technological scheme of the movement of material flows is required to implement complex biotechnology of soil remediation.

The main organizational requirements for the biotechnology scheme include the following:

- ease of execution and automation of equipment;
- the expediency of placing equipment under the direction of material flows;
- selection of the optimal mode of operation of technological equipment - continuous or periodic;
- carrying out processes in constant conditions;
- greenhouse gas emissions from biological treatment systems (Figure 8);
- selection of the final product of processing.

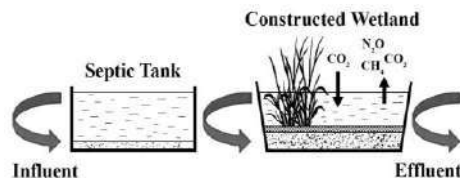


Figure 8 – Greenhouse gas emissions from biological treatment systems

A technological scheme of aerobic plants for soil biotodetoxification was developed (Figure 9).

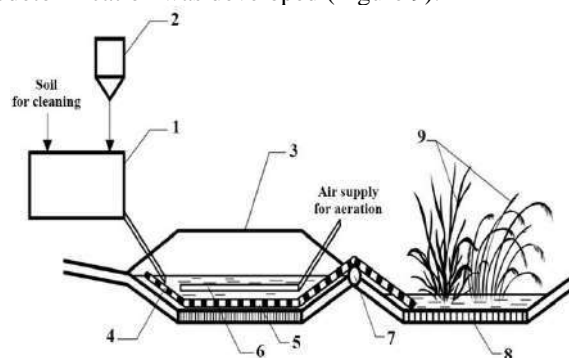


Figure 9 – Principle biotechnological scheme of soil biotodetoxification: 1 – hopper for mixing the crushed soil and biocomposite; 2 – batches for biocomposite supply; 3 – bioreactor; 4 - scraper conveyor; 5 - isolated bottom; 6 – aeration system; 7 – electric drive; 8 – platform; 9 – phytoremediation plants

The technological scheme works as follows. The crushed soil is contaminated with heavy metals, and the biocomposite fed from the dispenser enters the hopper for mixing. This mixture enters the bioreactor via a pipeline, made in a trench with an insulated bottom and a scraper conveyor, through which the soil is moved.

An aeration system is arranged above the conveyor, which air is supplied to the bioreactor to improve the aeration conditions. The bioreactor is equipped with an electric drive and is covered on top with a sealed opaque polymer coating.

Pre-cleaned soil with a scraper conveyor is fed to a particular site, where it is planted plants – remediates (9) for further cleaning, monitoring, and control of the content of pollutants.

Thus, cleaning the soil of heavy metals and restoring its fertility due to improved conditions for the development of soil microbiota is proposed in a two-stage process:

- 1) aerobic tillage together with the biocomposite;
- 2) stage of phytoremediation for purification.

5 Conclusions

The peculiarities of the processes of the heavy metal in the soil and the relationship with other components of the ecosystem are studied, and the factors on which the indicators of heavy metal adsorption depend are identified.

The existing methods of soil cleaning from heavy metals are reviewed, and it is substantiated that the restoration of technogenic contaminated soil with

biological methods is the most promising area that is developing dynamically and is considered environmentally friendly.

There are two groups of biological methods of soil purification, including methods using microorganisms and plant bioaccumulation and/or redistribution of pollutants in the soil while simultaneously affecting the biological and inert components of the soil. Features of bioaugmentation, the advantages, and disadvantages of this method are considered, and the influence of effectors, mainly chelated compounds, on the degradation of soil pollutants. Some of their features are determined based on a review of studies by foreign and domestic scientists.

A review of technological solutions for intensification of soil bioremediation processes, which will reduce the duration of treatment, using bioreactors, including fixed-layer reactors and suspension with stirring, analyzed methods, and technological means of activating the microflora, improving bioremediation processes improving aeration conditions by blowing the soil with air). Accordingly, a biotechnological scheme of soil detoxification has been developed and described, which has two stages: aerobic tillage and the biocomposite based on digestate, and stage of phytoremediation for purification and control of the content of toxicants in the soil.

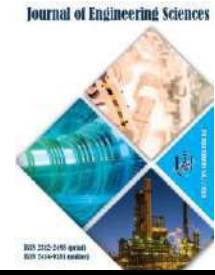
6 Acknowledgments

This research was carried out as a planned joint Ukrainian-Czech R&D project “Bioenergy innovations in waste recycling and natural resource management” (2021–2022).

References

1. Intergovernmental Forum on Chemical Safety Global Partnerships for Chemical Safety Contributing to the 2020 Goal. (2008). *Review of the problem of environmental pollution with cadmium, lead and mercury in Russia and Ukraine*. Retrieved from https://www.who.int/ifcs/documents/forums/forum6/eco_accord_ru.pdf.
2. Zhang, J., Cao, X., Yao, Z., Lin, Q., Yan, B., Cui, X., He, Z., Yang, X., Wang, C.-H., Chen, G. (2021). Phytoremediation of Cd-contaminated farmland soil via various *Sedum alfredii*-oilseed rape cropping systems: Efficiency comparison and cost-benefit analysis. *Journal of Hazardous Materials*, Vol. 419, 126489, doi: <https://doi.org/10.1016/j.jhazmat.2021.126489>.
3. Oladoye, P. O., Olowe, O. M., Asemoloye, M. D. (2021). Phytoremediation technology and food security impacts of heavy metal contaminated soils: A review. *Chemosphere*, 132555, doi: <https://doi.org/10.1016/j.chemosphere.2021.132555>.
4. Chernysh, Y. Y., Plyatsuk, L. D. (2018). Binding of heavy metals in the soil complex at the introduction biocomposite based on sewage sludge and phosphogypsum. *Young Scientist*, Vol. 1 (53). Retrieved from <http://molodyvcheny.in.ua/files/journal/2018/1/103.pdf>.
5. Pathak, P., Bhattacharya, D. (2021). Phytoextraction of heavy metals by weeds: Physiological and molecular intervention. *Handbook of Bioremediation. Physiological, Molecular and Biotechnological Interventions*, pp. 49–59, doi: <https://doi.org/10.1016/B978-0-12-819382-2.00004-1>.
6. Nedjimi, B. (2021). Phytoremediation: a sustainable environmental technology for heavy metals decontamination. *SN Applied Sciences*, Vol. 3, 286, doi: <https://doi.org/10.1007/s42452-021-04301-4>.
7. Biodegradation of hydrocarbons as a solution to the problem of oil pollution. Retrieved from <http://eco.com.ua/content/biodegradaciya-vuglevodniv-yak-vyrishennya-problemy-naftovogo-zabrudnennya>.
8. Nikovska, H. M., Ulberh, Z. R. (2003). *Method for removal of heavy metal and radionuclids from soil*. Patent of Ukraine, No. 58557.
9. Xinhui, D., Ping, T., Mengqi, M., Liang, M., Yunjun, Y., Zhenxing, W. (2021). The Study of Conditions for Bioleaching Heavy Metals from Polluted Soil and Metabonomics in *Penicillium chrysogenum*. *Journal of Biobased Materials and Bioenergy*, Vol. 15(1), pp. 117–124(8), doi: <https://doi.org/10.1166/jbmb.2021.2023>.

10. Nguyen, T. H., Won, S., Ha, M.-G., Nguyen, D. D., Kang, H. Y. (2021). Bioleaching for environmental remediation of toxic metals and metalloids: A review on soils, sediments, and mine tailings. *Chemosphere*, Vol. 282, 131108, doi: <https://doi.org/10.1016/j.chemosphere.2021.131108>.
11. Shtyka, O. S. Assessment of alternative remediation technologies of soils polluted with heavy metals. Retrieved from <http://tes.igns.gov.ua/materials/5n/Shtyka.pdf>.
12. Shweta, N., Samatha, S., Keshavkant, S. (2021). Mechanisms, types, effectors, and methods of bioremediation: The universal solution. *Microbial Ecology of Wastewater Treatment Plants*, pp. 41–72, doi: <https://doi.org/10.1016/B978-0-12-822503-5.00010-2>.
13. Raffa, C. M., Chiampo, F., Shanthakumar, S. (2021). Remediation of Metal/Metalloid-Polluted Soils: A Short Review. *Applied Sciences*, Vol. 11(9), doi: <https://doi.org/10.3390/app11094134>.
14. Akbari, S., Abdurahman, N. H., Yunus, R. M., Fayaz, F., Alara, O. R. (2018). Biosurfactants - a new frontier for social and environmental safety: A review. *Biotechnology Research and Innovation*, Vol. 2(1), pp. 81–90, doi: <https://doi.org/10.1016/j.biori.2018.09.001>.
15. Violante, A., Caporale, A. G. (2015). Biogeochemical processes at soil-root interface. *Journal of soil science and plant nutrition*, Vol. 15(2), pp. 422–448, doi: <http://dx.doi.org/10.4067/S0718-95162015005000038>.
16. Dobrovolsky, V. V. (2004). The role of soil organic matter in the migration of heavy metals. *Nature*, Vol. 7, pp. 35–39. Retrieved from http://vivovoco.astronet.ru/VV/JOURNAL/NATURE/07_04/35-39-0704.PDF.
17. Adejumo S.A., Togun A.O., Adediran J.A., Ogundiran M.B. (2011) Field Assessment of Progressive Remediation of Soil Contaminated with Lead-Acid Battery Waste in Response to Compost Application. *Pedologist*, pp. 182–193.
18. Balseiro-Romero, M., Monterroso, C., Kidd, P. S., Lu-Chau, T. A., Gkorezis, P., Vangronsveld, J., Casares, J. J. (2018). Modelling the ex situ bioremediation of diesel-contaminated soil in a slurry bioreactor using a hydrocarbon-degrading inoculant. *Journal of Environmental Management*, Vol. 246, pp. 840–848, doi: <https://doi.org/10.1016/j.jenvman.2019.06.034>.
19. Han, Zuozen, Dan Li, Hui Zhao, Huaxiao Yan, and Peiyuan Li. (2017). Precipitation of Carbonate Minerals Induced by the Halophilic Chromohalobacter Israelensis under High Salt Concentrations: Implications for Natural Environments. *Minerals*, Vol. 7(6), 95, <https://doi.org/10.3390/min7060095>
20. Li, J., Yang, H., Tong, L., Sand, W. (2021). Some Aspects of Industrial Heap Bioleaching Technology: From Basics to Practice. *Mineral Processing and Extractive Metallurgy Review*, doi: <https://doi.org/10.1080/08827508.2021.1893720>.
21. Yanin, E. P. (2014). Remediation of territories contaminated with chemical elements: general approaches, legal aspects, main methods (Foreign experience). *Environmental and natural resource issues*, Vol. 3, pp. 3–105. Retrieved from http://www.nparso.ru/images/docs/Remediation_of_the_territories.pdf.
22. Rosestolato, D., Bagatin, R., Ferro, S. (2015). Electrokinetic remediation of soils polluted by heavy metals (mercury in particular). *Chemical Engineering Journal*, Vol. 264, pp. 16–23, doi: <https://doi.org/10.1016/j.cej.2014.11.074>.
23. Hazrati, S., Farahbakhsh, M., Cerdà, A., Heydarpoor, G. (2021). Functionalization of ultrasound enhanced sewage sludge-derived biochar: Physicochemical improvement and its effects on soil enzyme activities and heavy metals availability. *Chemosphere*, Vol. 269, 128767, doi: <https://doi.org/10.1016/j.chemosphere.2020.128767>.
24. Cameselle, C., Gouvei, S., Akretche, D. E., Belhadj, B. (2013). *Advances in Electrokinetic Remediation for the Removal of Organic Contaminants in Soils*. Organic Pollutants - Monitoring, Risk and Treatment, M. Nageeb Rashed, IntechOpen, doi: 10.5772/54334.
25. Jankaitė, A., Vasarevičius, S. (2005). Remediation technologies for soils contaminated with heavy metals. *Journal of Environmental Engineering and Landscape Management*, Vol. 13(2), pp. 109–113, doi: 10.3846/16486897.2005.9636854.
26. Guidelines on remediation of contaminated sites. Retrieved from https://www2.mst.dk/udgiv/publications/2002/87-7972-280-6/html/kap09_eng.htm.
27. Chernysh Y., Ablicieva I., Makarekno N., Plyatsuk L., Trunova I., Burla O. (2021) Investigation of the directions of using a hybrid composition bioproduct for detoxification of a soil ecosystem contaminated with heavy metals and oil products. *Biodiversity & Environment*, Vol. 13(1), pp. 80–94.



Copyright Agreement

We, the Authors of the Article publishing in the Journal of Engineering Sciences, in the case of acceptance for publication, transfer to Founders and Editorial Board the underlined rights:

- publishing this article in English and distribution of the printed version;
- English translation of the article and distribution of the hard copy of the translation;
- distribution of the electronic version of the article through any electronic means (by hosted on the official website of the Journal, in electronic databases, repositories, etc.).

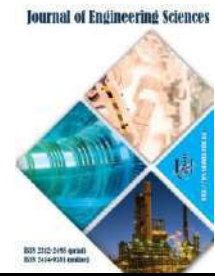
We reserve the rights without the consent of the Editorial Board or Founders:

- to use the article materials partially or in whole for educational purposes;
- to use the article materials partially or in whole to write own dissertations;
- to use the article materials for thesis preparing, conference materials, as well as for presentations;
- to post electronic copies (including the final electronic version downloaded from the official website of the Journal):
 - on the personal web-sources of all the co-authors (websites, webpages, blogs, etc.);
 - on the web-sources of authors working organizations (including electronic institutional repository);
 - on the International scientometric databases;
 - on non-commercial open-access sources.

In all cases, the presence of citations to the article or hyper-link to the electronic copy of the journal's official website is obligatory.

By this agreement, we also certify that the submitted article:

- does not violate the copyrights of other persons or organizations;
- has not been published previously in other publishing houses and submitted for publication in other Journals.



Dear Authors of the Journal of Engineering Sciences!

The Editorial Board of the Journal of Engineering Sciences pays special attention to the structure of the articles according to the **List of Scientific Professional Editions of Ukraine** (Category “B”, Minutes No. 1208 of 07.11.2018, Appendix No. 8). Only original articles by the authorship of up to 5 authors are accepted for publication according to the **Template** with the following elements:

- general statement of the problem and its relationship with the essential scientific or practical problems;
- analysis of the recent investigations and publications in the same research field;
- statement of the significance of the general problem that was not solved before;
- statement of the purpose of the research article;
- description of the initial data of the research with the justification of the achieved scientific results;
- conclusions and ways for further development of the research.

All the articles are reviewed by the independent double-blind procedure.

All the authors should send via e-mail jes@teset.sumdu.edu.ua the electronic version of the following materials:

- article **in English** according to the **Template**;
- information about authors and their affiliation with the related address.

ATTENTION!

If one of the mentioned components is not sent or there are many stylistic, orthographic, and grammatical errors, the article will not be considered by the Editorial Board and will not be reviewed.

The minimum size of the materials:

1. Scientific – theoretical articles (up to 25,000 symbols; about 14 pages) that deal with the theoretical research and descriptions of physical laws concerning the investigated phenomena; theoretical generalizations and fundamental principles proved by the experimental research data.
2. Scientific-practical articles (up to 10,000 symbols; about 6 pages) that deal with scientific experiments and recent experience. They include the proposed methods for the experimental research or means to observe the studied phenomena. An essential part of these articles is the description of the achieved results and their explanation acquired in immediate interaction with the object of investigations, its significance, and practical implementations.
3. Scientific-methodological articles (up to 15,000 symbols; about 8 pages) that deal with the review of processes, methods, instruments for solving scientific and applied problems; the statement of the new methodology, results of which allow creating more precise methodology based on an up-to-date methodology for the implementation of discovered laws.

Ministry of Education and Science of Ukraine
Sumy State University

JOURNAL OF ENGINEERING SCIENCES

Scientific Journal

Volume 8, Issue 2 (2021)

Відповідальний за випуск

I. В. Павленко

Комп'ютерне складання та верстання:

X. В. Берладір

Обкладинка:

V. O. Іванов

Коректор:

C. M. Симоненко

Responsible for release:

Ivan Pavlenko

Computer design and typesetting:

Kristina Berladir

Cover page:

Vitalii Ivanov

Corrector:

Svitlana Symonenko

Підписано до друку 30.06.2021. Формат 60x84/8.

Папір офс. Друк офс.

Ум. друк. арк. 17,91. Обл.-вид. арк. 24,36.

Наклад 100 прим. Замовлення №

Сумський державний університет, вул. Римського-Корсакова, 2, 40007, м. Суми, Україна

Свідоцтво про внесення суб'єкта видавничої справи до Державного реєстру

ДК № 3062 від 17.12.2007.

Надруковано у друкарні Сумського державного університету,
вул. Римського-Корсакова, 2, 40007, м. Суми, Україна

Editorial Board: 2, Rymkogo-Korsakova St., 40007, Sumy, Ukraine; Apt. M-211
Contact Phones: +380-993-845-740
E-mail: jes@teset.sumdu.edu.ua
Website: <https://jes.sumdu.edu.ua>

State registration certificate of the print mass-media No. 20499-10299 PR.